Université de Strasbourg

UNIVERSITÉ DE STRASBOURG

ECOLE DOCTORALE pcp

ÉCOLE DOCTORALE DE PHYSIQUE ET CHIMIE PHYSIQUE

Institut Pluridisciplinaire Hubert Curien

THÈSE présentée par:

Markéta JANSOVÁ

soutenue le: **27 Septembre 2018**

pour obtenir le grade de: **Docteur de l'université de Strasbourg**

Discipline/Spécialité: Physique des particules

Recherche du partenaire supersymétrique du quark top et mesure des propriétés des dépôts dans le trajectographe à pistes de silicium de l'expérience CMS au Run 2

THÈSE dirigée par:

Mme. COLLARD Caroline Institut Pluridisciplinaire Hubert Curien

RAPPORTEURS:

M. KAJFASZ Éric Centre de Physique des Particules de Marseille

M. TROCMÉ Benjamin Laboratoire de Physique Subatomique & Cosmologie Grenoble

---

AUTRES MEMBRES DU JURY:

Mme. BOUDOUL Gaëlle Institut de Physique Nucléaire de Lyon

M. BAUDOT Jérôme Institut Pluridisciplinaire Hubert Curien, Unistra

M. CHABERT Éric Institut Pluridisciplinaire Hubert Curien, Unistra

Acknowledgements

During my three years of PhD, I was fortunate to have many people who supported me and at this point, I would like to warmly thank them for it.

Especially I would like to thank my supervisors, Caroline and Eric. I am very pleased that they chose me from the large spectrum of candidates and that they always found time for me when I needed them. I would like to thank them for their trust in me to do my work well and for giving me a lot of freedom. I would like to thank Caroline for thoroughly correcting this thesis with calmness and a good mood even though this was a difficult task to do. I would also like to thank her for always bringing an interesting angle to any discussion. I would like to thank Eric for many hours spent discussing with me and for the patience during these discussions. I would like to thank him that he always listened to my arguments and ideas, tried to understand them and to prove me wrong or right. I would also like to thank him that during these years he tried to develop my skills on many levels from the scientific to the pedagogical. Sometimes it was hard but it paid off.

I would also like to thank remaining colleagues in the CMS group for providing me help or advice when I needed it. I would especially like to thank my friends from the CMS group and outside for patiently listening to my complaints, distracting me from my problems and spending the out-of-work time with me. I would like to thank them for all the fun we had.

One big thank you also belongs to my mum and dad. They warmly supported me in doing this PhD and always tried to cheer me up when I was down. I also have to thank my fiancé who was the target of the majority of my complaints, but despite that, he stayed with me. I am truly grateful to have my parents and my fiancé in my life. I cannot imagine finishing this thesis without them.

Contents

Introduction

This thesis started in October 2015, the same year as the beginning of the Run 2 data-taking period (2015-2018) during which the center-of-mass energy, the instantaneous luminosity and the bunch crossing frequency was increased compared to the Run 1 (2008-2013). Consequently, the possibilities for physics analyses were largely extended with a price of a larger fluence on the detector side, especially on the tracker which is the inner subdetector. With this increasing fluence, the detector suffers from a larger irradiation which could be a cause of performance issues. Moreover, the detector is also ageing with irradiation, leading to a change of some of its characteristics. Therefore it is very important to monitor closely the detector, to keep its stable performance and consequently the potential physics reach.

Particle physics is described by the standard model whose last piece, the Higgs boson, was discovered in 2012 by the CMS and ATLAS collaborations. Although the standard model is now complete and in general describes excellently the physics phenomena, it suffers from several shortcomings. This issue makes us believe that the standard model is an effective theory at low energy of a more fundamental theory which is to be determined. Over years, many theories were proposed and one, referred to as supersymmetry, became of a special interest due to its capability to address many of the standard model shortcomings.

Supersymmetry introduces a new partner to each standard model particle and therefore extensive searches for these particles have been performed by the CMS collaboration as well as other collaborations. One of these particles is the supersymmetric partner of the top quark, the stop, which is expected to have a mass around 1 TeV in natural supersymmetry and therefore be accessible at the LHC energies. No evidence for the stops was found in Run 1, but the increase in luminosity as well as the center-of-mass energy in Run 2 allows us to probe the stop masses beyond the Run 1 exclusion.

The description of the Compact Muon Solenoid (CMS) detector is given in the first chapter, Chapter 1, together with a brief introduction of the Large Hadron Collider. This chapter focuses on the silicon strip tracker, whose deeper understanding is required for the following chapters. This chapter also presents the reconstruction of the physics objects corresponding to particles passing through the detector.

In Chapter 2 a study of Highly Ionizing Particles (HIP) in the strip tracker is presented, motivated by the observation of the inefficiencies in tracking during years 2015 and 2016. These HIPs are induced by inelastic nuclear interactions in the sensitive volume of the tracker. The front-end electronics of the strip tracker is not designed to cope with the large HIP energy deposits, therefore a HIP interaction saturates the electronics and induces a dead-time. This chapter presents two studies I performed during my PhD on the HIPs. They lead to the first measurement, with the CMS data, of the probability that a HIP occurs in the tracker.

The third chapter, Chapter 3, focuses on the simulation of the CMS strip tracker. In order to be able to compare the results of the experiment with the theoretical expectations, the interactions of generated particles with the detector must be simulated. This chapter describes how the simulation in the strip tracker is implemented and how it can be improved. It is shown that several tracker properties and conditions are taken as parameters in the simulation. With the ageing of the detector these properties evolve and therefore need to be remeasured and updated in the simulation. In this chapter, I identify which parameters need to be reevaluated. In this context, a measurement of the cross talk, resulting from the capacitive coupling between neighboring strips, is presented using cosmic data. The impact of the newly measured cross talk parameters on the simulation is presented as well.

After an introduction of both SM and SUSY in Chapter 4, the search for the stop is presented in Chapter 5 in the single lepton final state with the data of Run 2 recorded in 2016 corresponding to an integrated luminosity of 35.9 fb^{-1}. In this analysis I was mainly responsible for the estimation of one of the SM backgrounds entering into the targeted signal regions. I also tried several options to improve the analysis performance (i.e. W-tagging).

Chapter 1

The CMS experiment at the LHC

There are several options how to study elementary particles, for example it can be studied via cosmic rays, astrophysical neutrinos, direct searches for the dark matter or at collider experiments. In Section 1.1 the largest existing collider, the LHC, and its experiments are introduced. In Section 1.2 the CMS detector, in which context this thesis is performed, is described. Then in Section 5.2.3, the object reconstruction techniques of the CMS collaboration applied on the CMS data are introduced. A special interest is put on the topics whose a deeper understanding is required for the following chapters of this thesis.

1.1 The Large Hadron Collider

The Large Hadron Collider (LHC) [1] is a particle accelerator with a circumference of 27 km, which is a part of the CERN accelerator complex [2] located near Geneva, Switzerland. The LHC project was approved in 1994 and designed to provide mainly collisions of protons. Part of the LHC operation time is also dedicated to collisions of heavy nuclei, but in this thesis only the proton collisions are described.

A schematic view of the CERN accelerator complex with its main experiments is presented in Fig. 1.1 [3]. At the beginning of the acceleration process the protons are obtained by stripping electrons from the hydrogen atoms. Protons are then accelerated through a chain of accelerators: Linac2, Booster, Proton Synchrotron (PS) and Super Proton Synchrotron (SPS). The proton beams accelerated to 450 GeV are injected from the SPS into the LHC using separate pipes, one beam turning clockwise and the other one anti-clockwise. In the LHC, the beams are further accelerated with eight radio-frequency (RF) cavities per beam, currently to the beam energy of 6.5 TeV. The LHC is equipped with 9593 magnets, mainly dipoles and quadrupoles, to bend and focus the beams. There is an ultrahigh vacuum of order of $10^{-10} - 10^{-11}$ mbar in the LHC tube to

avoid collisions of particles with gas. A vacuum of around 10^{-6} mbar is also used for the isolation of cryomagnets and the helium distribution line.

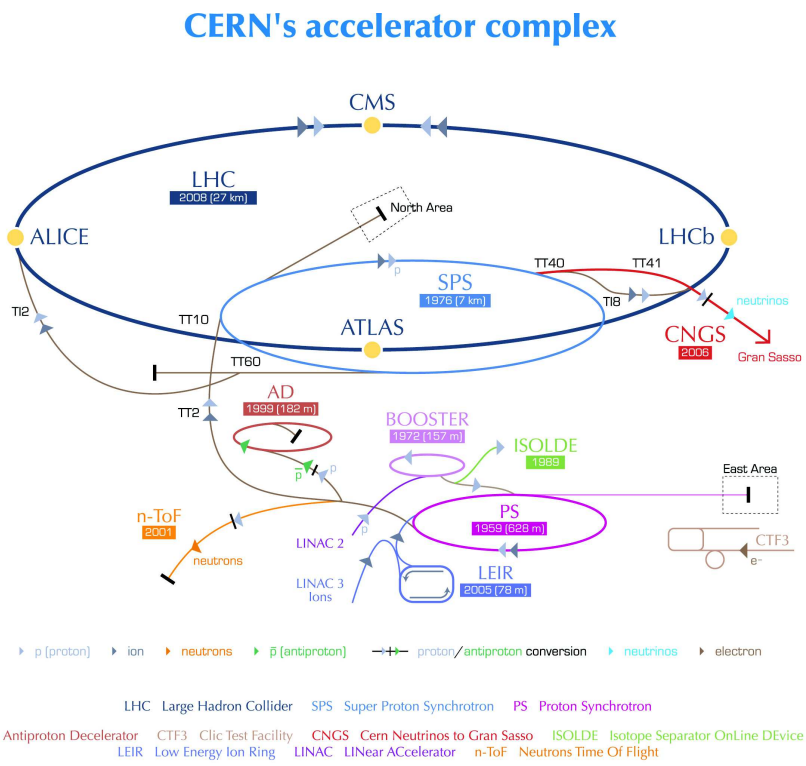

Figure 1.1: The CERN accelerator complex [3].

The proton beams are not homogeneous but composed of trains of bunches, each bunch containing around 100 billions of protons. Bunches within a given train are spaced by 25 ns. Time gaps between two different trains are longer, their duration depends on the beam structure and currently they start from seven times 25 ns. The LHC uses several beam structures, which are specified by the filling scheme. An example of a beam structure is shown in Fig. 1.2.

Up to now, the LHC operation has been divided into two eras, Run 1 and Run 2. The Run 1 started in 2008 and ended in 2013. During this era the center-of-mass energy of the pp collisions was first 7 TeV, then it was increased to 8 TeV in 2012, and the beam structure allowed collisions every 50 ns. The Run 2 started in 2015 and is still ongoing. In the Run 2 the collision center-of-mass energy increased to 13 TeV and the time between collisions was reduced to 25 ns. The Run 2 stops at the end of 2018, the Run 3 is scheduled to start in 2021.

The bunches of protons collide at four interaction points (IP), at which four main experiments are installed. The two general-purpose detectors, which are designed to cover

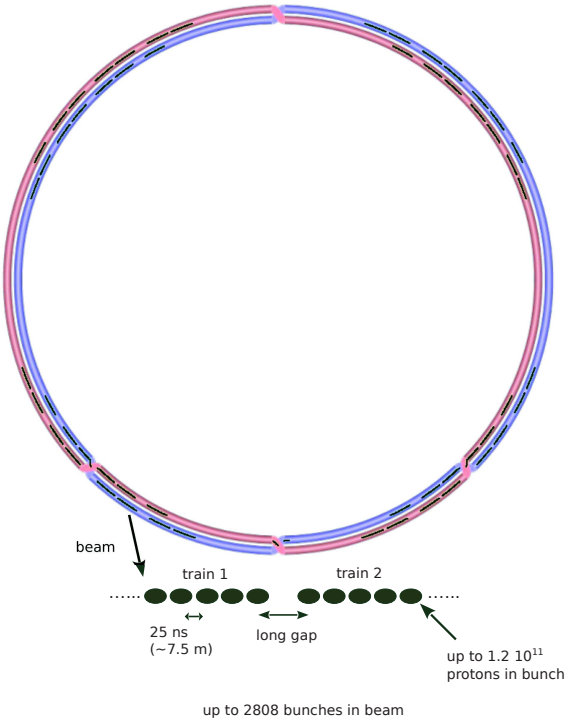

Figure 1.2: (top) An example of beam structure. The beam pipes are shown in red and violet and the beams are drawn in green. (bottom) An example showing the structure of two trains.

a wide range of physics, are ATLAS (standing for "A Toroidal LHC ApparatuS") [4] and CMS (standing for "Compact Muon Solenoid") [5]. The other two main experiments are ALICE (standing for "A Large Ion Collider Experiment") [6], mainly focusing on the physics of heavy-ion collisions and the study of the "quark-gluon plasma" which existed at the early Universe, and the LHCb (standing for "Large Hadron Collider beauty") [7] specialized in the physics of the b-quark. There are also three smaller experiments along the LHC, one of them is TOTEM [8] which is close to CMS and its principal goal is to measure the total cross section of protons at the LHC. LHCf [9], which is located near to the ATLAS experiment, studies particles moving very close to the proton beams. Finally MoEDAL [10], which is close to LHCb, focuses on the search of hypothetical particles, e.g. magnetic monopoles.

One of the main motivations for the LHC and its experiments was the search for the Higgs boson. After its discovery in 2012 by the ATLAS and CMS collaborations, the measurement of the Higgs boson properties has now entered into the physics program. A second important topic of research is the search for new particles and more generally for evidence of physics beyond the Standard Model, motivated mainly by cosmological observations, naturalness of the Higgs mass and the desire for unification of known interactions.

1.2 The Compact Muon Solenoid detector

The CMS ("Compact Muon Solenoid") detector [5] is a multipurpose detector of an overall length of 22 m, a diameter of 15 m and a weight of 14 t, located at the IP 5. The designed properties [11] of the CMS detector were to have high a quality tracking providing precise charged-particle momentum measurement and resolution around 1%-2% for 10 GeV muons in the majority of the CMS coverage being $|\eta| < 2.4$ and to have high efficiency of muon identification and reconstruction, leading to a requirement on a dimuon mass resolution of the order of 1% at 100 GeV. Furthermore it was designed to have the best possible measurement of the electromagnetic energy, leading to a resolution of diphoton and dielectron masses of around 1% at 100 GeV. These conditions have to be fulfilled in the LHC environment, with a bunch crossing (bx) every 25 ns, where every bunch crossing leads to tens of inelastic interactions on top of the interaction of the interest, referred to as "pileup" (PU), resulting in thousands of charged particles in the CMS detector every 25 ns. Because of this large radiation, the detectors and front-end electronics have to be radiation-hard.

To achieve the given requirements, CMS was built in layers around a large solenoidal magnet, with endcaps at each side. The CMS magnet is a superconducting solenoid providing a magnetic field of 3.8 T. The magnet is surrounded from outside by the steel yoke which returns the magnetic flux of the solenoid [12]. The radius of the magnet has to be kept relatively small and therefore the available space between the magnet and interaction point is limited.

Inside the magnet from the interaction point outwards, there is a pixel and silicon strip tracker, followed by the electromagnetic and hadron calorimeters. Outside of the magnet there is the outer hadron calorimeter and the steel return yoke with embedded muon chambers. The CMS detector layout is shown in Fig. 1.3 [13]. In the following sections, first the coordinate system of the CMS is described. Then the CMS subdetectors are introduced, starting from the innermost one. At the end, basic information on trigger, luminosity and pileup is given.

1.2.1 Coordinate system and conventions

The coordinate system used by CMS [5] is sketched in Fig. 1.4 [14]. In the CMS conventions, the cartesian coordinate system is centered at the IP, with the x-axis pointing into the center of the LHC, the y-axis going upwards and the z-axis going anti-clockwise along the beam direction. The azimuthal angle Φ is defined in the x-y plane and is mea-

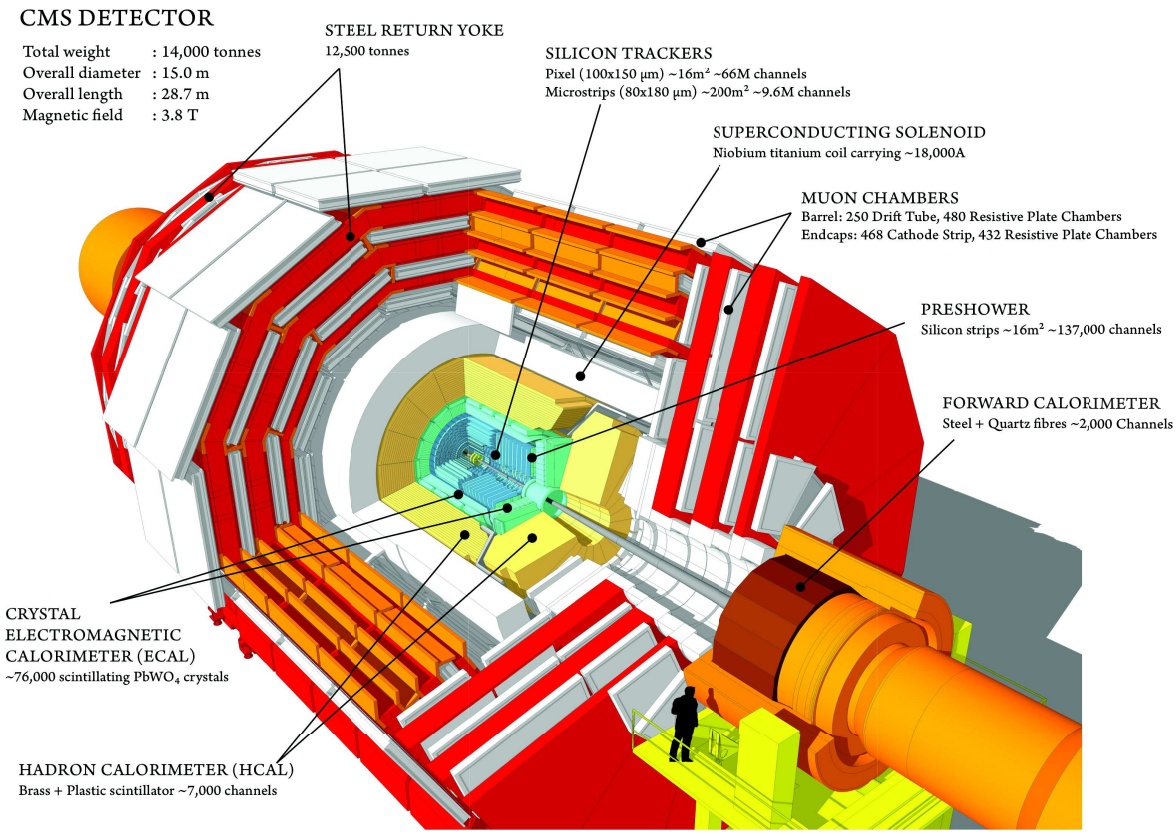

Figure 1.3: A schematic layout of the CMS detector [13].

sured from the x-axis. The polar angle θ is measured from the z-axis and is defined in the y-z plane. Finally r is a radial coordinate in the x-y plane. In this convention the pseudorapidity η is defined as

$$\eta = -\ln\left[\tan\left(\frac{\theta}{2}\right)\right]. \tag{1.1}$$

The angular distance between two points can be measured with the help of ΔR defined as

$$\Delta R = \sqrt{\Delta\Phi^2 + \Delta\eta^2}. \tag{1.2}$$

The transverse momentum p_T can be computed from the x and y momentum components as

$$p_T = \sqrt{p_x^2 + p_y^2}. \tag{1.3}$$

At the interaction point, the partons in proton beams have negligible momentum in

the x-y plane, and therefore the sum of momenta of all particles originating from the collision in this plane should be zero due to momentum conservation law. Therefore an imbalance of momenta in this plane, i.e. a non-zero total p_T, can be a sign of particles whose momentum is unmeasured, like neutrinos or hypothetical new particles.

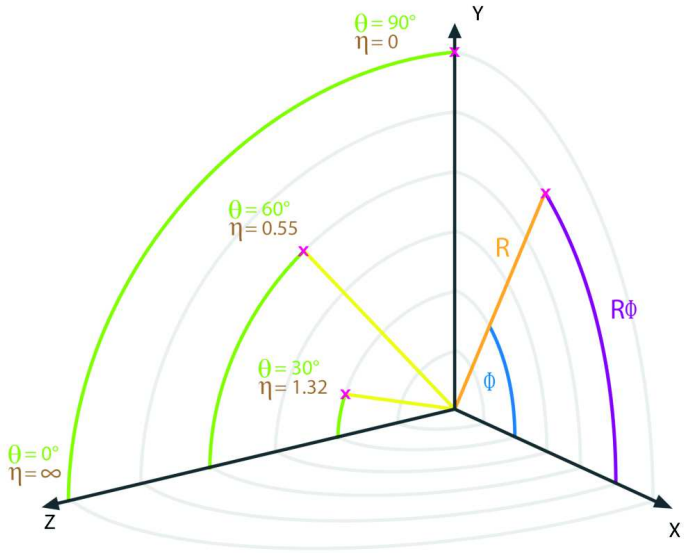

Figure 1.4: The CMS coordinate system with the three axes intercepting at the interaction point, the x-axis pointing inside the LHC ring, the y-axis going upwards and the z-axis pointing anti-clockwise along the beam [14].

1.2.2 The silicon tracker

The silicon tracker [15, 16] is the innermost subdetector of the CMS detector. The CMS tracker is divided into two parts, the inner (outer) part consists of a pixel (strip) detector. Its purpose is to reconstruct tracks from charged particle depositions, energy losses E_{loss}, in silicon sensors. In order to recognize from which interaction a given particle originates, the tracker is required to have a capability to reconstruct primary and secondary vertices. The reconstruction of primary vertices targets to find the positions where the interaction of interest or the PU interaction occurred. The primary vertices are determined by the vertex fitting procedure from the tracks [17]. The goal of the secondary vertex reconstruction is to spot the place where a particle with a long lifetime decays to other particles.

On the tracker level, the tracking is performed in 4 steps [18, 19]. It starts from hits reconstructed from particle depositions in the sensors. First, the *track seeding* is performed from three 3-D reconstructed hits in pixel and/or strip tracker or from two 3-D hits with a constraint on the beam spot. Then the algorithm proceeds with *track building* which aims to connect all hits originating from one particle. During the track building

the track is propagated to the neighboring layers of the tracker, testing the compatibility of the reconstructed hit with the track by a χ^2 test. Once the full track candidate is complete, the *track fitting* is performed to obtain the best parameters of the track and to recompute precisely the hit position using the track properties. The last step is a *track quality selection* rejecting tracks not fulfilling quality requirements, which are based on the χ^2 of the final fit, the number of layers with a hit associated to the track and the probability of the track to originate from the primary vertex.

The default track reconstruction [20] is using the software referred to as the Combinatorial Track Finder (CTF), based on the combinatorial Kalman filter [21]. The tracking uses an iterative approach: in the first iteration the easiest tracks to find are reconstructed (i.e. the ones with the highest p_T), then after these tracks are complete their hits are masked in order to avoid duplicities and reduce combinatorics for further iterations of tracks finding. In total there are 12 iterations and each iteration is focused on a specific type of tracks.

Due to the presence of the magnetic field, charged particles are bent according to their momentum and charge, thus the CMS tracker is able to measure the charge sign and the momentum associated to a track. To perform so, the tracker needs to have a good spatial resolution. It has to be as well extremely radiation-hard due to the large flux of incoming particles. Also the material was chosen carefully, in order to reduce multiple scattering, nuclear interactions or bremsstrahlung in the tracker material.

The flux of particles in the CMS detector decreases with the distance from the interaction point, the flux of charged particles in the barrel at a radius of 4 cm is around 10^8 cm^{-2}s^{-1} while at a radius of 115 cm it decreases to around 3×10^5 cm^{-2}s^{-1}. Consequently, the inner part of the tracker is made of silicon pixels, which are able to measure particle paths and their properties in a high particle density environment. Moreover a good resolution is needed for the vertex determination. In the outer part of the tracker, the particle density is low enough to use silicon strip sensors, which are cheaper mainly because they require less readout channels. Overall, the tracker pseudorapidity coverage is $|\eta| < 2.5$.

The silicon pixel tracker

Before 2017, the pixel barrel, referred to as BPIX, was located at a radius of 4.4 cm up to 10.2 cm, from the IP. The pixel endcaps (FPIX) extended on each side from 35 cm to 47 cm in the z direction. In total, there were three barrel layers and two endcaps layers on each side. During an extended winter shut-down in 2017, due to the high radiation exposure, the pixel tracker was replaced. The new pixel tracker has four barrel layers covering $3 \leq r \leq 16$ cm and three endcap disks at distances $29.1 \leq |z| \leq 51.6$ cm. The pixel

detector plays a crucial role in the track seeding, and the reconstruction of the primary and secondary vertices [22].

Silicon strip tracker

As the following chapters present studies of the silicon strip tracker and its simulation, let take now a deeper look into its design and properties. The silicon strip tracker is divided into four partitions. Each partition is composed by several layers of modules, which have either one side (mono) or two sides (stereo) of silicon sensors. In total the strip tracker is composed of 15148 modules. The Tracker Inner Barrel (TIB) is the innermost barrel part with two layers of stereo modules succeeded by two layers of mono modules. The Tracker Outer Barrel (TOB) surrounds the TIB. In the innermost part of TOB, there are two layers of stereo modules, the remaining four layers being mono. On each side of the barrel, Tracker Inner Disks (TID) and Tracker EndCaps (TEC) are located. There are three wheels (perpendicular to the z-axis) of TID with three module rings (parallel to the z-axis) and 9 wheels of TEC with four to seven rings of modules on each side. In each wheel there is a mixture of mono and stereo modules, but each ring has either mono or stereo modules.

In the barrel region, the silicon tracker is placed in radius between 20 cm up to 1.1 m from the IP. The disks start at 80 cm in the z-direction from the IP and the endcaps reach up to z=2.8 m from the IP. The overall layout of the silicon strip tracker can be seen in Fig. 1.5 [20].

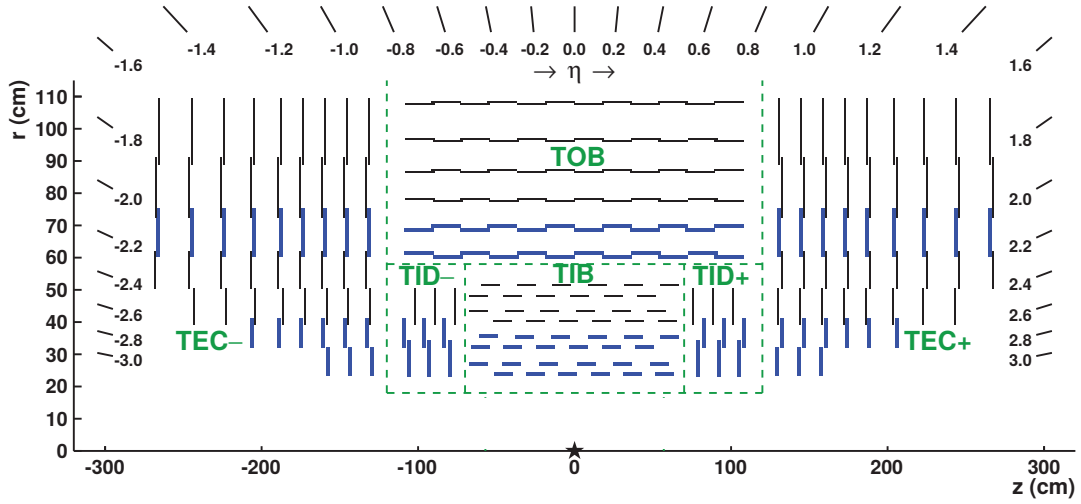

Figure 1.5: A schema of the longitudinal view of the upper half of the CMS silicon strip tracker and layout of its partitions. The star represents the IP. The modules in blue are stereo, while the mono ones are shown in black [20].

Each mono module holds 320 μm or 500 μm thick silicon sensors with either 512 or 768 silicon strips. The strip length range is from 8 to 25 cm. The distance between strips,

called pitch, varies between around 80 μm and 200 μm. In the barrel, the strips are parallel to the z-axis, or tilted by 100 mrad with respect to the z-axis in case of the stereo sensors. In TID and TEC, the strips are not parallel to each other and are aligned to be parallel to r, or tilted by 100 mrad with respect to the r in case of the stereo sensors. The strip width to pitch ratio is equal to 0.25.

The local module coordinates have their zero in the middle of the module, the z-axis going in the direction from the back-plane to the strips, the y-axis going along the strips, and the x-axis being perpendicular to the strips and traversing them. The local θ angle is measured from the z-axis. The local Φ is defined in the x-y plane and measured from the x-axis. The schematic view of the sensor local coordinates is shown in Fig. 1.6. The details about the module geometries for each layer of TIB and TOB and each ring of TID and TEC can be found in Table 1.1 [23].

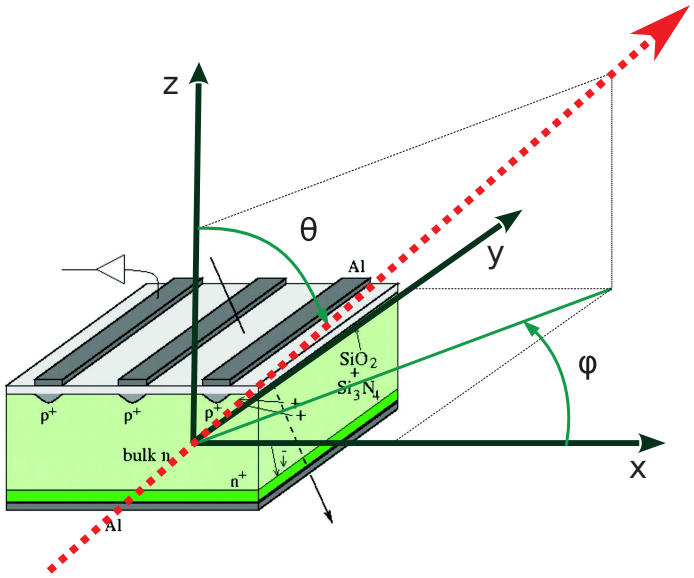

Figure 1.6: The sensor local coordinate system with the three axes intercepting in the middle of the sensor. The x-axis is perpendicular to the silicon and aluminium strips (represented by the dark gray bands on the top of the drawing), the y-axis goes along the strips and the z-axis points from backplane (represented at the bottom by the dark gray/green surface) to the strips.

The track resolution in p_T determined in 2011 before replacing the pixel detector, is of the order of 1.5% for non-isolated particles in the range $1 < p_T < 10$ GeV and $|\eta| < 1.4$ and of order of 2.8% for particles with $p_T = 100$ GeV and $|\eta| < 1.4$ [24]. The performance in p_T resolution is comparable after the upgrade as before. The spatial resolution of reconstructed hits for different barrel layers of the strip tracker is shown in Fig. 1.7 [25]: The typical strip hit resolution ranges between 15 and 45 μm in the barrel region of the silicon strip tracker.

Layer	Type	#Strips	Thickness [μm]	Pitch [μm]	Geometry label
TIB L1	stereo	768	320	80	IB1
TIB L2	stereo	768	320	80	IB1
TIB L3	mono	512	320	120	IB2
TIB L4	mono	512	320	120	IB2
TOB L1	stereo	768/512	500	122/183	OB2
TOB L2	stereo	768/512	500	122/183	OB2
TOB L3	mono	512	500	183	OB2
TOB L4	mono	512	500	183	OB2
TOB L5	mono	768	500	122	OB1
TOB L6	mono	768	500	122	OB1
TID R1	stereo	768	320	81...112	W1a
TID R2	stereo	768	320	113...143	W2a
TID R3	mono	512	320	124...158	W3a
TEC R1	stereo	768	320	81...112	W1b
TEC R2	stereo	768	320	113...143	W2b
TEC R3	mono	512	320	124...158	W3b
TEC R4	mono	512	320	113...139	W4
TEC R5	stereo	768	500	126...156	W5
TEC R6	mono	512	500	163...205	W6
TEC R7	mono	512	500	140...172	W7

Table 1.1: Module type, strip multiplicity, sensor thickness and pitch and module geometry label for layers or rings of the four silicon strip tracker partitions [23].

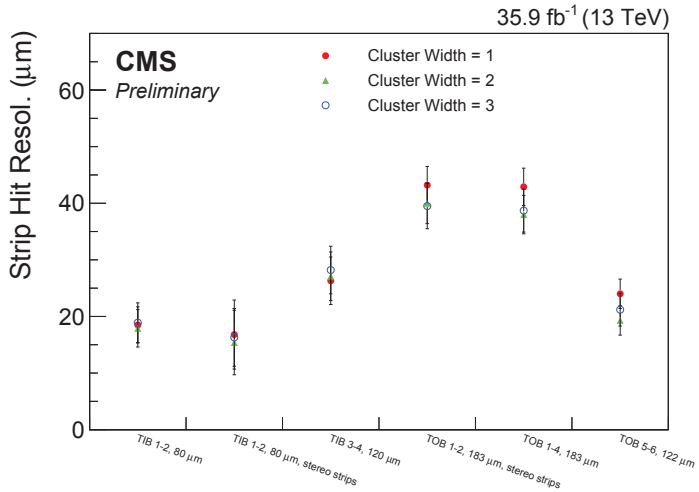

Figure 1.7: Measured resolution of reconstructed hit position for different layers of the strip tracker and different size of pitch between the strips. The red color corresponds to hits with a charge deposited in one strip, green in two strips and blue in three strips [25].

1.2.3 The electromagnetic calorimeter

The electromagnetic calorimeter (ECAL) [26] is a subdetector located on the outer side of the silicon tracker. In the barrel region the ECAL extends up to a radius of 1.77 m

from the IP. It is an homogeneous, fast, radiation resistant calorimeter with a good energy resolution. It is composed of 75848 lead-tungstate ($PbWo_4$) crystals and its purpose is to measure the energy of electrons and photons. The ECAL consists of one barrel (EB) covering $|\eta| < 1.479$ and two endcaps (EC) extending the coverage up to $|\eta| = 3$. A preshower is placed in front of the endcaps in order to separate highly energetic single photons from the photons originating from the decay of neutral pions. In the barrel part the ECAL has 25.8 radiation lengths in the radial direction, and in the endcap part 24.7 interaction lengths in the z-direction.

The energy resolution σ_E of the ECAL was determined [5] to be

$$\frac{\sigma_E}{E} = \frac{0.028}{\sqrt{E}} \bigoplus \frac{0.12}{E} \bigoplus 0.003, \tag{1.4}$$

where E is the energy. The first term ($\propto 1/\sqrt{E}$) is the stochastic part, it corresponds to e.g. fluctuations in number of particles. The second term ($\propto 1/E$) accounts for noise and the third term (constant) covers mainly the non-uniformities, energy leakage and inter-calibration issues.

1.2.4 The hadron calorimeter

The purpose of the hadron calorimeter (HCAL) [27] is to measure the energy of strongly interacting particles. The HCAL is a sampling calorimeter composed of four parts, out of them two are located between the ECAL and the magnet, which are the HCAL Barrel (HB) and Endcaps (HE). Both HE and HB have a brass absorber and their active material is made of plastic scintillators. The pseudorapidity coverage of HB is $|\eta| < 1.3$, and of HE $1.3 < |\eta| < 3$. The length of the HB in interaction lengths in the radial direction is around 6, and of the HE in the z-direction of around 10. The coverage is further extended up to $|\eta| = 5.2$ by the third part called the Forward calorimeter (HF). Installed 11.2 meters from the IP on both sides, the HF is made of steel as an absorber and quartz fibers creating the active volume. The technology of the HF is very radiation-hard as around one third of the particles produced in the collisions reaches HF. Because the available radial space between the ECAL and the magnet (i.e. in the region between r=1.77 m and r=2.95 m) is not large enough to build a calorimeter with enough stopping power, the last part of the calorimeter, the Outer calorimeter (HO), was added after the magnet. The HO is covering the region $|\eta| < 1.3$ and stops particles escaping the HB, for this reason it is sometimes also referred to as "tail catcher". The magnet material is in that case used as an absorber for the HO. A schematic layout of the HCAL is shown in Fig. 1.8 [5].

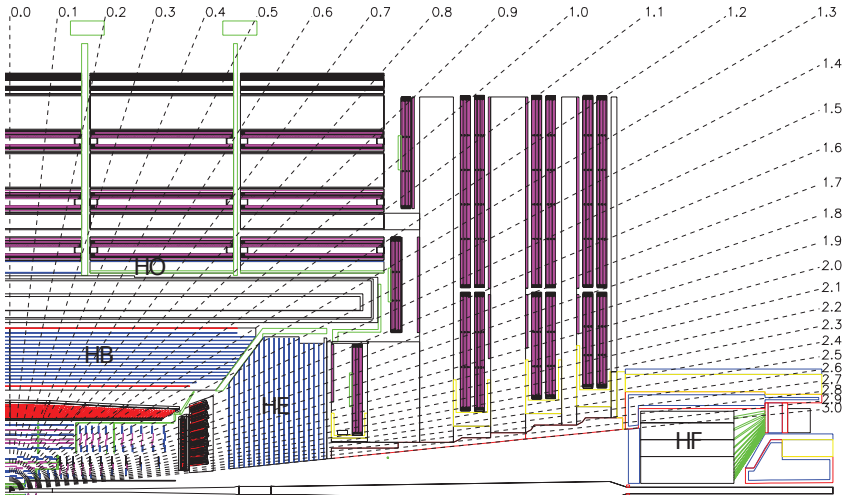

Figure 1.8: A schema of one quarter of the CMS HCAL with the layout of the HB, HE, HF and HO [5].

The hadron energy resolution from the combination of the ECAL and HCAL (barrel and endcaps) [28] was measured to be

$$\frac{\sigma_E}{E} = \frac{0.847}{\sqrt{E}} \bigoplus 0.074, \tag{1.5}$$

where the meaning of the terms is similar as for the ECAL.

1.2.5 The muon chambers

Because many interesting physics processes have a signature with muons in the final state, a good and precise measurement of muons is one of the main goals of CMS. This comprises muon identification, momentum measurement and triggering. The good triggering and momentum measurement is achieved with the help of the high magnetic field provided by the solenoid. The measurement of muons is done in three gaseous subdetectors, the Drift Tube (DT), Cathode Strip Chamber (CSC) and Resistive Plate Chamber (RPC) systems [29]. The combined three muon systems have in total 1400 chambers, which in radial direction are placed between around 4 m up to 7.5 m from the IP. The $|z|$ positions of the inner and outer part of muon systems are about 5.5 m-11 m, respectively. The layout of the muon systems is shown in Fig. 1.9 [30].

The DTs are located in the barrel region and are partly integrated into the return yoke. The pseudorapidity coverage is of $|\eta| < 1.2$. They are composed of plane cathodes with anode wires in between the planes. The smallest unit of DTs is the drift cell of dimensions 42×13 mm, in which one 50 μm thick anode wire is located. The drift time

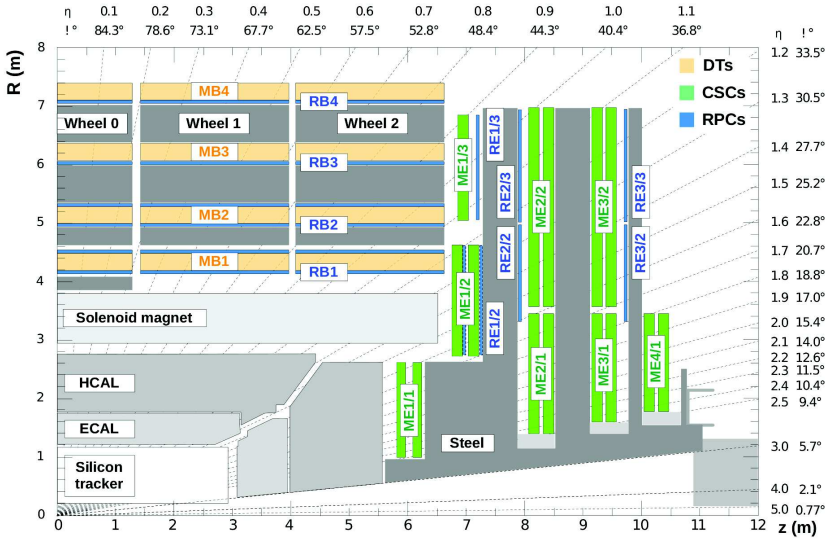

Figure 1.9: A schematic longitudinal view of one quarter of the CMS muon systems and their inner structure [30]. In case of DTs MB stands for "Muon Barrel" and in case of CSCs ME stands for "Muon Endcap". The notation for RPCs is RB for barrel and RE for endcaps.

of charge carriers can be up to around 400 ns.

The CSCs are located in the endcap areas outside of the return yoke. The CSCs coverage is $0.9 < |\eta| < 2.4$, which is partly overlapping with the DTs. The CSCs also contain cathodes with anode wires in between, but one cathode of the pair is segmented into strips. The DTs and CSCs provide a good triggering of muons.

To ensure the correct bunch crossing identification (i.e. from which bunch crossing a given muon originates), the complementary RPCs are present in both barrel and endcap regions. RPCs are composed of parallel plates of anodes and cathodes and readout strips. The RPCs are faster than DTs and CSCs, but provide a worse position resolution. The RPCs trigger is independent of the CSCs and DTs.

The spatial hit resolution per chamber differs for the three systems, for DTs it is 80-120 μm, for CSCs 40-150 μm, and for RPCs 0.8-1.2 cm [30].

In the following the time measurement in the DTs is introduced. The timing can be also measured with the CSCs and the ECAL in a very similar way, but for the purposes of the thesis, only the knowledge of the time measurement in the DTs is needed.

Muon timing measurement in the DTs

For each of the DT segment, a local muon timing measurement is performed. A muon going through the DT segment deposits its energy by ionization of the gas. The created charge carriers drift towards the wires as illustrated by the blue arrows in Fig. 1.10 [31]

and are read at the time t_{read}. The time, t_{cell}, when the muon arrives from the IP to the given drift cell can be calculated under the assumption of the muon production time and that it travels at the speed of light. With the knowledge of the drift velocity v_{drift}, the difference between t_{read} and t_{cell} can be converted into a distance between them. This distance $v_{drift}(t_{read} - t_{cell})$ is used to compute the hit positions (illustrated by the red crosses), where the muon crossed the cells. If the production time of muon is correctly assumed, the hits in the red crosses lie around a straight line. On the contrary, if the production time is not correctly assumed, then the line which connects the red crosses is no longer straight, but curly. To determine the production time, the hit positions in the red crosses are fitted by a three-parameter function, where the parameters are the position and slope of the line, and the production time t_i. This fitting procedure minimizes the δt distances, i.e. the differences between the hit positions at the red crosses and the positions predicted by the fit function (blue crosses), which depend on the production time t_i.

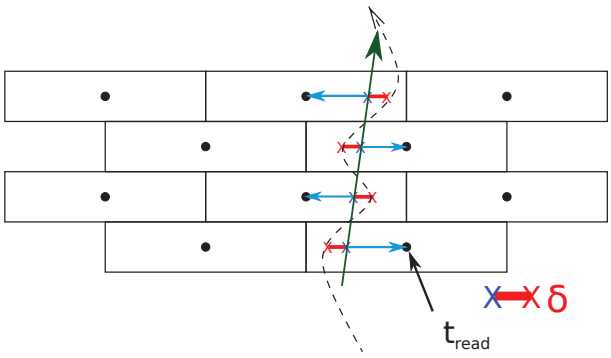

Figure 1.10: A schema of a transverse view of few drift cells of the DTs. The wires are shown as black dots, the drift direction as blue arrows, the reconstructed hits as red crosses and the fit function as green arrow. The distance between the reconstructed hits and the positions predicted by the fit function (blue crosses) is denoted as δt. The time when the charges were read by a wire is denoted as t_{read} [31].

The local timing measurements in segments are combined to produce, among others, the following variables:

time$^{\text{InOut}}_{\text{IP}}$ This variable corresponds to the time at which a muon was present at the interaction point, assuming that the muon moves at the speed of light from the IP outside of CMS. It is computed as a weighted average $\bar{t}$ of the measured t_i values, where i denotes a single segment measurement. In case of the DTs each weight is equal to $N_{s,i} - 2$, with $N_{s,i}$ being the number of hits in the segment of DTs in which the given t_i was measured. The formula is then

$$\bar{t} = \frac{1}{N} \times \frac{1}{\sum N_{s,\,i} - 2} \times \sum (N_{s,i} - 2) t_i, \tag{1.6}$$

where N is the number of timing measurements.

The error on the time measurement is computed as

$$\sigma^2 = \frac{1}{N-1} \times \frac{1}{\sum w_i} \times \sum (t_i - \bar{t})^2 w_i, \tag{1.7}$$

where the weight w_i is defined as $w_i = 1/\sigma_i^2$ with σ_i being a single timing measurement resolution and $\bar{t}$ is the above defined weighted average of the t_i measurements.

time$_{\mathbf{IP}}^{\mathbf{OutIn}}$ The $time_{IP}^{OutIn}$ is the muon time at the interaction point assuming that the muon moves from the outside of the CMS detector towards the IP. During the calculation, each t_i measurement is increased by twice the time-of-flight (TOF) of an in-time muon from the IP to the DT segment measuring the t_i to take into account that the OutIn muon which was at IP at the same time as the InOut one arrived to the DTs twice TOFs before the InOut muon. Then the computation of timing continues as for the $time_{IP}^{InOut}$.

Direction The direction variable provides a simple and robust estimate if the muon traveled from the IP out or in the opposite way. The evaluation takes into account the errors on the $time_{IP}^{OutIn}$ and $time_{IP}^{InOut}$ variables and assumes that the correct time hypothesis has the smallest error.

Free $1/\beta$ The free inverse beta (free $1/\beta$) variable is the c/v, where c is the speed of light and v the speed of the muon. It is obtained from the fit of muon time-of-flight measurements. The word "free" indicates that neither the production time, the direction nor the velocity is assumed and that all three are free parameters. The muons, originating from collisions reaching the muon chambers, travel from inside towards outside of detector at the speed close to the speed-of-light and therefore their free inverse beta is close to one. The free inverse beta for cosmic muons is around minus one due to the opposite direction.

The timing resolution for DTs is further discussed in Chapter 3.

1.2.6 Trigger and data acquisition

As bunches are colliding every 25 ns, thus with a rate of 40 MHz, fast and reliable triggering system [32] is required. The raw data size of one event is approximately 1 MB, therefore if there would not be any dedicated trigger, 40 TB of data per second would have to be stored, what is far beyond the current technical capacities. In CMS there are two levels of triggers which provide physics motivated selection of the interesting events. The first one, called Level-1 (L1), is hardware based and its decision-making is based

on information from the muon chambers and the calorimeters. The L1 is capable to take a decision within 3.4 μs and its output rate is up to around 100 kHz. The rest of the event is read upon the decision of the L1 and sent to the second level called High Level Trigger (HLT). The HLT is a software based trigger providing further selections. At the HLT level, information from all subdetectors is read and therefore the full event can be reconstructed. The output rate of the HLT is around 1 kHz. The time period of uninterrupted data-taking is called a run and ideally there is one run per a LHC fill, where a fill represents the lifetime of a given proton beam in the LHC machine. In the case of detector technical difficulties the run can be interrupted and a new one started. Once the beams are dumped the run is stopped and a new run of cosmics instead of collision data-taking can start.

During collision runs, most of the triggers are dedicated to record events useful for the physics analyses (triggering on events with the presence of e.g. one single muon, two muons, or a large E_T^{miss} value). Part of the triggers can be used for calibration purposes, such as the Zero Bias and Minimum Bias triggers which fire on any bunch crossing leading to a minimal activity in the detector.

1.2.7 Luminosity and pileup

In particle physics experiments it is very important to have information about an expected event rate during a time period. For this evaluation, the following formula can be used

$$\frac{\mathrm{d}N}{\mathrm{d}t} = \sigma \times \mathcal{L}, \tag{1.8}$$

where σ is the cross section of process of interest and $\mathcal{L}$ is the instantaneous luminosity given by

$$\mathcal{L} = \frac{N_b^2 n_b f \gamma}{4\pi\epsilon_n \beta^*} F, \tag{1.9}$$

where the variables in numerator are the number of particles per bunch N_b (around 10^{11}), the number of bunches per beam n_b and the bunch crossing frequency f (currently 40 MHz). In the denominator, ϵ_n is the normalized transverse beam emittance and β^* is the beam amplitude function at the IP. The β^* function is defined as the distance from the focus point (IP) to the point where the beam is twice as wide as at the focus point and is expressing how much the beam is "squeezed" before the collision: lower the β^* is, more the beam is squeezed. At the LHC, the ϵ_n is of the order of 4 mm μm and β^* of the order of 0.5 m. Lastly, because of the beam crossing angle, the reduction factor F is

introduced. Its value at the LHC is typically around 0.95.

By integration of the instantaneous luminosity over time, the integrated luminosity can be obtained:

$$L = \int \mathcal{L} \mathrm{d}t. \tag{1.10}$$

The LHC was designed to deliver an instantaneous luminosity of $1 \times 10^{34}\mathrm{cm}^{-2}\mathrm{s}^{-1}$. During Run 2, because of the smooth running and thanks to the large efforts of the LHC group, the LHC instantaneous luminosity was increased even beyond the designed luminosity, up to $2.06 \times 10^{34}\mathrm{cm}^{-2}\mathrm{s}^{-1}$ [33]. The integrated luminosity delivered to CMS over years 2010–2017 can be seen in Fig 1.11 [33]. A large fraction of integrated luminosity is good to be used in the physics analyses, the rest is being discarded due to a detector problem, for example. For example, in 2016 around 88% of the integrated luminosity was used for physics analyses.

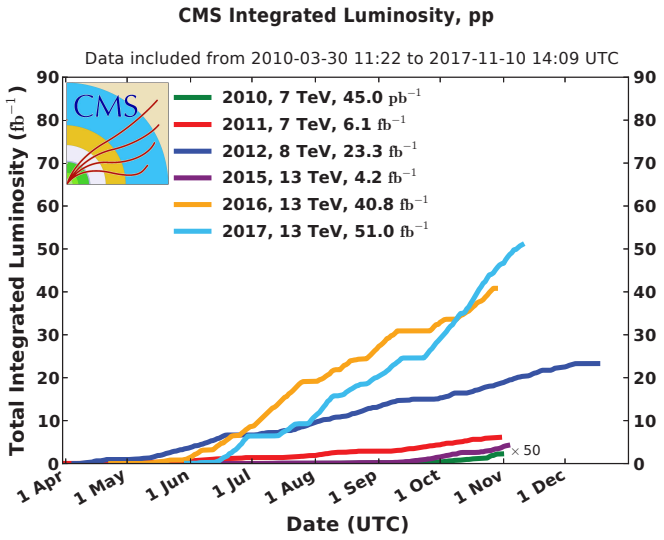

Figure 1.11: The delivered luminosity to the CMS detector for years 2010-2017 [33].

High luminosity is essential to study rare processes, but on the other hand it results in effect called pileup (PU) [34]. Pileup particles are particles which are not originating from the interaction of interest at a given bunch crossing. The pileup can be divided into two categories, in-time and out-of-time pileup. The in-time pileup is caused by multiple pp interactions in the event, the average pileup for all years of Run 2 is shown in Fig. 1.12. The out-of-time pileup (OOT PU) originates from particles produced before or after the bunch crossing of interest. The OOT PU is caused for example by slow particles looping in the detector for more bunch crossings or due to the duration of integration of the signal charge by the front-end electronics, resulting in a pulse shape which is typically longer

than 25 ns, depending on the subdetector. Because of the wide signal pulse shape, the signal from one particle can be read during more bunch crossings.

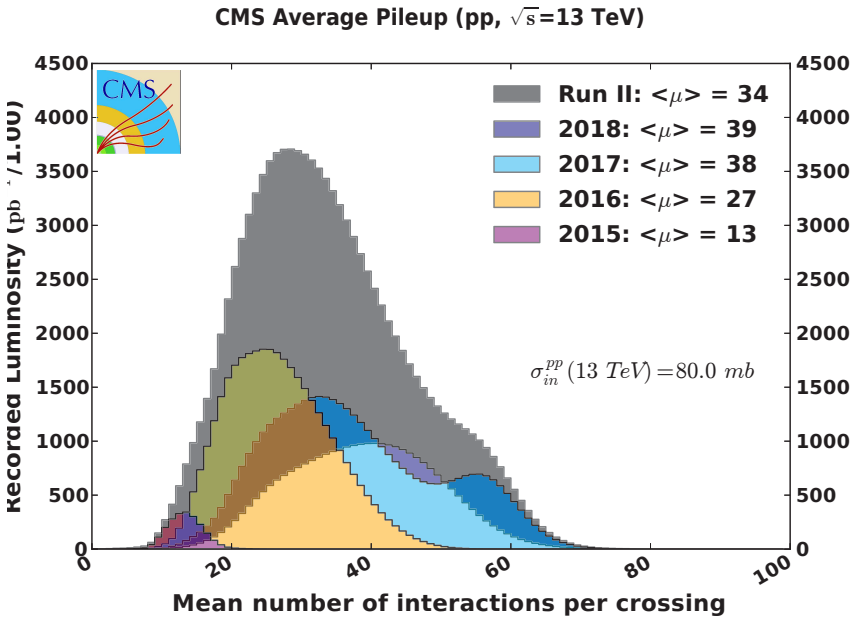

Figure 1.12: The average pileup for all years of Run 2 [33].

1.3 Event and object reconstruction at CMS

In this section several physics objects, which are important for the analyses discussed in this thesis, are introduced.

1.3.1 The Particle-Flow algorithm

As it can be seen in Fig. 1.13 [35] each kind of particle leaves a characteristic signature in the CMS detector. For example, an electron leaves a track in the tracker and then stops in the ECAL where it deposits the rest of its energy. The neutral hadron does not interact in the tracker but can leave energy both in ECAL and HCAL where it stops.

The CMS approach to reconstruct an event takes this into account and combines information from all subdetectors at once to reconstruct the objects. The algorithm used for this kind of reconstruction is called the Particle Flow (PF) algorithm [35]. This algorithm is linking particle deposits in the different subdetectors using specific procedures which depend on the subdetectors and particles. The PF charged hadrons are reconstructed by linking the deposits in an (η, Φ) window. In addition to a geometrical matching, the

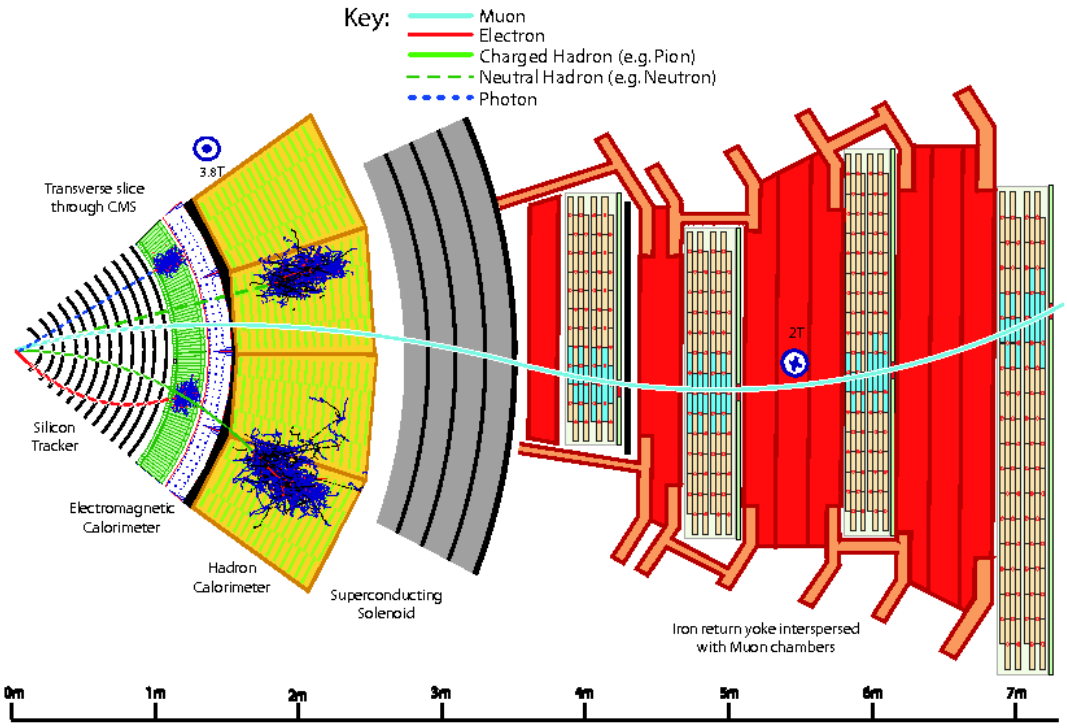

Figure 1.13: Transverse view through a sector of the CMS detector. The depositions of different particles in different subdetectors are indicated in the picture [35].

tracks from the tracker are matched with the clusters in calorimeters based on comparing the momentum and energy from tracker and calorimeters. The reconstruction of the PF charged hadrons is also ensuring that there is no deposit in the muon chambers. Such procedure improves both energy and direction determination of the charged hadrons. The PF neutral particles are reconstructed from the clusters in the calorimeters under the photon or neutral hadron hypothesis. The prompt PF electron reconstruction requires both the presence of ECAL and tracker deposits but the absence of HCAL deposits. The prompt PF muon is reconstructed from a track in the tracker and a track in the muon chambers and its momentum is determined either from the tracker measurement alone or from a combination of the two, depending which option is providing the best momentum measurement.

1.3.2 Leptons

1.3.2.1 Muons

Muons are traversing the whole CMS detector and therefore their tracks can be reconstructed in both the silicon tracker and the muon chambers. The “standalone muon” is

a muon track reconstructed from the hits in CSC, DT and RPC, while the "inner track muon" is reconstructed from the hits in the silicon strip tracker only. Additionally, there are two options how to reconstruct muons using both information from the muon chambers and the tracker. The first one leads to the collection of muons called "tracker muons". The tracker muons are first reconstructed in the tracker and then they are extrapolated to the muon chambers by matching the inner track with hits in the muon chambers. The second approach matches the standalone muon with an inner track based on geometrical criteria. Then the combined track is refitted and the resulting collection is called "global muons" [36].

The PF algorithm uses both global and tracker muons to identify a PF muon. The leptons originating from the hard scattering (prompt muons) are decay products of e.g. W, Z and H boson and therefore they are not expected not to have any other activity in the proximity. A requirement on muon isolation is added in order to select a muon and reject jets misidentified as muons or muons from decay of heavy flavor quarks. The selected muons are then tested by several quality requirements to balance the efficiency and purity of the muon selection. Based on given criteria, several muon identifications (IDs) and their working points are assessed, e.g. loose, medium, tight. Muons are being reconstructed up to $|\eta| = 2.4$ with a reconstruction and identification efficiency larger than 96%. The muon trigger efficiency is higher than 90% in the full η range. Using information from both tracker and muon chambers the p_T resolution for muons with $20<p_T<100$ GeV is 1.3–2.0% in the barrel region and better than 6% in the endcaps. For muons with p_T up to 1 TeV the transverse momentum resolution does not go above 10% [36].

1.3.2.2 Electrons

The electrons are reconstructed with the track information from the tracker and the energy deposits in the ECAL [37]. Because of bremsstrahlung, an electron looses part of its energy before reaching the ECAL, this amounts around 30% of its energy in average for example in $|\eta| \approx 0$. The energy deposit in the ECAL is reconstructed as a supercluster. A supercluster is a cluster extended in the Φ direction to take into account the bremsstrahlung photons. The electron track in the tracker is not reconstructed by the standard CTF algorithm, but the GSF algorithm is used instead to include also bremsstrahlung photons [38]. The GSF algorithm is starting either from the seed created by a few tracker hits or from the ECAL supercluster and then the track is extrapolated from the seed to the full tracker. In case of a tracker-based seeding, the next step is to match the ECAL supercluster with the electron track. Similarly as for the muons, an isolation criterion is requested for the prompt electrons as well as quality requirements on the reconstructed electrons are

imposed resulting in several electron IDs and categories of these IDs, e.g. loose, medium, tight.

Electrons are reconstructed up to $|\eta| = 2.5$, with an efficiency higher than 88% in the p_T range from 10 GeV to 100 GeV and $|\eta| < 2$. The energy measurement in the ECAL and the momentum measurement in the tracker are used to estimate the momenta of electrons. The resolution on the momentum measurement is evaluated from $Z \to ee$ decays and its is between 1.7%-4.5% for electrons with $p_T \approx 45$ GeV [37].

1.3.2.3 Taus

In around 2/3 of the cases the tau leptons decay hadronically to a mixture of charged and neutral hadrons and tau neutrino. The decay is very fast and thus it is difficult to reconstruct the secondary vertex. The algorithm which is used to identify the hadronically decaying tau is called Hadron-Plus-Strips (HPS) [39]. The probability to misidentify a jet, an electron or a muon as an hadronic tau depends on the objects identification requirement and was measured in data to be around 0.01%-4%, 0.1%-3% or 0.03%-0.3%, respectively. Large differences were found in misidentification rate between data and simulation, leading to data to simulation ratio up to 1.66 in the case of an electron, 1.86 in the case of a muon and between 0.8 and 1.2 in the case of a jet. The hadronic tau identification efficiency is of around 50-60% and is similar for data and simulation [40]. The probability to misidentify a jet, an electron or a muon as an hadronic tau depends on the objects identification requirement and was measured in data to be around 0.01%-4%, 0.1%-3% or 0.03%-0.3%, respectively. Large differences were found in misidentification rate between data and simulation, leading to data to simulation ratio up to 1.66 in the case of an electron, 1.86 in the case of a muon and between 0.8 and 1.2 in the case of a jet. The hadronic tau identification efficiency is of around 50-60% and is similar for data and simulation [40].

1.3.3 Photons

Photons do not leave tracks in the tracker and thus their energy is obtained only from ECAL measurements. The prompt photon identification is based on two categories of observables, its shower shape and its isolation from the remaining activity in the ECAL. Again, there are several photon identifications (IDs), for each of them three working points are defined: loose, medium and tight. Due to the high material budget before the ECAL, the photon can convert to the electron-positron pair before reaching the ECAL. The achieved resolution in the barrel region on both the unconverted and converted photon

energies varies between 1% and 2.5% for photons with an energy of tens of GeV. In the endcaps the photon energy resolution for unconverted and converted photons is of 2.5%-4% [41].

1.3.4 Jets

The production of quarks and gluons is followed by radiations and hadronization, this results in a large activity in a narrow cone. In order to reconstruct these particles the anti$-k_T$ (ak) clustering algorithm [42, 43] is used. Within this algorithm the distance between objects is defined as

$$d_{ij} = \min\left({p_T}^{-2}(i), {p_T}^{-2}(j)\right) \frac{(\eta_i - \eta_j)^2 + (\Phi_i - \Phi_j)^2}{R^2} = \min({p_T}^{-2}(i), {p_T}^{-2}(j)) \frac{\Delta R_{ij}^2}{R^2}, \tag{1.11}$$

where $p_T(i)$ is the transverse momentum, η_i the pseudorapidity and Φ_i the azimuthal angle of the object i. To reconstruct PF jets, the algorithm runs over PF reconstructed candidates such as electrons, muons, photons, charged and neutral hadrons. The parameter R is a jet distance parameter. In the standard jet reconstruction, R=0.4 in Run 2 while it was chosen to 0.5 in Run 1, this decrease is due to the change of the energy and pileup between these two Runs. In the case of boosted objects decaying to partons, two or more jets originating from the boosted parton can be merged. These topologies can be reconstructed as so called "fat jets", and for purpose of their reconstruction, the parameter R is increased to 0.8 or 1.0. The anti$-k_T$ algorithm, by definition, tends to cluster first the high p_T objects with the shortest distance between each other and continues with objects further apart. After all high p_T particles are clustered, the clustering algorithm adds all low p_T particles in the cone specified by the parameter R. The product of the clustering is a jet. The charged component of the jet can be reconstructed only up to $|\eta| = 2.4$ due to the tracker coverage, while the neutral component extends up to $|\eta| = 5$.

The measured jet energy is in general not equal to the energy of parton responsible for the jet, due to several inefficiencies and biases in the energy measurement. Therefore the jet energy must be calibrated and rescaled by the correction factor in order to have a correct jet energy scale. The jet energy corrections are obtained from simulations. An additional jet energy scale correction is derived from measured dijet, photon+jet, Z+jet, and multijet events to take into account differences between data and simulation [44]. The typical PF jet energy resolution is around 15% for 10 GeV jets, 8% for 100 GeV jets, and 4% for 1 TeV jets.

1.3.5 b-jets

In order to determine from which quark the jet is originating, flavor tagging techniques were developed. The target of the heavy flavor tagging techniques is to identify jets originating from a b quark (b-jets) or a c quark (c-jets). In the following, only b-jets are discussed. The b-quarks are forming B-mesons, which decay within about 1.5 ns creating a secondary vertex displaced by few mm up to cm from the primary vertex. The information on a displaced secondary vertex or displaced tracks in the jet, information about tracks originating from the secondary vertex and optionally information on soft leptons within the jet are used by b-tagging algorithms to tag jets formed from the b-quarks [45]. Due to the tracker geometry, b-jets can be reconstructed only up to $|\eta| = 2.4$.

There are several algorithms, whose purpose is to tag a b-jet. The first one is the Combined Secondary Vertex (CSVv2) algorithm, which combines information about displaced tracks with information on the secondary vertex. The DeepCSV algorithm improves the performance with respect to the CSVv2 algorithm by using a deep neural network. The Combined Multivariate Analysis (cMVAv2) technique takes into account a fact, that B-hadrons can decay leptonically and thus soft electrons or muons can be present in the b-jet. In this algorithm, the information about soft leptons is used in combination with other taggers. The efficiency to tag a b-jet versus the probability to misidentify a c or light flavor jet as a b-jet for different taggers is shown in Fig. 1.14 [45], as estimated from simulation. For each b-tagging algorithm, loose, medium and tight working points are defined. These working points are defined by requiring a threshold on the misidentification probability of around 10% for loose, 1% for medium and 0.1% for tight working points. As for many other objects, the scale factors are then derived to correct for different performances in data and simulation.

1.3.6 Missing transverse energy

If the momenta of all particles could be measured, the sum of all momenta in the plane transverse to the beam would be zero due to the momentum conservation law. But as neutrinos escape the detector undetected, an imbalance of momentum in this plane could be observed.

The Missing Transverse Momentum, for simplicity referred to as “Missing Transverse Energy” (E_T^{miss}) is the magnitude of the negative vectorial sum of the transverse momenta

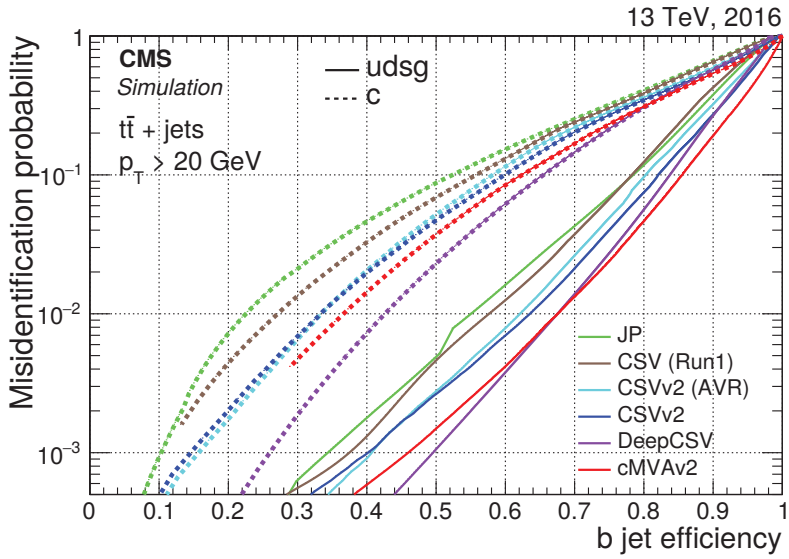

Figure 1.14: The probability to misidentify a c or light flavor jet as a b-jet versus the efficiency to identify a b-jet for different b-tagging algorithms. These curves were evaluated from simulated $t\bar{t}$+jets events, using jets with $p_T > 20$ GeV [45].

of all PF particles [46] and is computed as

$$E_T^{miss} = \left| -\sum_i \vec{p}_{T_i} \right|, \tag{1.12}$$

where $\vec{p}_{T_i}$ is the momentum of i-th PF particle. Because of energy thresholds in the calorimeters, inefficiencies in the tracker or non-linearity of the calorimeters' response for hadrons, the E_T^{miss} measurement can be biased and thus an energy correction factor must be used. This factor accounts for effects influencing the E_T^{miss} and is applied on the transverse momenta of the jets. The E_T^{miss} is then recomputed with the new transverse momenta of jets. The uncertainty on E_T^{miss} is evaluated by varying the p_T of each kind of object within its resolution. The E_T^{miss} distributions for $Z \to ee$ and $Z \to \mu\mu$ events are shown in Fig. 1.15 [46]. These plots show a good agreement between data and simulation. The $Z \to ee$ and $Z \to \mu\mu$ events have no genuine source of the E_T^{miss}, no neutrino in the final states. Therefore the E_T^{miss} is expected to be zero, but due to the E_T^{miss} resolution, non-zero values are observed.

The E_T^{miss} variable plays a crucial role in searches for physics beyond the Standard Model, as many theories predict stable weekly interacting particles which would enhance the E_T^{miss}.

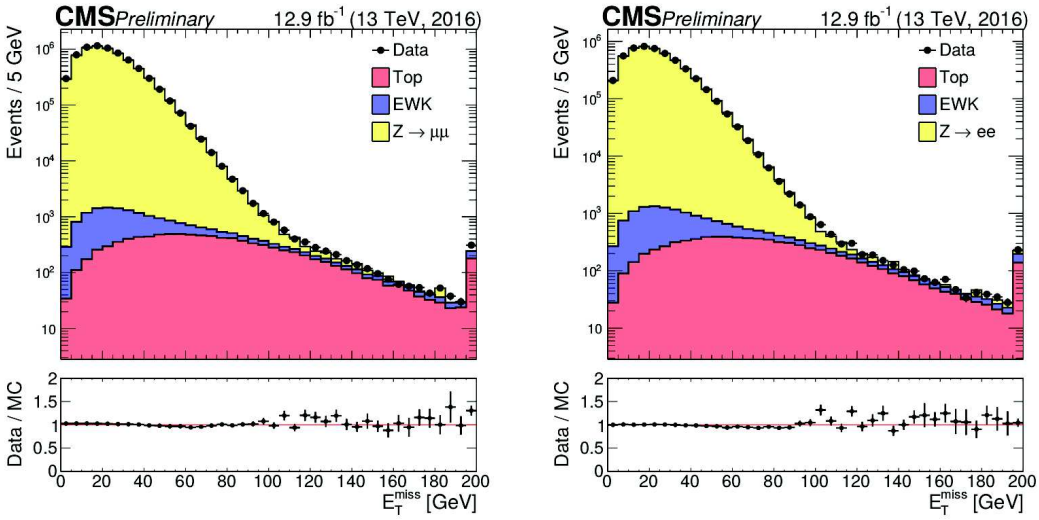

Figure 1.15: E_T^{miss} distributions for $Z \to \mu\mu$ (left) and $Z \to ee$ (right) events with the data to simulation ratio in the bottom canvas. There is also a contribution from two other groups of processes decaying to the dimuon or dielectron final states. The Top contribution originates from $t\bar{t}$ and single top processes, in which the W-bosons decay leptonically to a charged lepton and a neutrino and therefore these events have a genuine source of E_T^{miss}. The EWK group of processes consists of diboson, $Z\gamma$ and $W\gamma$ production processes, which are also partly present in the E_T^{miss} tail due to leptonically decaying W-bosons in some of them [46].

Chapter 2

Study of the highly ionizing particles in the silicon strip tracker

This chapter focuses on the tracking inefficiencies of the CMS silicon strip tracker observed during years 2015 and 2016 and on the studies of "Highly Ionizing Particles" (HIP) which were identified as a possible cause of these inefficiencies. First, the tracking inefficiencies are described as well as the HIP events. Secondly, details about the silicon strip tracker readout electronics and data reconstruction are introduced in order to understand the effect of highly ionizing particles on the silicon strip tracker and the data acquisition. Past studies in the laboratory conditions (with laser and test beam) of the highly ionizing particles are then shortly discussed as a starting point for my new studies based on CMS pp collision data. In Sections 2.4.2 and 2.4.4, two studies with the CMS pp collision data are performed, one in perspective of identifying highly ionizing particles as a source of the observed tracking inefficiencies. The second study uses data after the fix of the largest source of inefficiencies and aims to purely characterize a HIP event and its consequences in the CMS environment.

2.1 The tracking inefficiencies at the beginning of Run 2 and a first promising suspect

2.1.1 Observed inefficiencies in the tracking performance

At the start of the Run 2 in 2015, the time between collisions was shortened from 50 ns to 25 ns. During this era, the CMS collaboration started to observe large discrepancies between predicted and measured number of tracks: data showed less tracks and also in average shorter tracks than simulation. Such situation was a result of a cluster inefficiency

in the silicon strip tracker, the loss of clusters left by charged particles being translated into a loss of tracks.

The observed inefficiencies were shown to depend on the distance from the interaction point (IP) and also to scale with the instantaneous luminosity [25]. The left plot of Fig. 2.1 shows the hit efficiency, computed as the ratio of the number of hits associated to the reconstructed tracks to the number of expected hits, for the different layers of the barrel, the disks, and the endcaps. The right plot of Fig. 2.1 presents the hit efficiency as a function of the instantaneous luminosity. In these plots, the reduced hit efficiency, seen in runs recorded in 2016, is shown as red empty circles. In the figures it can be seen that the smallest hit efficiency was observed for the first layer of the TOB, in which up to 8% of the hits were lost during the highest luminosity runs. For comparison, the red full circles stand for hit efficiency of the runs taken at the end of 2016, once the source of the largest hit inefficiency was eliminated, as discussed in later sections.

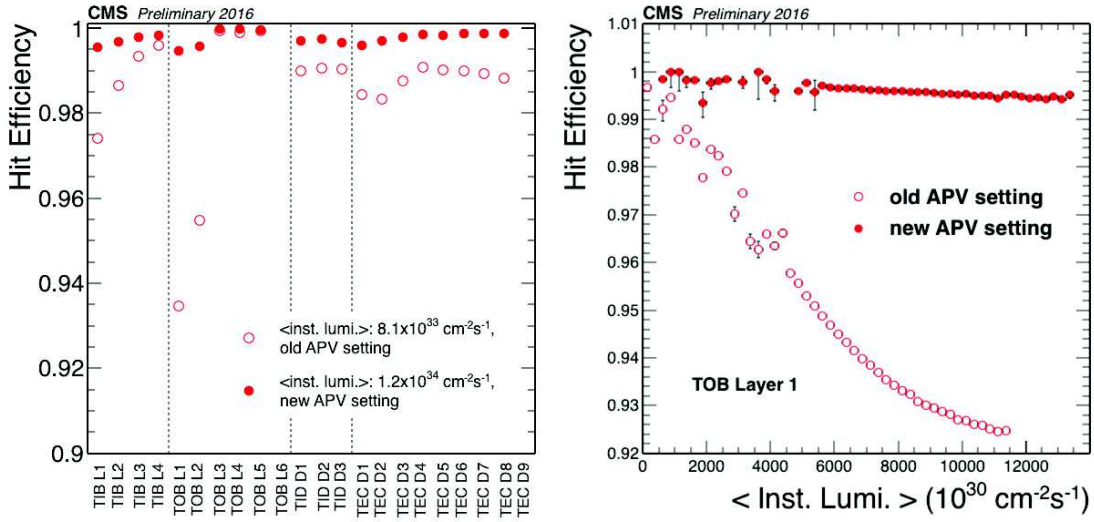

Figure 2.1: (left) Hit efficiency for all layers of the barrel, the disks and the endcaps. The empty circles represent the hit efficiency measurement for the old front-end electronics (APV) settings while the full circles depict the hit efficiency measurement after the new APV settings were deployed at the beginning of August 2016. The corresponding instantaneous luminosity for both runs is indicated in the legend. (right) Hit efficiency as a function of the instantaneous luminosity. The measurement is shown only for the first layer of the TOB for both the old (empty circles) and new (full circles) APV settings [25].

2.1.2 Investigating the highly ionizing particles

Among the various possible explanations of the observed hit inefficiencies, the hypothesis of highly ionizing particles was considered with a great interest. To understand the effect of the HIP on the hit efficiency, it is required to first discuss the energy loss mechanism

for charged particles in silicon. The main energy loss mechanism for charged particle in tracker silicon sensors is via the electromagnetic interaction, mainly via ionization and excitation described by the Bethe-Bloch formula [47]. Beyond it, the incoming particle can also deposit energy in sensors via elastic and inelastic nuclear interactions with the silicon nucleus. These two nuclear interactions result in a nuclear recoil in the elastic case and a nuclear recoil and fragmentation in case of inelastic interaction. A sufficiently energetic recoiled nucleus can also induce displacement of the other nuclei in its proximity. All affected nuclei as well as the nuclear fragments undergo energy loss by ionization, resulting in large and very localized energy depositions in the silicon volume.

By simulating these interactions in the silicon, it has been shown that elastic interactions do not lead to high energy depositions, while inelastic interactions can induce energy deposits up to about 100 MeV in 500 μm thick tracker sensors, which represents an energy deposit approximately 1000 times larger than the electromagnetic interactions [48]. The Most Probable Value (MPV) of the energy deposition in these sensors, originating from the inelastic interaction has been found to be around 10 MeV, corresponding to 100 times larger deposits w.r.t. to the majority of particle-silicon interaction which does not involve the nuclear interaction [49]. The readout electronics of the tracker modules is designed for energy deposits up to around ten times higher than expected, this threshold is dependent on the module design. Larger energy deposits than this threshold can result in a saturation of the electronics, dead-time in the charge collection and hit inefficiency.

In summary, a HIP event is an event in which typically the inelastic interaction of the incoming particle with the silicon is a source of highly ionizing particles. These particles ionize the volume of the silicon sensor by far more than the majority of particles coming from collisions and they can thus saturate the readout electronics. The saturated electronics can become therefore inefficient and insensitive to further incoming particles, resulting in a dead-time in a cluster reconstruction and thus in a loss of hits, which could explain the observed hit inefficiency.

2.2 The strip tracker readout system

As the saturation of the readout electronics by the HIP event was found to be a possible explanation of the observed inefficiencies, the tracker readout chain is introduced in this section to understand the behavior of the electronics under such conditions.

2.2.1 Overview

The charge carriers, created via the ionization of the silicon volume by a traversing particle, drift toward the electrodes. The current induced on the aluminium strips is read by an front-end chip called APV25 [50, 51], situated at the Front-End Hybrid, attached to the tracker module and bond to the tracker sensor. The analog signal from these chips is sent via optical links to the back-end electronic cards called Front-End Drivers (FED) [52] located in the control room. In standard data-taking configuration, the data are digitized and processed in the FEDs. The graphical overview of this data flow is shown in Fig. 2.2. All these parts of the tracker readout are introduced with more details in following subsections.

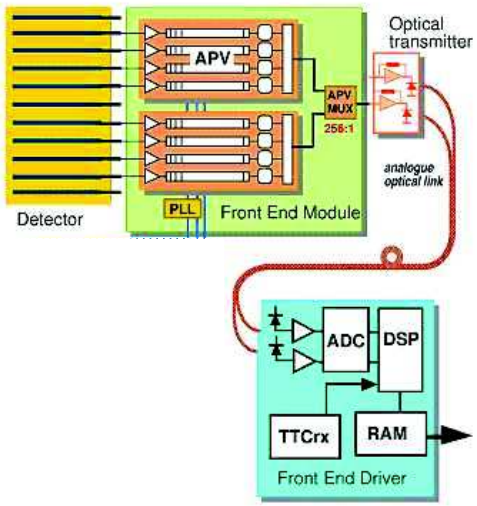

Figure 2.2: Overview of the tracker readout chain [53]. The charge collected by the silicon strip implants and subsequently induced on the aluminium strips is read by the on-detector APV chips. The output of two APV chips is multiplexed and converted into an optical signal which is sent via optical link to the off-detector Front-End Drivers for further signal processing. The data are later sent to the HLT farm for the reconstruction.

2.2.2 The silicon strip modules

The sensitive volume of the CMS tracker modules is composed of silicon strip sensors. A schematic sketch of a silicon strip sensor is shown in Fig. 2.3. Each silicon sensor is formed by a n-type bulk, which has on one side an uniform n+ backplane while p+ strip implants are located on the other side. The implants are connected to a reverse bias voltage to completely deplete the bulk of the sensors. The thickness of both p+ implants and n+ backplane is small and negligible compared to the bulk, almost the whole volume

of the sensor is thus depleted. The signal collected at the p+ strips induces a current on the aluminium strips separated from the silicon strips by a thin layer of the silicon dioxide and nitride (AC coupling). Each aluminium strip is connected by a wire bond to the read-out electronics. The distance between the silicon strips is called the pitch.

Depending on the type, the tracker modules have 512 or 768 p+ strips, and each 128 strips are connected to one front-end APV25 chip. The largest fraction of the modules has one layer of sensors (mono modules), while the remaining part holds two layers of sensors (stereo modules) mechanically attached back to back and with a relative tilt of strips of 5.7°. With two tilted sensor layers, stereo modules are able to provide 3-D information of the hit position in the global coordinates about the hit position, where the particle has hit the module. The mono modules give only 2-D hit measurement as the third dimension depends on the strip length which is around ten cm, what is orders of magnitude larger than the strip width and thickness. The modules also differ by the sensor thickness which is either 320 μm or 500 μm and the pitch between each strip which can vary from 80 μm up to 205 μm depending on the tracker layer and partition.

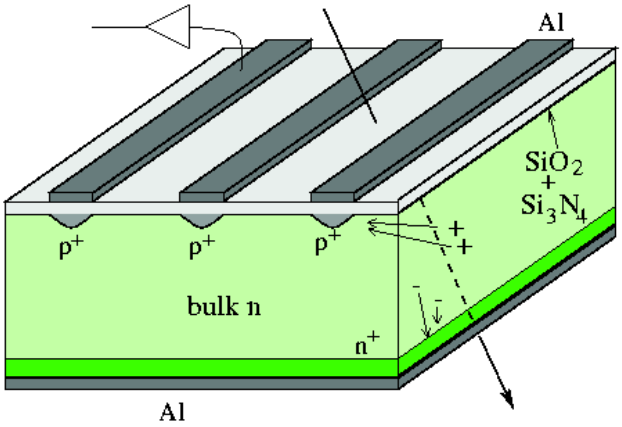

Figure 2.3: A schematic sketch of the silicon sensor with n-type silicon bulk, p+ strips and n+ backplane. An incoming particle and the movement of charge carriers left by it is also drawn [54].

When a charged particle crosses the silicon sensor, electron-hole pairs are produced along the path of the particle. The energy loss in the material can be described by the Bethe-Bloch formula [47] as a function of $\beta\gamma = p/Mc$, where β is the ratio of the interacting particle velocity to the speed of light, γ is the Lorentz factor, c is the speed of light, and p and M are the momentum and mass of the interacting particle. The Bethe-Bloch function has a minimum at $\beta\gamma \approx 3$. The majority of the charged particles produced in the pp collisions and passing through the CMS detector have in a good approximation minimal $\beta\gamma$ values and are thus called Minimum Ionizing Particles (MIP).

A signal starts to be induced on the aluminium strips once electrons and holes begin to drift towards the electrodes. Holes drift to the strips and electrons to the backplane (n+ implant). The current induced at the aluminium strips can be calculated using the Shockley Ramo theorem [55, 56]. In the framework of this theorem, it can be shown [57] that charge carriers drifting toward one strip induce as well current on the neighboring strips. The charge integrated over time on neighboring strips is zero and the collected charge on the main strip is equal to the charge created by ionization in the silicon bulk.

The number of strips collecting the charge carriers created by ionization depends on the charge sharing and the cross talk between the strips. The charge sharing is a result of the propagation of the particle and created charge carriers through the silicon sensor. It can be caused by trajectory inclination, effects of the magnetic field on the charge carriers, or by diffusion. On the contrary, the cross talk is independent of the propagation of charges in the bulk of the silicon sensor and arises from the strip coupling via inter-strip capacitance.

In case of inclined trajectories, the charge carriers from the different parts of the trajectory are drifting towards different strips.

If there is an absence of the magnetic field, the created charge carriers, electrons and holes, would drift directly towards the electrodes. But in the case of the tracker barrel (for TOB and TIB), a perpendicular magnetic field is applied and consequently the charge q of the carrier is deflected from the direction of the electric field due to the Lorentz force $\vec{F}$ defined by the equation

$$\vec{F} = q(\vec{E} + \vec{v} \times \vec{B}), \tag{2.1}$$

where $\vec{E}$ is the electric field, $\vec{v}$ is the velocity of charge carrier and $\vec{B}$ is the magnetic field. The angle between the electric field lines and the drift direction of the charge carriers in the magnetic field is called the Lorentz angle. This angle is independent of the track inclination and can be compensated by tilting the tracker modules w.r.t. the magnetic field as it was done for the TIB modules.

Finally, the diffusion of the charge carriers during the drift to the electrodes can also modify the path of the charge carriers from the straight line. However the spread of the charge carriers due to diffusion is in the order of few μm and therefore about two orders of magnitudes smaller than the pitch size. It can thus only result in a small amount of charge collected by neighboring strips just in case the particle has passed close to the middle of the pitch [57].

The cross talk arises from the sensor capacitive network. Strips are coupled to back-

plane via a backplane capacitance and to neighboring strips via an inter-strip capacitance. The capacitive network of the silicon strip sensor and its electronics is shown in Fig. 2.4. Due to the inter-strip capacitance, the charge collected by one channel (strip) is shared between the neighboring channels. The signal in the APV is sampled and depending on the sampling time, the charge shared to the neighboring strips is different, therefore the charge sharing, i.e. the cross talk, depends strongly on the signal sampling time [57], which can be different for different tracker readout modes. This effect has been studied numerically via the description of the capacitive network by the SPICE simulations [58].

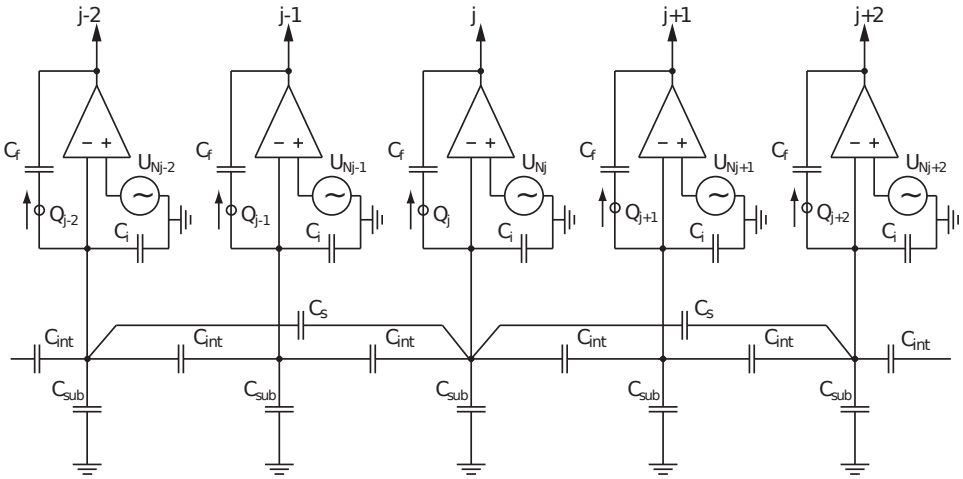

Figure 2.4: A schematic view of a generic capacitive network of a silicon strip sensor and its respective readout electronics. The strips are inter-connected via the inter-strip capacitance C_{int}. On top of this connection, second neighboring strips are directly coupled by the capacitance C_s. Each strip is connected to the backplane via the capacitance C_{sub}. The strips are connected to amplifiers located at the top part of the schema [59].

2.2.3 The APV25 readout chip

As already mentioned, the current of 128 channels is read out by one APV25 [50] chip, later referred to as APV, which is a front-end chip providing amplification, shaping and sampling into a single value of the signal received from each channel. To achieve this, the APV chip is equipped by a preamplifier, an inverter, a CR-RC shaper, an analog pipeline and a deconvolution filter for each of its 128 channels, as shown in Fig. 2.5. Although these different stages are separate for each channel, to reduce instabilities, all inverters of one chip are powered by a common supply rail via an external inverter resistor. This biasing scheme ensures a stable signal, but on the other hand it introduces another source of cross talk between channels of one APV.

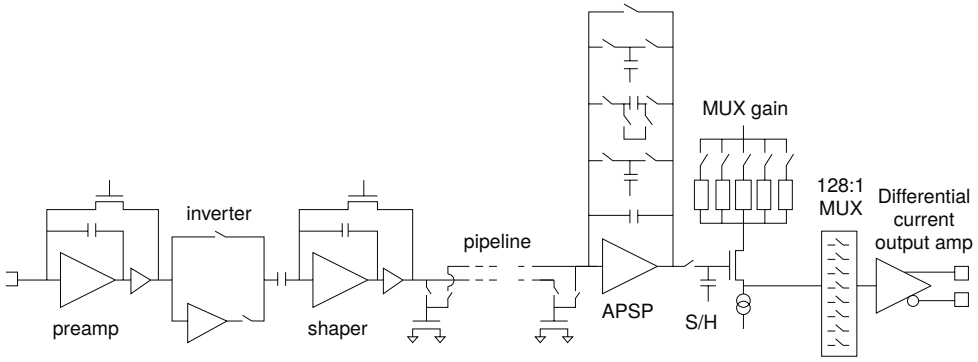

Figure 2.5: The schema of the internals of the APV25 chip. The stages before 128:1 MUX are implemented separately for each of 128 channels [60].

The amplified signal is sent to the inverter which is coping with the signal polarity and then to the CR-RC shaper to convert the strip signal into a voltage pulse with a peaking time of 50 ns. The output of the shaper is sampled with the frequency of 40 MHz and saved to the analog pipeline. The APV can work in the "peak mode", when only a single value of the pulse shape is used. This value corresponds to the maximum of the pulse shape for the given bunch crossing. In the "deconvolution mode" a weighted sum of the shaper sampled output from three consecutive bunch crossing is calculated in APSP instead. The computed continuous APV output in the peak mode (black curve) can be seen in Fig. 2.6. In the real situation the peak curve in black is sampled at its maximum to obtain peak mode output or by three steps of 25 ns to be able to obtain the deconvolution mode output. The illustration of the sampling points for peak (circle) and deconvolution (rectangles) modes is also presented in Fig. 2.6. From the weighted sum of three sampling points, the continuous APV output in the deconvolution mode (gray curve) is obtained. The deconvolution mode pulse is shorter as shown in Fig. 2.6, therefore this mode is the nominal mode as it reduces the out-of-time pileup and improves the separation of signals from two consecutive bunch crossings. To have the possibility to optimize the pulse shape, the feedback resistors of both preamplifier and shaper as well as the bias current and the voltage are fully programmable and their settings can be thus easily changed. For the calibration and test of the chip, an internal calibration circuit is present. This circuit enables to inject a charge to each channel separately to the stage prior to the preamplifier one.

The sampled output for all the 128 channels of one APV are extracted from the analog pipeline upon the request of the trigger. The average signal level from the 128 channels can be adjusted within the range of the APV, in order to reduce the signals exceeding the FED range. The signals from two APV chips are multiplexed by one APVMUX chip [17] into a single line and converted by laser from an electrical to analog optical signal, which is sent via an optical fiber to the service cavern. In the control room, the optical signal is

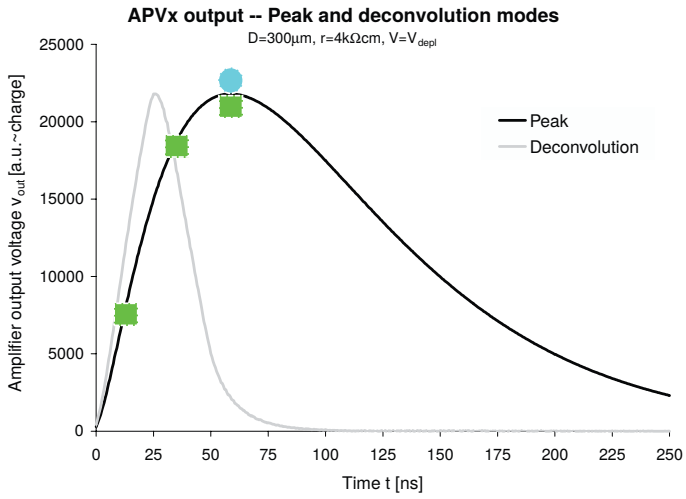

Figure 2.6: APV output in the peak (black) and deconvolution (gray) mode. Actually, the shaper output is sampled in the APV to obtain only maxima of the two curves. An example of the sampling points for the deconvolution mode is shown in green rectangles, the sampling point for the peak mode is represented by a blue circle [60].

then received by a pin diode which is an entry point of the FED.

2.2.4 The Front End Driver

One FED [52] is receiving data from 96 optical fibers, each sending the information originating from 2 APVs. The data in form of optical signals are converted to electrical signals, which are then reordered and synchronized. For each APV input, the signals per channel are extracted and digitized into 10-bit range Analog Digital Counts (ADC). The output signal for a given channel is referred to as "raw digi", which can be seen in Fig. 2.7.

In FED two subtractions are performed. First, there is a subtraction of pedestal, computed as the mean strip activity for a given strip when no particle is present. The strip noise, which cannot be further subtracted, is the variation around the pedestal value. Both are evaluated from special "pedestal runs" taken several times per year. In order to best use the FED range, not the pedestal value is subtracted, but the pedestal value minus a fixed offset, which is currently chosen to be 127 ADC. After pedestal subtraction, the Common Mode Noise (CMN or baseline) is the noise due to e.g. electronics or power supply origins, which is common to all channels of one APV and is calculated on an event by event basis as the median over the 128 channels. The data after subtraction of the pedestals and CMNs are also shown in Fig. 2.7 for one module.

After both subtractions of the pedestals and the CMNs, the channels with ADC values lower than zero are truncated to zero as the FED can only handle positive values. For all channels, the signal-to-noise ratio (S/N) is checked separately. If the S/N of the channel is larger than two or if the S/N of a group of neighboring channels exceeds a certain threshold, then the ADC values of these channels are kept while the values of the other channels are set to zero. Moreover the ADC range is truncated to 8 bits in a way that no change is applied for channels with charges lower than 254 ADC, but charges between 254 ADC and 1022 ADC included are set to 254 ADC, and charges exceeding 1022 ADC are stored as 255 ADC. Later only information about strips with non-zero ADC values are sent to the CMS Data Acquisition System (DAQ). This procedure, including pedestal and CMN subtraction, evaluation of the channels based on the S/N and suppression of the channels with zero ADC value, is called "Zero Suppression" (ZS). In the standard operation mode, the zero suppression mode is used for data-taking. The ZS output data size is 50 Mb/s per 1% occupancy compared to the 3 Gb/s before the zero suppression. Therefore thanks to the ZS procedure, the available data are reduced by a factor of around 60 considering 1% occupancy, which avoids an overload of the CMS DAQ system.

For testing purposes the FED is able to operate in other modes than the ZS one. There is an another mode referred to as the "Virgin Raw" (VR) data taking mode, in which no subtraction or suppression is applied. This mode is thus suitable for commissioning, debugging and deeper studies of the APV output.

2.2.5 The offline data treatment

The data collected by the FEDs are then treated offline. A clustering procedure is applied on the ZS digis. The default clustering algorithm is called the "three threshold algorithm", posing thresholds on the seed strip (strip with the largest signal), on the neighboring strips and on the cluster charge in terms of signal-to-noise ratio. The seed must pass the requirement of S/N>3, adjacent strips can be added if their S/N is larger than two. On top of these requirements, the total cluster charge (the sum of the charges of all channels) must be five times larger than the total cluster noise $\sigma_{cluster}$ which is defined as

$$\sigma_{cluster} = \sqrt{\sum_i \sigma_i^2}, \tag{2.2}$$

where σ_i is the noise of channel i within the cluster. In addition to its charge and noise, each cluster can be quantified by a cluster width, corresponding to the number of channels in the reconstructed cluster. An example of cluster obtained at the end of the clustering procedure is shown in Fig. 2.7.

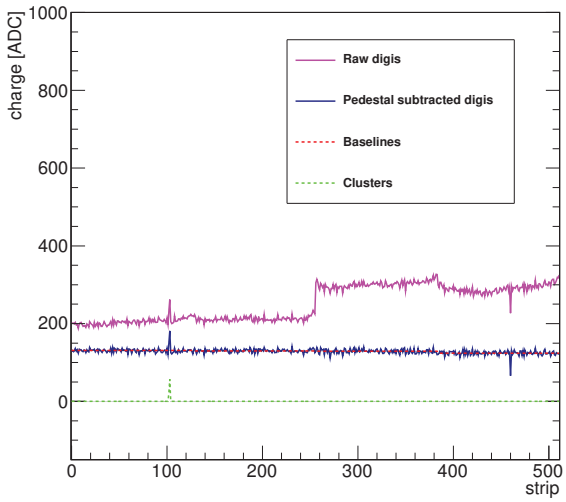

Figure 2.7: Example of data from one tracker module undergoing zero suppression and clustering. The raw digis are shown in pink. From the raw digis the pedestals are subtracted and the resulting digis are shown in blue. From pedestal subtracted digis the baselines shown in red are computed and subtracted. The final clusters are shown in green.

During clustering, the strip charge is calibrated by two factors: the tick-mark gain (G1) and the particle gain (G2). First, the tick-mark gain is correcting the signal for the transmission losses, mainly for the losses happening during the transmission of the signal through the O(100) m long optical fibers. To estimate this gain, a well-defined tick-mark signal is issued at the APV level. The G1 for the APV is then computed offline by re-scaling the output tick-mark to 640 ADC. By construction, the tick-mark gain aims to equalize the output among APVs. The main purpose of injections of tick-mark signals is the synchronization of the APVs to the central trigger.

Secondly, the particle gain is correcting for the differences at the sensor level and compensates for example for charge trapping. This gain is determined from the ionization of the silicon sensitive volume per unit of length of the particle traversing the sensor. The measured MPV of the ionization per unit of length is then used to equalize the response of different sensors to the MIP charge set to be 300 ADC/mm.

These calibrations need to be determined frequently as they are affected by the ageing of the detector (e.g. fibers and lasers for G1, sensors for G2) or some change of the operating conditions (e.g. temperature). During this step the cluster charge is corrected by the factor $1/(G1 \times G2)$.

Because of the observed discrepancy in the cluster position between the data recorded with the peak and deconvolution modes, which was found to be caused by a reduced efficiency of collecting charge close to the backplane in the deconvolution data, a correction

referred to as "backplane correction" must be applied to have the same cluster position in deconvolution and peak data. The derived backplane correction is not precise and its inaccuracy is further compensated by the alignment.

For the further reconstruction steps the clusters are converted to hits, whose position is obtained from charge-weighted positions of the channels in the cluster, corrected for the backplane correction in the deconvolution mode and for the Lorentz drift in the barrel, where the magnetic field is perpendicular to the module plane. In the case of stereo modules, the matching of hits between the two tilted modules is performed. The resolution on the hit position is also assessed at this step.

The reconstructed hits are then used to reconstruct tracks as described in Section 1.2.2. The clusters which are associated with tracks are referred to as "on-track" clusters, the remaining clusters are called "off-track" clusters.

2.3 Laboratory studies on the impact of highly ionizing particles on the APV25 chip

After an introduction of the tracker readout in the previous section, we can now study the effect of the HIP events on the electronics and output data in more details. Before the start of the LHC operation, several studies of the HIP events were performed in laboratory, during the beam tests at PSI [61] and CERN X5 [62]. The impact of large energy depositions on the electronics was also studied by charge injection in the calibration circuit of the APV or by laser tests [49]. Only the HIP studies performed at the PSI beam test are described in a larger extent in this section, because of the best projection of their results to the CMS environment.

2.3.1 Experimental setup of the PSI beam test

To test the behavior of the CMS tracker modules in conditions similar to the CMS ones, studies at the M1 beam-line at PSI were performed. This beam-line provided a continuous beam of protons and pions. For the module studies, the beam was tuned to pion momentum of 300 MeV to best mimic the CMS environment. The tracking system under test at PSI consisted of 12 layers of tracker modules (3×TIB, 3×TEC, 6×TOB), but for the study of HIP events only TIB and TOB modules were used. These TOB modules had 500 μm thick sensors with a strip pitch of 183 μm and were equipped by inverter resistors of either 50, 75 or 100 Ω. Special trigger bursts and APV settings were used to trigger

the HIP events and events after HIP, allowing to provide 29 consecutive events recorded every 25 ns, resulting in data over a 750 ns period. All modules were operated in peak mode and the output data were equivalent to the CMS VR data format.

2.3.2 Response of the readout electronics to the HIP events

As discussed previously, the highly ionizing particle leaves very localized large energy depositions up to the equivalent of ∼1000 MIPs and thus saturate the readout electronics. The affected channels collect a charge beyond the range of the readout electronics which is of order of a few tens of MIPs. The rest of the channels belonging to the same 128-channel APV is shifted towards low ADC values up to the point when the signal is so small that no light can be emitted by laser (zero-light level). This behavior is caused by the common biasing of the inverters described in Subsection 2.2.3, due to which a large signal appearing at one inverter is suppressing the other channels of the APV [53].

Because of the CMN shift, the HIP events can be easily identified thanks to a requirement on the value of the baseline. In this study, an APV chip, which exhibited baseline value lower or equal to -20 ADC at some point during the trigger burst period, was tagged as containing a HIP candidate. The response of the APV chip on the HIP event is shown in Fig. 2.8. Each plot in this Fig. 2.8 presents the data from 6 consecutive TOB modules (on the y-axis) after pedestal subtraction at a different time. The x-axis depicts all channels of one module and the individual y-axes show the ADC values for all these channels. There are four APVs in each module. A normally operating module is e.g. the top module in the bottom-left plot (T_{event} = 525 ns), where all APVs have their baseline around a nominal value. In this module a MIP signal can be seen in the second APV. In Fig. 2.8 a HIP signal can also be observed. The top-left plot (T_{event} = 300 ns) shows the first evidence of the HIP event: in the second module from the bottom, in the second APV, a large signal peak and a small shift of other channels towards low values of the APV range can be observed. After 50 ns (T_{event} = 350 ns) the channels of the affected APV, which are not collecting the HIP signal, are suppressed and the signal peak is thus fully revealed. The suppression of numerous channels as well as the large signal peak can be still observed at T_{event} = 525 ns. At T_{event} = 575 ns, the channels start to recover to their initial position. It is interesting to note that at T_{event} = 525 ns (for x∼33 mm) and T_{event} = 575 ns (for x∼33 and 50 mm) a MIP passes through all the six layers of the modules. The signal is observed in the APVs of all layers except of the one affected by the HIP event. The time period, during which the APV is insensitive to a MIP signal is referred to as the dead-time.

The CMN distribution of all baselines can be seen in the bottom plot of Fig. 2.9.

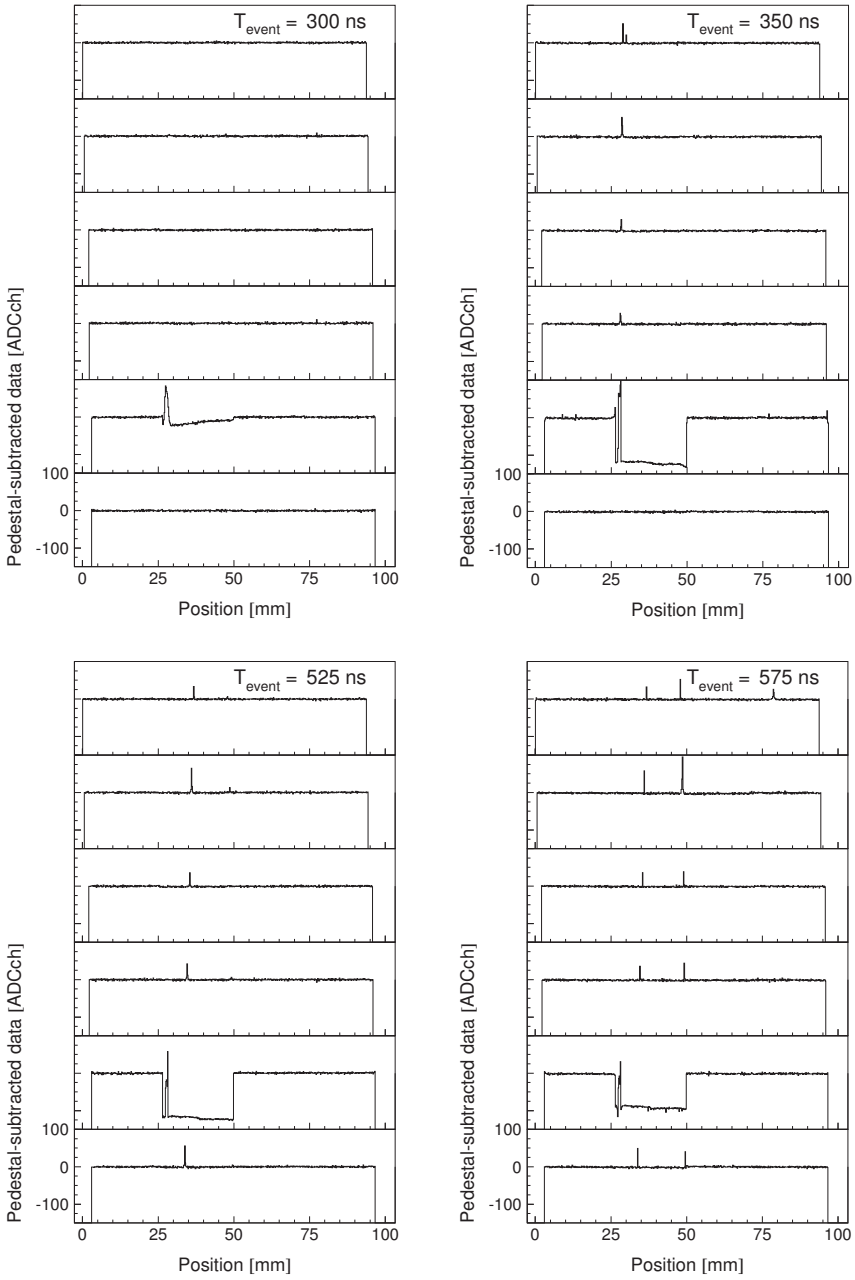

Figure 2.8: Example of the time evolution of the APV behavior as a response to a HIP event. The situation for six modules is depicted at four different times: $T_{event} = 300$ ns (top-left), $T_{event} = 350$ ns (top-right), $T_{event} = 525$ ns (bottom-left) and $T_{event} = 575$ ns (bottom-right). The ADC values of pedestal subtracted data (y-axis) of the six layers of the TOB modules (y-axis direction) are plotted for all channels of one module (x-axis). The HIP event appears at $T_{event} = 300$ ns in the second module from the bottom and can be followed in the same module for the remaining three timestamps. These results come from measurements obtained with the PSI data [53].

The CMN distribution is peaking around 0 ADC during the standard conditions, while a smaller peak around -100 ADC comes from suppressed baselines which are the result of the HIP events. In this analysis the selected HIP event satisfies the selection requesting

CMN≤-20 and a HIP cluster seed charge larger than 125 ADC. Therefore in Fig. 2.8 this happened for the event at $T_{event} = 350$ ns, but as shown in the example, the signal from the real HIP interaction occurred and was partially observed already 50 ns before this "selected HIP" event $T_{event} = 350$ ns.

As seen in the example, the HIP event is suppressing all channels which are not collecting the signal. Large enough HIP signals then result in a full suppression of the channels beyond the lower limit of the possible range, when the electrical signal is too small. The APV with fully suppressed channels exhibit a very small σ_{raw}, which is in this case computed as a standard deviation of the data before pedestal subtraction (raw data), when excluding 5% of the lowest and 25% of the highest channels in the APV. The standard deviation σ_{raw} of raw data is shown in the top part of Fig. 2.9, where the population in the large peak corresponds to the normal operation σ_{raw} values around ∼1.5 ADC, which are reproducing the spread of pedestals. The smaller peak population with an σ_{raw} lower than 0.5 ADC is coming from fully suppressed baselines. The tail of the distribution is populated with distorted baselines. The expression "distorted baseline" in this text refers to the APVs whose channels exhibit a large spread of signals from the baseline value, excluding the signal from particles passing trough. The distorted baselines usually originate from the HIP event, which results in a non-uniform suppression and recovery of the channels within and APV.

Based on these observations two event categories were defined: the "fully suppressed" and the "partially suppressed" baseline events. Events with "fully suppressed" baselines satisfy $\sigma_{raw} < 1$ ADC, due to no light emission. "Partially suppressed" baselines are required to have $\sigma_{raw} \geq 1$ ADC and CMN≤-20 ADC.

2.3.3 Dead-time induced by the HIP events

In other laboratory studies, during which a charge has been induced in tracker sensors by laser, the recovery of the baseline and the signal in terms of S/N has been studied [49]. It was shown in Fig. 2.10 that the S/N ratio recovers differently and by different time constants than the baseline. However, both recoveries of the baseline and the S/N takes about order of hundreds of nanoseconds. To estimate the dead-time and hit efficiency induced by a HIP event, it is necessary to know when enough of signal appears to be reconstructed in the cluster and not only study the baseline. In the following paragraph the method and results on the dead-time measurement using PSI beam test data are described.

In the PSI tests, the dead-time of the APV is calculated from a difference of hit

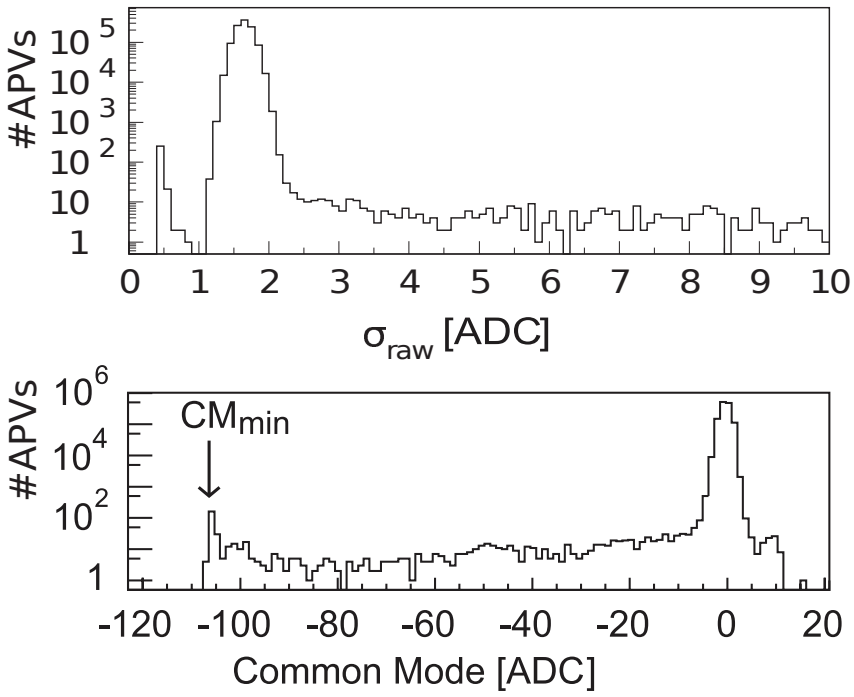

Figure 2.9: (top) The standard deviation of raw data (σ_{raw}). The large peak around 1.5 ADC corresponds to standard baselines, while the peak at $\sim$ 0.5 is caused by fully suppressed baselines. (bottom) The CMN distribution, in which the nominal baselines are located around zero and the fully suppressed baselines are peaking around -100 ADC. These results were obtained with PSI beam test data [53].

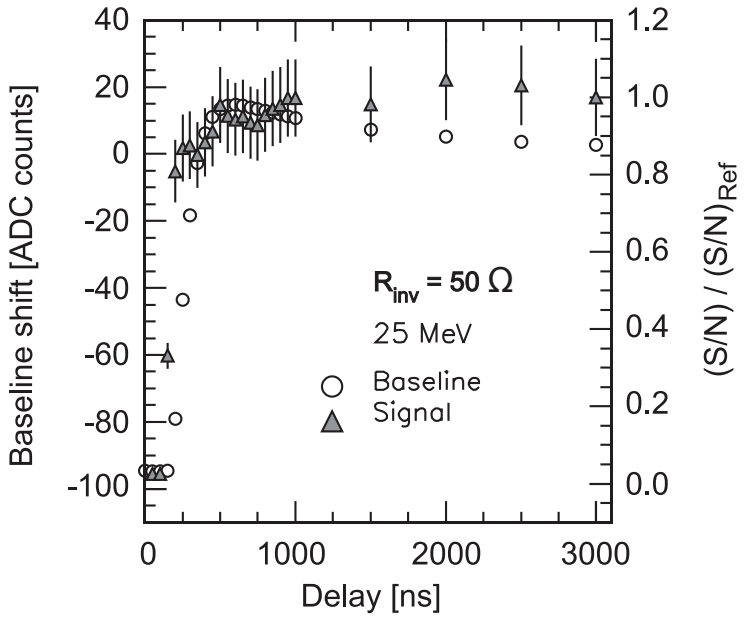

Figure 2.10: The recovery of the baseline (circles) and signal (triangles) expressed as the ratio of the measured S/N to the reference S/N, as a function of time. The evolution is shown for an inverter resistor value of 50 Ω and an energy deposit of 25 MeV [49].

efficiency. The hit efficiency ϵ_{hit} is computed separately for APVs influenced by the HIP event (ϵ_{hit}^{HIP}) and for "efficient" APVs which are not influenced by the HIP event (ϵ_{hit}^{good}). The hit efficiency is defined as $\epsilon_{hit} = N_{hit}/N_{tracks}$, where N_{hit} is the number of clusters reconstructed in the APV around the track intercept point, and N_{tracks} is the number of reconstructed tracks traversing the APV. The tracks were reconstructed by simple track finding algorithm using the least-squares linear fit of the clusters positions. The dead-time is the time interval during which the APV is not fully efficient ($\epsilon_{hit}^{HIP} < \epsilon_{hit}^{good}$). The averaged dead-times for the APVs with the fully suppressed baselines are shown in Table 2.1 for both inverter resistor values of 50 Ω and 100 Ω. The APVs with partially suppressed baselines exhibit much smaller dead-times compared to the APVs with fully suppressed baselines. The dead-times for APVs with fully suppressed baselines are typically of the order of a few tens of ns. In Table 2.1, it can be noticed that a reduced resistor value significantly decreases the dead-time and that the dead-time depends also on the sensor geometry. Although, diminishing the resistor value has a disadvantage which is the enhancement of the baseline distortions, leading to the reconstruction of "fake" clusters as only a flat CMN is subtracted [53]. In this analysis the fake clusters were observed to have a large charge and also a large cluster width of typically tens of channels. The increase of fake cluster multiplicity was found to be negligible and therefore the decision to equip tracker modules with 50 Ω resistors instead of 100 Ω was taken in order to reduce the dead-time.

Sensor type and R_{inv} [Ω]	Γ_{mean} [ns]	Γ_{max} [ns]
TIB 100 Ω	99.5 ± 12.0	200 ± 25
TIB 50 Ω	69.6 ± 9.4	250 ± 25
TOB 100 Ω	122.5 ± 12.6	275 ± 25
TOB 50 Ω	100.5 ± 3.6	275 ± 25
TIB Γ_{mean}(50 Ω)/Γ_{mean}(100 Ω)	0.70 ± 0.13	
TOB Γ_{mean}(50 Ω)/Γ_{mean}(100 Ω)	0.82 ± 0.09	

Table 2.1: The mean (Γ_{mean}) and maximum (Γ_{max}) dead-time of the APV chip induced by the HIP events for fully suppressed ($\sigma_{raw} < 1$ ADC) baseline events. The dead-times were evaluated for two different module geometries (TIB or TOB) as well as for two inverter resistor values (100 or 50 Ω). These results were obtained with PSI beam test data [53].

2.3.4 Probability of a HIP event in the tracker module

At the PSI beam test, the HIP probability per track was also measured. This HIP probability is defined as

$$P_{HIP}(CMN_{HIP} \leq CMN_{threshold}) = \frac{N_{HIP}(CMN_{HIP} \leq CMN_{threshold})}{N_{tracks}}, \tag{2.3}$$

where $N_{HIP}(CMN_{HIP} \leq CMN_{threshold})$ is the number of selected HIP events with a baseline value (CMN_{HIP}) lower than the threshold $CMN_{threshold}$ and N_{tracks} is the number of tracks traversing the sensor.

The HIP probability measurements were provided with a pion beam of 300 MeV energy, which is the most probable energy value for pions in the CMS tracker. The probability measured for different modules, using $CMN_{threshold} = -20$ ADC, was found out to be of the order of 10^{-3} for the TOB and 10^{-4} for the TIB. It was also concluded that the HIP probability per track does not scale with the particle flux, but rather with the sensor thickness. With a larger thickness of the sensor the probability of the nuclear interaction is increasing. A similar measurement was provided using a proton beam of 300 MeV/c momentum, which in this case is not compatible with the CMS conditions.

2.4 Studies of the HIP events with the CMS pp collision data

As described in the previous section, several HIP studies were performed in the laboratory, but the HIP events have never been studied with the CMS collision data. Though the PSI beam test conditions were supposed to be as close as possible to the CMS ones, the particle and energy spectra differ in these two cases, it is thus important to evaluate the HIP effect in the real CMS environment. Also at PSI only few modules were tested but not all of them.

The HIP studies with the CMS data that I performed during my PhD thesis are discussed in Subsections 2.4.2 and 2.4.4 after a first discussion on the strategy of these studies presented in Section 5.2. In Subsection 2.4.2 the HIP effect is studied from the perspective as a possible explanation of the observed hit inefficiency. Then Subsection 2.4.3 briefly presents the change of the APV setting which finally solved the inefficiency problem. A new study of data recorded after the fix allows to measure the HIP properties and the

consequences of the HIP on the read-out output, without any influence from the past issue.

2.4.1 Strategy of the HIP studies

As explained in the section 2.2.4 the Zero Suppression mode is used in the standard data-taking. During the ZS procedure, all negative channels after pedestal subtraction are truncated to zero, this mode is thus not suitable to study the HIP events, which are known for causing a drop of the CMN as described in Section 2.3. The solution is to request data-taking in the Virgin Raw mode, what comes with a cost of an increased event size. In the VR data, no subtraction or suppression is applied but the ZS can always be performed offline, providing then the possibility to compute the CMN and proceed with clustering and further data treatment. In the following analyses, the CMN is computed from all 128 raw digis after pedestal subtraction as a median over these 128 strips. The standard deviation (σ_{raw}) is calculated from the raw digis of 80% of the 128 channels having the lowest ADC value, to avoid the clusters in this computation. The ZS and clustering are performed as in the standard data-taking (i.e. truncation to zero, computation of the baseline after truncation, truncation of digis to 8 bits) to mimic the standard data-taking output.

The goals pursued in the further studies are to select a HIP event and study the influence of such event on the electronics and the clustering. As seen in previous studies in Section 2.3, the signal recovery time is of the order of hundreds of ns. Thus to be able to study the evolution of the CMN and the cluster properties, consecutive events in a window of a few hundreds of ns are needed. However the probability to record closely spaced events in time is very low without special trigger configuration. The possibilities for a new trigger configuration are very limited due to the increased size of the tracker information per event during the VR data-taking by factor of O(60) compared to the standard ZS data taking. Moreover in order not to overload the CMS data acquisition system, the following trigger criteria are imposed on the number of triggers in a given number of bunch crossings (bx) [63]:

- no more than 1 trigger in 3 bx,
- no more than 2 triggers in 24 bx,
- no more than 3 triggers in 100 bx,
- no more than 4 triggers in 240 bx.

For simplicity, in the following sections of this chapter are shown only plots for the first layer of the TOB, which exhibited the largest drop in the hit efficiency. The probability of the HIP event for a given APV is defined in a similar way as in the PSI study presented in subsection 2.3.4 as

$$p_{HIP} = f_{HIP}\frac{1}{N_{tracks}}, \tag{2.4}$$

with

$$f_{HIP} = \frac{N_{HIP}}{N_{all}}, \tag{2.5}$$

where N_{HIP} is the the number of selected HIP events per APV, N_{all} is the total number of events and N_{tracks} is the number of tracks per APV. The probability p_{HIP} is computed in average for all layers of the strip tracker in order to complement the study with a more global picture.

Alternatively the HIP probability can be defined as

$$p_{HIP}(PU) = f_{HIP}\frac{1}{PU}, \tag{2.6}$$

where PU is the peak pileup of the fill.

2.4.2 A first study of the HIP events in the CMS detector

2.4.2.1 Motivation to study the HIP effect in the CMS detector

As introduced in Section 2.1 the CMS detector faced important hit inefficiencies in 2015 and 2016. At that time, the HIP effect was identified to be most probably the source of these tracking inefficiencies. A lot of efforts were therefore put into studies of the HIP effect from many perspectives. One of the options was to analyze the Virgin Raw data, from which a pure output of the APV can be obtained. In the following study, the VR data are used to characterize the HIP effect and evaluate its impact on the electronics and clustering. The presented study provides first results on the HIP effect with the CMS data.

2.4.2.2 Experimental setup

This study uses the VR data taken on the 12^{th} of April 2016 in the run 273162 of the LHC fill 4915, where only the silicon strip tracker, trigger and data acquisition system were included. Due to the constraints from the LHC and CMS, a short run of around 30

minutes with an instantaneous luminosity of $1.5\times10^{33}\text{cm}^{-2}\text{sec}^{-1}$ was taken. During this run, the APVs were operating in the deconvolution mode. The LHC delivered beams with 601 bunches each, among which 589 pairs of bunches collided at CMS. The average pileup for this fill was 26 interactions per bunch crossing. The beams were mainly composed of trains of 72 bunches, in which bunches were spaced every 25 ns. The space between trains was composed by at least 36 empty bunches.

Closely spaced events in time were enriched in data by using a special trigger configuration, which forced the first bunch crossing in a fixed train to be triggered. After this trigger, two other bunch crossings in the same train were triggered randomly. Then the trigger waited for the same train in next orbit in order not to overload the data acquisition system.

2.4.2.3 Methodology

In Section 2.3, it has been observed that a HIP event can be identified via a low value of the baseline. Applying this approach to the CMS data allows to select the event shown in the left plot of Fig. 2.11. In this example the expected effect of the HIP event on the chip can be seen: a negative baseline, a large signal on few channels and a low standard deviation of the raw digis. But in many cases the large signal is not observed as shown in the right plot of Fig. 2.11, in contradiction to what has been observed in the study of Section 2.3. This difference can be explained by the different operation mode of the APV: a deconvolution mode was used for studies at CMS while for the HIP studies at PSI it was a peak mode. During studies of the APV chip behavior when large charges were injected to the calibration circuit [62], it has been shown that when APVs are operated in deconvolution mode, the large signal peak as seen in the left plot of Fig. 2.11 can be observed only for few ns and then the channels in which large signal was observed are also driven beyond the low limit of the measurable ADC values.

A reliable selection of the APVs influenced by the HIP events can be designed via the presence of the fully suppressed baselines in a similar way as in Section 2.3.3. From the analysis of the correlation of the baseline and σ_{raw} values in Fig. 2.12, it is obvious that the standard events with a nominal value of the baseline around 127 ADC have a σ_{raw} value around 8 ADC units. The second largest population has a value of σ_{raw} lower than 2.5 ADC and a fully suppressed baseline, which can be connected with large energy deposits in the sensor read by the given APV chip. To determine the value of σ_{raw} which selects fully suppressed baselines, the distribution in Fig. 2.13 of σ_{raw} is analyzed. Based on the knowledge of the baseline, σ_{raw} and their correlation, the selection of the HIP

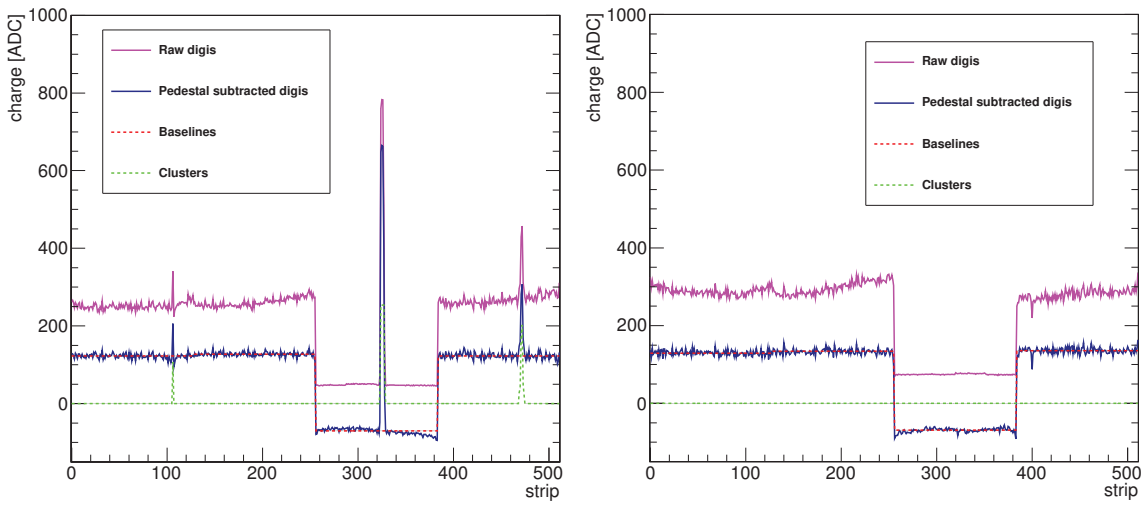

Figure 2.11: Example of distribution of raw digis (pink), pedestal subtracted digis (blue), baselines (red) and clusters (green) as a function of the strip number in one module. (left) The third APV in the module shows a behavior induced by a HIP event: a low charge variation for the suppressed raw digis and a large observed signal for few channels. (right) The third APV in the module shows a behavior induced by a HIP event: low charge variation for the suppressed raw digis, but in this case no peak is observed.

events has been chosen to be

$$baseline < -5 \text{ ADC and } \sigma_{raw} < 2.5. \tag{2.7}$$

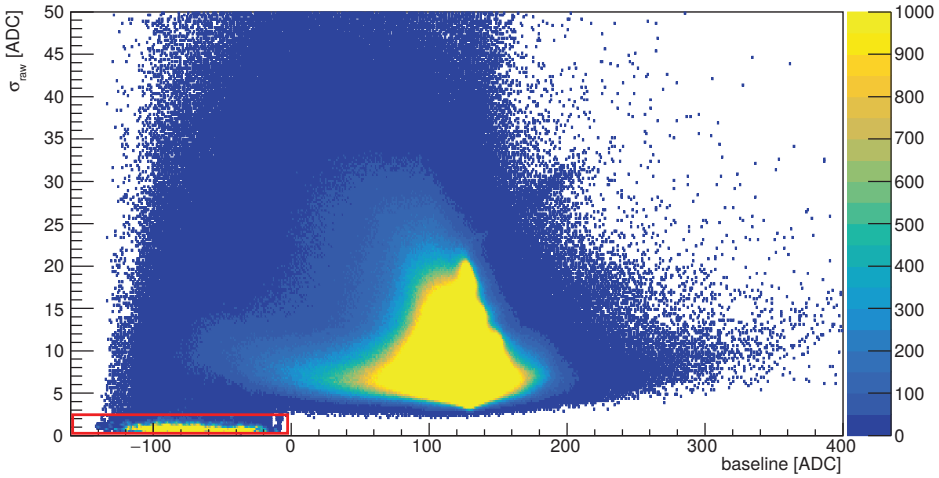

Figure 2.12: The 2-D distribution of the σ_{raw} of raw digis (y-axis) versus the baseline (x-axis) for the run 273162. The baselines selected as HIP events are indicated by a red box.

In the Fig. 2.12, there are many events with a negative value of baseline, but a large

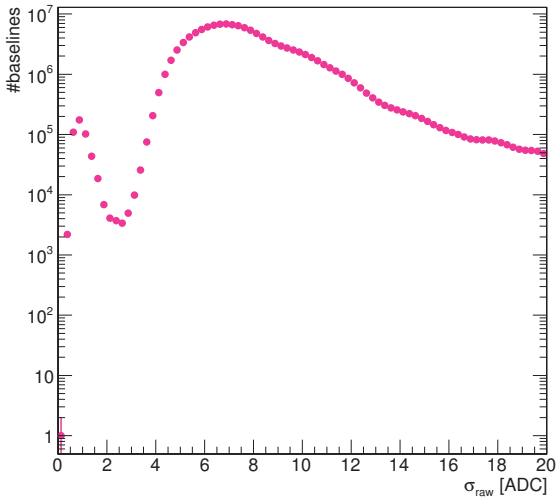

Figure 2.13: The σ_{raw} distribution for the run 273162.

value of σ_{raw}. These events can originate from a baseline drop, a baseline recovery or from large energy deposits, but not large enough to fully suppress the baseline. In order to disentangle the different populations, the partially saturated baseline events are not selected as HIP events.

It has also been observed that the full saturation can last for several bunch crossings as it is later shown in Section 2.4.2.5 and consequently for a given APV, several consecutive events could be selected as a HIP. In this case, only the first event of these possible events is defined as the selected HIP. In addition, as the saturation of the baseline is a consequence of the HIP interaction, the HIP event does not have to be selected at the time when the real HIP interaction has occurred in the sensor.

The analysis of the APVs influenced by a HIP event has been performed statistically considering together all the HIP events occurring in the first layer of the TOB. For that purpose, when a HIP event is selected, the bunch crossing of this event is redefined to bx=0, and the bunch crossings of two remaining events in the same train are set relatively to the selected HIP event, e.g. if another event is triggered five bunch crossings after the selected HIP, its bunch crossing is set to 5. The average information about clusters, baselines and raw digis per each bunch crossing is then used. The APV-averaged baseline distribution over the first layer of TOB as a function of the bunch crossing number, shown in the left plot of Fig. 2.14, allows to study what happened before and after the selected HIP. When following the baseline evolution in time, the baseline shows a stable value chosen by the tracker operation of around 127 ADC long before the HIP occurs (bx$\ll$0). Shortly before the selected HIP, the baseline starts to drop as a consequence of the large energy deposition in the sensor. At bx=0, by definition, the baseline is satu-

rated, i.e. reaches the zero-light level. The baseline recovers to normality in about 15 bx and slightly overshoots for the remaining duration of the train. The baseline overshoot can be understood as a consequence of the response of the APV chip to the large signals. The gap between bx=0 and the other bunch crossings is caused by the first trigger rule, which allows only one trigger in three bunch crossings.

A similar distribution for σ_{raw} as a function of the bunch crossing number is shown in the right plot of Fig. 2.14. Long before the HIP event, σ_{raw} is stable with a value around 8 ADC. Right before the selected HIP, σ_{raw} increases due to a non-uniform drop of the baseline, knowing that the σ_{raw} computation should remove the channels associated to the clusters. After the HIP event it recovers in around 10 bx. Up to this recovery point, the baseline can be fully or partly saturated what explains the low σ_{raw} value. This population is however mixed with distorted baselines which on the other hand have large σ_{raw} and therefore part of the distribution with bx>0 cannot be straightforwardly interpreted.

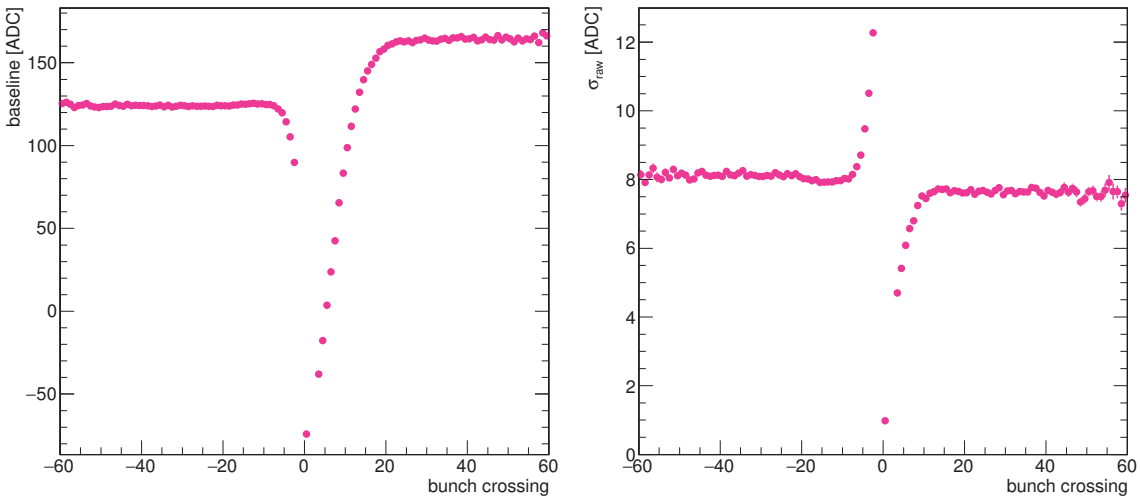

Figure 2.14: (left) The averaged baseline evolution as a function of the bunch crossing number for the run 273162. (right) The evolution of the averaged σ_{raw} of the raw digis as a function of the bunch crossing number for the run 273162. On both plots, the bunch crossing of the selected HIP event is translated to the position bx=0. Events before (after) the selected HIP have bx<0 (bx>0).

2.4.2.4 Results

As shown in Fig. 2.10, the signal recovery, i.e. the hit efficiency recovery, and the dead-time induced by the HIP event cannot be estimated from the baseline information and it is thus necessary to study clusters. The distributions of the average cluster multiplicity (i.e. the number of clusters to number of events per APV) and the maximal cluster charge (i.e. the charge of the cluster with the largest cluster charge) are shown as a function of the

bunch crossing in Fig. 2.15. In the rest of this chapter, the cluster charge refers to the cluster charge not calibrated by the gains. In the shown distributions, as previously, an averaging over the APVs is performed as well as the alignment of the selected HIP event with bx=0. The average cluster multiplicity presented in the left plot of Fig. 2.15 is stable for events long before the occurrence of the HIP. Around bx=-5, the multiplicity grows as additional clusters originating from the HIP interaction (recoil or fragments) may start to appear. The delay between the HIP event and the selected event is not know and is not a constant. As a consequence of the HIP deposit, the chip becomes inefficient for the signal collection, already at bx=0 when the cluster multiplicity drops significantly. The cluster multiplicity is recovered in around 10 bunch crossings. The average cluster multiplicity distribution for bx>10 is flat with a constant higher than for bx<-10, in contradiction with expectations. The maximal cluster charge per APV shown in the right plot of Fig. 2.15 exhibits a stable behavior for bx<-20, followed by an increase in charge. The cluster charge is the highest for the selected HIP as few channels can collect large charges induced by the HIP energy deposits. After bx=0, the cluster charge drops and recovers almost immediately after the selected HIP, but to a slightly lower level than before the HIP event, even though the same level as for bx$\ll$0 is expected.

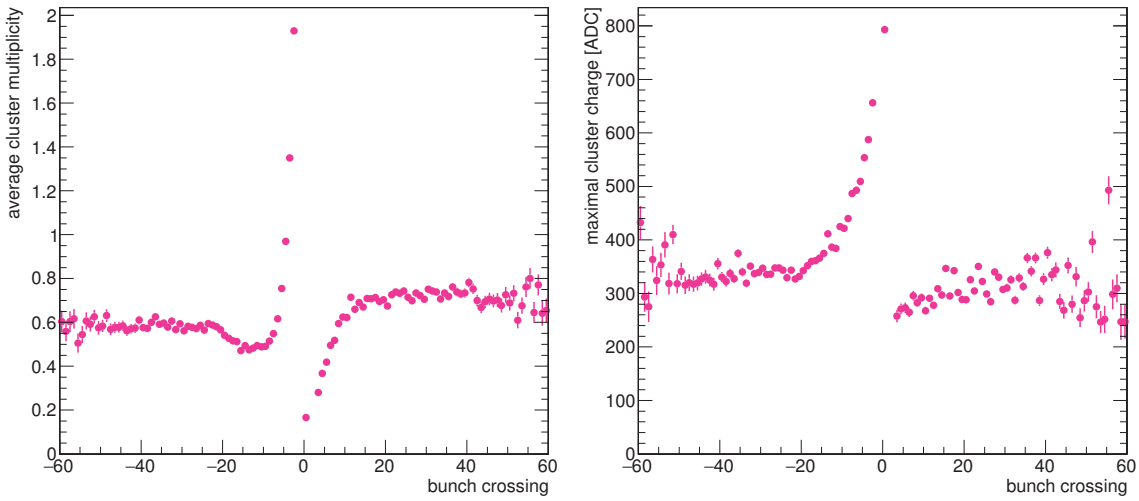

Figure 2.15: The averaged cluster multiplicity (left) and maximal cluster charge (right) as a function of the bunch crossing number for the run 273162. The bunch crossing of the selected HIP event is translated to the position bx=0.

The mismatch between the cluster properties for bx$\ll$0 and bx$\gg$0, as shown in Fig. 2.15, can be, at least partially, understood when analyzing the cluster charge distribution of clusters of the first event in the train and the two other events in the train in Fig. 2.16. For the first event in the train, the cluster charge distribution exhibits a double peak structure of similar peak heights with maxima around 50 ADC and 200 ADC,

while for the other events in the train, the height of the peak around 50 ADC is clearly dominant. The enhanced population of clusters around 50 ADC for the other events in the train is coming from out-of-time pileup contributions, which are not present in the first bunch crossing. In the train there are 3 events triggered, one of them is selected as a HIP event, so only the first or second event can be set to bx<0 and on the other hand only the second or third event can be set as bx>0. In consequence, the regions with bx<0 in Fig. 2.15 are dominated by a population with a lower out-of-time pileup and also a lower average cluster multiplicity and higher maximal cluster charge than the regions of the distributions with bx>0. To avoid the mixing of different populations of events, the first event in the train has been removed from the distributions. The average cluster multiplicity without the first bunch crossing in the train is shown in the left plot of Fig. 2.17 and the maximal charge without the first bunch crossing in the train in the right plot of Fig. 2.17. In both distributions, the removal of the first bunch crossing leads to a significant equalization between the levels for bx$\ll$0 and bx$\gg$0. The spikes in the distributions of Fig. 2.16 are coming from the the strip charge saturation, which appears when the charge on one or multiple strips exceeds 254 ADC.

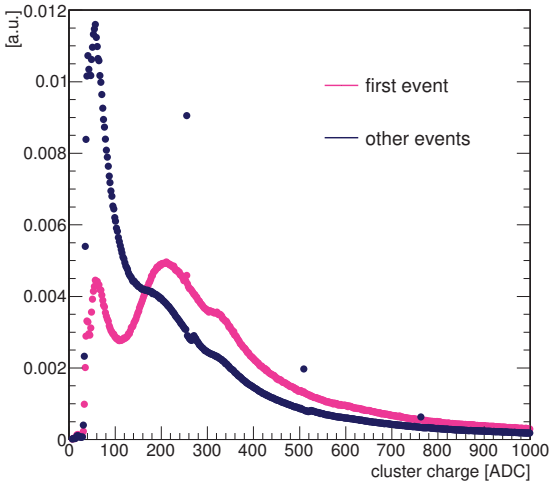

Figure 2.16: The normalized distribution of the cluster charge from the first (pink) and the other (blue) bunch crossings in the train for the run 273162.

The average dead-time for the modules of the first layer of the TOB can be estimated from the left plot of Fig. 2.17. The dead-time, in this case defined as the time interval between the selected HIP event and the full recovery of the average cluster multiplicity, appears to be around 250 ns (10 bx). This dead-time is approximate as no tracking on these data was performed and thus the hit efficiency cannot be accessed. The recovery of the cluster multiplicity does not imply the full recovery of the charge collection. For this purpose the maximal cluster charge distribution as a function of the bunch crossing number is studied in the right plot of Fig. 2.17. It is expected that the cluster charge

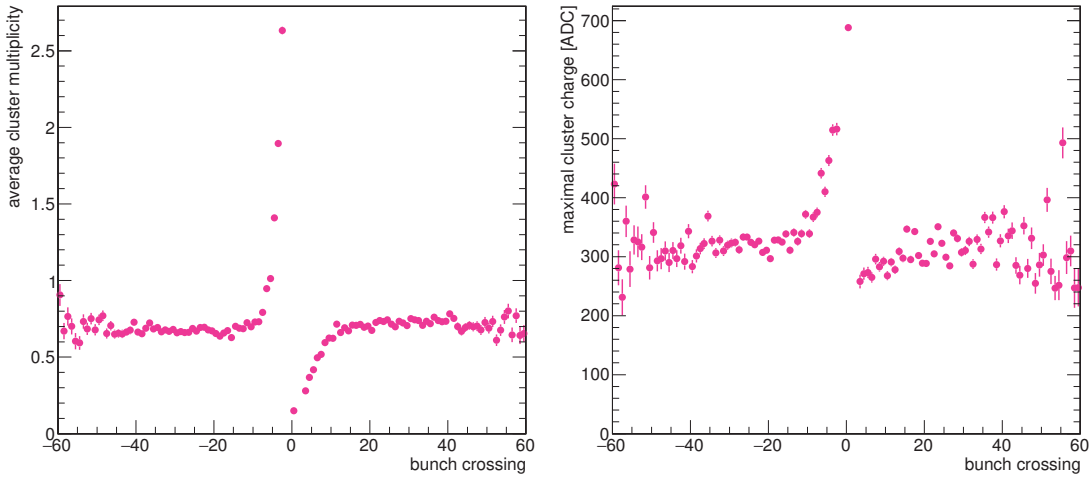

Figure 2.17: The averaged cluster multiplicity (left) and maximal cluster charge (right) as a function of the bunch crossing number for the run 273162. The bunch crossing of the selected HIP event is translated to the position bx=0. Contrary to Fig. 2.15, the events from the first bunch crossing in the train are not included in these distributions.

drops after the HIP event and then it recovers in the following bunch crossings. But the cluster charge seems to be recovered almost immediately and no obvious trend is observed. This effect is most probably caused by the mixing of real and fake clusters, i.e. clusters respectively associated and not associated with the tracks. This mixing could be reduced by using on-track clusters only. On the other hand the tracking would bias the analysis as the tracking efficiency is not 100%.

The fraction of HIP events averaged per APV in the first layer of the TOB, defined by Eq. 2.5, was estimated to be 4×10^{-3}. This fraction is dependent on the run instantaneous luminosity and therefore does not represent the probability of a HIP event as defined in Eq. 2.4. To estimate the HIP probability, the average number of reconstructed tracks per event per APV must be known. But even with the number of tracks it is not straightforward to compute the probability of the HIP event due to the limitations of the selection and data. The average fraction of HIP events is biased by the used trigger which forbids to record the second and third bunch crossings in the train, due to the first trigger rule. The HIP interactions, occurring in the first bunch crossing and fully suppressing the baseline only in the second and/or third bunch crossing of the train, are therefore never selected. In contrary, in the events which are not at the beginning of the train, the HIP events coming from more previous bunch crossings can be selected as the baseline can saturate for more bunch crossings.

2.4.2.5 Limitations of the study

Several limitations of the presented study have already been discussed in the text above. In summary, to the mentioned limitations belongs firstly the different fraction of out-of-time pileup in different events, this has been solved by removing the events from the first bunch crossing in the train from the clusters charge and width distributions. Secondly no tracking is performed in the data, and both real and fake clusters are thus used in this analysis. If tracking has been introduced, the majority of fake clusters would have been removed, but the statistics would have been largely reduced because of the track reconstruction criteria and the fact that no data was recorded in the pixel tracker. Thirdly, as a consequence of the HIP event, the fraction of real and fake clusters can change. Fourthly there is also an empty window in the triggered events caused by the first trigger rule.

A large limitation of this study comes from the ambiguity in the selection of the HIP events. It can be understood by looking at Fig. 2.18 which shows the σ_{raw} per APV as a function of the bunch crossing number, with bx=0 being the selected HIP event. In the bottom-right part of the plot, there is a large population of APVs with σ_{raw}<2.5 for bx>0, corresponding to very large energy depositions keeping the baseline fully suppressed for several bunch crossings. Due to this uncertainty, it is impossible to determine the exact time of the HIP interaction in the sensor and therefore all distributions shown above with the selected HIP aligned to bx=0 are spread over several bunch crossings. Moreover because of this selection uncertainty, the probability of a HIP interaction cannot be computed.

A possible improvement of the HIP selection was investigated by trying to define selection criteria on the clusters. A first tentative was to select large charge deposits by tagging the saturated clusters with an ADC value of at least one channel larger than 254 ADC. Fig. 2.19 shows the fraction of clusters with at least one saturated strip with respect to all clusters per APV as a function of bunch crossing, where bx=0 corresponds to the selected HIP by the criterion in Eq. 2.7. The fraction of saturated clusters is significantly high only for bx=0, which is already a selected HIP event. Moreover as discussed in the left plot of Fig. 2.17, the average cluster multiplicity per APV is very low for bx=0, so a requirement on the saturated cluster would only result in a large reduction of statistics. Another approach was to study the maximal cluster width per APV as a function of the bunch crossing number, shown in Fig. 2.20, but no obvious trend is observed in the distribution.

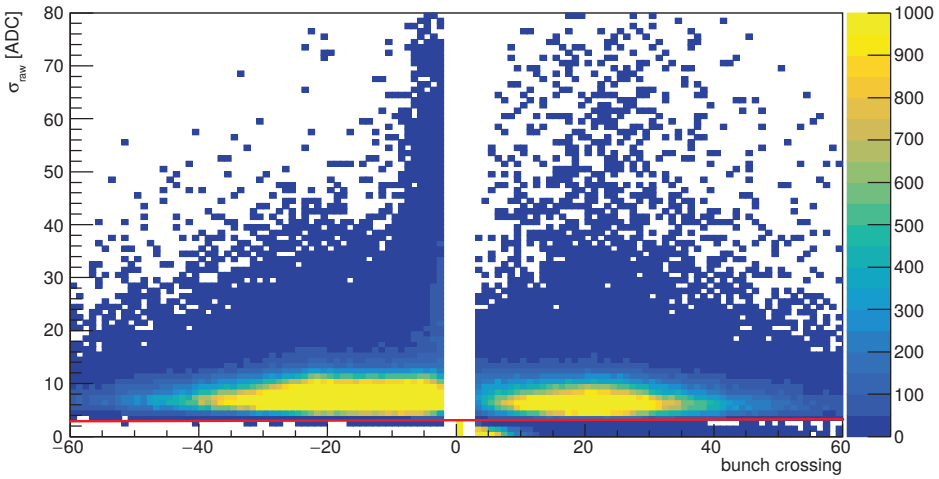

Figure 2.18: The 2-D distribution of the σ_{raw} (y-axis) as a function of the bunch crossing number (x-axis) for the run 273162. The bunch crossing of the selected HIP event is translated to the position bx=0. The limit of σ_{RMS}<2.5 is indicated by a red line.

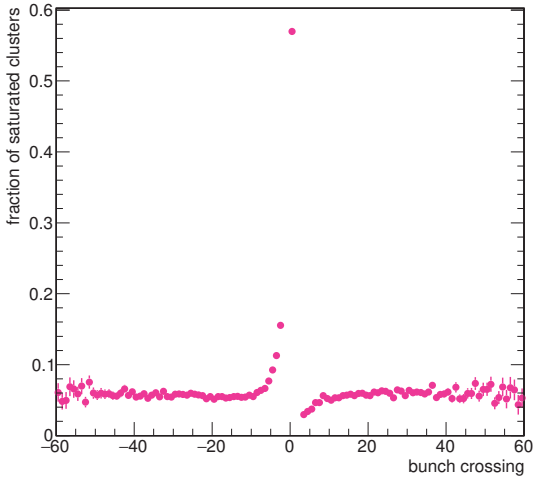

Figure 2.19: The averaged fraction of clusters with at least one saturated strip with respect to all clusters in an APV as a function of the bunch crossing number for the run 273162. The bunch crossing of the selected HIP event is translated to the position bx=0.

2.4.3 Change of the APV configuration settings

At the end of 2015 and during the first half of 2016, the HIP interaction in silicon sensors under the CMS conditions was studied from many perspectives. The probability of the HIP event was found to be too low to explain the magnitude of observed inefficiencies and the CMS collaboration has thus tried to find other causes of the hit inefficiency. In August 2016, the major source was found in the settings of the APVs.

For the data taking, the APV's Preamplifier Feedback Voltage Bias (VFP) was set

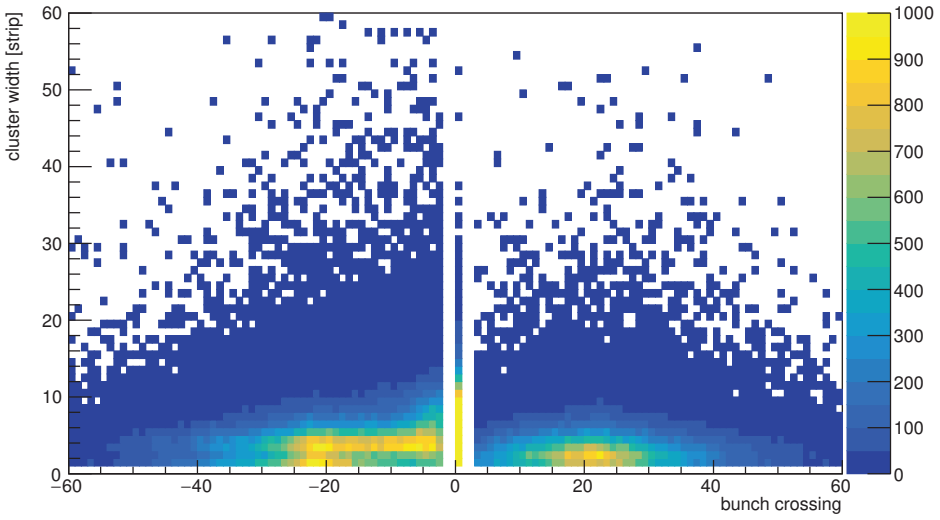

Figure 2.20: The 2-D distribution of the average cluster width versus the bunch crossing number for the run 273162. On the x-axis, the bx=0 corresponds to the bunch crossing of the selected HIP event.

according to the recommendations for APV to around 30 V to obtain an ideal CR-RC pulse shape. This parameter controls the drain speed of the preamplifier, a lower parameter resulting in a faster drain speed. Because of the increase of the APV occupancy, due to the shortening the bunch spacing and the increasing of the instantaneous luminosity, the drain speed was not fast enough anymore, leading to the saturation of the preamplifier by semi-large charge deposits (10-100 MIPs). The APV chip saturated by this effect became inefficient up to its recovery at the end of the train or the run. These findings led to a new setting of the VFP parameter to 0 V. Consequently a significant recovery of the hit efficiency has been observed as shown in Fig. 2.1 has been observed.

2.4.4 Study of the HIP events after the change of the APV settings

2.4.4.1 Motivation of the HIP study with the modified APV settings

After having identified and fixed the main source of APV inefficiencies, a new VR data run was scheduled and taken. This run has provided an opportunity to study a clean HIP effect, not affected by the incorrect APV settings. The goal of the study with this data is to check if HIP events can still be observed, if they manifest in a similar way and what are the consequences of such events.

2.4.4.2 Experimental setup

A new VR data run 281604 of a duration of 48 minutes and 45 seconds, was taken on 25^{th} of September 2016. The subdetectors included in this run were both the silicon pixel and strip tracker, the ECAL, the HCAL and all muon chambers. This run was part of the fill 5330, during which only four isolated bunches per beam were injected into the LHC. The peak pileup of the fill was 48 interactions per bunch crossing. The instantaneous luminosity of the run was around $17\times10^{30}\text{cm}^{-2}\text{s}^{-1}$. During the run, APVs were taking data in the deconvolution mode.

In this run the trigger fired on the fixed bx=2306 in each orbit, further referred to as the "first event". After the first trigger was followed by six other ones separated by 75 ns during 450 ns. This means that per one orbit, 7 events spaced by 3 bunch crossings were thus triggered, but only the first one contained a bunch collision. The trigger setup was very special as all trigger rules were violated at the trigger control level except the first one.

The properties of the run and the data-taking setup resulted in many differences compared to the study presented in Section 2.4.2, later referred to as the "first study". As bunches collided only during the first triggered event in a given orbit, the particle causing the HIP interaction had to originate from this bunch crossing, so in this sense, the time of the HIP occurrence is fixed. In addition, because of the fill structure with isolated bunches, there is no out-of-time pileup for the first event.

2.4.4.3 Methodology

In order to design the selection of HIP events dedicated to this run, the correlation of baseline and σ_{raw} per APV has been analyzed. The distribution presented in Fig. 2.21 is very similar to the one of the Fig. 2.12 for the first study. This implies that the manifestation of the HIP events has not changed with the change of the APV settings, consequently the same HIP selection, defined in Eq. 2.7, can be used. As the time associated to the creation of the particle causing the HIP event is fixed in this study to bx=2306, no redefinition of the bunch crossing position is needed and hence the properties of the selected HIP event and the other 6 events in the same orbit can be shown as function of their real bunch crossing number, respectively time.

The average baseline evolution as a function of the bunch crossing number is shown in Fig. 2.22. The recovery of the baseline occurs in less than 12 bunch crossings, which is a slightly faster recovery than in the first study. Here also the baseline overshoots from its nominal value of 127 ADC for the remaining events in one orbit, even to a higher level

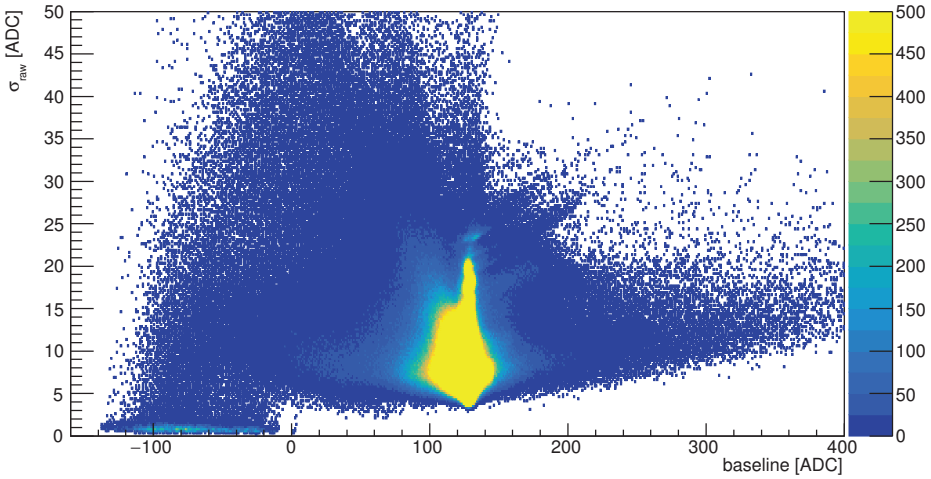

Figure 2.21: The 2-D distribution of the σ_{raw} of the raw digis in the APV versus the baseline for the run 281604.

than in the first study. Note that the baseline decreases between the first and second event, because not all baselines are fully suppressed yet during the first event. The study of the first occurrence of the fully suppressed baseline as a function of the bunch crossing has shown that in approximately half of the cases the baseline is already saturated in the first event, the remaining half corresponds to the second event.

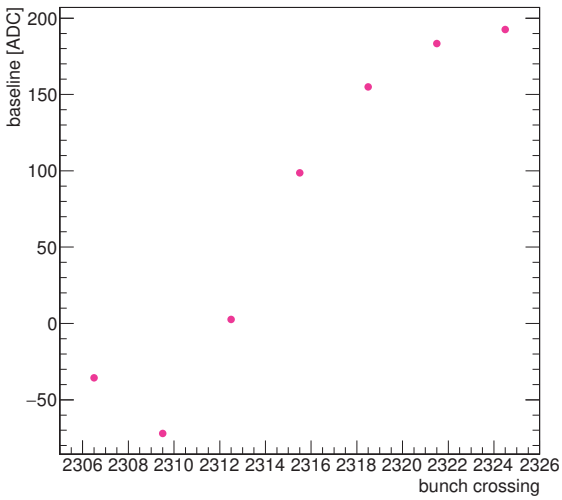

Figure 2.22: The averaged baseline evolution as a function of the bunch crossing number for the run 281604.

The main results of this study, on the HIP probability measurement, are presented first, in the following Subsection 2.4.4.4. Then the cluster properties per APV are discussed in Subsection 2.4.4.5. For that purpose, four categories of events are defined, as shown in Table 2.2. For an APV influenced by a HIP event, the cluster information of the first

event in a given orbit belongs to the first category, the remaining events to the second category. The cluster information of APVs for which no HIP event has happened during the given orbit belongs to the third category in case of the first event in the orbit or to the fourth category otherwise. Thus in categories 2 and 4, only fake clusters are expected as no colliding bunches in the CMS were present at these bunch crossings, in contrary to categories 1 and 3 which are populated by both real and fake clusters. The last two Subsections (2.4.4.6 and 2.4.4.7) focus on the fake clusters resulting from the HIP and the origins of these clusters.

Category	Name	Features
1	HIP	Collision event when a HIP occurred
2	After HIP	Event in the same orbit of a selected HIP Not a collision event Fake clusters
3	Collision non-HIP	Collision event without any HIP
4	Non-collision, non-HIP	No HIP selected in a same orbit Not a collision event Fake clusters

Table 2.2: The four categories of clusters used for the study of run 281604.

2.4.4.4 HIP probability measurement

The probability of a HIP event given by Eq. 2.4 is in this study estimated in average separately for each layer and wheel or ring of the silicon strip tracker. The f_{HIP} is calculated according to Eq. 2.5 and the number of tracks traversing the part of the sensor corresponding to a given tracker APV is computed from simulated events. The final result can be seen in Fig. 2.23 for the barrel, TID/TEC wheels in the left and rings in the right plot. The probability of a HIP event per track is of order of $10^{-3} - 10^{-2}$, which is about one order of magnitude larger than the results provided by the HIP study at the PSI described in Section 2.3.4. In this CMS study, the simulated number of tracks traversing the tracker modules does not take into account neutral particles, because they do not ionize the sensor and thus do not leave hits. Then the probability of the HIP event is thus increased by not taking into account all particles. The two analyses also differ by the HIP selection, trigger conditions, and particle and energy spectra.

In the left plot of Fig. 2.23 it can be observed that the probability of the HIP interaction per track is different for different layers. The probability increases with the module thickness as the path of the particle in thicker modules is longer. The change of the probability because of the larger thickness can be typically seen when comparing TIB

sensors which are 320 μm thick and TOB sensors which have a thickness of 500 μm. The HIP probability increases also with the module pitch. A possible explanation is that larger the pitch is, less channels read the HIP charge and thus it is easier to reach the zero-light level. In the left plot of Fig. 2.23, no clear evolution for the TID and TEC wheels is observed. This is caused by a mixture of modules with different pitches and thicknesses in one wheel. On the other hand the rings are composed by the same modules and it can be noticed that the probability per ring shown in the right plot of Fig. 2.23 has a similar evolution with the ring distance from the beamline as the probability for the TOB.

The particle flux decreases approximately as a function of the distance from the beamline, and therefore when comparing the same modules a decrease in the HIP probability as a function of distance from the beamline can be expected. Despite the modules are almost similar in the case of the TOB (change in pitch between layer 4 and 5 from 183 to 122 μm), the HIP probability is increasing as a function of distance from the beamline, and not decreasing. As the charged particles are bent in the magnetic field, only highly energetic charged particles reach the outer layers of the tracker, what is not the case for the neutral particles. Because of this effect, the particle energy spectra as well as the ratio of charged to neutral particles change with the distance from the beamline. Specifically, the fraction of neutral to charged particles increases with the distance from the beamline and as the tracking is reconstructing only charged particles, rescaling by the number of tracks biases the HIP probability differently as a function of the distance from the beamline. Moreover, the tracking is not 100% efficient. Due to this issue, the probability evolution can be the opposite of what is expected. Furthermore, the inelastic cross section of the nuclear interaction changes with the kind of particle and particle energy and therefore it can be also responsible for a change in the probability of the HIP event between different layers.

The estimation of the HIP probability, which is not sensitive to the tracking, is defined in Eq. 2.6. This probability is defined per pileup interaction and thus should be invariant with change of the fill structure, given that the pileup is the same. This probability can be re-computed for different filling schemes by dividing the probability by the PU of the fill of run 281604 and rescaling it by the PU of the fill of interest. The f_{HIP} rescaled by the peak fill pileup of 48 is shown in Fig. 2.24 again for layers/wheels (left) and layers/rings (right) of the TIB, TOB, TID and TEC. The probability has been evaluated to be of the order of $10^{-6} - 10^{-5}$. As expected from the evolution of fluence with distance from the beamline, the probability shown in Fig. 2.24 is decreasing with the distance from the beamline. This is observed for the layers of the TOB. It is also true for the TEC rings (right plot of Fig. 2.24) from TEC1 to TEC4 and TEC5 to TEC7. The probability

also increases with the sensor thickness as it can be seen in the right plot of Fig. 2.24 in the probability change between the TEC4 (thickness of 320 μm) and TEC5 (thickness of 500 μm) rings. The increase of the probability with the sensor thickness can also be observed when comparing the probabilities for the TIB and TOB. The increase of the probability due to the pitch size can be seen when comparing the first two and second two layers of the TIB. The information on the module geometries can be found in Table 1.1. For the TID and TEC wheels shown in the left plot of Fig. 2.24 there is again no clear evolution because of mixture of the different modules.

This probability per PU changes from layer to layer because of the differences in module geometry, particle composition and energy spectra, but the relative change of probability between given layers for the different fills should remain the same and therefore the mentioned rescaling by the PU should be sufficient to evaluate this probability for different filling schemes.

However as previously, both computed probabilities of the HIP events can be biased by the trigger conditions. Only baselines which are already fully suppressed in the first event or which are still fully suppressed in the second event (after 75 ns) can be selected as HIP events, what potentially decreases the probability.

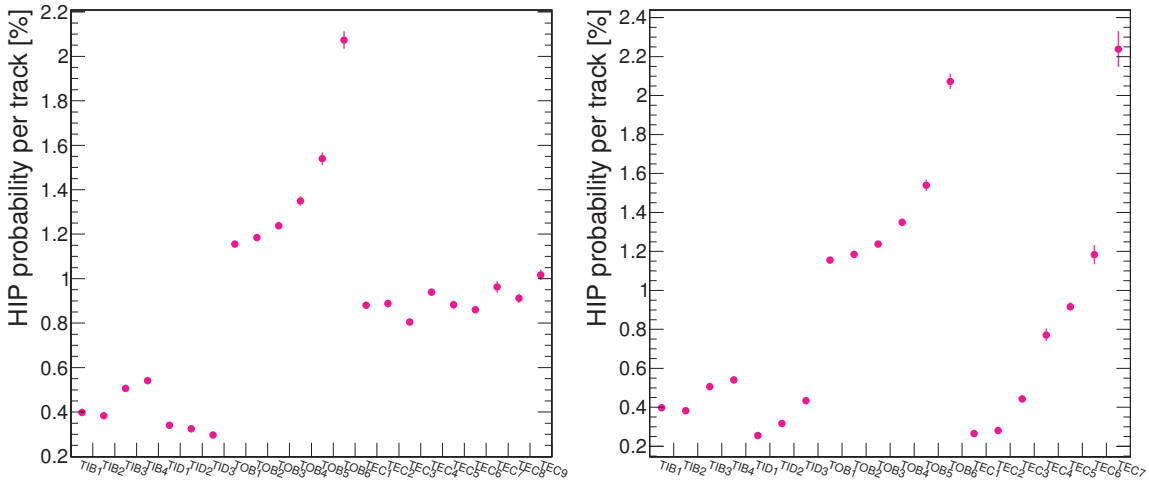

Figure 2.23: The average probability of a HIP event per track for layers (left, right) of TIB, TOB, and wheels (left) or rings (right) of the TID and TEC partitions of the silicon strip tracker, computed from the data run 281604.

2.4.4.5 Comparative study of the cluster properties

In this subsection, we compare the behavior of the different clusters, based on the categorization presented in Table 2.2, in order to point the impact of the HIP. The average

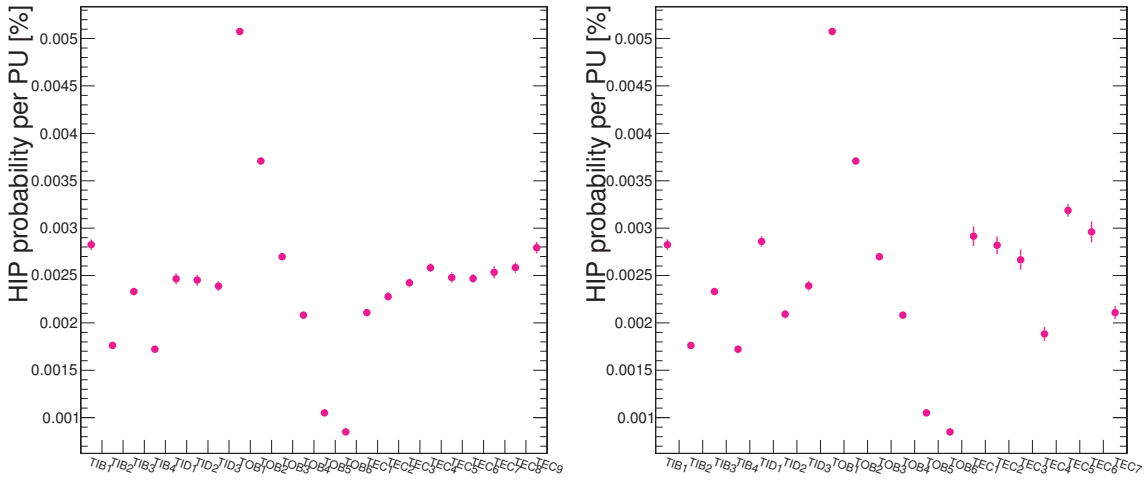

Figure 2.24: The average probability of a HIP event per PU for layers (left, right) of TIB, TOB, and wheels (left) or rings (right) of the TID and TEC partitions of the silicon strip tracker, computed from the data run 281604.

cluster multiplicity per APV is shown in the left plot of Fig. 2.25 both for orbits influenced by a HIP event, in triangles (categories 1 and 2), and non-HIP orbits, in rectangles (categories 3 and 4). The average cluster multiplicity for the first event is non-zero due to the presence of collisions and it falls then to almost zero for other events where only fake clusters are present. In the case of the HIP-orbits, the average cluster multiplicity for the first event is higher than in the standard case because of additional clusters originating from the HIP event. The other events exhibit also a significantly larger average multiplicity of the fake clusters compared to non-HIP orbits. The average fake cluster multiplicity is increasing in time up to a constant level and does not diminish during the 6 events, which translates to 150 ns.

The average cluster charge shown in the right plot of Fig. 2.25 reveals that the charge is larger for a HIP event than a standard event in the case of the collision event. This effect appears because large charge clusters can be present during the HIP event. Then in the remaining bunch crossings, standard fake clusters have a charge around 250 ADC, which is not the case for the fakes induced by the HIP event. In the latest case, the average cluster charge of fakes first drops up to $\sim$ 150 ADC, and then later with time, grows even above the level of the real clusters.

Distributions of the cluster charge, multiplicity and width for the four categories defined in Table 2.2 are shown in Figs. 2.26 to 2.28, respectively. The left plot of Fig. 2.26 shows the cluster charge distribution for collision events. It can be noticed that the HIP events often lead to the saturation of one or more channels (spikes) and that a large part of the population has a cluster charge of around 1400 ADC. These clusters are HIP clusters

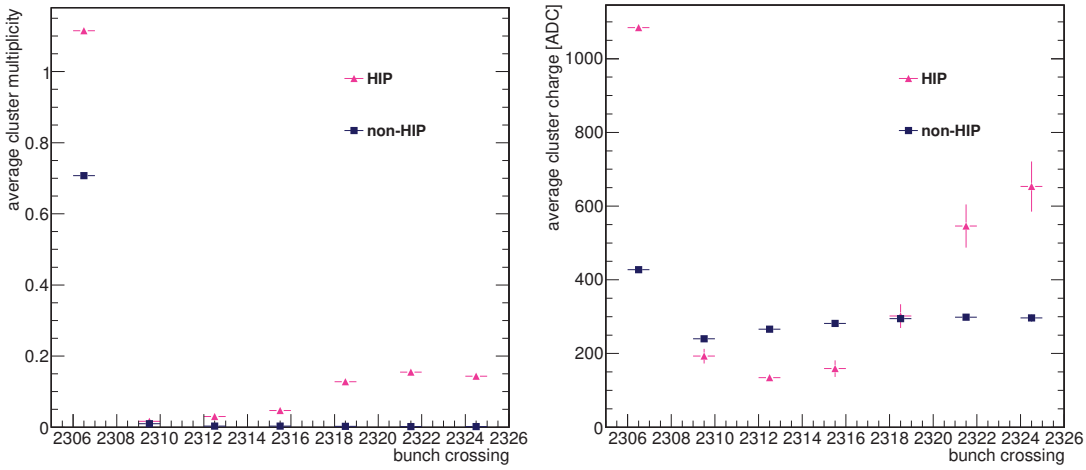

Figure 2.25: The average cluster multiplicity (left) and average cluster charge (right) as a function of the bunch crossing number for the run 281604. In pink triangles is the average cluster multiplicity of the HIP event and events later while the blue squares are for the non-HIP events.

or they originate from baseline distortions induced by the HIP and therefore they bring a possibility to identify the HIP event as an event with a large charge cluster. But as the probability of the HIP interaction is low, studying distributions which are not rescaled to unity reveals that more clusters with such large charge are produced in average in non-HIP collision events than in the HIP events. Furthermore the positions of peaks at low cluster charges are different in the two distributions. This can be caused by different fractions and origins of fake clusters, but also by a loss of the charge when reconstructing a real cluster in an APV with a dropped baseline. The right plot of Fig. 2.26 shows the cluster charge distributions for non-collision events. It can be noticed that a large fraction of the standard fake clusters have one saturated channel.

In Fig. 2.27 the cluster multiplicity, i.e. the ratio per APV of the number of clusters to number of events, is shown for collision HIP and non-HIP events on the left and for non-collision HIP and non-HIP events on the right. As discussed before, in average the HIP event leads to a larger cluster multiplicity because of the HIP cluster or baseline distortions compared to the non-HIP collision events. The same applies for the fake clusters after the HIP event w.r.t. the normal fakes. The left plot of Fig. 2.28 reveals that the cluster width is in average higher and its distribution is broader for HIP events compared to the non-HIP collision events, which is caused by the different origin of the clusters. The low cluster width population for the HIP events can appear due the drop of a baseline which causes that not all channels reading signal from particle can reach the clustering threshold. Similar conclusion applies for the two distributions in right plot of Fig. 2.28.

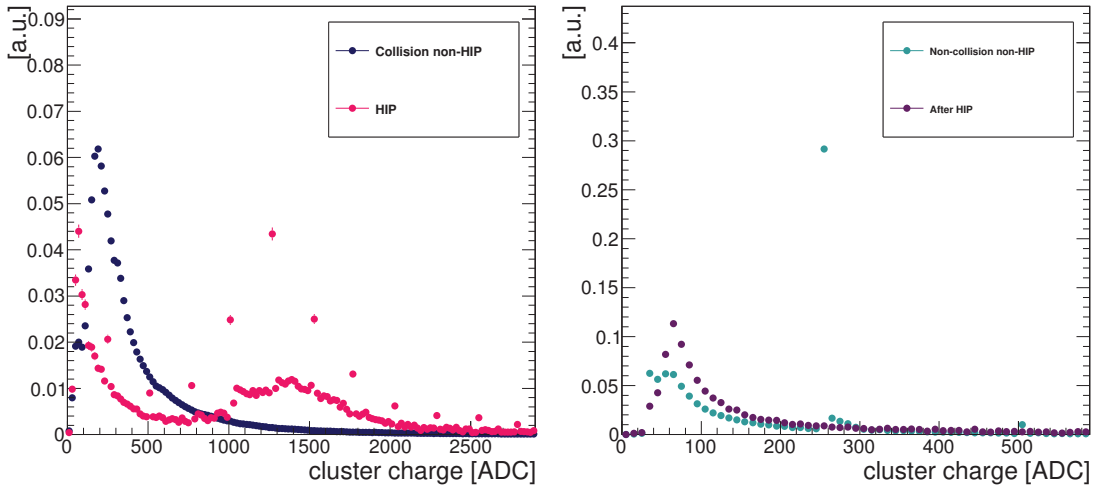

Figure 2.26: The cluster charge distribution in run 281604 for collision HIP and non-HIP events (left), and for after HIP and non-collision non-HIP events (right).

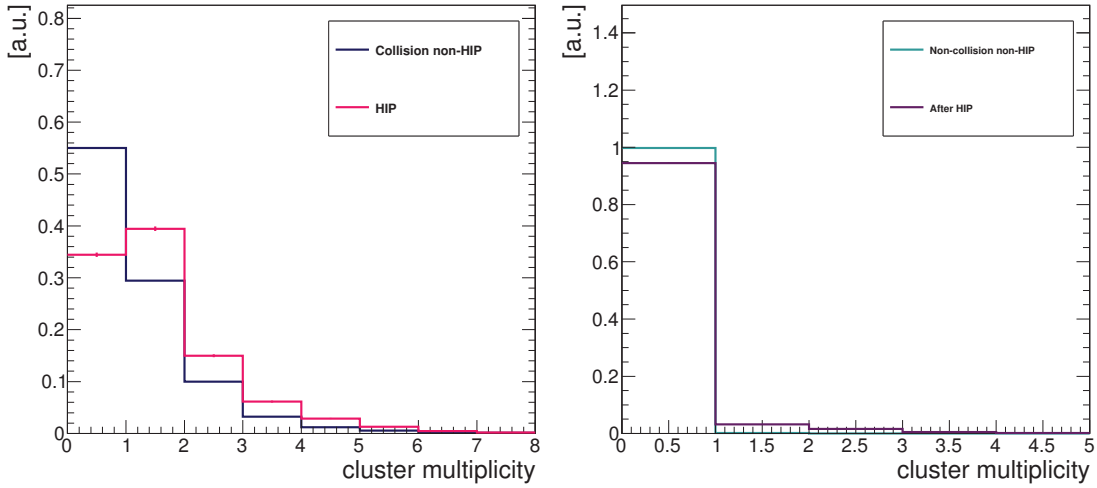

Figure 2.27: The cluster multiplicity distribution in run 281604 for collision HIP and non-HIP events (left), and for after HIP and non-collision non-HIP events (right).

In this subsection it was shown that the cluster width, charge and multiplicity are influenced by the occurrence of the HIP event. Especially, we found out that the fake cluster multiplicity is increased after the HIP event. These fake clusters are further discussed in following subsections.

2.4.4.6 Characterization and quantification of fake clusters induced by HIP

To understand the properties of the fake clusters and numerically support the conclusions of the previous subsection, the average cluster multiplicity, charge and width are calculated in Table 2.3. In the table it can be noticed that the average multiplicity of fake clusters

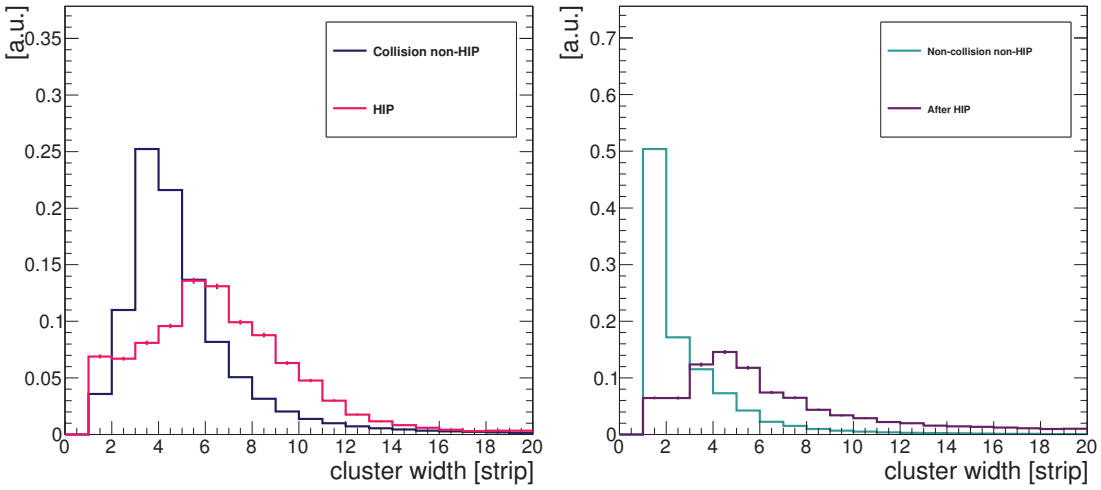

Figure 2.28: The cluster width distribution in run 281604 for collision HIP and non-HIP events (left), and for after HIP and non-collision non-HIP events (right).

appearing after the HIP interaction is higher than the average multiplicity of the standard fake clusters. This could potentially cause a problem for a tracking algorithm which may use fake clusters to reconstruct a track. The lower limit on the probability to have at least one fake cluster which is used to reconstruct a track can be estimated by the following formula:

$$p_{fake}(PU) = f_{HIP}/PU_1 \times T \times N_{fake}/PU_1 \times PU_2^2 \times \frac{\sigma_{position}}{N_{strips} \times p}, \tag{2.8}$$

where f_{HIP} is defined in Eq. 2.5, the time window T is the number of bunch crossings in one orbit for which the fake clusters are observed, p is the pitch size, N_{strips} is number of strips per APV and the position resolution $\sigma_{position}$ is the estimate of the space window around the reconstructed track in which the fake cluster is close enough to be used for the track reconstruction. N_{fake} is the average fake multiplicity over the time window T. The pileup PU_1 is chosen to be the currently studied fill peak pileup. The factor $(PU_1/PU_2)^2$ can transfer the results of the studied run 281604 with PU_1 to different run conditions with a different pileup PU_2. For the studied run, the PU_2 is equal to PU_1 and therefore the Eq. 2.8 can be rewritten as

$$p_{fake}(PU) = f_{HIP} \times T \times N_{fake} \times \frac{\sigma_{position}}{N_{strips} \times p}. \tag{2.9}$$

A cluster is used for the track reconstruction if it passes a certain charge threshold, which depends on the thickness of the sensor and the track inclination. Considering a normal track, the cluster charge cut for the sensors of the first layer of the TOB, which

Events/Quantities	Average cluster charge [ADC]	Average cluster multiplicity	Average cluster width [strip]
HIP	1094	1.254	8
After HIP	254	0.099	9
Collision non-HIP	426	0.712	5
Non-collision, non-HIP	219	0.002	4

Table 2.3: The average cluster charge, multiplicity and width for the four categories defined in Table 2.2 for the run 281604. These quantities are computed from both on-track and off-track clusters.

have a thickness of 500 μm, is around 140 ADC in the case of the tightest cut. As shown in the right plot of Fig. 2.25, all fake clusters pass in average this requirement. The values for the first layer of TOB needed for the probability estimation in Eq. 2.9 are $f_{HIP} = 0.0024$, $T = 18$, $N_{fake} = 0.099$ obtained from Tab. 2.3. The $\sigma_{position}$ is taking into account the cluster and alignment position resolutions which are for the first layer of TOB of around 40 μm each and is estimated to be $\sigma_{position} = 2\sqrt{2} \times 40$ μm. Inserting these values into Eq. 2.9 gives the lower limit on the probability for the first layer of TOB to have at least one fake cluster originating from HIP event, which is used to reconstruct a track. This probability has been calculated for the fill peak pileup $PU_1 = 48$ to to be 0.002% , which is very low and therefore the impact of these fake clusters on tracking is negligible, but it is just a lower limit as there are only 7 consecutive events and the behavior of fake clusters after these events is unknown. Moreover this probability scales with the pileup.

The fake cluster multiplicity is increased after the HIP event as shown in Table. 2.3, but the HIP probability is low and therefore it is also important to compute the average multiplicity of the fake clusters in the run by dropping the last term in Eq. 2.8 describing the position window. To evaluate its impact, this multiplicity can be compared to the other off-track cluster multiplicities. One of them is the multiplicity of the normal fake clusters originating mainly from the noise, which is determined in Table 2.3 to be 0.002. The second off-track contribution is due to OOT PU. The fraction of the OOT pileup clusters in an event has been computed from the comparison of the cluster multiplicity in the first and other events in the train for a standard collision run (run 273162) as in the first event there is no OOT PU. The fraction of the OOT pileup has been evaluated to be around 50% of all clusters in the other events in the train. Knowing this fraction, the OOT PU cluster multiplicity can be determined for the run 281604. The average cluster multiplicities of these three categories for the first layer of TOB are shown in Table 2.4. It can be noticed that the average cluster multiplicities of normal fake clusters and fake clusters resulting from the HIP event are of the same order of magnitude. However

the average multiplicity of clusters originating from OOT PU is around two orders of magnitude larger than the average cluster multiplicity of the other two categories.

Off-track cluster category	average cluster multiplicity
Fakes after HIP	0.004
Normal fakes (noise)	0.002
OOT PU	0.722

Table 2.4: The average cluster multiplicity in the run for three categories of off-track clusters for the first layer of TOB and run 281604.

The origin and properties of the fake clusters after the HIP event can be studied in the non-collision events after the HIP. In the distributions of Fig. 2.29, the average cluster multiplicity and width are shown as a function of the σ_{raw}. In the standard case, the nominal value of the σ_{raw} is around 8 ADC. For a σ_{raw} value of 8 ADC, the fake multiplicity is the lowest as shown in the left plot of Fig. 2.29. Compared to this point, the fake cluster multiplicity is significantly increased when the value of σ_{raw} around 2 to 5 ADC and for a σ_{raw} larger than 10 ADC, suggesting that the distorted baselines, those with large σ_{raw}, lead to an increased multiplicity of the fake clusters. In the right plot of Fig. 2.29 it can be noticed that the average cluster width is increasing with σ_{raw}.

To understand the occurrence of the fake clusters, the fake cluster multiplicity can be also shown as a function of the baseline as done in the left plot of Fig. 2.30. In this distribution it can be seen that after the baseline saturation, the fake cluster multiplicity remains low for a while and then during the recovery the fake cluster multiplicity starts to increase up to baseline of about 0 ADC. The multiplicity falls then to its minimum, which is around the baseline normality (baseline=127 ADC). After that, the baseline overshoots and the average cluster multiplicity starts to increase significantly. Here it is important to remind that the clusters are reconstructed as in the ZS data-taking, i.e. with the truncation to zero. Therefore a highly distorted baseline does not have to lead to reconstructed cluster(s) if the charges of the cluster channels do not exceed 0 ADC. As seen in the left plot of Fig. 2.29, the majority of the fake clusters appear for a σ_{raw} larger than 10, but a substantial population is also observed for the RMS of 2-5 ADC. The distribution of σ_{raw} as a function of the baseline in the right plot of Fig. 2.30 shows that both baselines with value of around 0 ADC and larger than 200 ADC have increased σ_{raw} with respect to normality. σ_{raw} of 2-5 ADC corresponds to the baselines between approximately -70 ADC and -20 ADC.

To conclude, it was shown in this subsection that thanks to the small probability of the HIP event, in average this fake cluster multiplicity is small and therefore the influence on the tracking is negligible. It has also been observed that a higher fake cluster multiplicity

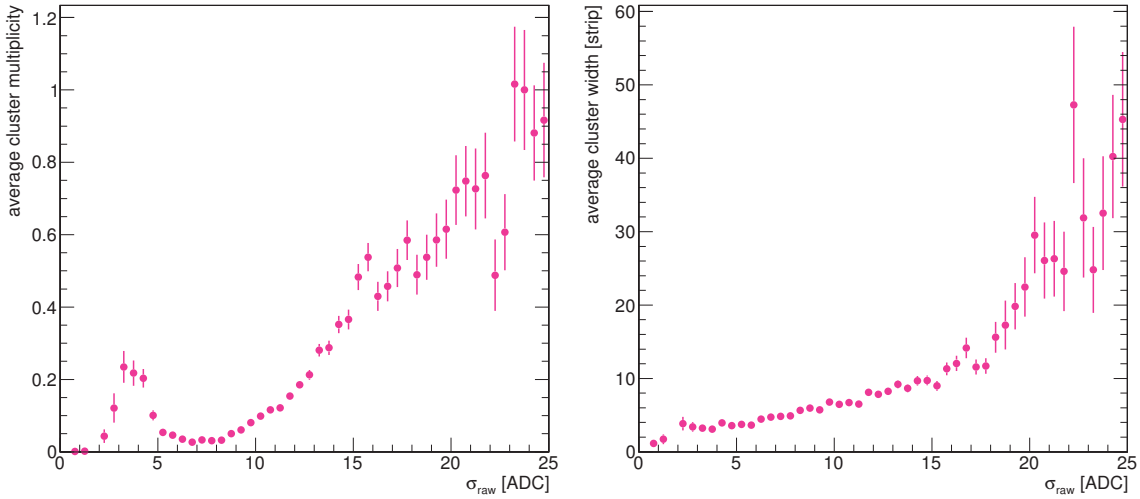

Figure 2.29: The average cluster multiplicity (left) and average cluster width (right) as a function of σ_{raw} of the non-collision events after the HIP for the run 281604.

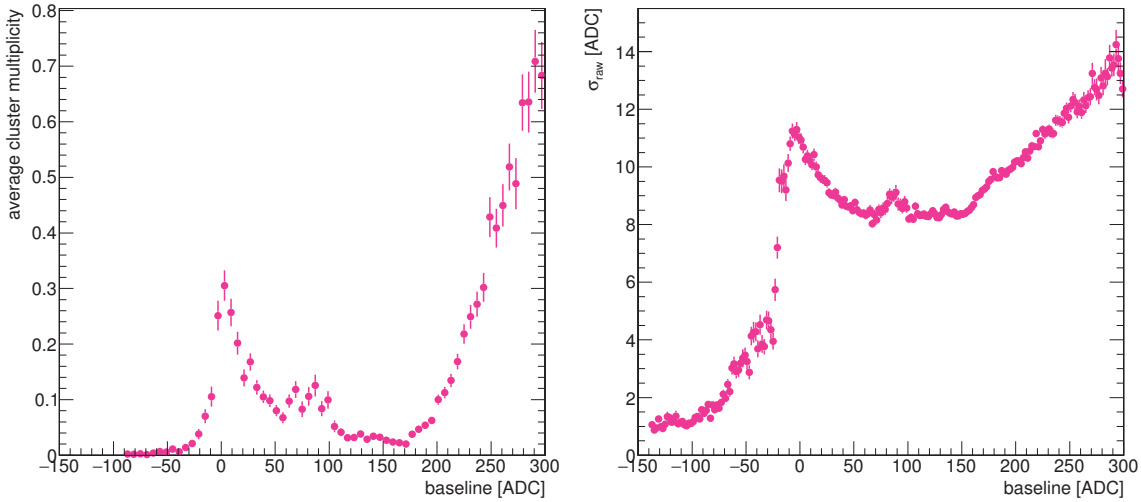

Figure 2.30: The average cluster multiplicity (left) and σ_{raw} (right) as a function of the baseline of the non-collision events after the HIP for the run 281604.

happens for distorted baselines (i.e. those with large σ_{raw}) which appear for both low and high values of baseline. Some examples of events inducing fake clusters are illustrated in the next subsection.

2.4.4.7 Examples of the baseline distortions resulting from HIP

Based on the observations in the previous subsection, several examples of APVs with different values of σ_{raw} and baseline are later shown in order to study the behavior of the baseline which can lead to the reconstruction of fake clusters. In the five plots in Fig. 2.31,

Fig. 2.32 and Fig. 2.33 the evolution of raw digis, pedestal subtracted digis, baselines and clusters is shown.

A first example of behavior, which can lead to fake clusters is the distorted baseline due to the partial recovery of the saturated baseline (or not a full suppression) as shown in sixth APV of the left plot of Fig. 2.31. In this example, σ_{raw} is equal to 4.4 ADC and the baseline value is -57 ADC for this APV. In this case the baseline distortion did not lead to the cluster reconstruction, because all pedestal subtracted digis are below zero. But once part of the pedestal subtracted digis is larger than zero, these digis can be easily reconstructed into a cluster as displayed in the right plot of Fig. 2.31. The second APV of this module presents a distorted baseline (with a value of -11 ADC and σ_{raw} of 21 ADC) and two clusters are reconstructed, the first one is the HIP cluster and the second originates from the baseline distortion. This second cluster, reconstructed between channels 195 and 256, is also significantly larger than expected for a MIP.

Another example of event with a large σ_{raw} of 21 ADC and a low baseline value of -66 ADC can be seen in the sixth APV of Fig. 2.32. In this event, a baseline distortion appears, but of a different kind, here the baseline exhibits a large dip for few strips.

Another source of fake clusters are baselines with larger than nominal values. Two examples of APVs with high baseline and σ_{raw} values are shown in Fig. 2.33. The baselines of these APVs are not only sloping but it can be noticed that they are also distorted by dips. These dips are not understood but they create significant distortions which can lead to the reconstruction of wide fake clusters.

In these few examples it was demonstrated that the baseline distortions can lead to the reconstruction of fake clusters. It was also shown that the baseline distortions can have different shapes and can appear for both baselines with lower and higher value than the normality.

2.5 Conclusion

The large increase of hit inefficiencies in the silicon strip tracker during 2015 and 2016, has triggered deep investigations of the highly ionizing particles as a possible cause of these inefficiencies. In this chapter the VR data are used to perform a qualitative study of the HIP events as well as a quantitative estimate of the rate of these events. The initial aim of this study was to understand if the HIP event can be the main cause of the observed hit inefficiencies. Rapidly it was realized that the HIP event occurrence is not sufficient to explain the inefficiencies and later the solution was found in the settings of the APV

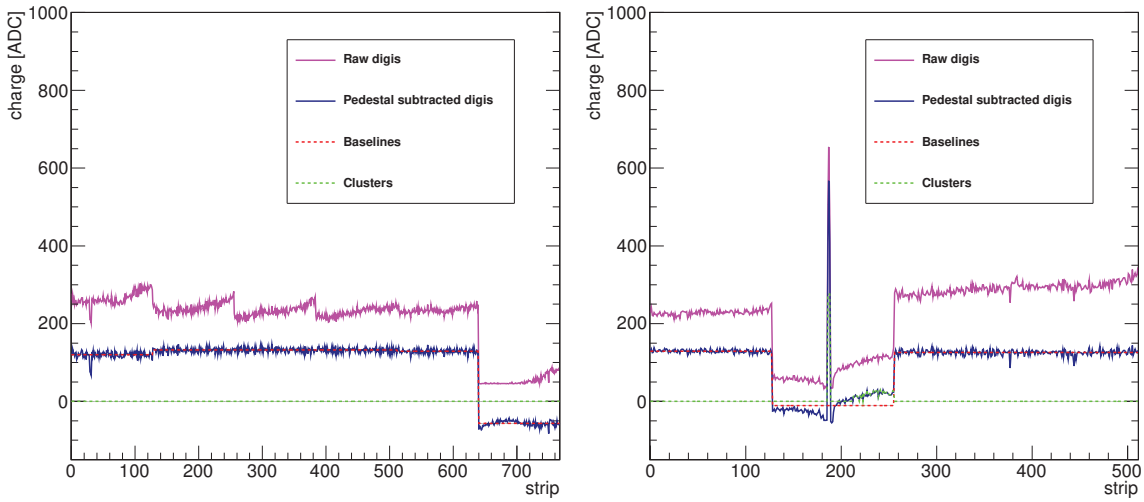

Figure 2.31: Examples of data from one tracker module undergoing zero suppression and clustering. The raw digis are shown in pink. From the raw digis, the pedestals are subtracted and the resulting digis are shown in blue. The baselines shown in red are computed and subtracted from pedestal subtracted digis. The final clusters are shown in green. (left) For the sixth APV σ_{raw} is 4.4 ADC and the baseline value is -57 ADC. (right) The second APV has a baseline with value of -11 ADC and σ_{raw} of 21 ADC.

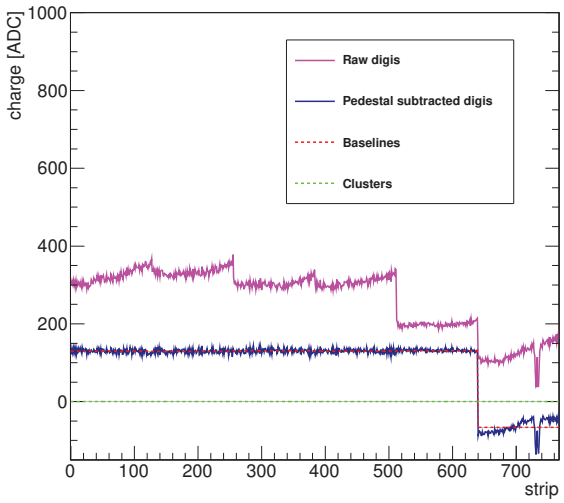

Figure 2.32: Example of data from one tracker module undergoing zero suppression and clustering. The raw digis are shown in pink. From the raw digis, the pedestals are subtracted and the resulting digis are shown in blue. The baselines shown in red are computed and subtracted from pedestal subtracted digis. The final clusters are shown in green. The sixth APV has a σ_{raw} of 21 ADC and a baseline value of -66 ADC.

parameters. Later, a new VR data-taking was scheduled, which provided an opportunity to perform the first measurements of the HIP events at the CMS environment, not influenced by the wrong APV settings. Due to the data-taking conditions it is however not

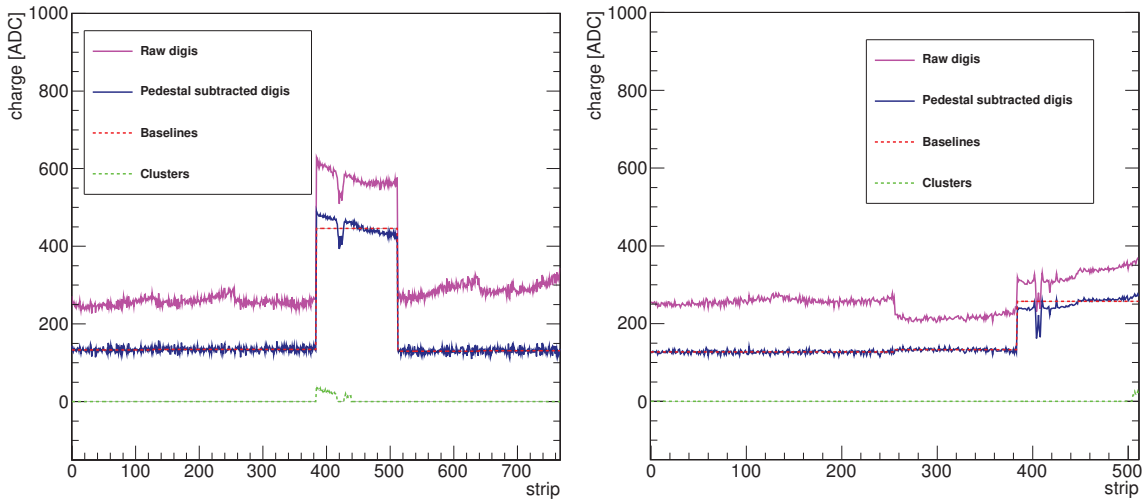

Figure 2.33: Examples of data from one tracker module undergoing zero suppression and clustering. The raw digis are shown in pink. From the raw digis, the pedestals are subtracted and the resulting digis are shown in blue. The baselines shown in red are computed and subtracted from pedestal subtracted digis. The final clusters are shown in green. (left) The fourth APV has a σ_{raw} of 14 ADC and a baseline value of 446 ADC. (right) The fourth APV has a σ_{raw} of 21 ADC and a baseline value of 257 ADC.

possible to estimate the dead-time in this data, but on the other hand the trigger conditions allowed to study the baseline distortions and the fake cluster properties in detail. With this data the probability of a HIP event defined by Eq. 2.4 is computed to be of order of $10^{-3} - 10^{-2}$, which is around an order of magnitude larger than the HIP probability per track measurement performed at the PSI beam test. The increased probability is found to be a result of different experimental conditions of the two studies. Because of the dependency of this probability on the tracking, we defined a second probability in Eq. 2.6 which is independent of tracking. This probability scales with the fill pileup and is computed to be of the order of $10^{-6} - 10^{-5}$. The evolution of these probabilities for different layers/wheels/rings of the tracker was discussed and it was concluded that these probabilities evolve as expected.

Chapter 3

Improvement of the silicon strip tracker simulation

In particle physics, a direct comparison between and theory cannot be made due to the complex nature of the interactions and the apparatus. By consequence, the reconstructed event data are directly compared to the ones simulated by the MC technique for measurement or hypothesis test purpose. Further, the simulations are also important for the development and understanding of specific analysis methods and for derivation and validation of calibrations. The detector performance indicators such as resolutions and efficiencies rely as well to a large extent on the simulation.

In Section 3.1 the general simulation workflow of CMS is introduced. In the following Section 3.2 a deeper explanation of the simulation of particle charge deposits in the CMS silicon strip tracker is given. In this Section the effects of tracker ageing and simplifications used in simulation are also discussed. The chapter ends with Section 3.3 presenting a new measurement of the cross talk parameters in the tracker and their impact in the simulation on cluster properties.

3.1 An introduction to the CMS simulation

The CMS simulation workflow [64, 65, 66] is divided into several steps. The beginning of the simulation chain starts with the generation of the physics events. In this step the particles resulting from the interactions between colliding particles are generated as well as their kinematics. The final state particles produced by the generator are then sent to GEANT4 to pass through the "simulated" detector in which these particles interact and leave energy deposits. The last step is the simulation of the response of the detector and its electronics to particle traversing the detector. The output of this procedure is

RAW data, which can be later reconstructed and slimmed for the purposes of the physics analyses. The overview of the simulation steps, which are described in larger detail in the following subsections, can be seen in violet in Fig. 3.1 [67]. The official production of the simulated samples is handled centrally [68] by the CMS collaboration.

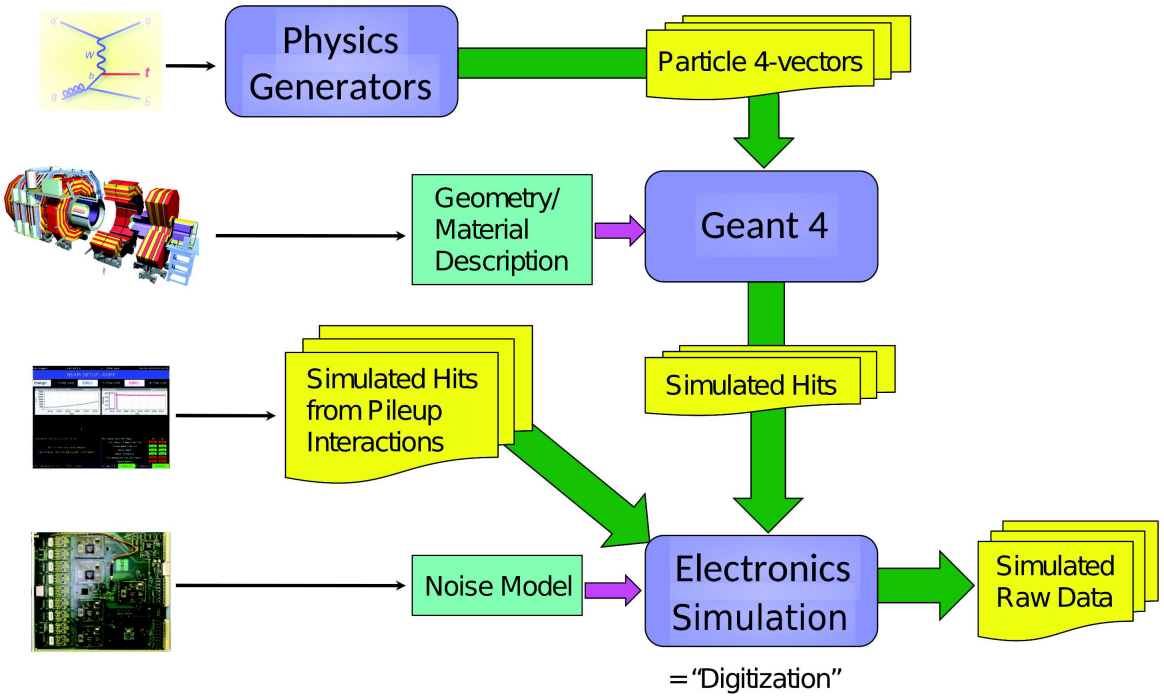

Figure 3.1: A diagram of the simulation workflow. The four-vectors of generated particles together with the detector description enter to the GEANT4 simulation whose output are simulated hits. Optionally the simulated hits from pileup interactions can be added on top of the simulated hits from the process of interest and the mixture of these hits is digitized during the electronics simulation. In this step the description of the electronics, for example the noise and the detector conditions (like the temperature), is added. The output of the digitization is the RAW data. Later steps are similar for both data and simulated events [67].

3.1.1 Step 1: Monte Carlo event generation

The Monte Carlo (MC) generator is a complex software designed to produce physics events according to a physics model. In the majority of cases three kinds of generators are used by the CMS collaboration [69, 70].

General-purpose generators: These are for example Pythia 8 [71] or Herwig++ [72].

They provide the complete description of the result of the proton collision. To generate outgoing particles originating from the interaction of colliding particles, many theoretical models and aspects have to be plugged in the generation process, such as the description of soft and hard interactions mainly in the leading order, parton distribution functions (PDFs), initial and final state radiations (ISR and FSR), multiple parton interactions, hadronization of partons and decay of particles.

Matrix Element calculators: The generators such as Powheg [73] or MadGraph5_aMCatNLO [74] were developed to provide the next-to-leading order (NLO) calculations. These calculators give the final state description at the parton level and their output needs to be plugged into one of the general-purpose generators to generate radiations and proceed with the full hadronization.

Specific generators: These generators are used to generate specific kind of events e.g. diffractive or cosmic events.

3.1.2 Step 2: Simulation of the particle interactions in the detector

To be able to describe data by simulations, the generated particles need to be propagated through the volume of the CMS detector. This is achieved via the GEANT4 [75, 76] toolkit, into which a detailed description of the CMS detector, its active and inactive material dimensions, layout and properties, are plugged. The GEANT4 toolkit propagates the generated particles through the detector, simulates the interactions with material and models the physics processes which happen during the passage of the particles through the detector. This procedure gives as output the simulated hits left by particles interacting with the active volumes of the subdetectors. These simulated hits can originate from primary particles generated by the MC generator, or from the secondary particles which are the result of the GEANT4 simulation process.

The simulation of the pileup events is done separately from the simulation of the events of interest. The input to the GEANT4 simulation of in-time and out-of-time pileup is a pool of Minimum Bias single interaction events. To simulate a given luminosity profile a specific distribution of the number of interactions per bunch crossing has to be chosen.

The complete simulation performed with GEANT4, also called Full Simulation (FullSim), is very CPU intensive. Due to this a Fast Simulation (FastSim) [77, 78, 79] was developed as an alternative to the FullSim. The FastSim uses simplified detector geometry and interactions with material, this speeds the simulation by a factor of around 100. The interaction with material is in the FastSim taken into account on the hit level. The com-

parison of physics objects of FullSim and FastSim shows that FastSim is a reliable alternative that reproduces the FullSim high level objects within around 10% accuracy [77, 80]. The FastSim is widely used to produce for example samples of supersymmetric processes, where large scans with different parameter values are needed. Typically for one fixed parameter set, few tens of millions of events are produced.

3.1.3 Step 3: Simulation of the detector and electronics response to the particle signal

To obtain the output electronic signal from the detector, the signal hits from GEANT4 are collected by the subdetectors. Then the response of the readout electronics to the collected signal is simulated. This step is also called "digitization" and its direct input are hits from events of interest and pileup events. There are three domains providing digitization of the given subdetectors, which are SimTracker, SimCalorimetry and SimMuon [81]. The digitized samples are in the RAW format and can be further reconstructed in a similar way as data.

3.2 Simulation of the silicon strip tracker response to the particle signal

In order to rely on the simulated samples, they have to describe the data as well as possible. In the case of the tracker, the output of the standard simulation is composed of zero suppressed data, which are further reconstructed into clusters during the reconstruction step. These clusters are used for tracking and physics object reconstruction, therefore a good and reliable description of data by simulated samples at the cluster level is necessary.

The following Figs. 3.2 to 3.6 show data and simulation comparisons of several important cluster quantities. A zero bias data sample recorded in 2017 and corresponding to run 305064 in fill 6298 is compared to a simulated sample of minimum bias events produced in the FullSim configuration. Both data and simulated samples were produced in the deconvolution mode. To avoid fake clusters and clusters originating from out-of-time pileup, only quantities related to the on-track clusters, i.e. clusters associated to reconstructed tracks, are used along this chapter.

The charge collected in a sensor from a given track divided by the track length in this sensor, further referred to as "cluster charge", is shown in Fig. 3.2. The division of the cluster charge by the track length gives the cluster charge per unit of length. Therefore

the cluster charge does not depend on the different track lengths caused by the different thickness of the sensors or the inclination of the tracks. The data to simulation ratio fluctuates around 1 within around ±0.1 in the bulk of the cluster charge distribution, but the description worsens for very small and very large cluster charges. Overall the cluster charge distribution in simulation is narrower than in data.

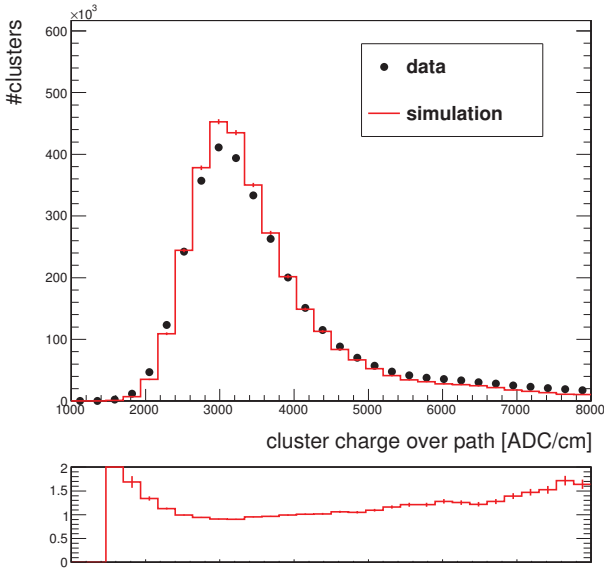

Figure 3.2: Data and simulation comparison of on-track cluster charge divided by the track length. The simulated distribution is rescaled to the number of clusters in data. The bottom plot represents the data to simulation ratio.

The cluster width depends on the sensor geometry and therefore has to be shown separately for different geometries. The possible geometries and their location in the tracker can be found in Table 1.1. The data to simulation comparisons for inner and outer barrel geometries are shown in Figs. 3.3 and 3.4, respectively. In all cases there is a very poor description of the cluster width in data by the simulation. The mentioned dependency of the cluster width on the geometry can be seen for example when comparing the cluster width between the different barrel geometries. The IB1 sensors have a smaller pitch with respect to the IB2 ones and therefore the IB1 clusters are in average wider, as in the IB1 case a larger number of strips would collect the charge from the same track. The sensors of IB2 and OB1 have a similar pitch, but the OB1 sensors are thicker which leads to a larger cluster width in the OB1 than in IB2, because the particle path in a sensor is longer. Moreover the cross talk is larger for OB1 than IB2, leading to a larger enhancement in OB1 cluster width compared to IB2.

Another cluster quantity is the charge on the strip having collected the largest charge among all strips in the cluster rescaled to track path in the sensor, which is later referred to as “cluster seed charge”. The cluster seed charge shown in Figs. 3.5 and 3.6 is also

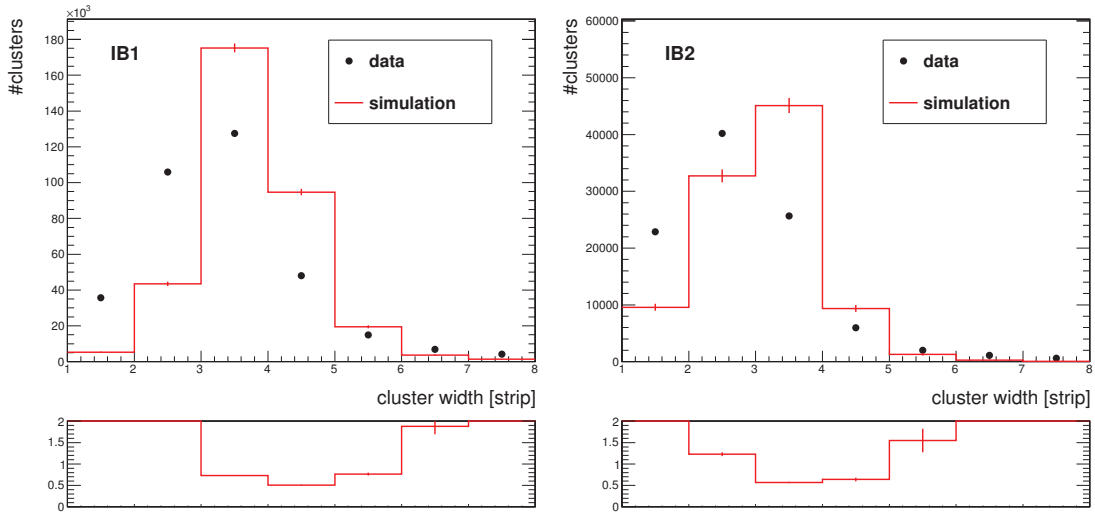

Figure 3.3: Distribution of the on-track cluster width for the IB1 (left) and IB2 (right) geometries in data and simulation. The simulated distribution is rescaled to the number of clusters in data. The bottom plots represent the data to simulation ratio for a given geometry. The pitch of the IB1 sensors is 80 μm and of IB2 sensors 120 μm, all IB sensors have thickness of 320 μm.

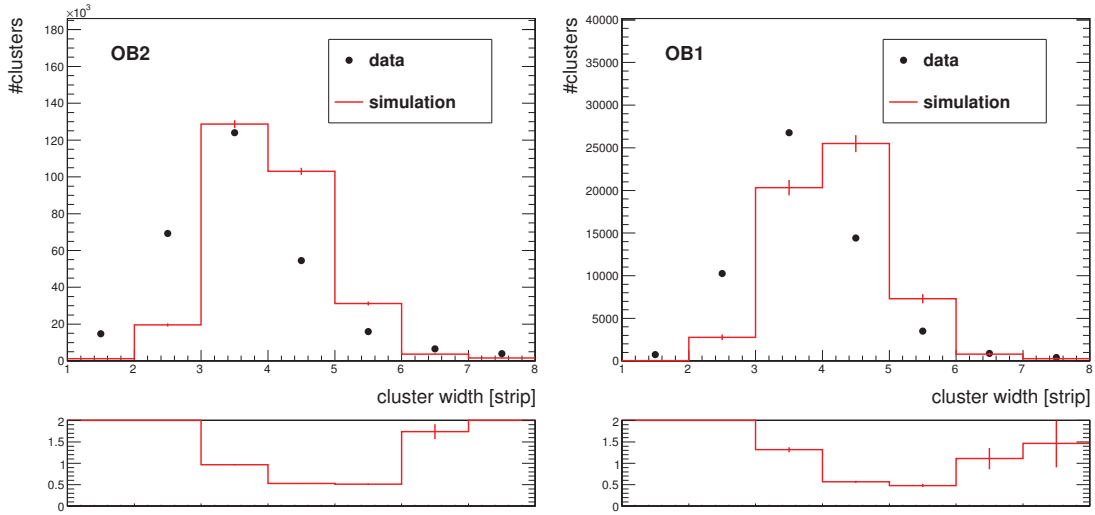

Figure 3.4: Distribution of the on-track cluster width for the OB2 (left) and OB1 (right) geometries in data and simulation. The simulated distribution is rescaled to the number of clusters in data. The bottom plots represent the data to simulation ratio for a given geometry. The pitch of the OB2 sensors is 122/183 μm and of OB1 sensors 122 μm, all OB sensors have thickness of 500 μm.

dependent on the module geometry and therefore is presented for the four different barrel geometries. In these plots, it can be seen that the simulation in average predicts in all cases a lower cluster seed charge, a clear trend in data to simulation ratio is present. It can also be observed that with a larger pitch, the seed charge increases, as the charge from a larger part of the sensitive volume is read by one strip. Moreover, differences in

the seed charge for IB2 and OB1 are observed. However these two parts of the detector have a similar pitch size and the difference in the module thickness is taken into account by rescaling the collected charge by the path length. The difference between the two geometries comes in fact from a larger cross talk in OB1, leading to a smaller seed charge.

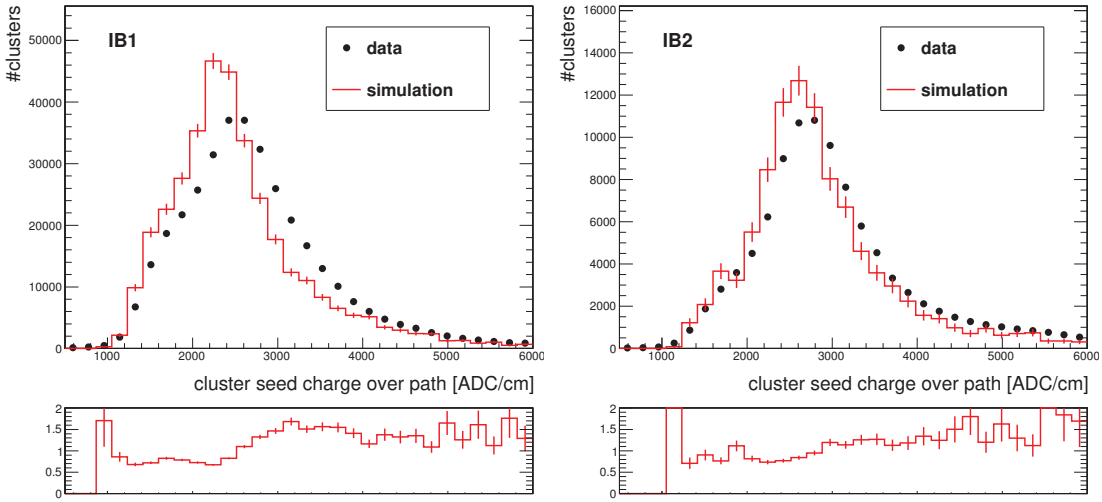

Figure 3.5: Distribution of the on-track cluster seed charge for the IB1 (left) and IB2 (right) geometries in data and simulation. The simulated distribution is rescaled to the number of clusters in data. The bottom plots represent the data to simulation ratio for a given geometry.

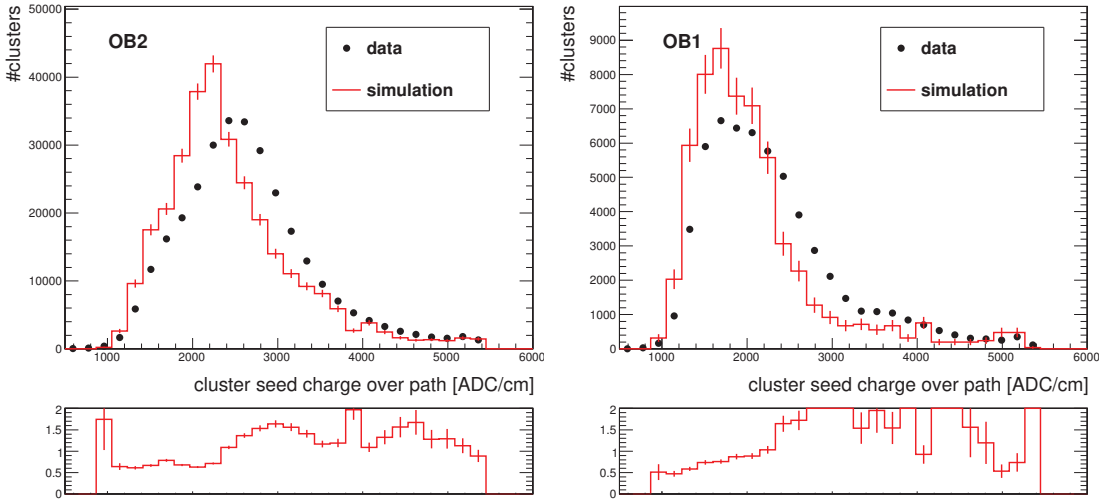

Figure 3.6: Distribution of the on-track cluster seed charge for the OB2 (left) and OB1 (right) geometries in data and simulation. The simulated distribution is rescaled to the number of clusters in data. The bottom plots represent the data to simulation ratio for a given geometry.

To summarize, the simulation tends in general to overestimate the cluster width and to underestimate the charge on the seed strip. Large variations in the data to simulation

ratio are observed. Therefore it is necessary to identify the sources leading to the observed disagreements between data and simulation, and to propose possible corrections.

To achieve such goal, the simulation flow of the silicon strip tracker (step 3) is described in detail in the rest of this section, starting from GEANT 4 output in Subsection 3.2.1 and going through all the simulation steps in a detector unit up to the final digitization in Subsections 3.2.2 to 3.2.5. The potential issues in the simulation approach are identified and discussed at each of these steps. For simplicity, in the majority of cases, the cluster seed charge and width distributions are shown only for the OB2 geometry which has the largest number of layers. As the standard data-taking mode is the zero suppression mode with APVs operating in the deconvolution mode, the simulation steps are described for these conditions. At the end a possibility of simulating virgin raw data is briefly discussed is Section 3.2.6.

3.2.1 The GEANT4 output

A simulated hit in the tracker produced by the GEANT4 toolkit is stored in the CMSTrackerHit [82] object. The later is created for each particle entering in the tracker and for each sensitive detector unit, which in case of the silicon strip tracker represents one side of sensors of one module. The CMSTrackerHit object stores the information on the particle entry and exit points in the reference system of the detector unit (x_i, y_i, z_i). The other quantities are the energy (E_{ent}) of the particle at the point where track enters the detector unit and the total amount of energy (E_{loss}) deposited in the detector unit by the given particle. The time-of-flight (TOF) of the particle from the primary interaction point to the detector unit, the identification number of the detector unit $(DetID)$ and of the track $(trackID)$ are stored as well. A sketch of a detector unit and the information stored by GEANT4 per detector unit and track is shown in Fig. 3.7. In the following, the detector unit will be referred to as "module".

3.2.2 Dividing the energy deposit simulated by GEANT4 along the path of the track and the timing of the tracker

GEANT4 provides the information on the total energy E_{loss} deposited in the detector unit, in the form of the charge carriers created in the module. But depending on the arrival time of particle to the module, a different fraction of this total energy is read due to the electronic signal shape. To determine this fraction, the time-of-flight (TOF) of a given particle is compared to the time-of-flight of a reference photon traveling at the speed of light. The reference photon is assigned to a given bunch crossing and its time-of-

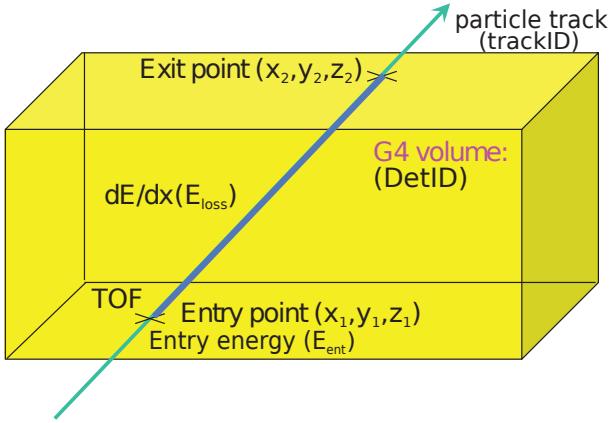

Figure 3.7: Sketch of a detector unit and the corresponding information saved for each simulated hit by GEANT4. The hits are stored with the detector unit ($DetID$) and track ($trackID$) identification numbers. They also contain the particle entry energy (E_{ent}), the total energy deposited (E_{loss}) by the particle and the time-of-flight (TOF) of the particle from the interaction point to the detector unit. The entry and exit points of the particle in the local frame (x_i, y_i, z_i) are stored as well [67].

flight is computed from the speed of light and the distance between the interaction point and the entry point of the given particle in the given module. The maximum amount of charge is read when the time-of-flight difference between the reference photon and the given particle is zero. Larger is the difference from zero, smaller is the collected fraction of the particle charge. Because of the bunch crossing assignment, the time-of-flight difference between the reference photon and the particle can be either negative or positive. If the particle originates from the studied bunch crossing the difference is always negative or equal to zero, but if it was created before (OOT PU), the difference can be positive as well. Therefore according to the delay between the reference photon and the particle at the entry point to the module, the time response of the module to the signal left by the particle can be determined. The schema of this time response (pulse shape) to the signal currently used in simulation can be seen in Fig. 3.8. This shape corresponds to the electronic pulse shape convoluted by a physical signal (flat with a duration of 20 ns). It can be noticed that the time response of the module to the particle signal can take several tens of ns. It is longer than the time between collisions, which is 25 ns, and therefore in the bunch crossing of interest it is possible to read signal from preceding and succeeding bunch crossings. This effect is one of the sources of the OOT pileup. The other sources are particles arriving with a delay, for example slow particles and loopers.

GEANT4 hit stores only a total energy deposition information per one module but in the real data-taking, the particle looses its energy as it traverses the module. To mimic this effect, the track is divided into a certain number of equidistant segments. Currently the number of sectors is evaluated as a fixed factor multiplied by the expected number of

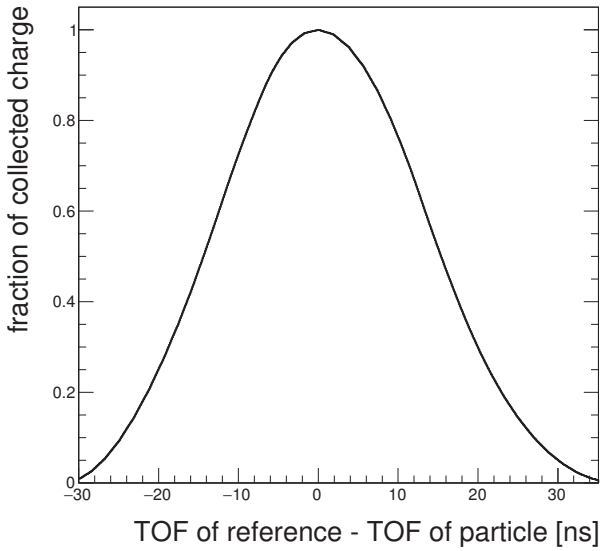

Figure 3.8: The approximated deconvolution pulse shape plugged into the simulation. This pulse shape was derived from the laser measurements [83] and its maximum was aligned to the 0 ns corresponding to the reference (photon) time, for which the maximum of the charge is collected.

strips reading the particle signal. The total energy reduced by the time response value, as described in the previous text, is then divided into the track segments and for each segment it is fluctuated according a Landau function. The fluctuated charge per segment is then normalized to keep the sum of the segment energies equal to the initial energy. The local coordinates of the track segment together with the fluctuated normalized energy deposit are saved in an object referred to as "energy deposit unit".

In the energy division procedure there are several simplifications which can lead to discrepancies between the properties of simulated clusters and clusters in data. The GEANT4 provides only the total deposited charge, therefore the charge has to be divided into discrete and equidistant tracks segments. Moreover it is assumed that the energy loss is constant along the track, but according to the Bethe-Bloch formula there is an evolution of the energy loss with the particle momentum. Other issues of this step are discussed in detail in the following paragraphs.

Cut-off on the delta ray production δ

The charge of each track segment is being fluctuated by the GEANT4 routine. This routine is initialized with a parameter called δ specifying a cut-off on the delta ray production. The delta rays are already part of the previous GEANT4 output and therefore this cut-off has to be the same as the one in the previous step in order to avoid any mismatch. The dependency of the cluster charge, cluster seed charge and cluster width on the delta ray cut-off, which was varied up to $\pm 20\%$ around its default value of 0.120425,

is shown in Figs. 3.9 and 3.10. From these figures it can be concluded that the change of distributions of the cluster properties is almost negligible in the given range of the cut-off variation.

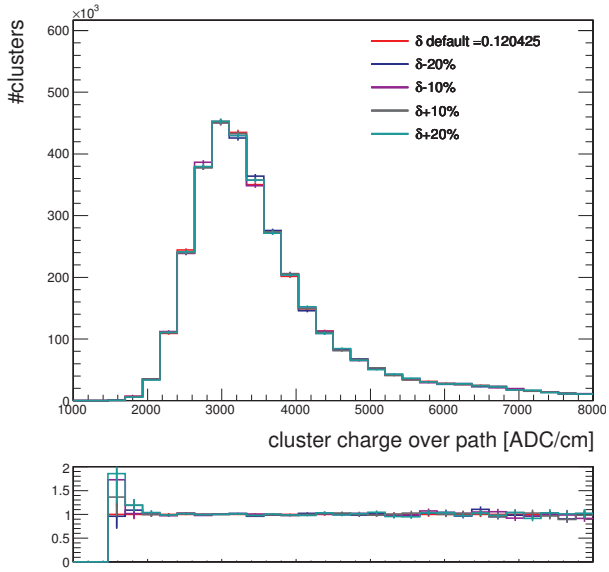

Figure 3.9: On-track cluster charge in simulation for different values of the delta ray production cut-off δ. The simulated distributions are normalized by the same factor as in Fig. 3.2. In the ratio plot the default simulation is divided by different simulation scenarios.

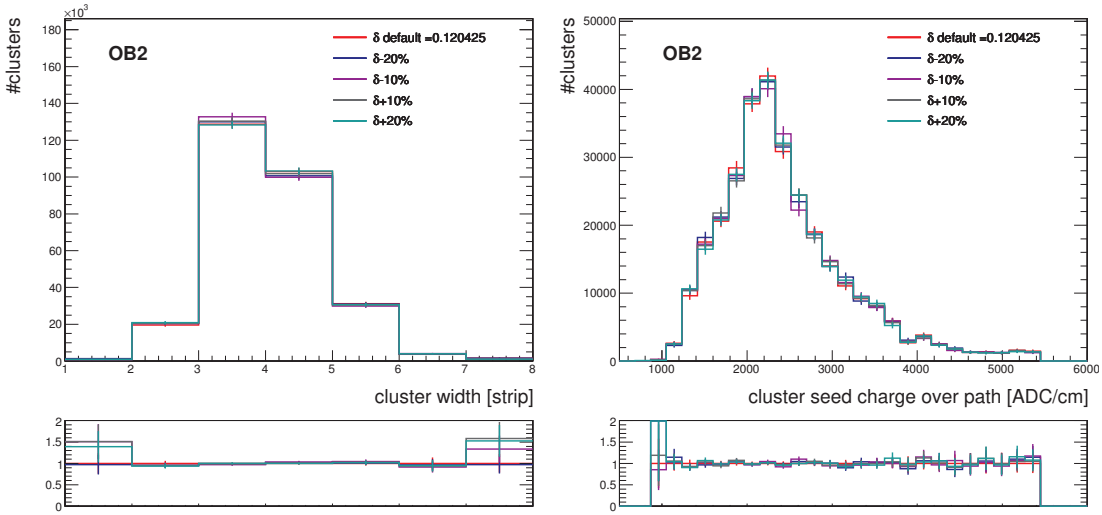

Figure 3.10: On-track cluster width (left) and cluster seed charge (right) in simulation for the OB2 geometry and for different values of the delta ray production cut-off δ. The simulated distributions are normalized by the same factors as in the left plots of Figs. 3.4 and 3.6, respectively. In the ratio plots the default simulation is divided by different simulation scenarios.

Pulse shapes

The deconvolution pulse shape used in simulation, presented in Fig. 3.8, was determined by the parametrization of results obtained in [83]. These results were obtained from laser studies of the TOB modules before the start of the LHC operation. Fig. 3.11 presents the results, when a single strip was hit by the laser. In this plot, the resulting pulse shape from the hit strip and the two neighbors on each side is shown. The neighboring strips read non-zero charge purely due to the electronic cross talk, which is a result of the coupling of the strips via inter–strip capacitance as shown in Fig. 2.4.

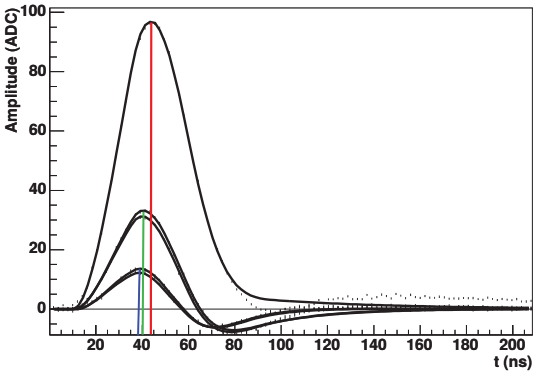

Figure 3.11: The deconvolution pulse shape obtained from focusing a laser on one strip of the TOB module. The charge read by the first and second neighboring strips on both sides are shown as well. The largest signal is collected by the hit strip, a lower fraction by its first neighbors and the lowest fraction by second neighboring strips. The black curves correspond to the theoretical fits of the data, while the dots are measured data. The vertical lines indicate the time of the maximum of the pulse shapes [83].

It can be noticed that there are several differences between the pulse shape obtained from laser measurements and the one in simulation. First, the times corresponding to the measured maxima of the pulse shapes are not same for the hit strip and for its neighbors. This fact is omitted in the simulation. Secondly, measured pulse shape can have negative values, while it is not the case in simulation. Thirdly, a pulse shape does not take into account any ageing effects of the modules of the CMS tracker. Moreover in 2016 the VFP parameter changed in order to avoid saturation of the electronics, which resulted in a change of the pulse shape in data [84]. This change was not propagated into the simulation. Therefore the dynamics is not correctly modeled, but in average the on-track cluster charge is well described. In order to provide more realistic simulation of clusters, the pulse shapes should be updated in future.

Furthermore there is a dynamics which modifies the pulse shape and which is not modeled in the simulation. For example, the only charge carriers which are present in the simulation are holes drifting to the strips, but the presence of electrons is omitted.

The backplane correction

In 2009, discrepancies in the cluster position between data recorded in peak and deconvolution modes were observed [85]. The disagreement was found to be worse for thick sensors and the problem was quickly identified as an issue of the charge collection from the whole sensor. In the deconvolution mode the charge carriers which are created close to the backplane are not read as efficiently as those produced close to the strips and therefore the cluster position in the deconvolution mode is shifted with respect to the peak data, where such problem is not present. To correct the cluster position between peak and the deconvolution data, an ad-hoc correction called "backplane correction" is applied on top of the deconvolution data during the reconstruction step. The derived backplane correction is not precise and its inaccuracy is further compensated by the alignment. As in the deconvolution mode the strip sensor appears effectively thinner, this effect does not only impact the cluster position, but it could also influence the cluster charge, the cluster seed charge and the cluster width. However, this effect is not considered in simulation.

3.2.3 Charge drift of the energy deposits through the sensor

To simulate the drift to the electrodes of the charge carriers created after the passage of a particle through a module, the energy deposits have to be propagated separately from each track segment to the strips. In simulation the energy deposits are not directly converted to the charge carriers, but the energy deposits are drifted as the charges would do.

As in the barrel region the electric field is perpendicular to the magnetic field, the drift of the charge carriers is deflected from the direction of electric field, i.e. the local z-axis, by the Lorentz angle. Thus the drift direction of the charges towards the surface of the sensor must be corrected accordingly to the Lorentz angle and the local magnetic field.

Moreover the charge carriers undergo diffusion in the silicon volume during the drift and therefore the energy deposit from each track segment is collected smeared at the surface due to the diffusion effects. The spread of the energy distribution is computed from the knowledge of the drift time and a diffusion constant, which depends on the type of material through which the charge drifts and the temperature of the sensor. The drift time from the track segment to the sensor surface depends on:

- **The sensor thickness**: The drift time is longer for thicker sensors
- **The depletion and applied voltages**: The former is the voltage which fully

depletes the sensor while the later is the total voltage applied, including the depletion voltage. Both influence how fast the charge carriers drift

- **The charge mobility**: Depending on the material properties, its temperature, the electric field and the concentration of the charge carriers, the charge mobility influences how fast the charge carriers drift. For example the mobility of holes is lower than the one of the electrons
- **The coordinates of the track segment**: They are used to determine the distance that the charge has to drift through

The output from the previous step, as described in Subsection 3.2.2, is in the form of energy unit after having applied now the drift and diffusion procedures and is stored as an object referred to as "signal point", which contains the information about its coordinates at the surface, the energy and its spread.

In order to keep the processing time relatively short, the description of the drift is simplified. It does not take into account any radiation damages of the sensors, ageing of modules, or non-uniformities of the electric filed. However, the charge drift depends on several parameters which can be subject of ageing. The description of these parameters and the impact of a variation around their default values in the simulation is presented in the following paragraphs.

Applied (AV) and depletion (DV) voltages

As mentioned, the spread of the diffused energy distribution depends on the drift time which depends on the applied and depletion voltages. The depletion voltage changes during the operation of the tracker because of the ageing of modules, but this information is not updated in the simulation. The applied voltage has not been changed during the operation of CMS, but it will become necessary once the depletion voltage will be larger than the applied one. To evaluate the effect of a voltage change on the cluster charge, seed charge and width, these distributions are shown for several values of depletion and applied voltages in Figs. 3.12 to 3.15. The depletion and applied voltages, whose default values are 170 V and 300 V, respectively, are varied in the figures within a ±20% around the default. It can be concluded that the following change of the cluster properties is negligible.

Temperature (T) and charge mobility (μ)

The diffusion constant D can be expressed as

$$D = \frac{\mu k_B T}{q}, \tag{3.1}$$

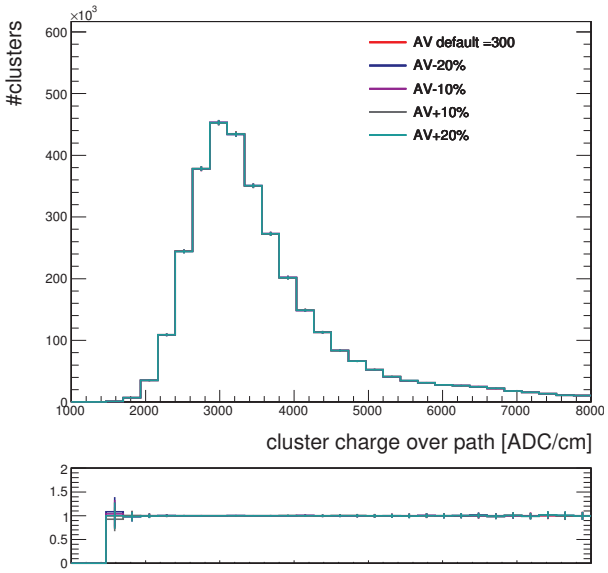

Figure 3.12: On-track cluster charge in simulation for different values of the applied voltage AV. The simulated distributions are normalized by the same factor as in Fig. 3.2. In the ratio plot the default simulation is divided by different simulation scenarios.

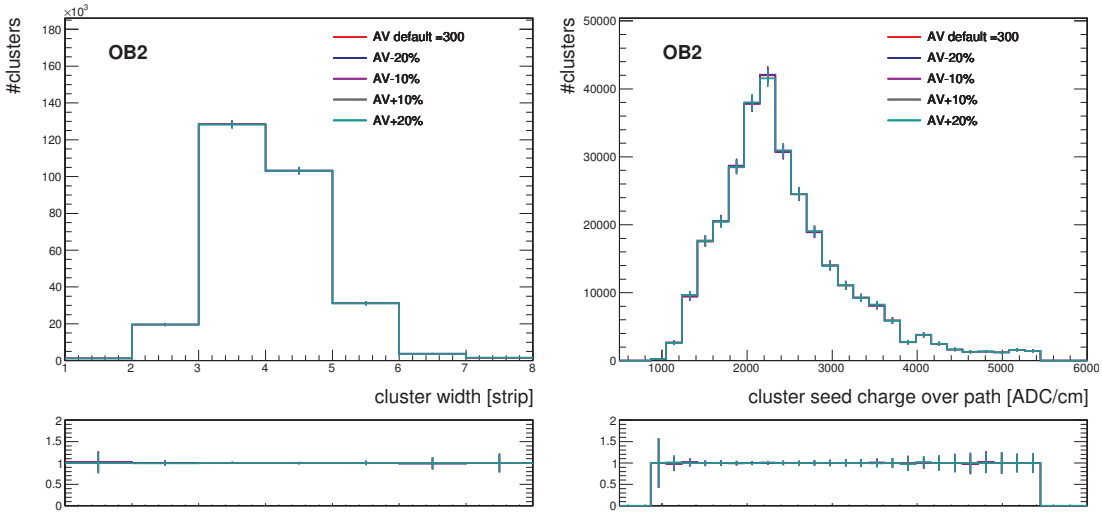

Figure 3.13: On-track cluster width (left) and cluster seed charge (right) in simulation for the OB2 geometry and for different values of the applied voltage AV. The simulated distributions are normalized by the same factors as in the left plots of Figs. 3.4 and 3.6, respectively. In the ratio plots the default simulation is divided by different simulation scenarios.

where μ is the charge mobility in units $cm^2/(V \cdot s)$, k_B the Boltzmann constant, T the absolute temperature of the material and q the electrical charge of the particle. Between Run 1 and Run 2 the temperature of the tracker was changed from 4°C to -15°C and between 2017 and 2018 from -15°C to -20°C. As this change was not propagated into the simulation, it is therefore important to evaluate its effect. The cluster charge, width and seed charge are shown in Figs. 3.16 and 3.17 for the default value of temperature

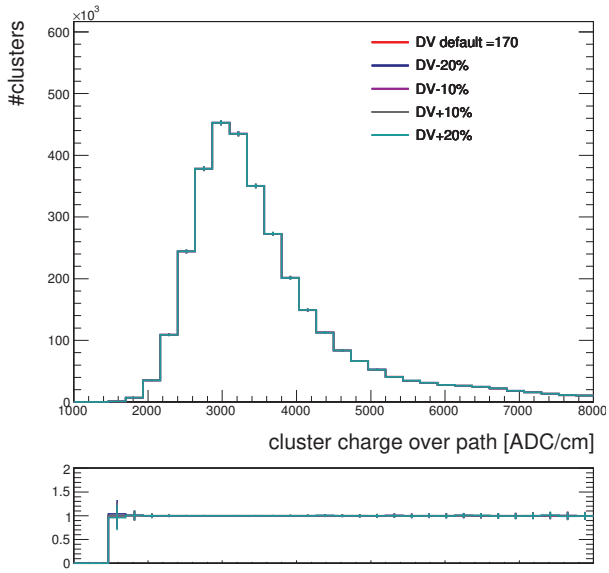

Figure 3.14: On-track cluster charge in simulation for different values of the depletion voltage DV. The simulated distributions are normalized by the same factor as in Fig. 3.2. In the ratio plot the default simulation is divided by different simulation scenarios.

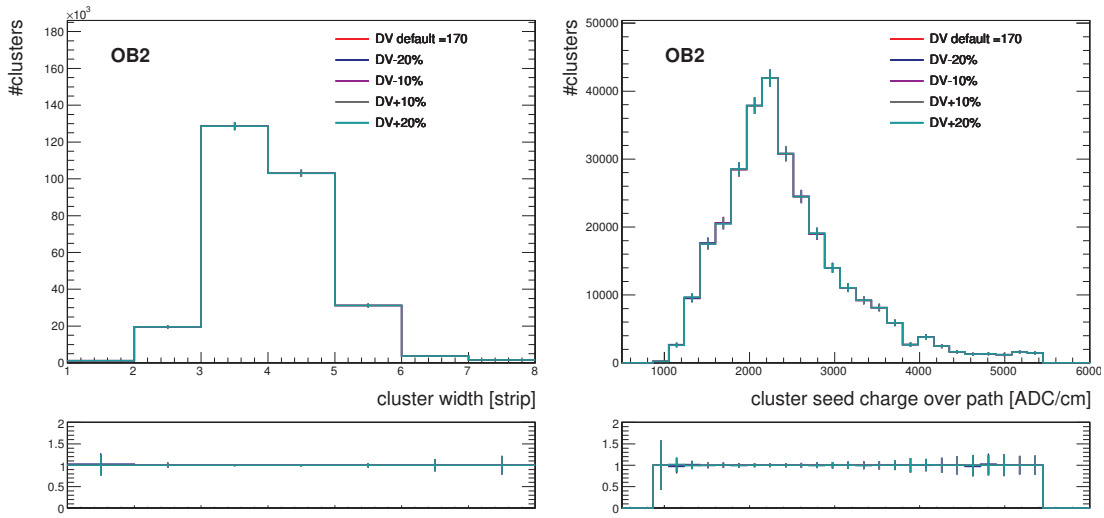

Figure 3.15: On-track cluster width (left) and cluster seed charge (right) in simulation for the OB2 geometry and for different values of the depletion voltage DV. The simulated distributions are normalized by the same factors as in the left plots of Figs. 3.4 and 3.6, respectively. In the ratio plots the default simulation is divided by different simulation scenarios.

$T = 273$ K used in simulation as well as for variations up to $\pm 20\%$. No dependency of the cluster charge, width and seed charge on the temperature is observed.

The charge mobility μ intrinsically also depends on the temperature, as well as on the concentration of defects which change in time and therefore this parameter should in principle also be adjusted in the simulation. Figs. 3.18 and 3.19 are not revealing

any change of the cluster charge, width and seed charge when altering the default charge mobility of 310 $\mathrm{cm}^2/(\mathrm{V}\cdot\mathrm{s})$ by up to $\pm 20\%$.

In summary, there is almost no change in the simulated cluster properties due to parameters influencing diffusion of the charge carriers because the magnitude of diffusion is much smaller than the pitch size.

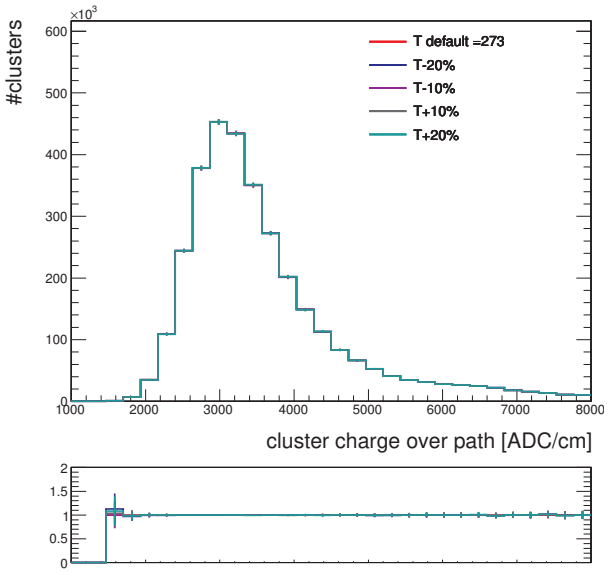

Figure 3.16: On-track cluster charge in simulation for different values of the temperature T. The simulated distributions are normalized by the same factor as in Fig. 3.2. In the ratio plot the default simulation is divided by different simulation scenarios.

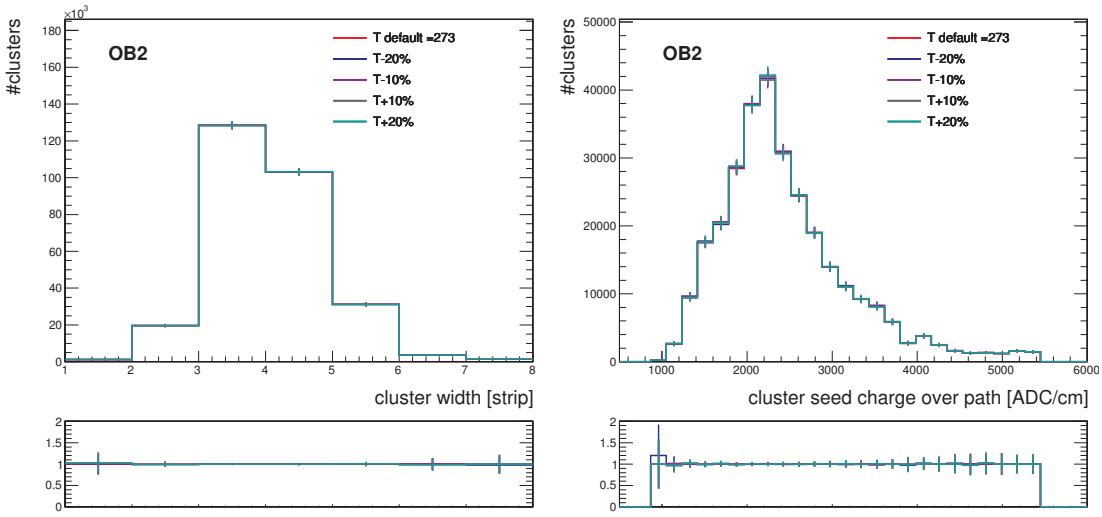

Figure 3.17: On-track cluster width (left) and cluster seed charge (right) in simulation for the OB2 geometry and for different values of the temperature T. The simulated distributions are normalized by the same factors as in the left plots of Figs. 3.4 and 3.6, respectively. In the ratio plots the default simulation is divided by different simulation scenarios.

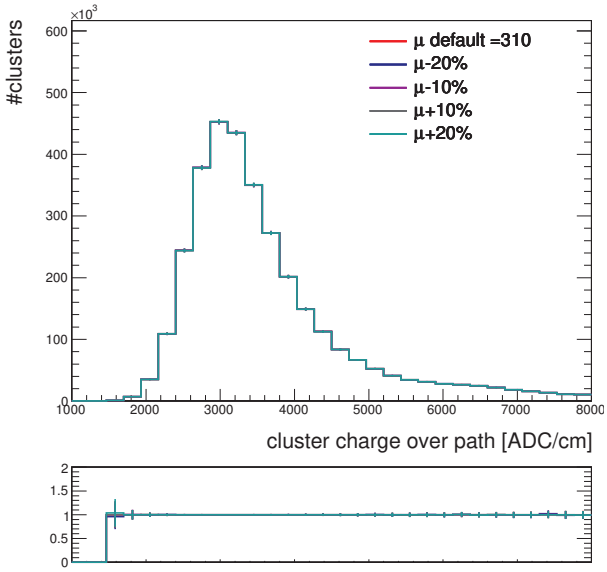

Figure 3.18: On-track cluster charge in simulation for different values of the charge mobility μ. The simulated distributions are normalized by the same factor as in Fig. 3.2. In the ratio plot the default simulation is divided by different simulation scenarios.

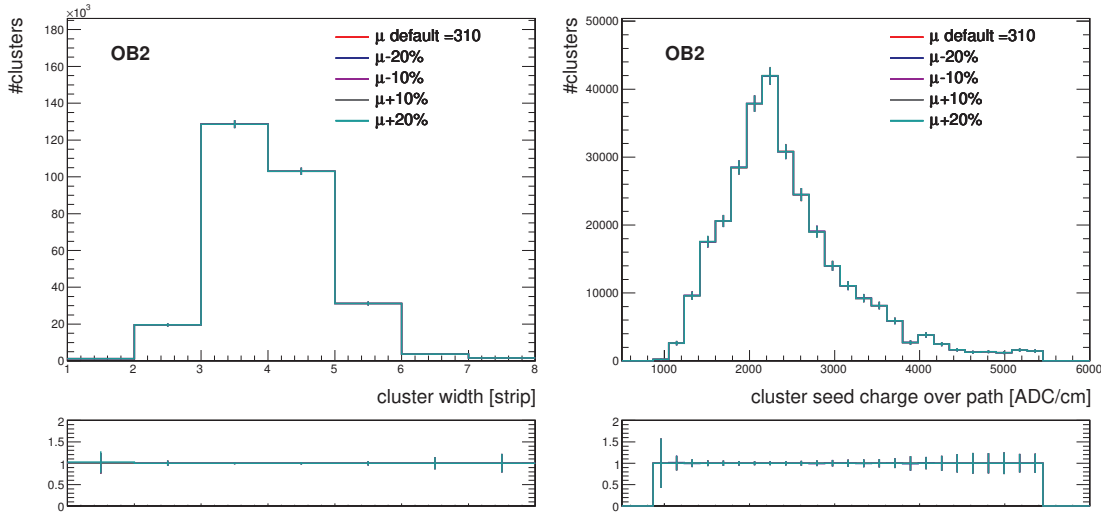

Figure 3.19: On-track cluster width (left) and cluster seed charge (right) in simulation for the OB2 geometry and for different values of the charge mobility μ. The simulated distributions are normalized by the same factors as in the left plots of Figs. 3.4 and 3.6, respectively. In the ratio plots the default simulation is divided by different simulation scenarios.

Lorentz angle (LA)

The Lorentz angle used in simulation is dependent on the electric and magnetic field and therefore the Lorentz angle should be updated with the change of voltage. The effect of the Lorentz angle on the simulated cluster charge, width and seed charge is shown in Fig. 3.20 and 3.21. The Lorentz angle injected into the simulation is specific for

each module and it is read from the offline condition database. This database contains information about tracker conditions, such as Lorentz angle, noise, list of bad modules and gains. The distribution of the Lorentz angles in the OB2 geometry per cluster was fitted by a Gaussian distribution to obtain its mean value and standard deviation. Then a mean value altered by up to twice the standard deviation was injected into the simulation to obtain the varied simulated samples. It can be concluded that within the range of injected Lorentz angle values there is a negligible effect on the description of the shown cluster properties. The Lorentz angle impacts the position of the cluster and therefore within the tracker local reconstruction group, there are intents to remeasure and update the Lorentz angle values to improve the cluster position in simulation.

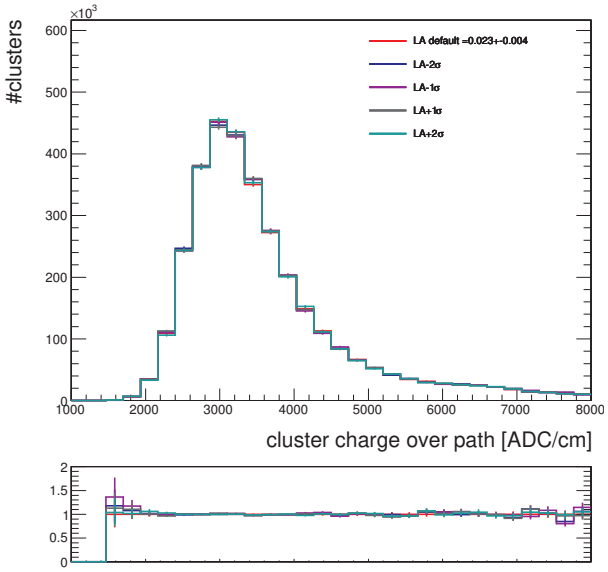

Figure 3.20: On-track cluster charge in simulation for different values of the Lorentz angle LA. The simulated distributions are normalized by the same factor as in Fig. 3.2. In the ratio plot the default simulation is divided by different simulation scenarios.

3.2.4 Induced charge on the strips

Once the energy deposits are drifted to the surface, the amount of electrons induced on the given aluminium strips is simulated. The energy cannot be divided between strips purely based on geometrical criteria, due to the capacitive coupling (cross talk) between the silicon strips. The cross talk induces that the charge collected by one strip is partially shared with its first and second neighboring strips on both sides. The sharing with second neighboring strips is larger in the deconvolution mode than the peak mode. In the peak mode the sharing with second neighboring strips is negligible.

The signal point at the surface is associated to the closest strip. There the energy is

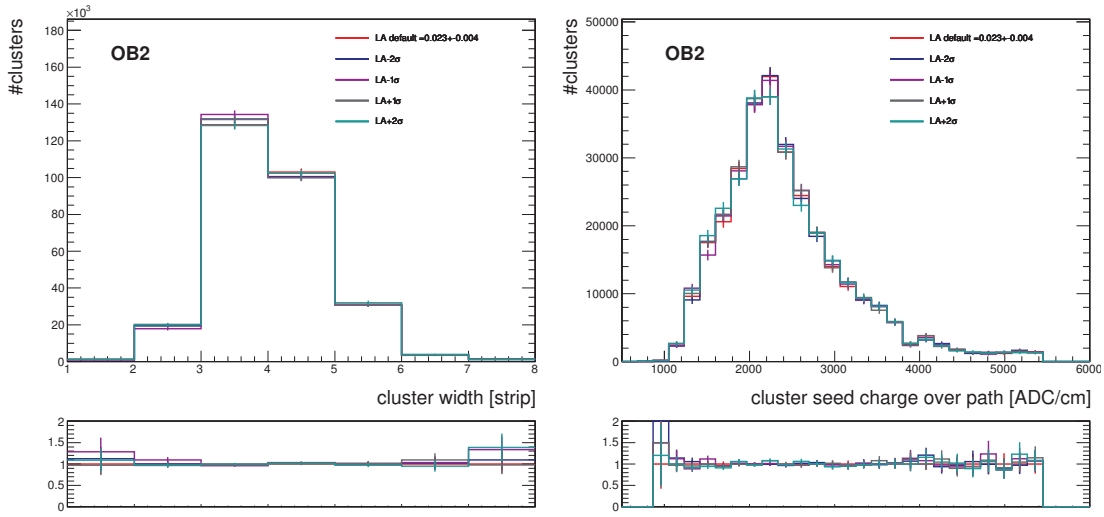

Figure 3.21: On-track cluster width (left) and cluster seed charge (right) in simulation for the OB2 geometry and for different values of the Lorentz angle LA. The simulated distributions are normalized by the same factors as in the left plots of Figs. 3.4 and 3.6, respectively. In the ratio plots the default simulation is divided by different simulation scenarios.

converted to a number of electrons corresponding to a given charge. The charge is then divided between the neighboring strips according to the energy spread originating from the diffusion. This is repeated for all signal points. If one strip obtains signal from many signal points, these charge deposits are summed. On top of the assigned charge to the strips, the cross talk effect is applied. The simulation iterates over all strips from left to right, and shares the charge of a given strip in between its neighbors.

At this step, several more parameters have to be plugged into the simulation. All these parameters can evolve with the ageing of the modules and therefore the impact of their change on the cluster properties is discussed in following paragraphs.

The cross talk (XT)

While in reality the current is already induced on the aluminium strips once the electrons and holes start to drift to the backplane and silicon strips, respectively, the simulation is simplifying the description, by decomposing these steps: first only holes are drifted towards the strips, second the charge on the strips is collected and then the cross talk is applied. The cross talk could change in time due to radiation damages of modules. The change in cross talk would have a small impact on the cluster charge, but the cluster width and cluster seed charge would change largely as the sharing between strips is impacted. In Figs. 3.2 to 3.6, it was observed that the simulation describes well the cluster charge in data, but there is a large disagreement between data and simulation for the cluster width and seed charge, therefore a change in cross talk would be a good

candidate to explain the observed discrepancies.

To evaluate, what would be the impact of a non-correct description of the cross talk, Figs. 3.22 and 3.23 show the cluster charge, width and seed charge distributions for several cross talk configurations. In these plots it can be indeed seen that the cluster width and seed charge, which are poorly described in simulation, are strongly dependent on the cross talk.

To evaluate if there is a cross talk parametrization which could be injected into simulation to describe the measured data, a matrix of simulated samples was produced. In these samples both the charge sharing between the first and second neighboring strips was varied. The cluster width distribution of each simulated sample was compared to data, based on a χ^2 test. The sample with the best χ^2 is shown in green in Figs. 3.22 and 3.23. In the figures it can be noticed, that a decrease of the charge sharing between the central strip and both its first and second neighboring strips, with respect to the values in the default simulation, is required in order to better describe data. After this procedure the data and simulation agreement for the cluster width and seed charge is vastly improved, but it is still not perfect as the parameters and conditions which cause minor source of discrepancies have to be updated as well. The remaining discrepancies could be then caused by a simplification of the cluster simulation. More details about the cross talk and the dedicated measurement performed during this thesis are given in Section 3.3.

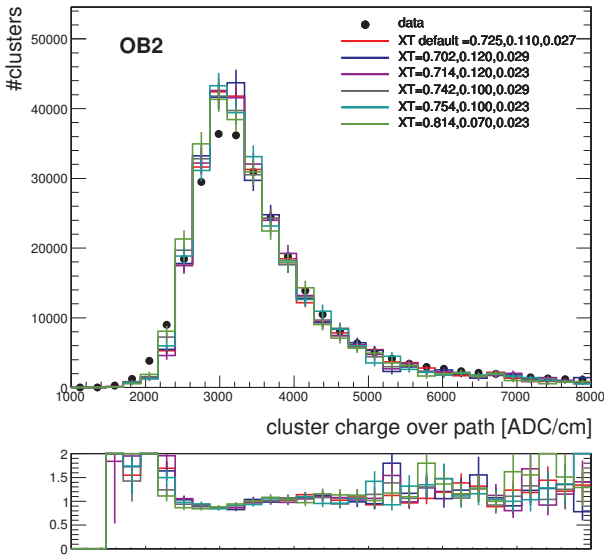

Figure 3.22: Data and simulation comparison of the on-track cluster charge divided by the track length for the OB2 geometry and for different values of the cross talk XT. The first of the three XT numbers corresponds to the fraction of charge induced on the seed strip, the second and third number represent the fractions of charge induced on each first and second neighboring strips, respectively. The simulated distributions are rescaled to the number of clusters in data. The bottom plot represents the data to simulation ratios.

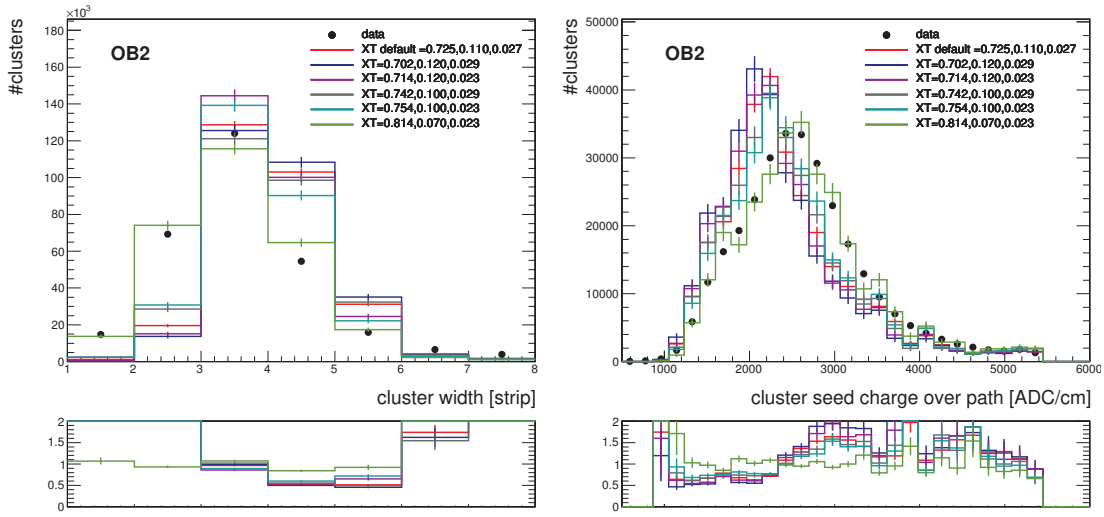

Figure 3.23: Distribution of the on-track cluster width (left) and cluster seed charge (right) in data and simulation for the OB2 geometry and for different values of the cross talk XT. The first of the three XT numbers corresponds to the fraction of charge induced on the seed strip, the second and third number represent the fractions of charge induced on each first and second neighboring strips, respectively. The simulated distributions are rescaled to the number of clusters in data. The bottom plot represents the data to simulation ratios.

The energy to electron conversion factor (Ee)

With the ageing of the modules, the conversion of the energy into a number of electrons can evolve. The data and simulation comparisons of the cluster charge, width and seed charge are shown in Figs. 3.24 and 3.25. A set of simulations, produced by changing the conversion factor by up to ±20% with respect to its default value of 3.61×10^{-9} GeV, is plotted as well. In these figures it can be noticed that a change in the conversion factor between the deposited energy and the electron multiplicity by up to ±20% leads to significant changes in all cluster quantities. However, it can be concluded that a single change of this conversion factor does not allow to provide a good data and simulation agreement in all these three quantities at the same time. Moreover as there realistic gains are applied, the possible evolution of the conversion factor is already taken into account by the gain calibration procedure. The details are discussed in the next section when the factor converting electrons to ADCs is introduced.

3.2.5 Conversion of the analog signal to a digital one

Before the digitization of the signal, few more effects must be considered. First, in the detector around 4% of channels are flagged as bad. The information about bad channels is stored in the condition database, read by the simulation, and if a bad channel has a

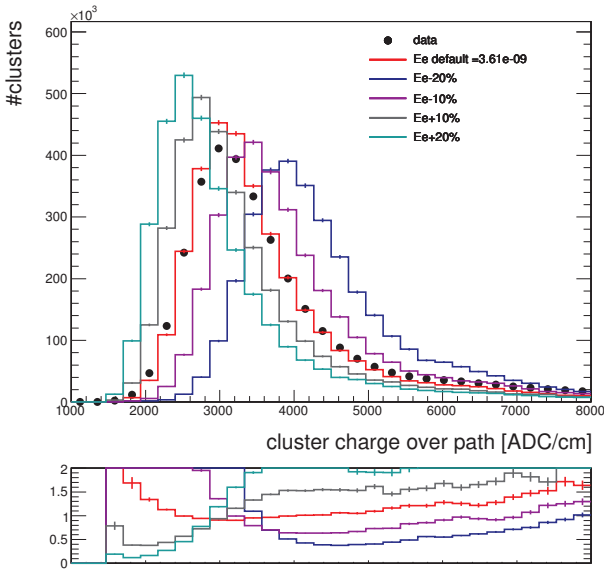

Figure 3.24: Data and simulation comparison of the on-track cluster charge divided by the track length for the OB2 geometry and different values of the energy to electrons conversion factor Ee. The simulated distributions are rescaled to the number of clusters in data. The bottom plot represents the data to simulation ratios.

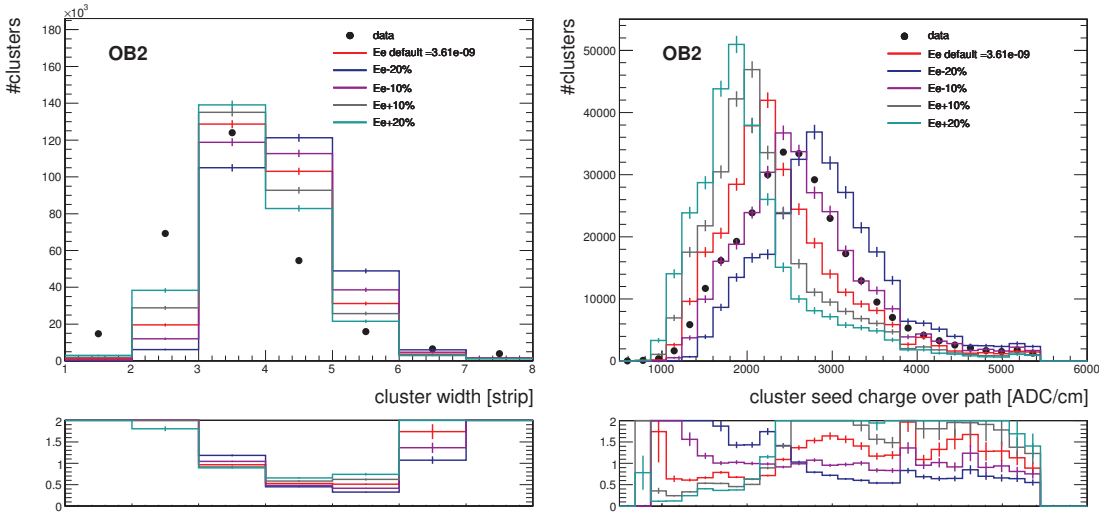

Figure 3.25: Distribution of the on-track cluster width (left) and cluster seed charge (right) in data and simulation for the OB2 geometry and different values of the energy to electrons conversion factor Ee. The simulated distributions are rescaled to the number of clusters in data. The bottom plots represent the data to simulation ratios.

non-zero value of its simulated charge, it is set to zero. Secondly, to mimic real conditions, the noise, which is stored in the condition database, has to be added to each strip. The noise per strip is determined from the the fluctuation of the strip charge after pedestal and CMN subtraction in data runs in absence of collision. The noise is stored in ADCs, therefore it has to be converted to a number of electrons by a dedicated conversion factor.

Moreover because of differences between modules in the detector, the noise has to be rescaled by the gains of the modules to correct for module differences. The gain used in simulation (Gsim) is set to be the G1 gain described in Section 2.2.5 determined from the simulation. Another option for the Gsim is to smear randomly the G1 value determined from data to take into account the fluctuations of G1 over time and the accuracy of its measurement. The G2 gain for simulation is then calculated from a simulated $t\bar{t}$ sample with all the other conditions applied, by targeting the MPV of the MIP response to be 300 ADC/mm.

The sum of signal and noise on the strips in electron units is then converted to ADCs by a conversion factor and scaled by Gsim gain to mimic the output from the detector. During the reconstruction step, both data and simulation are corrected by 1/(G1×G2) to eliminate differences in modules, and compensate for the drop of signal due to losses in the signal collection and during the signal transmission. Therefore it would be possible not to apply any gain on the simulated data as in the simulation itself no inefficiencies or differences between similar modules are introduced. And indeed, for the first simulations, no gains were applied, but later it was decided to apply gains to be able to simulate saturation effects. In FED, the charge in ADCs is truncated into 8-bit range, therefore the Gsim gain is applied to mimic the realistic output of detector. The simulated data in ADCs are zero suppressed and stored as digis.

The gains, noise as well as the conversion factor between electrons and ADCs change during the operation of the CMS because of the change of operating conditions and radiation damage of the modules. The evolution of these quantities is discussed in the following paragraphs.

Gains and noise

The noise is strongly dependent on the tracker operating temperature and both noise and gains change with the radiation damage. Therefore they need to be measured several times per year and updated regularly for needs of the data reconstruction. These values are not propagated to the simulation, which is using conditions from a different condition database, updated with a much smaller frequency. The difference of noise and gains between data and simulation can lead to different zero suppression results and also different reconstruction results. If the noise is larger in one case than the other, it can appear that a strip with a given charge can fail the S/N threshold criterion in one case and pass in the other. This effect can lead to discrepancies in the cluster width and charge between data and simulation. To evaluate the current status, the cluster seed noise rescaled by gains, further called only as “seed noise”, is shown in Fig. 3.26. From these plots it is obvious that the difference in the seed noise between data and simulation is huge. This

finding triggered the update of these conditions by the responsibles of the tracker local reconstruction group. The gains in the simulation will be updated during 2018.

For the update of 2018 conditions in simulation, the G1 gain, noise and bad components conditions are taken directly from data, the Gsim gain is taken to be a smeared version of G1 and the G2 gain is recomputed by a strategy similar as before.

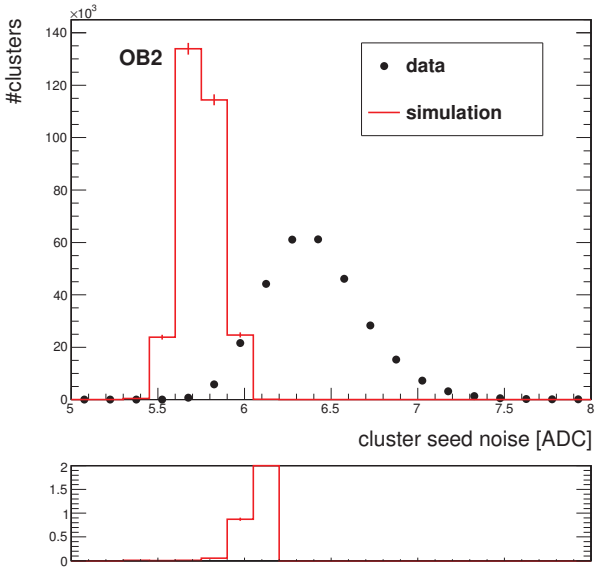

Figure 3.26: Data and simulation comparison of the on-track cluster seed noise rescaled by gains for the OB2 geometry. The simulated distribution is rescaled to the number of clusters in data. The bottom plot represents the data to simulation ratio.

The electrons to ADCs conversion factor ($eADC$)

Similarly, as the conversion factor Ee, the conversion factor from electrons to ADCs $eADC$ is sensitive to the ageing of modules. The comparisons of data with different simulations are shown in Figs. 3.27 and 3.28 for the cluster charge, width and seed charge, the simulations are using an $eADC$ conversion factor within up to ±20% from the default value of 247 ADC^{-1}. By its nature the impact on the cluster quantities of the variations of $eADC$ is very similar to the case with varied Ee factor and again the conversion factor $eADC$ alone cannot be taken as the responsible for the non-description of the data by simulation.

As already suggested the evolution of the conversion factors is already taken into account by applying the gains. In data the (G1 × G2) factor corrects for the electronics effects and the differences at the sensor level by tuning the MPV of the MIP response to be 300 ADC/mm. The gain calibration procedure then guarantees that the cluster charge is stable through the operation of CMS even if due to radiation effects the inefficiency, for example in the charge collection, can increase. In simulation, the (G1 × G2), if well

calibrated, also targets the charge to be the one of the MIP. Therefore the product of Ee and $eADC$ conversion factors is already fixed by this calibration procedure.

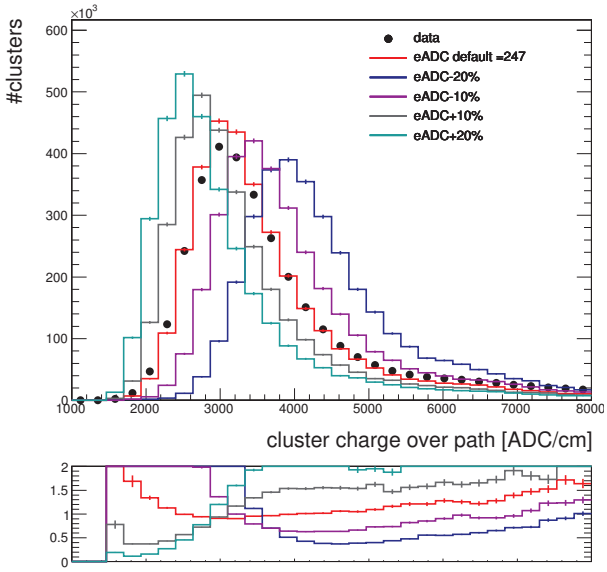

Figure 3.27: Data and simulation comparison of the on-track cluster charge divided by the track length for the OB2 geometry and different values of the conversion factor $eADC$. The simulated distributions are rescaled to the number of clusters in data. The bottom plot represents the data to simulation ratios.

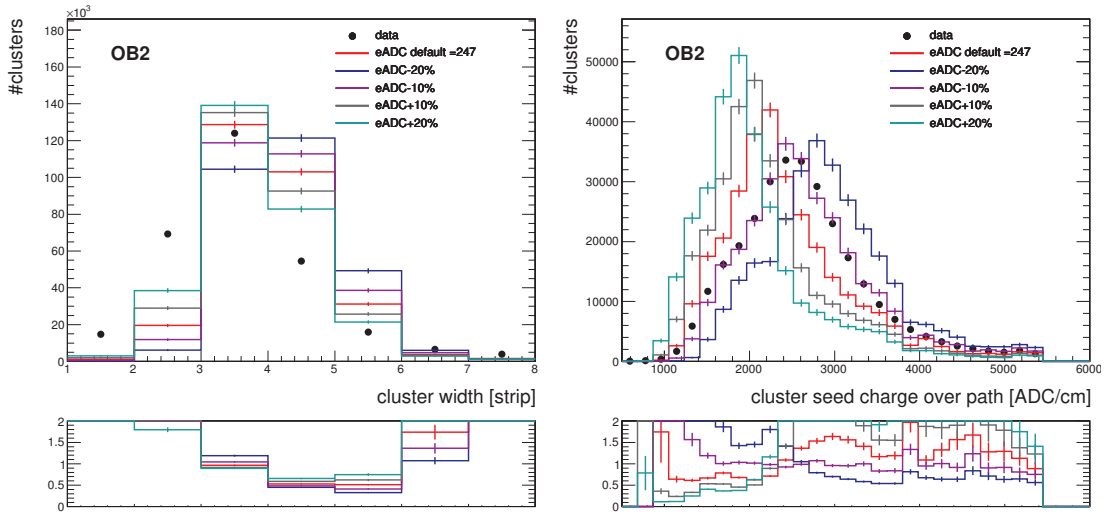

Figure 3.28: Distribution of the on-track cluster width (left) and cluster seed charge (right) in data and simulation for the OB2 geometry and different values of the conversion factor $eADC$. The simulated distributions are rescaled to the number of clusters in data. The bottom plots represent data the to simulation ratios.

3.2.6 Virgin raw simulation

Besides the standard zero suppressed simulation, the tracker digitization step brings a possibility to simulate Virgin Raw data. In this case, several steps need to be added to the simulation steps described above. After inducing the charge on the strips, the APV saturation due to the HIP effect can be simulated. This option is by default switched off. Then the APV baseline is shifted down from its designed position of 127 ADC, accordingly to the amount of charge collected by a given APV and the number of channels reading the charge. The strip noises, CMNs and pedestals are finally added and the result is stored.

3.3 The cross talk measurement to improve the simulation

As identified in the above sections a change in the cross talk parameters could lead to a better description of data by simulation. There are several possibilities how to update the cross talk parameters. The first possibility was already introduced in Subsection 3.2.4, by tuning the cross talk on data to simulation comparisons. A matrix of samples with each of the fractions of charge shared to the first and second neighbors changed in steps, can be produced. Then the cross talk which is best improving the description of data by simulation is chosen. Before such tuning of the cross talk, it is necessary to perform an update of the bad channels, noise and gains in the simulation as their update after the tuning could destroy the obtained data-simulation agreement. Indeed, the noise and gains are measured conditions, which are influencing the cluster properties and therefore it is indispensable to update them prior to the cross talk tuning.

The second option is to measure the cross talk parameters from data. The measurement from data has an advantage that it is not sensitive to the other potentially outdated parameters in simulation like the mentioned tuning. In following Subsection 3.3.1, the results on a cross talk measurement are presented and then compared with the results obtained by the tuning of cross talk on data to simulation comparisons. Because of the low data statistics in TID and TEC, the cross talk could be measured only in barrel. To obtain new cross talk parameters for TID and TEC, a third option was developed, which combines measurement from data and the tuning based on data to simulation comparisons. It is presented in Subsection 3.3.3.

3.3.1 The cross talk measurement in the barrel

In this section, the data-taking used for the cross talk measurement is first discussed. It is followed by a description of the methodology used for the cross talk measurement and a discussion on the dependence of the cross talk as a function of time. Later, results of the cross talk measurement and their validation are then presented. In the last subsection, the evolution of the cross talk with the radiation is studied.

3.3.1.1 Data-taking for the cross talk measurement

The cross talk parameters used in simulation were measured using the 0 T cosmic VR data at the beginning of Run 1. After having identified that the outdated cross talk values could lead to large discrepancies between data and simulation, the decision to remeasure the cross talk was taken. The new data for the cross talk measurement were taken in the virgin raw mode at the end of March 2018. These data are CRUZET, i.e. cosmic events recorded with no magnetic field in the CMS solenoid, implying that there was no magnetic field and no collisions in the detector during the data taking, therefore only cosmic muons were triggered. The trigger used during this data-taking, was first designed for triggering cosmics during collisions (CDC), which was requested by the tracker alignment group. Its advantage is that it increases the probability of triggering muons which passed through the tracker. The CDC trigger bit [86] assumes that the muon passes through the whole CMS in around 30 ns, implying that the top leg of the muon, i.e. the part of the muon track in the top part of the detector, should be seen in the top part of the detector one bunch crossing before seeing the bottom leg in the bottom part of the detector. Moreover the two legs should be back to back, leading to the requirement on the angle between the legs to be $\pi \pm 1/6\pi$. To further enhance cosmics passing through the tracker, the following criteria on Φ and η are imposed. The top leg must pass the requirement $|\Phi| < 1/2\pi \pm 1/3\pi$ and the bottom leg $|\Phi| < 3/2\pi \pm 1/3\pi$, the pseudorapidity of muon is required to satisfy $|\eta| < 1.202$. The requirement on η results in muons which are almost exclusively measured by DTs only. In totality 145854 events were collected and saved, corresponding to runs 312627, 312972, 312973, 312974 and 312977.

The absence of the magnetic field is important to decompose the effects of the Lorentz angle from the cross talk in the data. Furthermore the data need to be in the VR mode in order not to suppress the strips which have a non-zero charge because of the cross talk but is small enough to be zero suppressed.

3.3.1.2 The cross talk measurement method

When there is no cross talk effect, the total charge Q should be collected by only one strip in case where the track passes only through the sensitive volume of the sensor belonging to that strip. But as shown in Fig. 3.29, due to the cross talk effect, the charge is shared with two neighboring strips on each side and the charge collected by this seed strip is not Q but only a fraction x_0 of the original charge Q. The neighboring strips obtain smaller fractions x_1 and x_2 of this charge Q. The total charge has to be conserved, leading to the requirement on the fractions to be

$$1 = x_0 + 2x_1 + 2x_2. \tag{3.2}$$

At first attempt, the strategy of the previous cross talk measurement was reused, a selection on the angle of the track imposed in order to reduce the probability of the track traversing the sensor area to belong to more than one strip. The selection on the track was chosen to be the same as in the previous measurement:

$$|\tan\theta\cos\varphi| < 0.5 \times (p/t), \tag{3.3}$$

where θ and φ are the local track angles defined in Fig. 1.6, p is the pitch between the strips and t is the sensor thickness. This selection is ensuring that the track projected to the xz plane is close to be perpendicular to the x-axis. The track passing such a criterion is shown in Fig. 3.30 and is denoted as "accept". On the contrary tracks like the one denoted as "reject" are rejected by this criterion. Furthermore, quality criteria on the number of hits in the track ($N_{hit} > 6$) and on the χ^2 ($\chi^2/dof < 10$) of the track are imposed to select only good tracks.

The cross talk can then be measured from the strip charges within clusters originating from the accepted tracks. For the purpose of the cross talk measurement, each cluster is reconstructed from pedestal and CMN subtracted digis with no truncation of strips with negative charge. We reconstruct a cluster by forcing it to have five strips, two on each side around the central one. Then the fraction of shared charge can be computed as

$$x_i = \frac{\eta_{\pm i}}{1 + 2\eta_{\pm 1} + 2\eta_{\pm 2}}, \tag{3.4}$$

with η_i defined as

$$\eta_{\pm i} = \frac{q_{\pm i}}{q_0} = \frac{x_i}{1 - 2x_1 - 2x_2}, \text{ with } i = 1, 2, \tag{3.5}$$

where x_1 is the fraction of charge received by the first neighboring strip, x_2 is the fraction of

charge received by the second neighboring strip and x_0 is obtained from the normalization condition $x_0 = 1 - 2x_1 - 2x_2$. q_0 is the charge on the seed strip and q_i the charge registered by the neighboring strips. The distributions of $q_{\pm1}/q_0$ and $q_{\pm2}/q_0$ are each filled twice per cluster and fitted separately by a Gaussian function, avoiding the tails. The mean values of these functions are inserted in the Eq. 3.4 in order to compute the fraction of charge shared with the neighboring strips. The cross talk depends on the pitch size, strip length and width, and thus it has to be measured separately for each geometry.

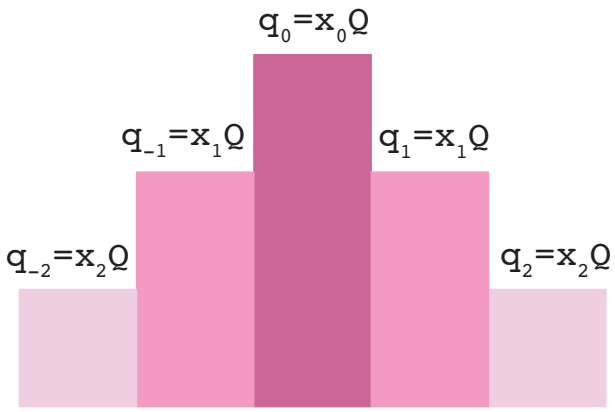

Figure 3.29: A schema of charge sharing between neighboring strips.

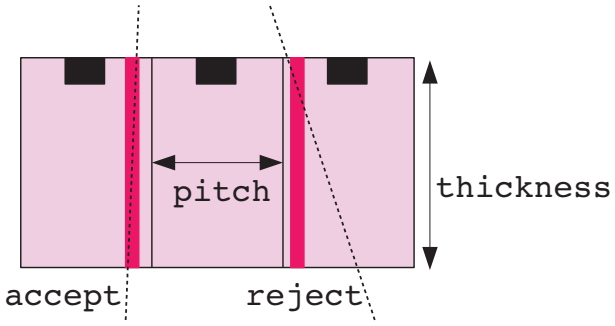

Figure 3.30: A schematic view of the track selection for the cross talk measurement.

3.3.1.3 The dependence of the cross talk on time

As discussed, the observed pulse shapes for the seed strip and the neighboring strips are different and they peak at different time (see Fig. 3.11), leading to the conclusion that the cross talk evolves as a function of time. To test such hypothesis the time information of the muon is required. The time of the muon is given at the interaction point and details about its computation can be found in Section 1.2.5. In the data collected in 2018 two kinds of muons were observed: Ones having hits only in the top part of the DTs as sketched in the left part of Fig. 3.31, further referred to as "top muons", and the other having hits only in the bottom part of the DTs as shown in right part of Fig. 3.31, in later

referred to as "bottom muon". In around 90% of the cases both top and bottom muons are present in one event, as they are two legs of the same muon, but both are associated with a different time.

The goal of this analysis is to find the muons which passed the IP at the same time as a muon in collision would be produced. Having access to the time information it is possible to study the evolution of the cross talk as a function of time. The muon originating from pp collisions would be produced at $time_{IP}^{InOut} = 0$ and would move from the IP outside similarly as the bottom muon. This is not the case for the top muon, which travels from outside towards the IP. There can be two times associated to one track reconstructed in the tracker, one coming from the bottom muon leg and the second from the top muon leg. Only the time of the bottom muon leg is taken into account as this muon leg has the same direction as the muon produced in the pp collision.

As also displayed in the right part of Fig. 3.31, there are two kinds of hits left in the tracker by cosmics: One in the top part of the tracker in green, referred to as "top hits" and others in blue in the bottom part, referred to as "bottom hits". The timing of the tracker, i.e. the sampling of a pulse shape in cosmic events, is the same as in collisions and is tuned for collisions. The situation is simpler for bottom hits, for which in case of the collision and cosmic muon being at the IP at the same time, the arrival time to the given module has to be the same. In case of top hits, the cosmic muon goes from outside towards the given module and then to the IP, while for the collision muon the direction is opposite, it starts at IP and then passes through a given module and continues towards outside of CMS. Therefore in this case both cosmic and collision muons with the same time at the IP reach the given module in the top part of tracker at a different time, specifically the cosmic muon arrives there before the collision one. For this reason of timing mismatch in the top part of the tracker, only hits in the bottom part of the tracker are used.

The distribution of time for the bottom legs of the muons is shown in Fig. 3.32. In principle, the time distribution for cosmic muons should be uniform due to the random arrival time of cosmics to the interaction point. But as mentioned in [87], the trigger efficiency is the highest for muons arriving to the interaction point in a time window of ± 5 ns around the collision time. The time distribution in Fig. 3.32 peaks around -3.5 ns. The muons with a time equal to zero passed the interaction point at the same time that a collision muon would be produced at IP. Twice the standard deviation of the time distribution is 13.2 ns. To evaluate which fraction of the spread is caused by the time resolution in DTs, the timing distribution from DTs of muons produced in collisions is shown in Fig 3.33 with a Gaussian fit. The collision muons are produced at a time equal to zero, therefore there is no ambiguity on the production time as for the cosmic muons.

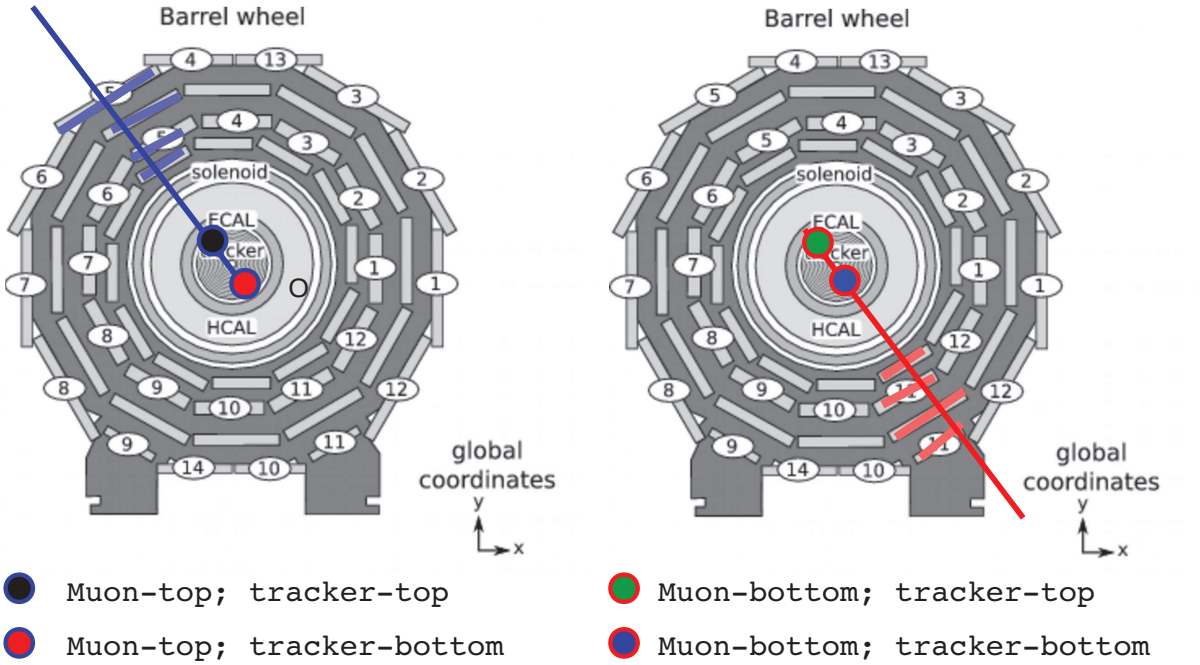

Figure 3.31: A schema of possible configurations of muon legs and hits in the tracker.

But a bias originates from the fact that the muon time is computed with an assumption that muon travels at the speed of light. Twice the standard deviation of the collision muon time computed from the fit gives 3.3 ns. The cosmic muon timing distribution is more than four times larger because of the natural spread in arrival time of the cosmics. Another bias in the time measurement can appear due to the assumption used in the time computation that the muon passes through the interaction point.

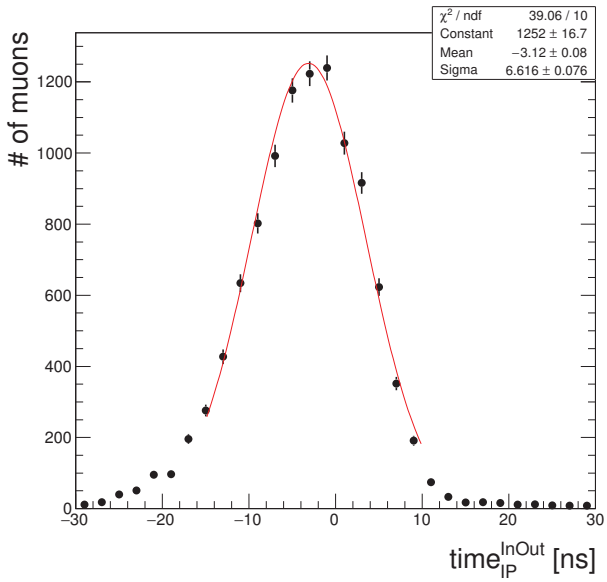

Figure 3.32: The distribution of the time $time_{IP}^{InOut}$ at the IP of the bottom muon legs in 2018 CRUZET VR data. In red is displayed the result of a Gaussian fit.

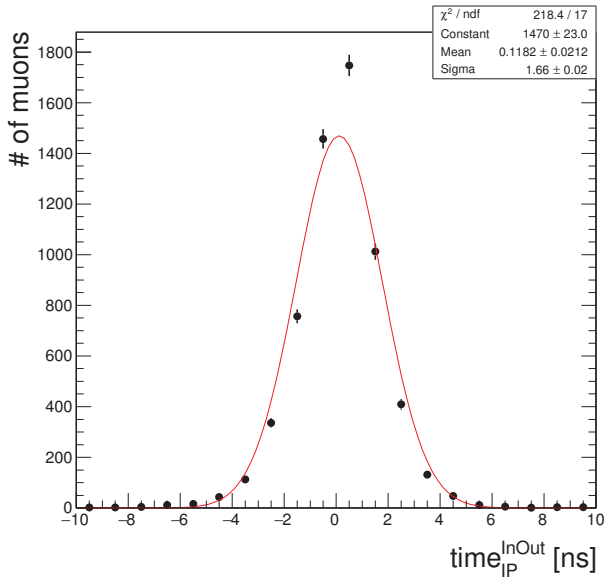

Figure 3.33: Time distribution of muons originating from pp collisions recorded during the 2017 era F. In red is displayed the result of a Gaussian fit.

The timing of the pulse shape sampling in the tracker is tuned in such a way that the cluster seed charge is required to be maximal. Such timing adjustments are done with particles originating from collisions, their production time is thus fixed to zero. Therefore to evaluate if the cosmic muon time is synchronized with the collision one, the cluster seed charge distribution can be studied as a function of the muon time as depicted in the left plot of Fig. 3.34. As mentioned earlier, there is a bias in the time measurement coming from the fact that cosmic muons do not have to pass through the interaction point, but that the muon time computation is extrapolating the muon time to the interaction point. This effect could shift the maximum of the seed charge away from the time equal to zero. We can evaluate what is the dependency of the maximum of the cluster seed charge as a function of the closest distance of track from the IP. This closest distance, further referred only as "distance", is determined as the closest approach distance of the track to the IP. Four different cases of tracks passing at different distances to the IP are shown in Fig. 3.34 (left). It can be noticed that the maxima of the cluster seed charge for the four cases are at different positions and none of them is around 0 ns. All cluster seed charge distributions peak at negative times and larger is the distance, smaller is the corresponding peak time (larger in absolute value). Because of the observed dependence of the maximal cluster seed charge with the distance from the IP, the muon time has to be corrected as a function of this distance. A time correction factor can be estimated from a linear fit of the time positions (t_{max}) of the maxima obtained from the Gaussian fits in the left plot of 3.34 as a function of the distance (d). The fit displayed in the right

plot of Fig. 3.34 is giving the following relation between time and distance

$$t_{max} = (0.05 \pm 0.01) \times d - (7.9 \pm 0.4), \tag{3.6}$$

leading to the conclusion that the cluster seed charge is maximal for muon which passed directly through the interaction point at a time equal to -7.9 ± 0.4. The dependency of the time with the track distance can be resolved by subtracting the factor $0.05 \times d$ from the muon time.

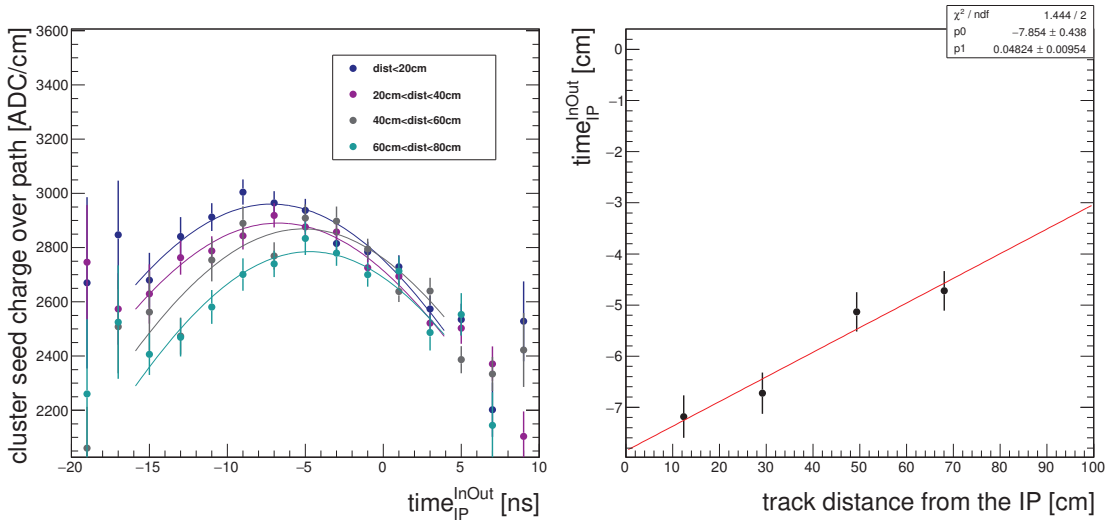

Figure 3.34: (left) The cluster seed charge profiles as a function of time for four different distances of the muon track from the IP in 2018 CRUZET VR data, the results of Gaussian fits are also displayed. (right) The time of the maxima extracted from the fits performed in the left plot as a function of the mean track distance from the IP, these points are fitted with a straight line.

As suggested above, the cross talk depends on time. To prove this hypothesis, the $\eta_{\pm1}$ and $\eta_{\pm2}$ are studied as a function of time. As the available statistics does not allow to consider the $\eta_{\pm1}$ and $\eta_{\pm2}$ distribution per bin of 1 ns, overlapping time windows of 4 ns are used for the muons. The $\eta_{\pm1}$ and $\eta_{\pm2}$ distributions are filled for each time window and then fitted by Gaussians. The estimated means are shown in Fig. 3.35 for the OB2 geometry and allow to evaluate the time evolution of the charge sharing. Each bin of this figure corresponds to the middle of the 4 ns interval in which the fit was performed, for example the time equal to zero is in reality integrated over clusters from muons arriving to the IP in a time window of 0 ± 2 ns. The dependence of $\eta_{\pm1}$ and $\eta_{\pm2}$ as a function of time in Fig. 3.35 confirms that the time window in which to perform the cross talk measurement has to be selected with care. The time window -8 ± 2 ns, for which the cluster seed charge is maximal, is therefore of special interest for the cross talk measurement as it corresponds to the collision conditions. The width of the time window is also close to

the time spread in the DTs shown in Fig. 3.33. The $\eta_{\pm1}$ and $\eta_{\pm2}$ distributions resulting from muons within the -8 ± 2 ns time window are shown in Fig. 3.35, together with the Gaussian fits. The width of these distributions is due to the strip noise. The tails in charge sharing are caused by inclination of track or diffusion.

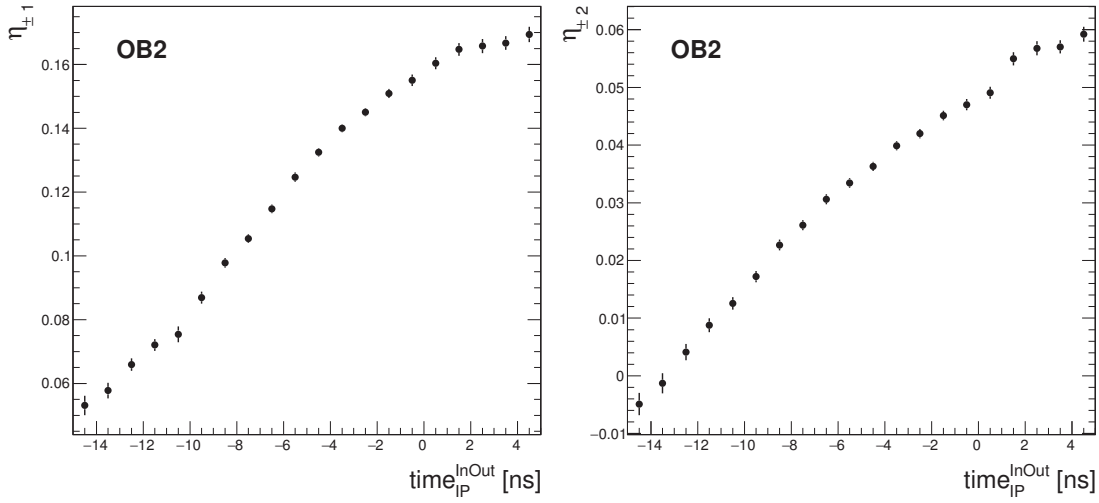

Figure 3.35: The time evolution of the charge shared with the first (left) and second (right) neighboring strips divided by the seed charge for the OB2 geometry in 2018 CRUZET VR data.

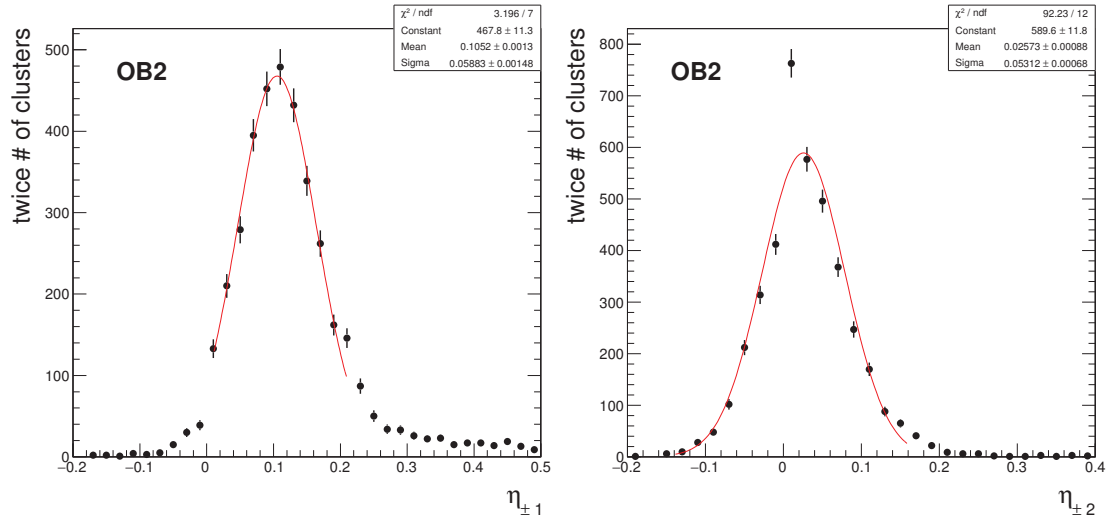

Figure 3.36: The $\eta_{\pm1}$ (left) and $\eta_{\pm2}$ (right) distributions of bottom muon tracks in the time window of -8 ± 2 ns for the OB2 geometry in 2018 VR CRUZET data. The results of Gaussian fits are indicated in red.

3.3.1.4 The results on the cross talk measurement

The cross talk parameters are computed from Eq. 3.4 for all barrel geometries in the time window of -8 ± 2 ns from the Gaussian fits of the corresponding $\eta_{\pm1}$ and $\eta_{\pm2}$ distributions

as shown for OB2 in Fig. 3.36. The measured values together with the values currently used in the simulation corresponding to an old measurement are recorded in Table 3.1. It can be noticed that in all cases the new sharing of the charge, i.e. the cross talk, decreases. There is no information in the documentation if, during the previous cross talk measurement, any timing requirement was taken into account and therefore part of the change can originate from including the time information to evaluate the cross talk. In addition, there is also a real change in the cross talk expected from the radiation effects.

Geometry	Type	x_0	x_1	x_2
IB1	current measurement	0.836 ± 0.009	0.070 ± 0.004	0.012 ± 0.002
IB1	currently in simulation	0.775	0.096	0.017
IB2	current measurement	0.862 ± 0.008	0.059 ± 0.003	0.010 ± 0.002
IB2	currently in simulation	0.830	0.076	0.009
OB2	current measurement	0.792 ± 0.009	0.083 ± 0.003	0.020 ± 0.002
OB2	currently in simulation	0.725	0.110	0.027
OB1	current measurement	0.746 ± 0.009	0.100 ± 0.003	0.027 ± 0.002
OB1	currently in simulation	0.687	0.122	0.034

Table 3.1: The cross talk measured in 2018 CRUZET VR data and the cross talk values used currently in simulation for barrel geometries.

Ref. [88] discusses that, due to the surface radiation damages of the silicon strip sensors, the inter–strip capacitance increase and inter–strip resistance decrease, and consequently an increase in cross talk is expected. In the presented measurement a decrease of the cross talk is observed contrary to the literature. The cross talk change can also depend on the change of the strip implant to backplane capacitance, of the strip implant to the aluminium strip capacitance, and of the depletion and applied voltages. Therefore the expected direction of the cross talk change is difficult to evaluate as one could thus assume that the other capacitances may have changed as well.

3.3.1.5 Validation of the new cross talk parameters

To evaluate if the new cross talk measurement contributes to an improvement in the data and simulation comparison, the cross talk parameters are injected into the simulation and compared with data and the default simulation. For this validation the 2018 minimum bias simulated samples and 2018 zero bias data from run 317649 are used. The cluster charge, width and seed charge distributions for barrel geometries are shown in Fig. 3.37 to 3.42. In these plots it is obvious, that newly measured cross talk parameters largely improve the overall cluster width and seed charge description. The cluster charge remains almost unchanged, as the cross talk influences only the charge sharing between channels, not the total charge.

For OB2, the measured cross talk fractions (x_0, x_1, x_2) are (0.792±0.009, 0.083±0.003, 0.020±0.002). When tuning the cross talk parameters in Section 3.2.4 to best describe the cluster width in data, the best obtained fractions are (0.814, 0.070, 0.023), which suggest even a smaller cross talk than the measured one, but no uncertainties were evaluated for these tuned parameters.

Even though the large improvement, there are still discrepancies in the description of data by simulation. These discrepancies could be caused by the outdated conditions, such as gains and noise. These conditions can have an impact on the cluster width, charge and seed charge description and therefore they are as well being currently updated. The discrepancies can also arise from the fact that the simulation is simplified and many parameters in the simulation are outdated as discussed previously. Thus the cross talk in simulation does not have to purely describe the cross talk itself, but it can compensate for other effects as well.

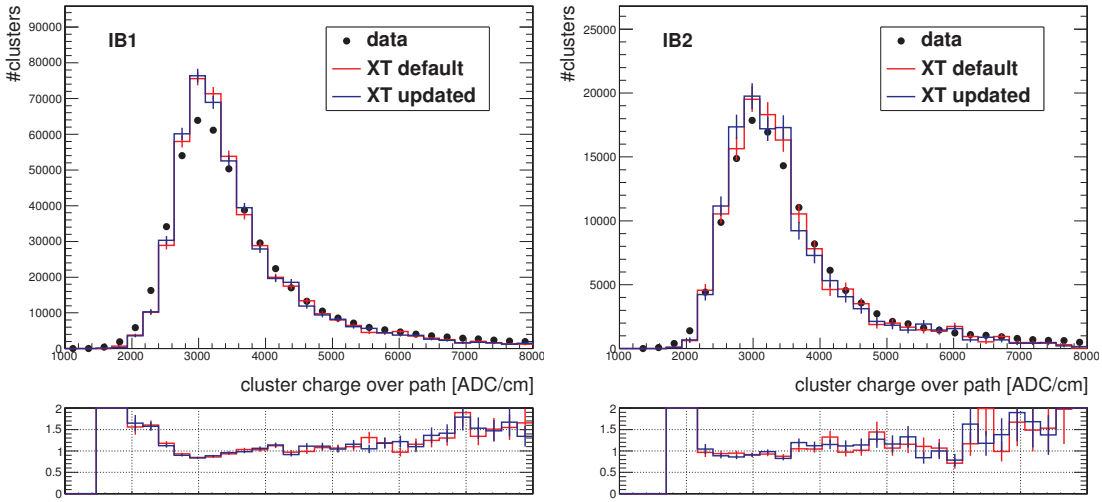

Figure 3.37: Distribution of the on-track cluster charge in data and simulation for the IB1 (left) and IB2 (right) geometries for the current (default) and newly measured (updated) cross talk parameters (XT). The simulated distributions are rescaled to the number of clusters in data. The bottom plots represent data to simulation ratios.

3.3.1.6 The cross talk evolution with tracker ageing

Fig. 3.43 shows the ratio of the new x_1 parameter to the default value used in the simulation for the four barrel geometries as a function of the distance from the beamline. This ratio is fitted by a straight line. From the slope of 0.0012 ± 0.0005 it can be seen that the change in the parameter x_1 depends on the distance of a geometry from the beamline and is the largest for the closest geometry. As the fluence of particles decreases as a function of distance from the beamline, the closest geometry suffers therefore from the

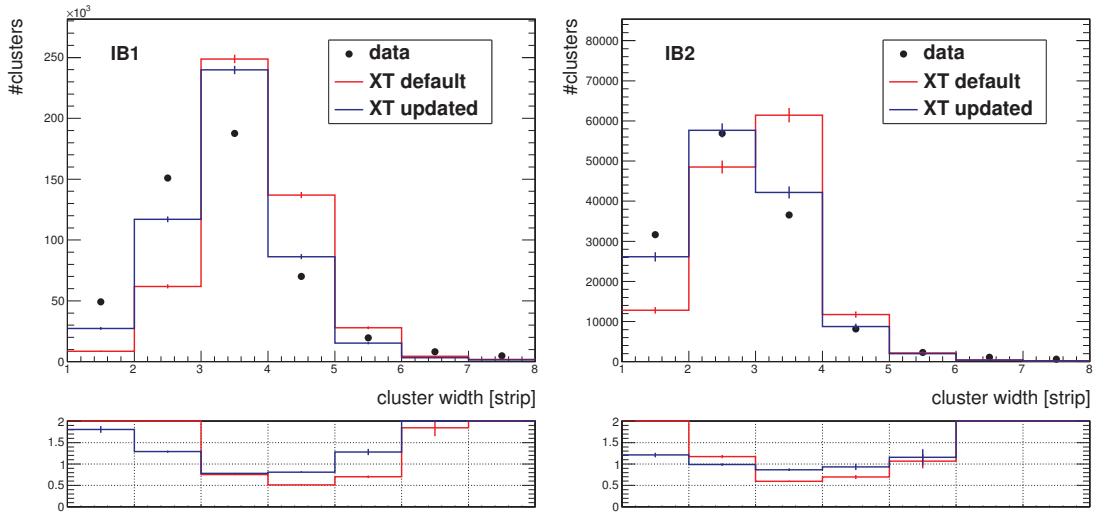

Figure 3.38: Distribution of the on-track cluster width in data and simulation for the IB1 (left) and IB2 (right) geometries, for the current (default) and newly measured (updated) cross talk parameters (XT). The simulated distributions are rescaled to the number of clusters in data. The bottom plots represent the data to simulation ratios.

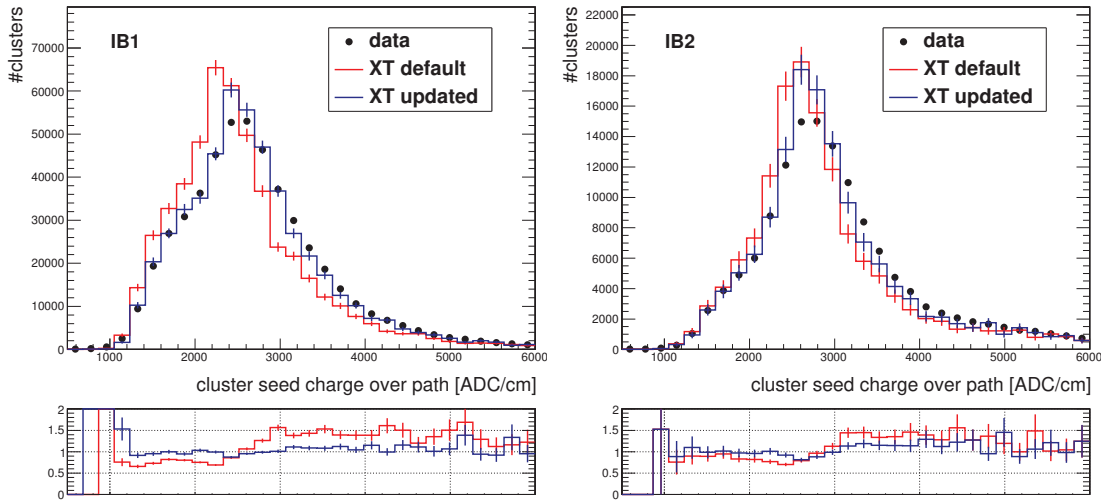

Figure 3.39: Distribution of the on-track cluster seed charge in data and simulation for the IB1 (left) and IB2 (right) geometries, for the current (default) and newly measured (updated) cross talk parameters (XT). The simulated distributions are rescaled to the number of clusters in data. The bottom plots represent the data to simulation ratios.

largest fluence, its radiation damage is the largest and consequently its cross talk change is the largest.

But the sensors in different geometries are not the same and therefore for a given fluence the radiation damage of different sensors is different. To decouple the two effects and evaluate purely the fluence dependence, the cross talk can be studied for different layers of a single geometry. The time dependence of the $\eta_{\pm 1}$ and $\eta_{\pm 2}$ distributions is shown

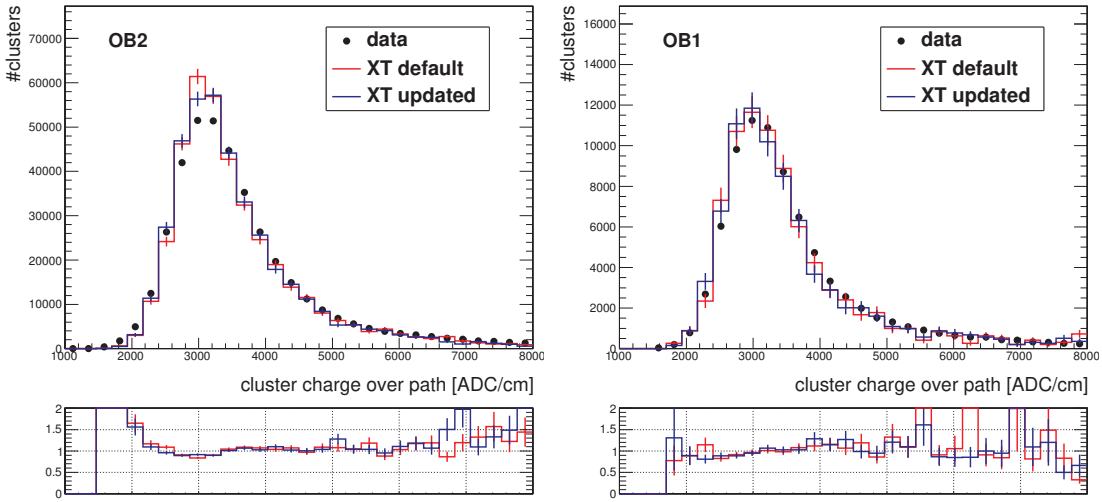

Figure 3.40: Distribution of the on-track cluster charge in data and simulation for the OB2 (left) and OB1 (right) geometries, for the current (default) and newly measured (updated) cross talk parameters (XT). The simulated distributions are rescaled to the number of clusters in data. The bottom plots represent the data to simulation ratios.

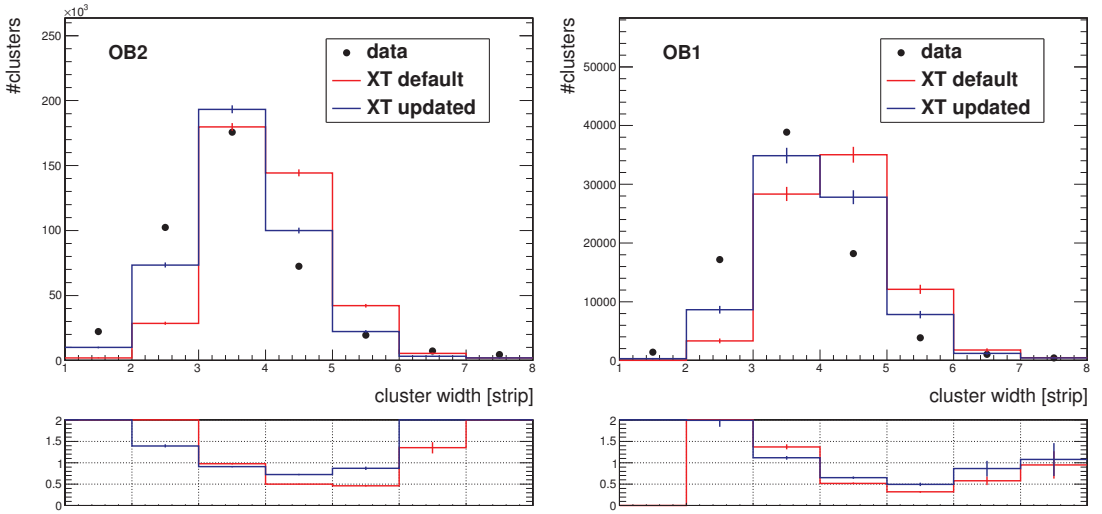

Figure 3.41: Distribution of the on-track cluster width in data and simulation for the OB2 (left) and OB1 (right) geometries, for the current (default) and newly measured (updated) cross talk parameters (XT). The simulated distributions are rescaled to the number of clusters in data. The bottom plots represent the data to simulation ratios.

in Fig. 3.44 for the four layers of OB2 separately. The plots were obtained similarly as the plots in Fig. 3.35, but this time the time window for each bin is 6 ns in order to gain in statistics. The charge sharing is larger for the first two layers, compared to the layers three and four. In $\eta_{\pm 1}$ distribution there is also a visible difference in the charge sharing between layer three and four, whose ratio varies from one by up to $\pm 10\%$.

The first two layers are composed of double-sided modules, while the second two have

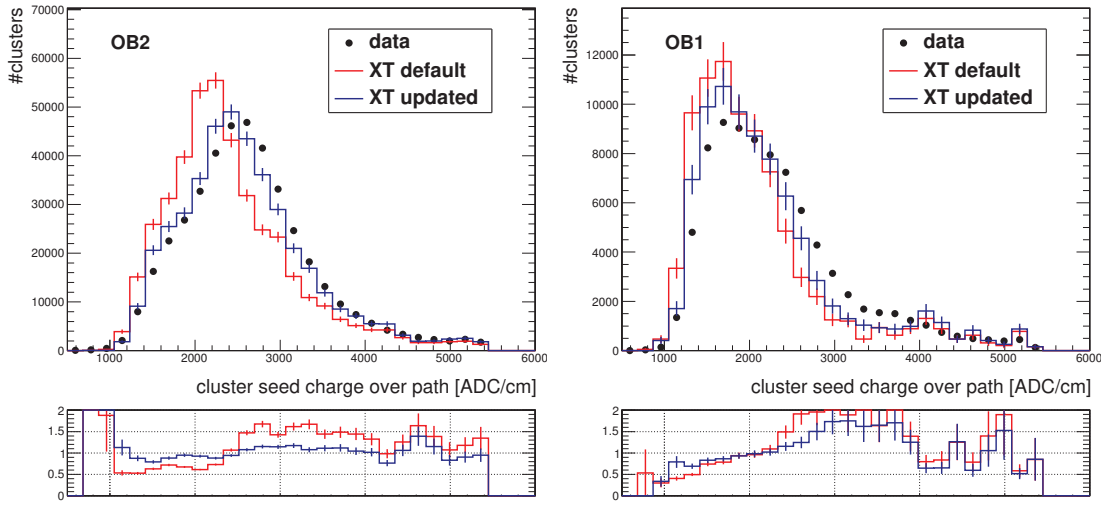

Figure 3.42: Distribution of the on-track cluster seed charge in data and simulation for the OB2 (left) and OB1 (right) geometries, for current (default) and newly measured (updated) cross talk parameters (XT). The simulated distributions are rescaled to the number of clusters in data. The bottom plots represent the data to simulation ratios.

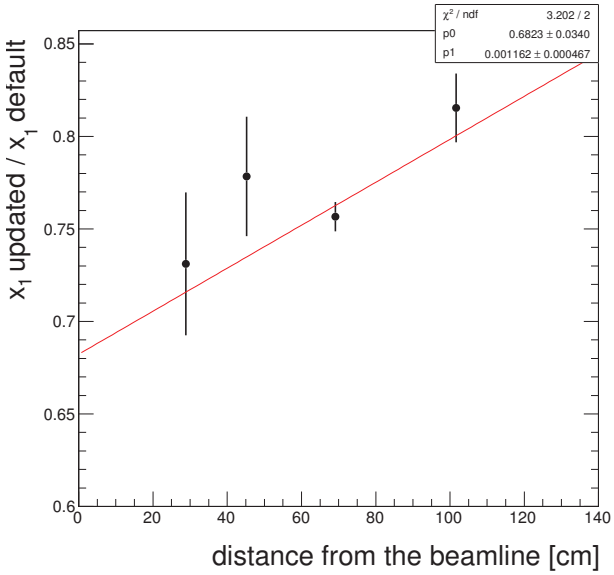

Figure 3.43: The ratio of the new measurement of the x_1 parameter (updated) to the default value currently used in simulation (default) as a function of the distance from the beamline of the four different barrel geometries. The result of a linear fit is indicated in red.

only one side of sensors. In the double-sided modules, the sensors are back to back, therefore a particle going from the IP outside the CMS is entering one sensor from the side of the strips and the second from the backplane. The formation of the signal could be different depending from which side the particle enters the sensor and therefore there can be a different cross talk between the mono and stereo sides of one module. The $\eta_{\pm1}$ and $\eta_{\pm2}$ as a function of time, for decomposed mono and stereo sensors of modules in the

OB2 layers one and two are shown in Fig. 3.45. In these plots, in the majority of bins of the $\eta_{\pm1}$ and $\eta_{\pm2}$ distributions, the sharing for modules in one layer is similar or larger for stereo sensors than mono. This would explain that the first two layers of OB2, which are composed of double-sided modules, exhibit a larger charge sharing to the first neighboring strips than the second two, which are single-sided, as discussed in Fig. 3.44.

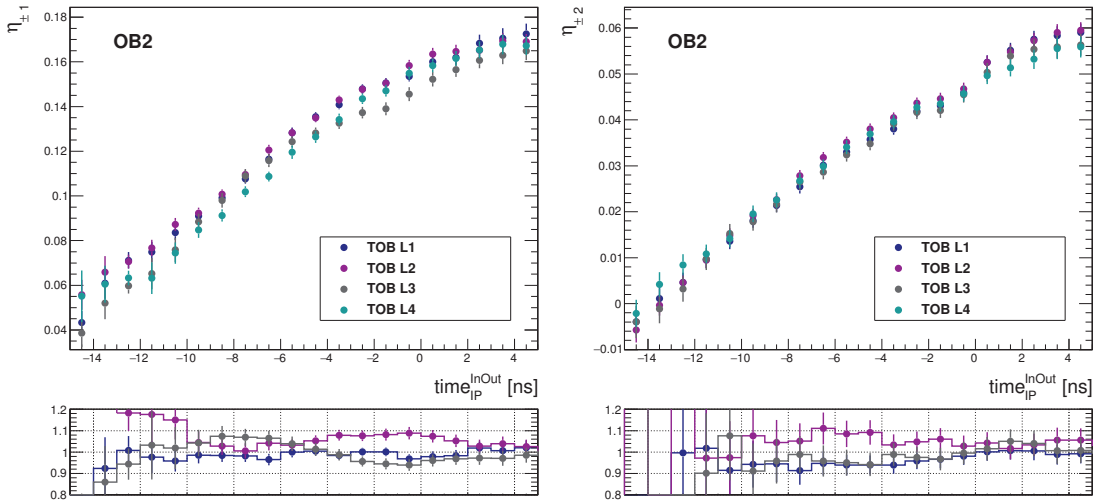

Figure 3.44: The time evolution of the charge carried by the first (left) and second (right) neighboring strips divided by the seed charge for the four layers of the OB2 geometry in the 2018 CRUZET VR data. The ratio plots are shown in the bottom, the blue line corresponds to the ratio of L1 to L2, the violet line corresponds to the ratio of the L2 to L3, and the gray line corresponds to the ratio of the L3 to L4 distributions.

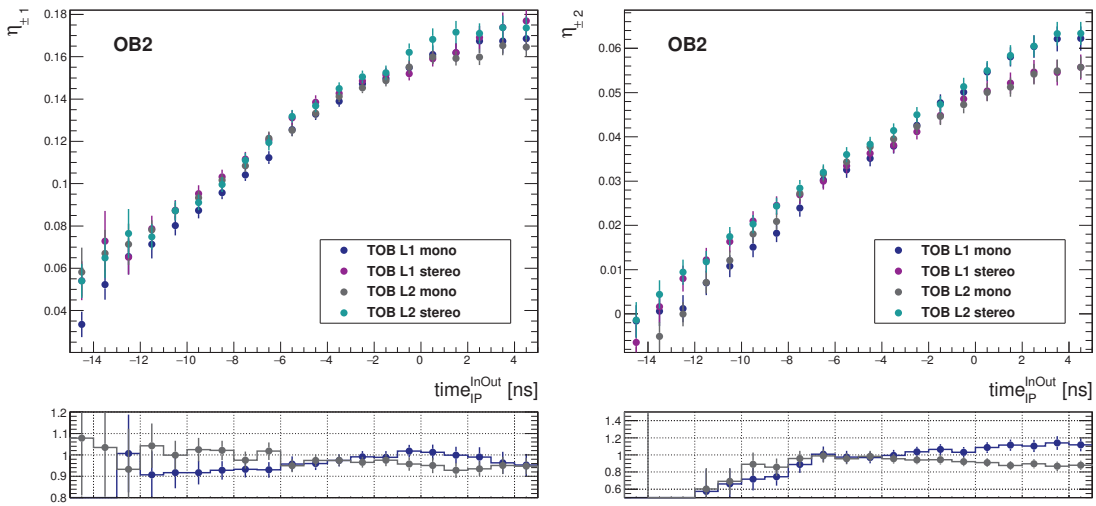

Figure 3.45: The time evolution of the charge carried by the first (left) and second (right) neighboring strips divided by the seed charge for the mono and the stereo sensors of first two layers of TOB in the 2018 CRUZET VR data. The ratio plots are shown in the bottom, the blue line corresponds to the ratio of L1 mono to stereo, and the gray line corresponds to the ratio of the L2 mono to stereo distributions.

3.3.2 The cluster seed charge evolution with time

With the data used for the cross talk measurement, it is also possible to study the evolution of the charge on the seed strip and the neighboring strips as a function of the muon arrival time as shown in Fig. 3.46. These charge evolutions can be compared to the past measurements of the pulse shapes depicted in Fig. 3.11, obtained from focusing a laser on one strip of the TOB module. In order to compare these figures, the time axis of the Fig. 3.11 should be reverted (from positive to negative values) so that it represents the muon arrival time. Indeed a muon which arrives with a positive delay with respect to the reference (i.e. after the reference) is on the rising part (on the left) of its pulse shape and has not yet reached its maximum. Similarly to the past measurement, the neighboring strips peak at the higher arrival times than the seed one, what corresponds to the earlier positions at the pulse shapes. Moreover, negative contributions are observed for the second neighboring strips, the time range not being sufficient to observe a similar behavior for the first neighbors. This undershoot is also clearly visible in Fig. 3.11. The ratio of the maximal charge on the first to the second neighboring strip is similar for both measurements, around three. However, there is a large difference between these two measurements in the ratio of the maximal charge of the first neighbors to the seed strip: This ratio is around three for the past measurement, but around five for the current measurement.

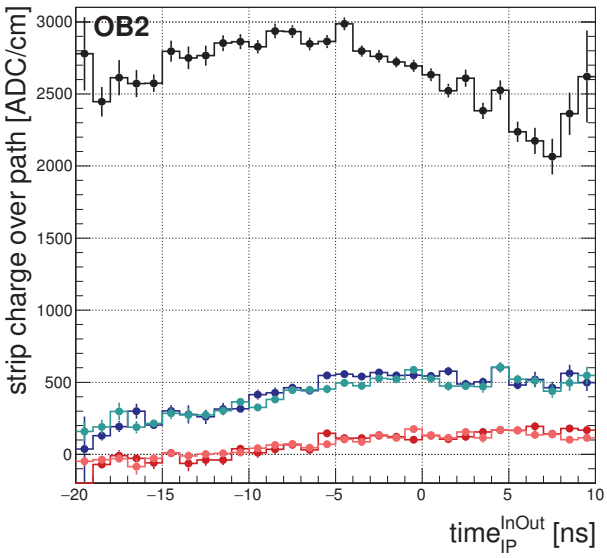

Figure 3.46: The charge on the strip for the seed strip and two neighbors on each side for the OB2 geometry. The black curve corresponds to the seed strip, blue and red curves to the first and second neighboring strips respectively. The neighbors on the left side from the seed are depicted in the lighter shades.

3.3.3 Evaluation of the cross talk for TID and TEC

Because of the insufficient statistics of clusters for TID and TEC in the available CRUZET VR data, the cross talk for these partitions had to be evaluated differently. For the barrel, the change of x_1 scales linearly with the distance from the beamline and it can be expected that the same applies for TID and TEC. But the fluence and module geometries in TID and TEC are more complicated than in the case of the barrel and the x_1 change for the TID and TEC does not evolve linearly as a function of distance from beamline. Moreover there is no guarantee that the cross talk currently used in simulation is correct.

The change in cross talk in the TID and TEC rings can be studied in the cluster seed charge distribution, which is a direct proxy to the x_0 parameter. The data to simulation ratio of the mean cluster seed charge is shown in Fig. 3.47. The ratio is always larger than one, revealing that the mean seed charge is larger in data than in simulation and consequently the charge sharing is smaller in data than in simulation. No clear trend as a function of the distance from the beamline is observed in this ratio.

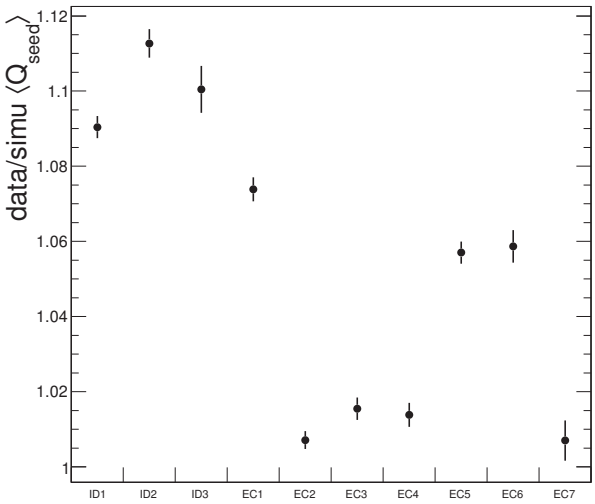

Figure 3.47: The data to simulation ratio of the mean cluster seed charge for rings of TID and TEC.

As the cluster seed charge is a proxy to x_0, the updated x_0^u can be evaluated as

$$x_0^u = \frac{\langle Q_{seed}^{data} \rangle}{\langle Q_{seed}^{simu} \rangle} x_0^d, \tag{3.7}$$

where $\langle Q_{seed}^{data} \rangle$ and $\langle Q_{seed}^{simu} \rangle$ are the mean cluster seed charge in data and simulation, respectively, and x_0^d is the default value of x_0 currently used in simulation.

The change of x_2 is found to be constant for all the barrel geometries and it is evaluated

from a fit to be 0.76. We decided to apply this factor to rescale x_2 in TID and TEC. The updated value x_2^u is computed as

$$x_2^u = 0.76\ x_2^d, \tag{3.8}$$

with x_2^d being the default value of x_2 currently used in simulation. The x_2 parameter is small in absolute and therefore the other parameters do not largely depend on it.

The updated value of x_1 can then be evaluated from the normalization condition $x_1 = (1 - x_0 - 2x_2)/2$. The updated values of cross talk can be seen in Table. 3.2.

Geometry	Type	x_0	x_1	x_2
W1a	new values	0.8571	0.0608	0.0106
W1a	currently in simulation	0.786	0.093	0.014
W2a	new values	0.8861	0.049	0.008
W2a	currently in simulation	0.7964	0.0914	0.0104
W3a	new values	0.8984	0.0494	0.0014
W3a	currently in simulation	0.8164	0.09	0.0018
W1b	new values	0.8827	0.0518	0.0068
W1b	currently in simulation	0.822	0.08	0.009
W2b	new values	0.8943	0.0483	0.0046
W2b	currently in simulation	0.888	0.05	0.006
W3b	new values	0.8611	0.0573	0.0121
W3b	currently in simulation	0.848	0.06	0.016
W4	new values	0.8881	0.0544	0.0015
W4	currently in simulation	0.876	0.06	0.002
W5	new values	0.7997	0.077	0.0231
W5	currently in simulation	0.7566	0.0913	0.0304
W6	new values	0.8067	0.0769	0.0198
W6	currently in simulation	0.762	0.093	0.026
W7	new values	0.7883	0.0888	0.0171
W7	currently in simulation	0.7828	0.0862	0.0224

Table 3.2: The updated cross talk for rings of TID and TEC.

The validation plots of the cluster charge, width and seed charge are shown in Figs. 3.48 to 3.50 for two chosen examples which are W1a (left) and W5 (right). By definition of the cross talk update procedure there is an improvement in the description of the cluster seed charge. The updated cross talk also leads to the large improvement in the description of the cluster width.

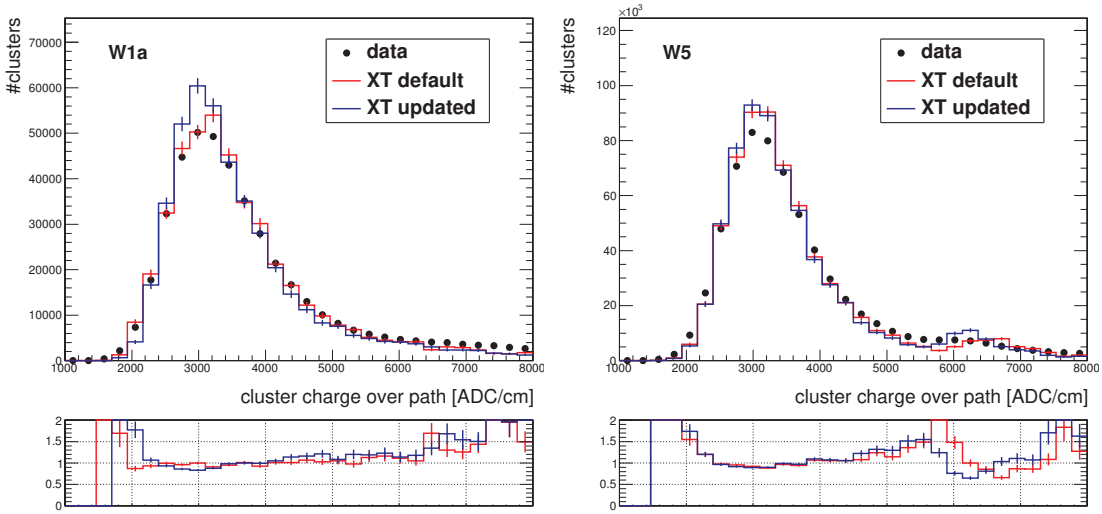

Figure 3.48: Distribution of the on-track cluster charge in data and simulation for the W1a (left) and W5 (right) geometries, for current (default) and newly updated cross talk parameters (XT). The simulated distributions are rescaled to the number of clusters in data. The bottom plots represent the data to simulation ratios.

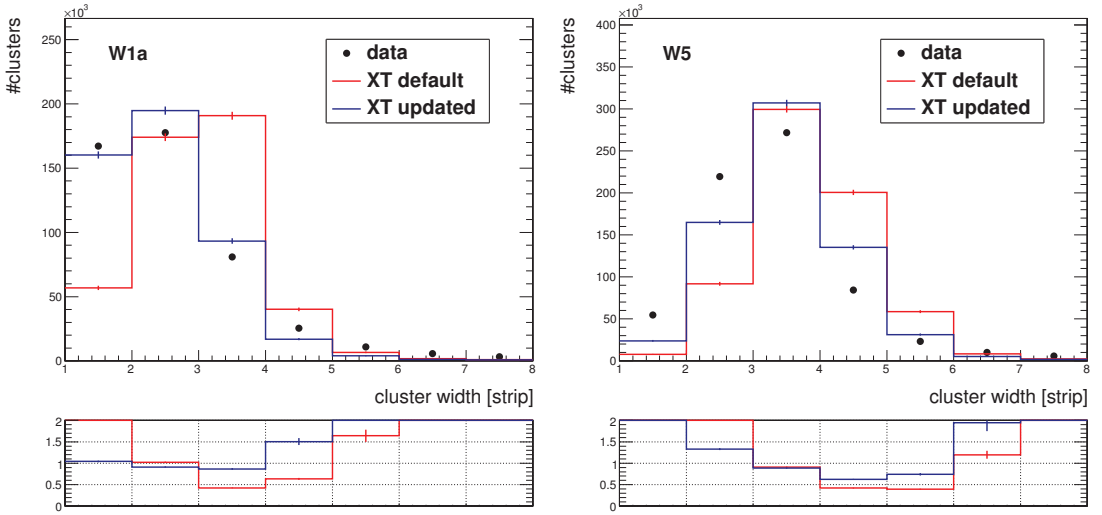

Figure 3.49: Distribution of the on-track cluster width in data and simulation for the W1a (left) and W5 (right) geometries, for the current (default) and newly updated cross talk parameters (XT). The simulated distributions are rescaled to the number of clusters in data. The bottom plots represent the data to simulation ratios.

3.3.4 Conclusion

This section presents the results of a new cross talk measurement. The cross talk parameters used in simulation were measured at the beginning of Run 1, and as demonstrated in this section, the cross talk changes with the ageing of the detector, therefore it had to be remeasured. We show that the cross talk depends on the particle arrival time to the module, which probably was not taken into account during the Run 1 measurements.

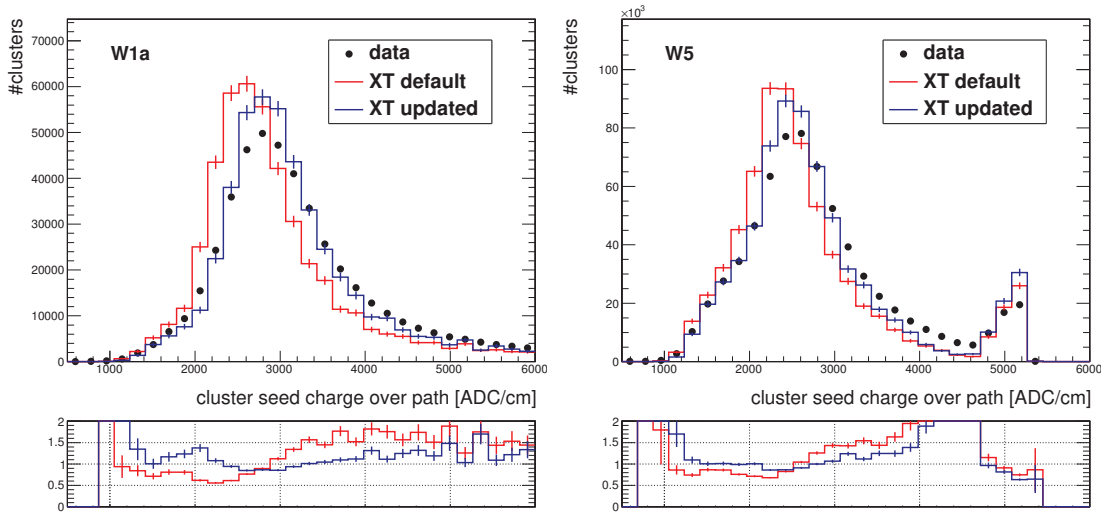

Figure 3.50: Distribution of the on-track cluster seed charge in data and simulation for the W1a (left) and W5 (right) geometries, for the current (default) and newly updated cross talk parameters (XT). The simulated distributions are rescaled to the number of clusters in data. The bottom plots represent the data to simulation ratios.

The newly measured cross talk improves the description of the cluster seed charge and width in simulation although discrepancies between data and simulation can still be observed. These discrepancies can be caused by the outdated database conditions and therefore they are being updated for the 2018 simulated samples. If after the update of database conditions some discrepancies remain between data and simulation, it can be the sign that the simulation is over-simplified and that the update of the cross talk is not sufficient to well describe the cluster properties in data.

Due to the limitations of the 2018 CRUZET VR data, it is not possible to measure the cross talk in the disks and endcaps. A newly designed procedure to update the cross talk parameters in these regions rescales the cross talk currently used in simulation by well motivated factors.

The new obtained cross talk parameters considerably improve the cluster width and seed charge description and therefore they are now integrated into the official release of the CMS software and are going to be used for the central production of the simulated samples. The impact of the cross talk change on the high level objects is not expected to be large as the cluster charge remains the same and only the charge sharing differs, but there could be a non-negligible impact on tracking due to several reasons. Because of the different charge sharing and threshold effects in the clustering, the hit position computation can give different results, this has an impact on the tracking. The change of the hit position and cluster width also influences the hit resolution, from which the cluster position error used in the tracking is calculated. Due to the reduced cluster width,

previously merged clusters might be distinguished, which is also influencing tracking. Because of the decrease of the cluster width and the smaller sharing of the charge, the OOT PU clusters which did not pass the clustering threshold can pass it now and vice versa, again playing a role in tracking.

Chapter 4

Supersymmetry as a possible extension of the standard model

In this chapter the basics of the standard model are discussed. In section 4.1 the description of the elementary particles and interactions is presented as well as an idea on how the standard model was derived. This section ends with a discussion of several shortcomings of the standard model, which motivate physicists to formulate beyond the standard model theories. Section 4.2 then describes supersymmetry (SUSY), which is a promising extension of the standard model, due to its ability to solve many of the standard model issues. In this section, the results of the Run 1 SUSY searches are also presented.

4.1 The standard model and its shortcomings

The Standard Model (SM) of particle physics is based on Quantum Field Theory (QFT) and gauge symmetries [89]. It was developed during 1960's, finished in 1970's, but it was only in 2012 that the last predicted particle of the SM, the Higgs boson, was discovered by the ATLAS and CMS collaborations [90, 91]. The SM describes all fundamental interactions (except gravity), namely the electromagnetic, weak, and strong interactions, and characterizes all known elementary particles.

The interactions in the SM are mediated via an exchange of (gauge) bosons which have an integer spin. There are 12 bosons with a spin of one. The mediators of the electromagnetic and weak interactions are the massless photon γ and the massive $W^{\pm}$ and Z bosons, respectively. The $W^{\pm}$ and Z bosons acquire their mass through a spontaneous breaking of the electroweak symmetry as explained later in the text. The gauge bosons of the strong interaction are eight massless gluons, each holding an unique color charge which is a combination of one color and one anticolor. The gluons are massless, indicating

that the strong symmetry is unbroken. The last boson belonging to the SM is a scalar boson, the Higgs boson, which arises from the electroweak symmetry breaking.

In addition to bosons, the particles of matter are fermions, thus carrying half integer spin. Fermions can be divided into leptons and quarks. There are three generations of leptons formed respectively by the electron e, the muon μ, and the tau τ, with their corresponding neutrinos (ν_e, ν_μ, ν_τ). Leptons have an integer charge (0, 1) of $\pm e$ with e being the elementary electric charge and do not carry any charge of color. Therefore they interact only via electromagnetic and weak interactions as they can have non-zero quantum numbers with respect to these interactions, which are the weak isospin (t_3) and hypercharge Y. There are also three generations of quarks, the first one is formed by up (u) and down (d) quarks, the second by charm (c) and strange (s) quarks and the third one by top (t) and bottom (b) quarks. The u, c, t quarks have a charge of $2/3$ e while the d, s, b quarks have a charge of $-1/3$ e. Each quark exists in three color versions (red, green and blue) and thus quarks can participate in the strong interaction. Quarks can hold weak isospin and hypercharge and thus they can also interact via electromagnetic and weak interactions. Due to the phenomena referred to as "color confinement" [92], quarks are always bound inside a composite object called "hadron" and cannot be found isolated in nature. This is true for all quarks except top quark which decays before the hadronization. Each SM fermion has an antiparticle denoted with a bar over its symbol. The antiparticle differs from the particle by the sign of its charge and its projection of the spin to the z-axis. The overview of all SM particles can be seen in Fig. 4.1.

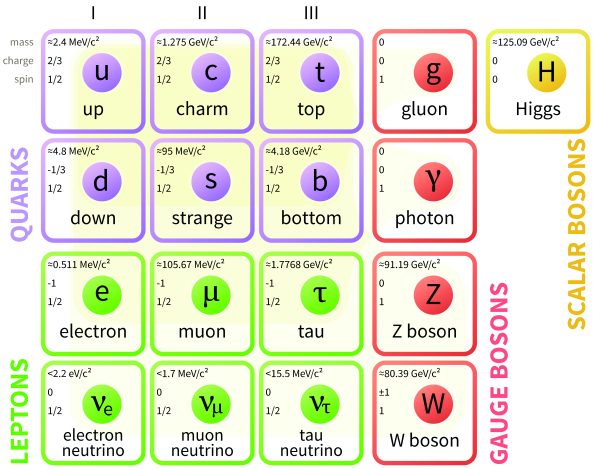

Figure 4.1: Overview of the particles present in the standard model.

The symmetry group of the SM is

$$SU(3)_C \otimes SU(2)_L \otimes U(1)_Y, \tag{4.1}$$

where C stands for the color charge of the strong interaction, L for left-handed particles, which have, unlike the right-handed ones, a non-zero weak isospin, and Y represents the weak hypercharge. The SM group and the interactions originating from it, are discussed part by part in the following sections 4.1.1 to 4.1.4. As the standard model is a field theory which requires invariance towards certain transformations of its Lagrangian, to better understand the derivation and the features of the SM, the basics of the quantum field theory and gauge transformations are described in the following sections. Finally, the last Section 4.1.5 presents the shortcomings of the SM.

4.1.1 Quantum field theory and gauge symmetries

In classical mechanics, the motion of a given system can be calculated by solving the Euler-Lagrange equation [93]. This equation can be generalized in order to build a relativistic theory, in which the space and time coordinates must be treated similarly. In the relativistic case, the Euler-Lagrange equation is given by the formula

$$\partial_\mu \left(\frac{\partial \mathcal{L}}{\partial(\partial_\mu \phi_i)} \right) = \frac{\partial \mathcal{L}}{\partial \phi_i}, \tag{4.2}$$

where the physics describing the system is contained in the Lagrangian $\mathcal{L}$ which depends on the fields ϕ_i and their space-time derivatives $\partial_\mu \phi_i$.

In the case of a scalar (spin-0) field, the Lagrangian $\mathcal{L}_{KG}$ can be written in the form

$$\mathcal{L}_{KG} = \frac{1}{2}(\partial_\mu \phi)(\partial^\mu \phi) - \frac{1}{2}\left(\frac{mc}{\hbar}\right)^2 \phi^2, \tag{4.3}$$

where ϕ is a single scalar field, m is its mass, $\hbar$ is the Planck constant and c is the speed of light. From now on, the standard convention of $\hbar = c = 1$ is used. The scalar field Lagrangian defined in Eq. 4.3 and plugged into the Euler-Lagrange Eq. 4.2 gives the Klein-Gordon equation

$$\partial_\mu \partial^\mu \phi + m^2 \phi = 0, \tag{4.4}$$

which describes a scalar particle of mass m.

The field of a half-spin particle is a four-component spinor field ψ. The Euler-Lagrange

equation applied on the field $\bar{\psi}$, using the Lagrangian $\mathcal{L}_D$

$$\mathcal{L}_D = i\bar{\psi}\gamma^\mu\partial_\mu\psi - m\bar{\psi}\psi \tag{4.5}$$

where γ_μ are the Dirac matrices, gives the Dirac equation describing a half-spin particle of mass m:

$$i\gamma^\mu\partial_\mu\psi - m\psi = 0. \tag{4.6}$$

Equations for particles with spin one can be derived similarly.

In the above Lagrangians defined by Eq. 4.3 and 4.5, only non-interacting fields are present. To include interactions between fields, the impact of local and global transformations of the fields on the corresponding Lagrangian must be studied. The Dirac Lagrangian given by Eq. 4.5 is invariant under the global phase transformation

$$\psi \to e^{i\theta}\psi, \tag{4.7}$$

with the phase θ being an arbitrary real number. But this Lagrangian is not invariant under the local phase transformation

$$\psi \to e^{i\theta(x)}\psi, \tag{4.8}$$

where the phase $\theta(x)$ is this time dependent on the space-time coordinate x. To preserve the invariance of the Lagrangian of Eq. 4.5, the term

$$-(q\bar{\psi}\gamma^\mu\psi)A_\mu, \tag{4.9}$$

with the field A_μ which transforms as

$$A_\mu \to A_\mu + \partial_\mu\lambda \tag{4.10}$$

can be added to the Dirac Lagrangian. The field A_μ is a new vector (spin-1) field. To obtain the full Lagrangian, the free field Lagrangian for the vector field A_μ must also be added to the Dirac Lagrangian in Eq. 4.5. The summed Lagrangian is locally invariant only in the case when the field A_μ is massless and therefore the term for the free field Lagrangian of the field A_μ can be written as

$$\frac{-1}{4}F^{\mu\nu}F_{\mu\nu}, \text{ where } F^{\mu\nu} \equiv \partial^\mu A^\nu - \partial^\nu A^\mu. \tag{4.11}$$

The total Lagrangian is then

$$i\bar{\psi}\gamma^{\mu}\partial_{\mu}\psi - m\bar{\psi}\psi - \frac{1}{4}F^{\mu\nu}F_{\mu\nu} - (q\bar{\psi}\gamma^{\mu}\psi)A_{\mu}, \tag{4.12}$$

which generates the quantum electrodynamics (QED), where the field A_{μ} corresponds to the electromagnetic potential.

The global transformation of a field ψ can be understood as the multiplication of this field by an unitary matrix U ($\psi \rightarrow U\psi$). In the given example of quantum electrodynamics, the size of matrix is 1×1 and therefore the symmetry of this theory is referred to as "$U(1)$ gauge invariance" as the group of all such matrices is $U(1)$. A similar strategy of a local phase invariance of the Lagrangian can be applied on other groups, which was found to be the way how to generate the standard model.

4.1.2 The electroweak interaction

In 1954, Yang and Mills [94] applied local invariance on the $SU(2)$ group to describe the weak interaction and later Glashow, Salam and Weinberg [95, 96, 97] showed, that if the group $SU(2) \otimes U(1)$ is considered, the weak and electromagnetic interactions can be unified. Moreover they separated the left and right chiral components of the fermion fields. The doublet Ψ_L is composed by two left-handed fermion field spinors corresponding to the left-handed charged lepton and its corresponding neutrino. The singlet Ψ_R consists of one right-handed fermion field spinor. The locally invariant Lagrangian of the electroweak (EW) interaction (without symmetry breaking) can be written as the following

$$\mathcal{L}_{EW} = -\frac{1}{4}\sum_{a=1}^{3} F^{a}_{\mu\nu}F^{a\mu\nu} - \frac{1}{4}B_{\mu\nu}B^{\mu\nu} + i\bar{\Psi}_L\gamma^{\mu}D_{\mu}\Psi_L + i\bar{\Psi}_R\gamma^{\mu}D_{\mu}\Psi_R, \tag{4.13}$$

where D_{μ} is the covariant derivative, the tensors $F_{\mu\nu}$ are composed of the vector fields W^{a}_{μ} and their derivatives, and the tensor $B_{\mu\nu}$ is composed of the derivatives of the vector field B_{μ}, similarly as shown in Eq. 4.11.

In the case of the $SU(2)$ group the covariant derivative D_{μ} is

$$D_{\mu} = \partial_{\mu} - ig\sum_{a=1}^{3} t^{a}W^{a}_{\mu}, \text{ with } a = 1, 2, 3. \tag{4.14}$$

The matrices t^{a} are the generators of the $SU(2)$ group composed by Pauli matrices and g is a constant. The t_3 component is called the weak isospin. The covariant derivative D_{μ}

for the $U(1)$ group is

$$D_\mu = \partial_\mu - ig'YB_\mu, \tag{4.15}$$

where Y is the weak hypercharge and g' is a constant. The charge Q of a particle is then given by the relation between its weak isospin and hypercharge: $Q = t_3 + \frac{1}{2}Y$.

The group of the electroweak interaction is often denoted as $SU(2)_L \otimes U(1)_Y$, where L is related to the difference of behavior between left-handed (doublet) and right-handed (singlet) fields w.r.t. the weak interaction. This group produces two massless gauge fields W^1 and W^2 which mix and create the W^+ and W^- bosons. These bosons interact only with the left-handed components of the fermion field (maximum parity violation). The remaining W^3 and B gauge fields interact with both the left- and right-handed fermions and they mix into the Z boson and the photon γ. As mentioned previously all these bosons have to be massless in order to preserve gauge invariance, but the $W^\pm$ and Z bosons were expected to be massive because the weak interaction is a short range interaction. Later, the discovery of the $W^\pm$ and Z bosons confirmed that they are massive and have masses of 80 GeV and 91 GeV respectively. Because these bosons are massive, the electroweak symmetry must be broken. It is also important to note that the EW Lagrangian gives a maximum parity violation for neutrinos because only the left component of the neutrino field exists.

4.1.3 Quantum Chromodynamics

The theory of strong interaction, called Quantum Chromodynamics (QCD), is based on the $SU(3)$ group. The corresponding Lagrangian of QCD is

$$\mathcal{L}_{QCD} = -\frac{1}{4}\sum_{a=1}^{8} F^a_{\mu\nu}F^{a\mu\nu} + \sum_{j=1}^{n_f} \bar{q}_j(iD_\mu\gamma^\mu - m_j)q_j, \tag{4.16}$$

where the quark fields q_j are summed over the number of different quark flavors n_f, and m_j are the associated masses. A quark field q_j is composed of three quark spinors, one for each color. The tensors $F_{\mu\nu}$ are a combination of gluon fields g^a_μ and their derivatives. The index a runs over eight independent color charges of the gluons. The covariant derivative in this case is

$$D_\mu = \partial_\mu - i\sqrt{4\pi\alpha_s}\sum_{a=1}^{8} T^a g^a_\mu, \tag{4.17}$$

where α_s is the strong coupling constant and T^a are the generators represented by the Gell-Mann matrices.

The coupling of colored objects is weak at short distances (asymptotic freedom) [98], but it grows with distance (confinement) [99]. Therefore colored objects always have to be bound inside colorless hadrons, where they are quasi-free, and can never be observed separately. There are two kinds of hadrons, the baryons holding three quarks of different colors and the mesons composed of a quark-antiquark pair.

4.1.4 The electroweak symmetry breaking

As discussed, the $W^{\pm}$ and Z bosons are massive, but the mass term for these bosons cannot be incorporated into the Lagrangian of the electroweak interaction, because it would break the invariance of the Lagrangian under a local phase transformation. This problem is solved by the "Brout-Englert-Higgs mechanism" (BEH), based on a phenomenon referred to as "spontaneous symmetry breaking" of the SU(2) symmetry [100, 101]. This kind of breaking keeps the equations symmetric, but not their solution. The BEH mechanism introduces a new scalar doublet field Φ, defined as

$$\Phi = \begin{pmatrix} \phi^+ \\ \phi^0 \end{pmatrix}. \tag{4.18}$$

The Lagrangian for this field and its interactions can be expressed as

$$\mathcal{L}_{Higgs} = (D_\mu \Phi)^\dagger (D^\mu \Phi) - V(\Phi^\dagger \Phi), \tag{4.19}$$

where $V(\Phi^\dagger\Phi)$ is the Higgs potential and the covariant derivative D_μ is

$$D_\mu = \partial_\mu - ig \sum_{a=1}^{3} t^a W_\mu^a - ig' Y B_\mu, \text{ with } a = 1, 2, 3. \tag{4.20}$$

The Higgs potential $V(\Phi^\dagger\Phi)$ is defined by the equation

$$V(\Phi^\dagger \Phi) = -\frac{1}{2}\mu^2 \Phi^\dagger \Phi + \frac{1}{4}\lambda (\Phi^\dagger \Phi)^2, \tag{4.21}$$

where μ and λ are real parameters. Because both μ^2 and λ are positive numbers, the potential $V(\Phi^\dagger\Phi)$ takes the shape of a "Mexican hat", as shown in Fig. 4.2. The shape of the potential is such that the value of field Φ at the ground state, i.e. the vacuum expectation value (VEV) of the field Φ, is non-zero. The ground state is degenerated and can be chosen to be

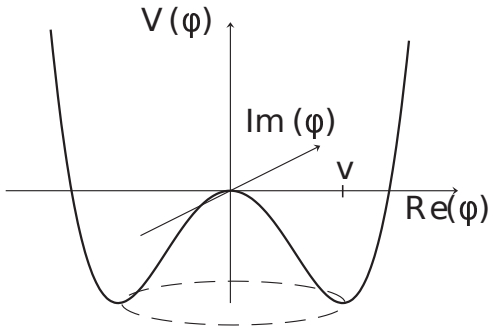

Figure 4.2: The shape of the Higgs potential V for the complex field Φ with positive values of real parameters μ^2 and λ. The parameter v denotes the vacuum expectation value.

$$\langle 0|\Phi|0\rangle = \frac{1}{\sqrt{2}}\begin{pmatrix}0\\v\end{pmatrix}, \tag{4.22}$$

with

$$v = \sqrt{\frac{\mu^2}{\lambda}} \tag{4.23}$$

being the ground state energy of the field Φ. Then the excitation of the field Φ can be written as follows

$$\Phi = \frac{1}{\sqrt{2}}\begin{pmatrix}0\\v+H\end{pmatrix}, \tag{4.24}$$

where H is the scalar field called the Higgs boson. The vector bosons $W^{\pm}$ and Z become massive via the interaction with the Higgs field present in the first term of the Higgs Lagrangian of Eq. 4.19. The masses of the fermions can be also generated via the interaction of the fermion field Ψ with the Higgs boson H by adding, to the Lagrangian of the SM Yukawa, terms of type $\lambda_Y \bar{\Psi}_L \Phi \Psi_R + h.c.$ with λ_Y representing the Yukawa coupling proportional to the mass of the fermion. The full Lagrangian of the standard model in the above defined notation can then be written as

$$\mathcal{L}_{SM} = \mathcal{L}_{QCD} + \mathcal{L}_{EW} + \mathcal{L}_{Higgs} + \mathcal{L}_{Yukawa}. \tag{4.25}$$

It can be noticed that the Yukawa interaction with the Higgs boson flips the chirality of a fermion from left to right and vice versa. Therefore the masses of neutrinos cannot be generated in this way, as there are only left-handed neutrinos in the SM. The parameters μ and λ of the Higgs potential are not predicted by the standard model, i.e. they are free parameters which are measured experimentally. The mass ($m_{H,0}$) of the Higgs boson at

tree level depends on the parameter μ:

$$m_{H,0} = \sqrt{2}\mu, \tag{4.26}$$

and therefore is as well not predicted by the SM.

4.1.5 Limitations of the standard model

Even though the standard model proved to be very successful in describing and predicting results of a large part of high energy physics experiments, phenomena which cannot be explained by the SM are observed as well [89]. For this reason it is widely believed that the standard model is an effective theory of a more fundamental one. Before discussing the possible extensions of the SM in Section 4.2, some of the shortcomings and open questions of the standard model are first briefly described.

The naturalness problem

As mentioned in Section 4.1.4, the mass of the Higgs boson at the tree level is defined by Eq. 4.26, but this mass must be corrected for contributions of virtual particles. An example of a virtual fermion loop contributing to the Higgs mass is shown in Fig. 4.3. The mass of the Higgs boson can be thereby decomposed as $m_{H,0}$ as:

$$m_H^2 \approx m_{H,0}^2 + \Delta m_H^2, \tag{4.27}$$

where Δm_H^2 is the correction from the virtual fermion loops. This correction is quadratically divergent and depends quadratically on the fermion masses due to their Yukawa couplings. Therefore the largest correction to the Higgs mass comes from the virtual top quarks which are the heaviest fermions. More precisely, the correction Δm_H^2 follows the relation

$$\Delta m_H^2 \propto m_f^2 \Lambda^2, \tag{4.28}$$

where m_f is the fermion mass and Λ is a cutoff on the momentum of the considered virtual particle. This cutoff is expressing up to which scale the standard model is valid and is usually taken to be the Planck mass $m_P \sim 10^{19}$ GeV. Knowing the term Δm_H^2, the Higgs mass can be written as

$$m_H^2 \sim m_{H,0}^2 + k\ m_P^2, \tag{4.29}$$

where k includes constants and SM couplings.

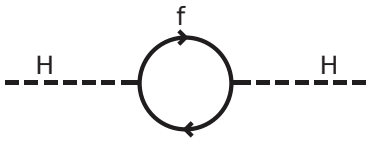

Figure 4.3: A virtual fermion contributing to the mass of the Higgs boson.

The mass of the Higgs boson was experimentally measured to be of 125 GeV [90, 91], which is orders of magnitude lower than Planck mass. This mismatch between the order of magnitude of the Higgs and the Planck masses, for which there is no physical reason, is referred to as the "hierarchy problem". Moreover to obtain this relatively small mass of the Higgs boson, there must be a large cancellation between the two terms $m^2_{H,0}$ and $k\ m_P$ in Eq. 4.29. The cancellation of the terms has to happen in around thirty orders of magnitude. Such fine-tuning is not natural and this problem of fine-tuning is referred to as the "naturalness problem".

Dark matter and dark energy

Cosmological observations suggest that the ordinary matter and energy, described by the standard model, account for only $\sim$ 5% of the total mass (energy) of the universe [102, 103]. The remaining $\sim$95% is divided between the dark matter ($\sim$27%) and dark energy ($\sim$68%).

Dark matter has been observed only indirectly as it does not emit any radiation. Therefore if it is associated to an elementary particle, it should have no color or electric charge. The first observation supporting the dark matter existence came from the measurement of the rotation curves of galaxies [104, 105]. These curves show the dependency of the star orbital velocity on the distance of the star from the center of galaxy. From the knowledge of the distribution of matter in the galaxies, the rotation curves can be theoretically computed, and it was found out that the measured and theoretical curves agree at short distances. With increasing distance the observed curves remain constant, while theoretically they are expected to decrease [102]. This phenomenon can be explained by the presence of a halo of new particles which interact by gravitational force. It was also found out that these particles must be stable and non-relativistic (cold). The requirement on the cold dark matter comes from the observations of the large scale distribution of the dark matter in the universe. However it was shortly realized that there is no candidate for dark matter within the standard model.

Dark energy arises from the need to introduce a cosmological constant in the Einstein equation [106]. Without it, it would not be possible to explain the accelerated expansion of the universe. Dark energy can be interpreted as a vacuum energy, but there is a

mismatch of ∼120 orders of magnitude between the vacuum energy estimation from the cosmological constant and quantum field theory calculations.

Other shortcomings of the standard model

Another problem of the SM is the asymmetry between matter and antimatter. In our universe there is an abundance of matter, even though the matter is supposed to have been produced in the same amount as antimatter during the big bang. Weak interaction violates the combined charge conjugation and parity (CP) symmetry [107], which could lead to an asymmetry between matter and antimatter. But the known sources of the CP violation cannot describe a so large asymmetry and therefore there is no mechanism within the SM which could explain the observed asymmetry between matter and antimatter.

Then, as mentioned, there are only left-handed neutrinos in the SM and therefore their masses cannot be generated via the interaction with the Higgs boson, which flips left-handed fermions to right-handed ones. But neutrino oscillations have been observed [108, 109] and are only possible if neutrinos are massive. Thus one needs to introduce a mechanism to generate mass terms for neutrinos in the SM Lagrangian. However, this fact in itself is not a conclusive argument in favor of a physics beyond the SM (BSM).

As mentioned earlier in this chapter, the gravitation is not included in the SM. This model is based on a QFT model which is based on the special relativity. Currently, there are big efforts to combine the general relativity and quantum field theory to formulate a theory of quantum gravity.

Finally, in the SM, the coupling constants are dependent on the energy. At higher energies the constants of weak, electromagnetic and strong interactions become of similar strengths, giving a hope for unification of these interactions at a large energy scale. There is no certainty that the three forces are unified, but the idea of grand unification is historically based on the success or previous unifications, such as of electricity and magnetism, or electromagnetic and weak interactions, and therefore unification of the three forces is expected. A requirement for the unification of the interactions is the convergence of the coupling constants at a large energy scale. This unification is not achieved within the SM and would request a theory beyond the SM.

4.2 Supersymmetry

To address the mentioned shortcomings of the standard model, many extensions of the SM were proposed over the past decades. In general there are several possibilities how to formulate theories beyond the standard model. The extension can be achieved by,

for example, adding "extra dimensions" [110], adding new symmetries, postulating new particles or proposing new interactions. An example of a theory adding a new symmetry is SUperSYmmetry (SUSY) [111], which became very popular due to its capability to solve many issues of the SM. SUSY started to be developed in the 1970's around an idea of introducing a spin symmetry relating fermions and bosons.

Supersymmetry introduces the symmetry operator Q, which acts on fermions f and bosons b in the following way:

$$Q \mid f\rangle \rightarrow \mid b\rangle, \tag{4.30}$$

$$Q \mid b\rangle \rightarrow \mid f\rangle. \tag{4.31}$$

The operator Q changes the spin of the particle by 1/2, therefore transforms a fermion to a boson and vice versa, and does not change any other quantum number or particle property. Within this symmetry Q, each SM fermion has a bosonic SUSY partner with the same quantum numbers except of the spin, and similarly each SM boson has an associated fermionic SUSY partner. The supersymmetric partners of the SM particles are referred to as "sparticles". To build a theory which takes into account the chiral nature of the fermions (the left-handed fermions transform differently under the gauge group than the right-handed ones), the operator Q must satisfy the following (anti)commutator relations [112, 113]:

$$\{Q, Q^\dagger\} = P^\mu,\ \{Q, Q\} = \{Q^\dagger, Q^\dagger\} = 0,\ [P^\mu, Q] = [P^\mu, Q^\dagger] = 0, \tag{4.32}$$

where P^μ is the four-momentum operator. It can be noticed that $-P^2$, which is the mass-squared operator, commutes with both Q and $Q^\dagger$ and therefore a particle and its SUSY partner have the same mass. But as no SUSY partners have been observed, this symmetry must be broken. Many symmetry breaking scenarios can be built, leading to many possible realizations of the supersymmetric theory.

The naming convention for SUSY particles is to add the prefix "s" to the SUSY partners of fermions, therefore "sfermions" are bosons. The SUSY partners to bosons get the suffix "ino", for example the SUSY partner of gluon is the gluino, which is a fermion. In addition, the symbols of the superpartners have a tilde.

There are many realizations of supersymmetry, but further in the text only the minimal supersymmetric standard model, which is the most popular one, is considered.

4.2.1 The minimal supersymmetric standard model

The Minimal Supersymmetric Standard Model (MSSM) [111] is a supersymmetric extension of the SM which adds a minimum of new particles, but does not introduce any additional gauge interactions. For example, in the MSSM there are two Higgs doublets in order to avoid gauge anomalies and to be able to have Yukawa couplings of both up- and down-type quarks. Both Higgs doublets have a non-zero vacuum expectation value. The Lagrangian of the new theory can be written as

$$\mathcal{L} = \mathcal{L}_{MSSM} + \mathcal{L}_{soft} = \mathcal{L}_{free} + \mathcal{L}_{int} + \mathcal{L}_{soft}, \tag{4.33}$$

where $\mathcal{L}_{MSSM}$ is the supersymmetric part of the Lagrangian and the term $\mathcal{L}_{soft}$ introduces the "soft" breaking of supersymmetry. The breaking of supersymmetry must be mild in order to end up with only a small tuning of the Higgs boson mass.

The large advantage of supersymmetry is that, in its unbroken form, it is able to solve the hierarchy problem. The virtual correction from the fermion loop Δm_H^2 to the Higgs boson mass as shown in Fig. 4.4 is in the context of the MSSM proportional to

$$\Delta m_H^2 \propto (m_f^2 - m_{\tilde{f}}^2) \ln\left(\frac{\Lambda}{m_{\tilde{f}}}\right), \tag{4.34}$$

where m_f is the mass of the fermion f, $m_{\tilde{f}}$ the mass of the sfermion $\tilde{f}$ and Λ a cutoff. The Δm_H^2 term is equal to zero if the masses of the particle (f) and its partner ($\tilde{f}$) are the same and therefore no fine-tuning is needed. The virtual contributions to the Higgs mass in the context of the MSSM are visualized in Fig. 4.4. The fermion and sfermion loop contributions are of the same value but with an opposite sign and therefore cancel.

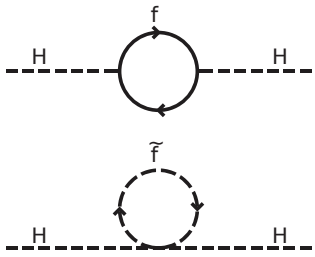

Figure 4.4: Virtual fermion and boson loops contributing to the mass of the Higgs boson.

In the broken theory though the masses are not the same anymore and the term Δm_H^2 has a logarithmic divergence. Larger is the mass difference between the particle and sparticle, more fine-tuning is needed. Therefore to preserve the naturalness of the theory, it is required that SUSY is broken only slightly and that the supersymmetric partners do

not have a mass hugely larger than the SM particles. Especially, as the largest virtual contribution to the Higgs mass comes from the top quark, the mass difference between the top quark and top squark (also called "stop") should be reasonably small, leading to a constraint on the top squark mass to be of order of around 1 TeV [111, 114, 115]. Newly explored natural SUSY models even permit the stop mass to go up to 3 TeV [116].

The spectrum of the SUSY partners can be seen in Tab. 4.1 both as gauge and mass eigenstates. Indeed, the left and right components of the third generation of squarks, associated to the left and right chiral components of the fermion fields, mix together due to the large mass of the third generation of quarks and therefore large Yukawa couplings which are proportional to m/v, where m is the fermion mass and $v = \mu/\sqrt{\lambda}$ is related to the Higgs potential. So for example the $\tilde{t}_L$ and $\tilde{t}_R$ stop eigenstates mix into the mass eigenstates $\tilde{t}_1$ and $\tilde{t}_2$, $\tilde{t}_1$ being the lightest one. The same happens for the tau lepton.

As a consequence of the electroweak symmetry breaking, the charged fields $\tilde{W}_{1,2}$ mix into the positive and negative winos ($\tilde{W}^{\pm}$) and the neutral fields $\tilde{B}_0$ and $\tilde{W}_3$ mix into the zino ($\tilde{Z}$) and photino ($\tilde{\gamma}$). The higgsinos mix with these flavor eigenstates of the SUSY partners of the $SU(2) \otimes U(1)$ gauge bosons to give rise to the gaugino mass eigenstates. Thus the two charged higgsinos ($\tilde{H}_u^+,\ \tilde{H}_d^-$) mix with $\tilde{W}^{\pm}$ to form four charginos ($\tilde{\chi}_{1,2}^{\pm}$). The four neutralinos $\tilde{\chi}_{1,2,3,4}^0$ are a mix of the zino, photino and the two neutral higgsinos ($\tilde{H}_u^0,\ \tilde{H}_d^0$).

Names	Spin	Gauge Eigenstates	Mass Eigenstates
squarks	0	$\tilde{u}_L\ \tilde{u}_R\ \tilde{d}_L\ \tilde{d}_R$ $\tilde{s}_L\ \tilde{s}_R\ \tilde{c}_L\ \tilde{c}_R$ $\tilde{t}_L\ \tilde{t}_R\ \tilde{b}_L\ \tilde{b}_R$	(same) (same) $\tilde{t}_1\ \tilde{t}_2\ \tilde{b}_1\ \tilde{b}_2$
sleptons	0	$\tilde{e}_L\ \tilde{e}_R\ \tilde{\nu}_e$ $\tilde{\mu}_L\ \tilde{\mu}_R\ \tilde{\nu}_\mu$ $\tilde{\tau}_L\ \tilde{\tau}_R\ \tilde{\nu}_\tau$	(same) (same) $\tilde{\tau}_1\ \tilde{\tau}_2\ \tilde{\nu}_\tau$
neutralinos	1/2	$\tilde{B}_0\ \tilde{W}_3\ \tilde{H}_u^0\ \tilde{H}_d^0$	$\tilde{\chi}_1^0\ \tilde{\chi}_2^0\ \tilde{\chi}_3^0\ \tilde{\chi}_4^0$
charginos	1/2	$\tilde{W}_{1,2}\ \tilde{H}_u^+\ \tilde{H}_d^-$	$\tilde{\chi}_1^{\pm}\ \tilde{\chi}_2^{\pm}$
gluino	1/2	$\tilde{g}$	(same)
gravitino	3/2	$\tilde{G}$	(same)

Table 4.1: The gauge and mass eigenstates of the sparticles [111]. The subscripts L, R denote the left and right chiral components of the sparticle fields. The mixing of the first two generations of sfermions is assumed to be negligible.

The MSSM brings 105 new free parameters on top of the 19 free parameters in the standard model. Most of these parameters come from the supersymmetry breaking part of the Lagrangian. It is not possible to search for SUSY in such a large parameter-space

and therefore the collider experiments usually search for SUSY in the context of simplified models, referred to as "Simplified Model Spectra", which reduce considerably the number of free parameters. More details on these simplified models are given in Section 4.2.2. Another option to reduce the number of parameters is to apply well motivated assumptions. For example the phenomenological MSSM (pMSSM) allows to reduce the number of parameters to 19, defined at the electroweak scale [117].

The left ($\tilde{t}_L$) and right ($\tilde{t}_R$) stop eingenstates mix into the mass eignestates ($\tilde{t}_1,\ \tilde{t}_2$). In the pMSSM, the masses of the $\tilde{t}_1$ and $\tilde{t}_2$ can be determined from the mass matrix $M_{\tilde{t}}$ in the ($\tilde{t}_L,\ \tilde{t}_R$) basis [118]. The mass matrix $M_{\tilde{t}}$ can be written as

$$M_{\tilde{t}} = \begin{pmatrix} m^2_{\tilde{t}_L} + m^2_t + \Delta_{\tilde{u}_L} & m_t(A^*_t - \mu\ \cot\beta) \\ m_t(A_t + \mu\ \cot\beta) & m^2_{\tilde{t}_R} + m^2_t + \Delta_{\tilde{u}_R} \end{pmatrix}, \tag{4.35}$$

where $m_{\tilde{t}_L}$ and $m_{\tilde{t}_R}$ are the masses of the left and right component of the stop field, respectively, m_t is the top quark mass, μ is the higgsino mass parameter, β is the ratio of the Higgs VEVs, A_t is the trilinear coupling and the Δ terms are coming from the quadrilinear interactions of the squarks and the Higgs boson which represent small contributions compared to the other terms.

Through the radiative corrections, the Higgs mass is sensitive to the stop mass. Fig. 4.5 shows the dependence of the Higgs mass on two parameters, $m_{\tilde{t}_R}$ and X_t defined as

$$X_t \equiv A_t + \mu\ \cot\beta. \tag{4.36}$$

The other pMSSM parameters are fixed to the physically motivated values. Therefore the observed value of the Higgs mass puts a constraint on the stop parameters. It can be noticed, that even when masses of $\tilde{t}_L$ and $\tilde{t}_R$ are around 3 TeV a configuration of parameters being compatible with the observed Higgs mass can be found.

In the total MSSM Lagrangian, in principle there could be terms which would violate the baryon or lepton number conservation. Under such conditions, the proton could decay, what was not experimentally observed [119]. To avoid such violation, a symmetry referred to as "R-parity" (P_R) is considered. The P_R being defined as

$$P_R = (-1)^{3(B-L)+2s}, \tag{4.37}$$

where B is the baryon number, L the lepton number and s the spin of the particle. All SM particles have $P_R = 1$ and their SUSY partners $P_R = -1$. The consequence of R-parity conservation is that sparticles can be produced only in an even number and each of them can decay only into an odd number of sparticles. In addition, the lightest supersymmetric

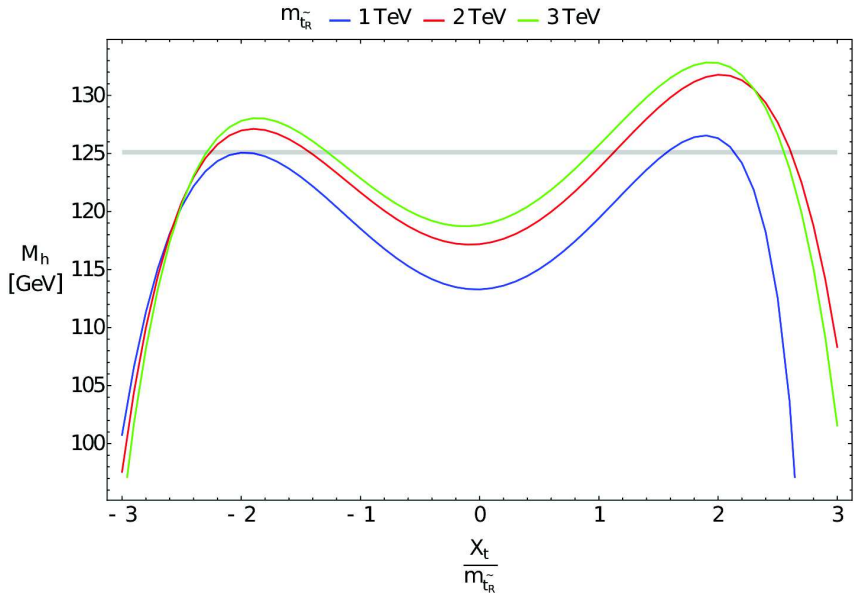

Figure 4.5: The predicted mass of the lightest Higgs boson M_h as a function of the ratio of the stop parameters X_t and $m_{\tilde{t}_R}$ for three different values of $m_{\tilde{t}_R}$ (1 TeV in blue, 2 TeV in red and 3 TeV in green). For the computation the parameters were fixed to $m_{\tilde{t}_L} = m_{\tilde{t}_R} + 100$ GeV, $A_t = \left|1.3\ m_{\tilde{t}_R} + \mu\ \cot\beta\right|$, μ=1 TeV and $\tan\beta = 50$. The gray horizontal line corresponds to the observed Higgs mass. More details can be found in [118].

particle (LSP) must be stable. In that case the LSP is a dark matter candidate and can be either the lightest neutralino, sneutrino or gravitino, depending on the specific realization of the MSSM.

Another advantage of the MSSM is that the energy dependence of the coupling constants of the SM interactions is modified as a result of the introduction of sparticles. Consequently these coupling constants can be unified at a large energy scale referred to as the "GUT scale". Within supersymmetry it is also possible to create models of supergravity by imposing the locality of supersymmetry.

4.2.2 Simplified Model Spectra

The parameter-space of the MSSM can be reduced by fixing the sparticles decay modes and branching ratios and the mass hierarchy between sparticles. Such restrictions give only a limited number of possible SUSY models called "Simplified Model Spectra" (SMS) [120, 121, 122].

A typical SMS scenario for the stop production is illustrated in Fig. 4.6. In this case only the masses of the stop and the neutralino are considered to be free parameters. All the other sparticles are assumed to be much heavier and do not influence the studied process.

The associated branching fraction for the decay of the stop (here $t\tilde{\chi}_1^0$) is arbitrarily fixed, most of the cases to 100%.

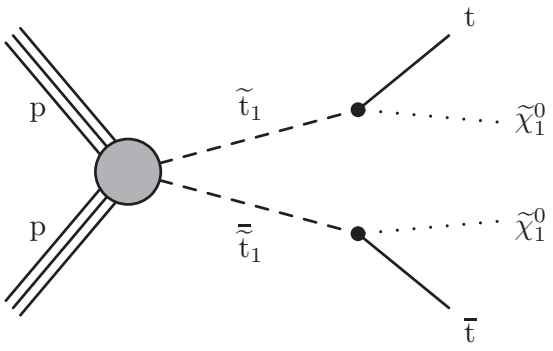

Figure 4.6: An example of diagram of direct stop pair production. In this diagram both stops decay to a top quark and a neutralino.

At the end of the analysis, the results are interpreted in a 2D plane of the free parameters.

4.2.3 Results on the SUSY searches in Run 1

In Run 1, many analyses searching for the SUSY particles were performed. In particular for the stop production, the naturalness constraint and the mixing of gauge eigenstates of the stops suggest that the lightest stop $\tilde{t}_1$ could be relatively light, of about 1 TeV, and therefore accessible at the LHC energies. The combined results of stop decaying either to $t\tilde{\chi}_1^0$ or $c\tilde{\chi}_1^0$ are shown in Fig. 4.7. This figure shows the exclusion limits on the stop and LSP masses in three different kinematic regions categorized as a function of the mass difference $\Delta m = m_{\tilde{t}} - m_{LSP}$.

For $m_{LSP} < \Delta m < m_W$ the stop can decay either to $c\tilde{\chi}_1^0$ or to four bodies where the intermediate top quark and W boson are off-shell in $t\tilde{\chi}_1^0$, the region $\Delta m < m_{LSP}$ being kinematically forbidden. The decay of the stop to the $c\tilde{\chi}_1^0$ is possible via loops or flavor changing neutral currents. Once $m_W < \Delta m < m_t$, the decay $t\tilde{\chi}_1^0$ undergoes a three body decay via off-shell quark, but with an on-shell W boson. When $\Delta m > m_t$ the stop can decay to $t\tilde{\chi}_1^0$. The analyses whose results are presented in the Fig. 4.7 do not only differ by the coverage of the kinematic regions, but also by the analysis strategy, for example they may require a different number of leptons in the final state. In general, less leptons there are in the final state, larger is the branching ratio, and therefore the expected yield. But on the other hand the analyses requesting more leptons suffer less from SM background contributions.

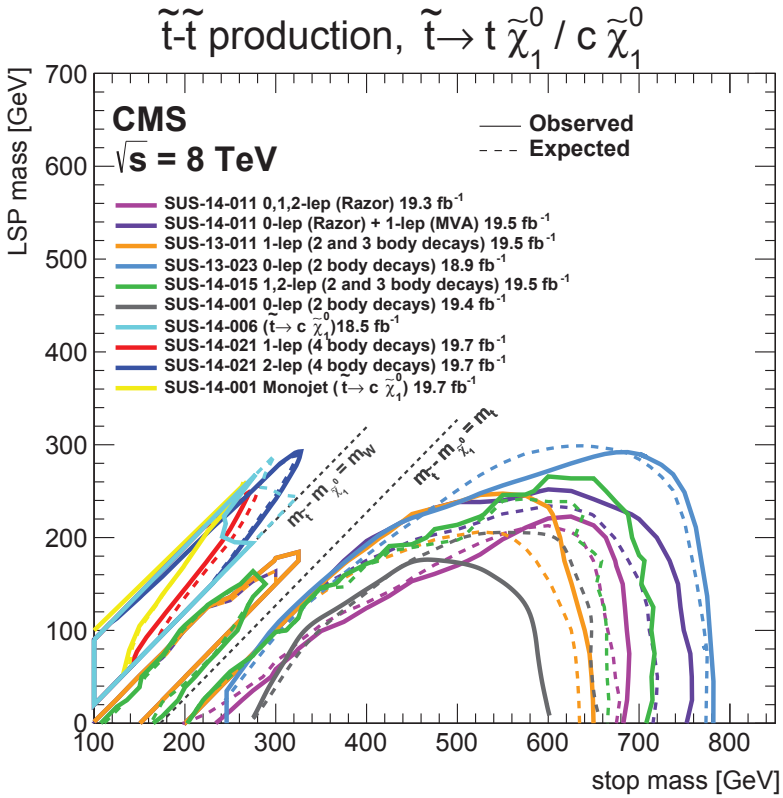

Figure 4.7: The exclusion limits on the stop and LSP masses for the $t\tilde{\chi}_1^0$ and $c\tilde{\chi}_1^0$ decay modes. The results from several Run 1 analyses are combined in this plot [123].

The strongest exclusion limit on the stop mass was put by the analysis [124] (light blue in the Fig. 4.7) searching for fully hadronic final states. This analysis is interpreted in the context of SMS and excludes top squark masses up to 755 GeV for a neutralino mass below 200 GeV. Probing the higher stop $\tilde{t}$ masses is difficult with the current dataset, given that the production cross section falls steeply as a function of the mass as illustrated in Fig. 4.8.

On the diagonals where $\Delta m \sim m_W$ and $\Delta m \sim m_t$, the final state topologies for signal are very similar to the ones of the SM background, the analyses have therefore a low sensitivity in these regions and are not able to derive limits on them with the Run I data.

The summary plots of excluded masses of SUSY particles obtained by SUSY searches at Run 1 can be seen in the Fig. 4.9 and Fig. 4.10 both for the ATLAS and CMS collaborations, respectively. Depending on the SUSY model and decay channel, the gluino masses up to around 1.8 TeV, the stop and sbottom masses up to around 700 GeV, the chargino masses up to around 700 GeV, and the slepton masses up to around 300 GeV were excluded at Run 1.

The increase of the center-of-mass energy between Run 1 and Run 2, from 8 TeV to

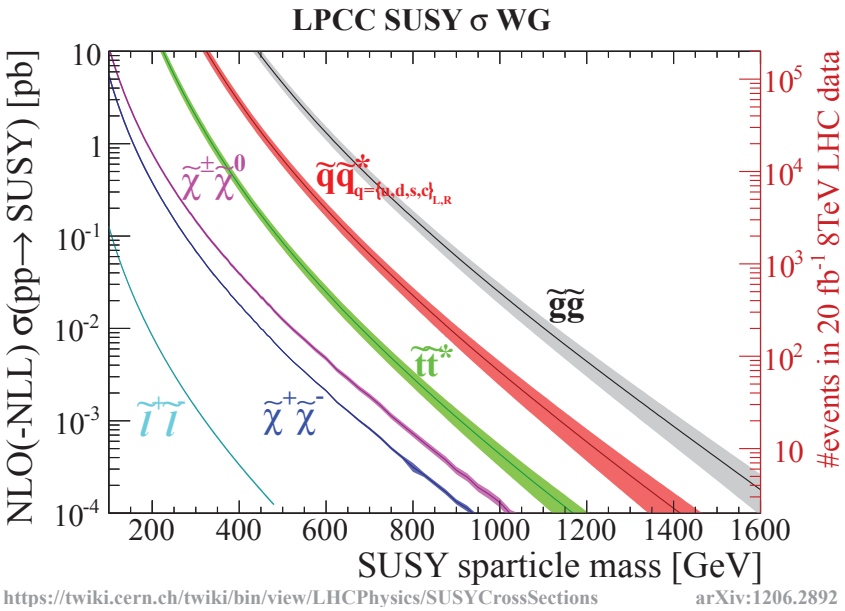

Figure 4.8: The cross sections of selected SUSY processes [125].

13 TeV, permits to further probe higher SUSY masses thanks to the parton luminosity increase: for example the pair production of stops of 700 GeV is increased by a factor 8.4 as shown in Fig. 4.11, while the gain of typical SM backgrounds is much smaller.

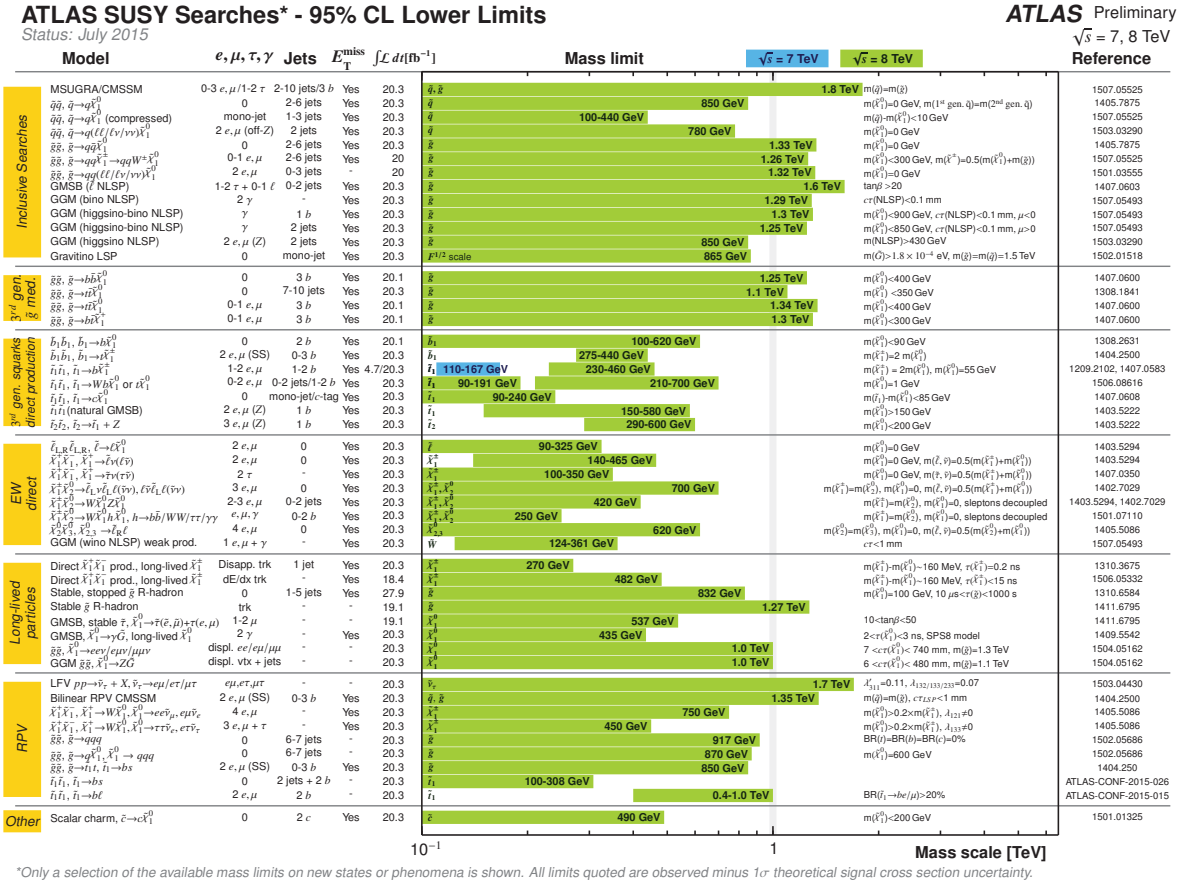

*Only a selection of the available mass limits on new states or phenomena is shown. All limits quoted are observed minus 1σ theoretical signal cross section uncertainty.

Figure 4.9: Summary of the masses of SUSY particles excluded by the ATLAS collaboration with the Run 1 dataset [126]. The SUSY models, decay channels and assumptions are directly indicated in the plot. More details can be seen in the documentation of the analyses.

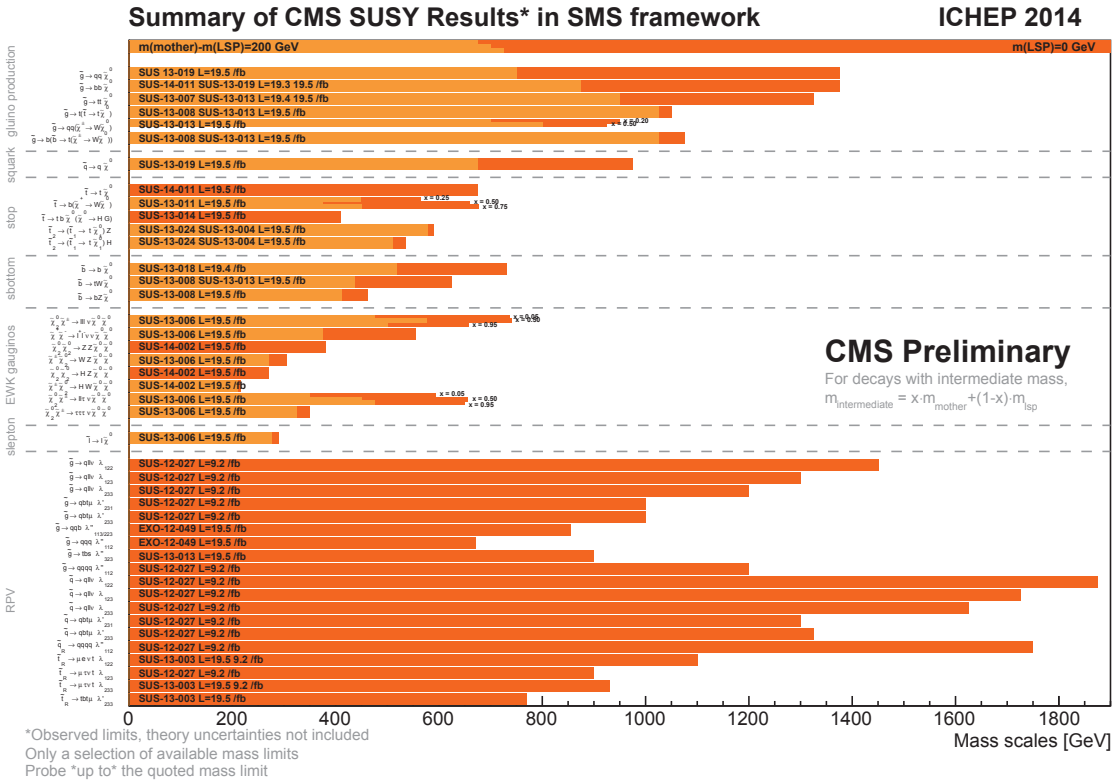

Figure 4.10: Summary of the masses of SUSY particles excluded by the CMS collaboration [123]. The limits in darker shades are given for a massless LSP, while lighter shades limits are for m(mother)-m(LSP)=200 GeV. More details can be seen in the documentation of the analyses.

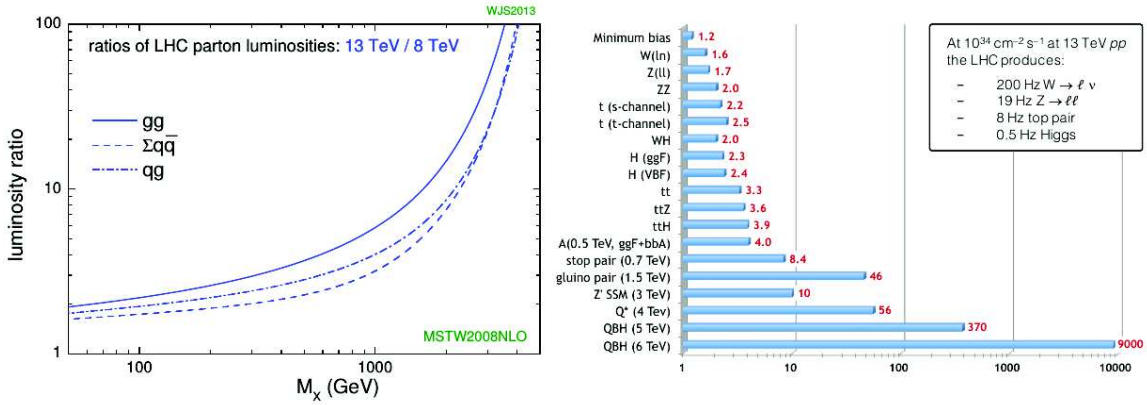

Figure 4.11: (left) The ratios of 13 TeV to 8 TeV LHC parton luminosities as a function of a produced particle mass M_X. (right) The value of this ratio for several SM and beyond SM processes [127].

Chapter 5

Search for top squark pair production in pp collisions at $\sqrt{s}$=13 TeV in Run 2 using single lepton events

In the previous chapter, we have introduced supersymmetry as the most popular extension of the standard model, due to its capability to address many shortcomings of the SM. Among others, it provides a natural solution to the hierarchy problem and a dark matter candidate. Within supersymmetry each SM particle has a SUSY partner with the same quantum numbers except the spin which is differing by one half. This chapter focuses on the direct pair production of the lightest SUSY partner of the top quark, referred to as the top squark or stop ($\tilde{t}_1$), this $\tilde{t}_1$ being in fact a mass eigenstate from the mixing of the two scalar stops $\tilde{t}_R$ and $\tilde{t}_L$ as previously described in Section 4.2.1.

In this chapter, SMS scenarios in which the R-parity is conserved are considered, leading to the stops being produced in pair. The LSP is the lightest neutralino $\tilde{\chi}_1^0$. As we will see later, directly produced stop pair decays into two b quarks, two W bosons and two neutralinos. The neutralinos interact only weakly and escape the detector unmeasured. Although undetected particles can be spotted by the presence of the missing transverse energy, which can be especially large in case of final states with more neutralino(s) and neutrino(s). Therefore SUSY signal can have an unique experimental signature compared to the standard model processes.

This chapter describes the search for direct top squark pair production in pp collisions at $\sqrt{s}$=13 TeV using single lepton events [128] corresponding to an integrated luminosity of 35.9 fb^{-1} collected during 2016. This analysis is further referred to as the "full 2016

analysis". I also worked on the previous versions of this analysis [129, 130], based first on data from 2015 corresponding to an integrated luminosity of 2.3 fb^{-1} and referred to as the "2015 analysis" and then on data from the beginning of 2016 with an integrated luminosity of 12.9 fb^{-1} referred to as the "ICHEP2016 analysis" as it was presented at the ICHEP conference in 2016. Several differences between the three versions are briefly discussed, but in general the strategy of the analyses remains similar. In the following sections I especially highlight some chosen personal contributions.

In the Section 5.1 the signal topologies targeted by full 2016 analysis are presented. The following Section 5.2 defines the strategy of the analysis. Then in Section 5.3 the background estimation techniques in the search region are discussed, starting from the estimation of background referred as "$Z \to \nu\bar{\nu}$" which I provided during my PhD thesis. Within the subsections on the relevant backgrounds, the systematic uncertainties on the background estimates are identified. Finally Section 5.4 summarizes the results of this analysis and provides their interpretation.

5.1 Signal topologies

As the lighter stop $\tilde{t}_1$ is expected in natural SUSY to be lighter than the gluino [131], the stop pair can be produced either directly as shown in Fig. 4.6 or via the gluino mediated production (see Fig. 5.1). Only the first process is considered in this thesis, the later being studied in e.g. [132, 133].

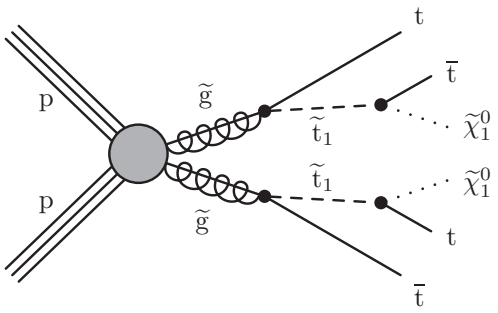

Figure 5.1: An example of diagram of gluino mediated stop production. In this case gluinos are produced in pairs and both decay to a top quark and a top squark. Both stops decay to a top quark and an LSP.

There are different possible decay modes for the stop depending on the mass difference between the stop and the neutralino $\Delta m = m_{\tilde{t}} - m_{\tilde{\chi}_1^0}$. The stops can decay via two, three or four body decays leading to final states with b or c quarks. In this thesis three decay modes are considered for the stop pair in the kinematical region $\Delta m > m_W + m_b$.

The first of the three considered decay chains of the stop pair is shown in the left part of Fig. 5.2 and referred to as "T2tt", in which both stops decay in 100% of cases to a top quark and a neutralino, followed by the decay of each top quark to a W boson and a b quark:

$$\tilde{t}_1\bar{\tilde{t}}_1 \rightarrow t\tilde{\chi}_1^0\bar{t}\tilde{\chi}_1^0 \rightarrow bW^+\tilde{\chi}_1^0\bar{b}W^-\tilde{\chi}_1^0. \tag{5.1}$$

Note that if $\Delta m < m_t$, then the decay of the stop is a three-body decay, with the top quark being off-shell.

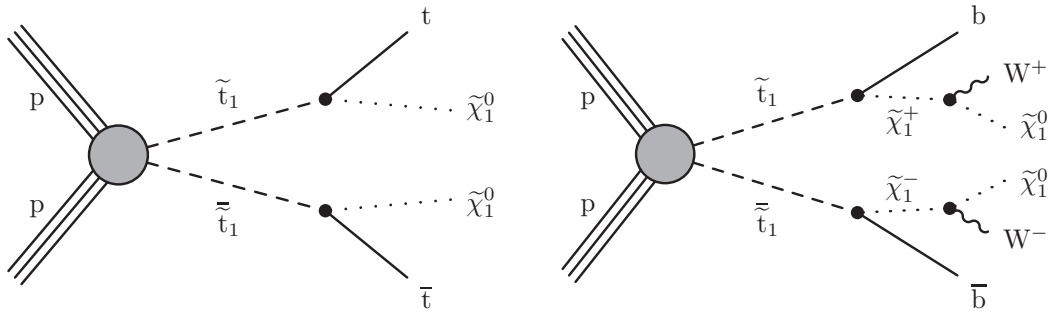

Figure 5.2: The SMS diagrams for the direct stop pair production. In the left diagram each stop decays to $t\tilde{\chi}_1^0$ (T2tt), while in the right one they decay to $b\tilde{\chi}_1^\pm$ (T2bW) [134].

The second possibility depicted in the right part of Fig. 5.2 is referred to as "T2bW" and in this case both stop quarks decay in 100% of cases via an intermediate chargino which decays as $\tilde{\chi}_1^\pm \rightarrow W^\pm\tilde{\chi}_1^0$:

$$\tilde{t}_1\bar{\tilde{t}}_1 \rightarrow b\tilde{\chi}_1^+\bar{b}\tilde{\chi}_1^- \rightarrow bW^+\tilde{\chi}_1^0\bar{b}W^-\tilde{\chi}_1^0. \tag{5.2}$$

The chargino mass $m_{\tilde{\chi}_1^\pm}$ is fixed by the relation

$$m_{\tilde{\chi}_1^\pm} = x\ m_{\tilde{t}_1} + (1-x)\ m_{\tilde{\chi}_1^0}, \tag{5.3}$$

where $m_{\tilde{t}_1}$ is the stop mass, $m_{\tilde{\chi}_1^0}$ the neutralino mass and x is a fixed fraction between 0 and 1, which was for CMS searches usually chosen to be 0.25, 0.5 or 0.75 at Run 1, while x is chosen to be equal to 0.5 at Run 2.

The third decay, shown in Fig. 5.3 and referred as "T2tb" combines the previous two decay modes of the stop: one of the stops decays to a top quark and a neutralino, while other one decays to a bottom quark and a chargino:

$$\tilde{t}_1\bar{\tilde{t}}_1 \rightarrow t\tilde{\chi}_1^0\bar{b}\tilde{\chi}_1^- \rightarrow bW^+\tilde{\chi}_1^0\bar{b}W^-\tilde{\chi}_1^0. \tag{5.4}$$

In the T2tb model, the chargino and neutralino are taken as almost mass degenerate, the chargino mass is fixed by relation $m_{\tilde{\chi}_1^\pm} = m_{\tilde{\chi}_1^0} + 5$ GeV. Such model is motivated by the low mass difference between the chargino and neutralino obtained in the case when bino and wino masses are larger than the parameter μ [135]. In addition, the results of the thesis [136] show that if $\mu = 200$ GeV, $\tan\beta = 10$ and the bino mass is set to 3 TeV, the mass difference between the lightest chargino and neutralino is lower than 5 GeV, depending on the mass of the wino. In our case, because of this small difference between the chargino and neutralino masses, the W boson is produced off-shell, its decay products have low transverse momenta and are typically not selected or even reconstructed.

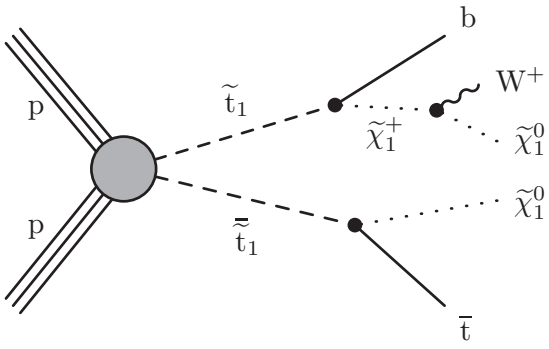

Figure 5.3: The SMS diagram for the direct stop pair production considering the mixed decay of the stop pair $\bar{t}\tilde{\chi}_1^0 b\tilde{\chi}_1^+$ [134].

All decay modes considered by this analysis lead to states with two b quarks, two W bosons and two neutralinos, the targeted final states having one leptonically and one hadronically decaying W boson, resulting in one charged lepton (1ℓ) in the final state: $\tilde{t}_1\bar{\tilde{t}}_1 \to b\bar{b}\ell\nu_\ell q\bar{q}\tilde{\chi}_1^0\tilde{\chi}_1^0$. The advantage of this 1ℓ channel is the low occurrence of the standard model backgrounds compared to the full hadronic search, and its relatively high branching ratio compared to the dilepton channel. The stop pair decays in around 32% of cases to the final states with one prompt lepton (e, μ) or leptonically decaying tau lepton.

The final state kinematics differ depending on the decay mode and Δm. The Δm plane is shown in Fig. 5.4. In the part of the plane where $\Delta m < m_t$, often referred to as the "compressed spectra" region, the decay products are softer and subsequently not selected. On the other hand when the Δm is large, boosted topologies can be expected.

5.2 Analysis strategy

Because of the two neutralinos, the signal processes (T2tt, T2bW and T2tb) can have final state signatures largely differing from the SM background ones. The knowledge about

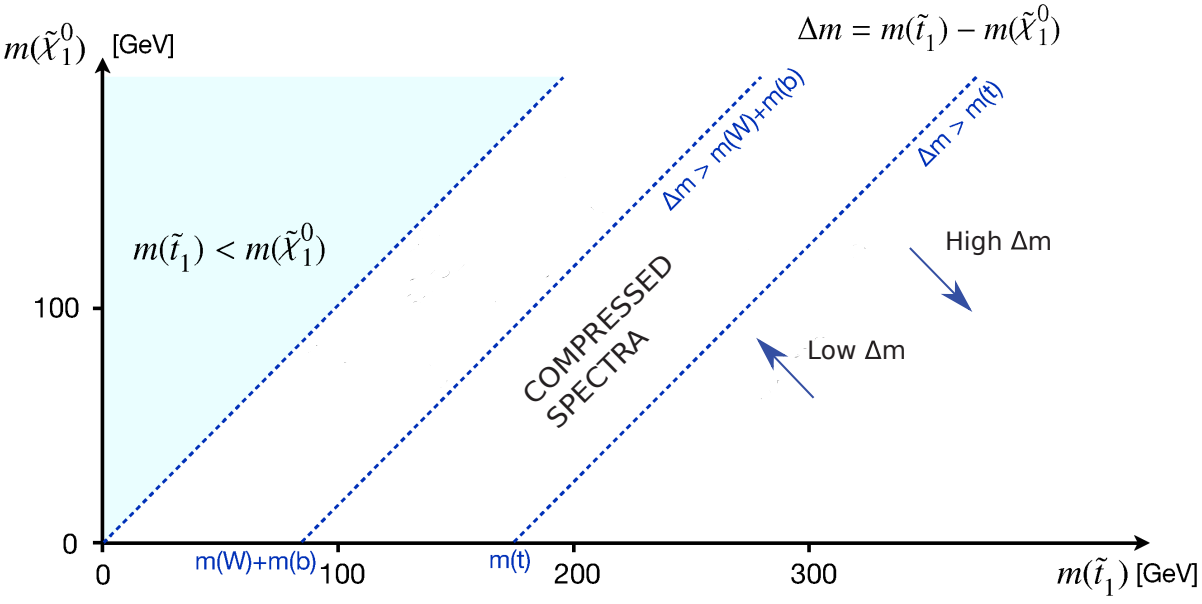

Figure 5.4: The plane of stop ($\tilde{t}_1$) versus LSP ($\tilde{\chi}_1^0$) masses [137].

the signal and background signatures is used to define a "baseline region" of the search, in which the SM backgrounds are suppressed.

In the baseline search region there are three groups of backgrounds present. The leading background is referred to as the "lost lepton" background which has a final state with two W bosons, both decaying into leptons and one of the charged leptons being lost due to acceptance or a problem of reconstruction or identification. This background, mainly coming from the dileptonic decay of the top pair production ($t\bar{t} \rightarrow 2\ell$) and single top quark process, is reduced by applying a veto on the presence of a second lepton passing looser criteria, but even after this it remains the largest background. The subleading background is the "one lepton" (1ℓ) background, which is predominantly composed of associated W boson plus jets production ($W + jets \rightarrow 1\ell$) and top pair production ($t\bar{t} \rightarrow 1\ell$) with one W boson decaying leptonically. The last relevant background is denoted as "$Z \rightarrow \nu\bar{\nu}$" and comes from processes such as $t\bar{t}Z$ and WZ in which the Z boson decays to two neutrinos and one of the W bosons decays leptonically.

Starting from this baseline region, tighter selections are applied with the help of discriminating variables, to define smaller signal regions. The goal is to define regions in which the signal to background ratio is enhanced either by an enrichment in signal, or by a high suppression of the backgrounds. Different signals are expected to populate differently these signal regions, allowing to discriminate between the signal scenarios in case of discovery. The remaining backgrounds in each signal region is estimated from data-driven techniques or simulations.

Hypothesis tests are performed on the signal, estimated background and observed

data yields in all signal regions. In case of no observed excess from the SM expectation, the results are interpreted in term of exclusion limits on a given signal models. For the purpose of the analysis optimization and limit setting, the procedure of hypothesis testing in the LHC searches is briefly described in the Section 5.2.1. Then the triggers and objects used in this analysis are introduced in Sections 5.2.2 and 5.2.3.

In the following Section 5.2.4, the variables designed to define the baseline search region and its categorization in signal regions are introduced and justified on the examples of signal topologies. The backgrounds behavior with regard to the choice of the variables is discussed as well. Once the most discriminating variables are identified, the final definition of the baseline and signal regions is presented in Section 5.2.5 and 5.2.6.

The introduced analysis strategy is general for all types of signal topologies. But to better target the very challenging signal final state scenario in the compressed region of T2tt, a separately optimized "compressed" analysis has also been designed. As the signal regions defined in the nominal and compressed analyses are not exclusive, based on the sensitivity of both analyses for different Δm, it has been decided to use the compressed analysis for T2tt signals in the Δm range between 100 and 225 GeV and the nominal one everywhere else. It is interesting to note that this low Δm range does not cover only the off-shell decays, but is also relevant for cases when the top quark is produced on-shell.

5.2.1 Hypothesis testing in LHC searches

The hypothesis testing and limit setting procedure chosen by the CMS collaboration is a modified frequentist method referred to as the "CL_s" method [138, 139]. There are two hypotheses to be tested, the background only hypothesis H_0 also referred to as the "null hypothesis" and the signal plus background hypothesis H_1 usually called as the "alternative hypothesis". These hypotheses are functions of $b + \mu s$, where b and s are the expected background and signal yields and μ is the signal strength modifier. In the case of the background only hypothesis H_0, the signal strength μ is zero. The signal and background estimates entering into the hypothesis testing are burdened by many systematic uncertainties, which are treated as nuisance parameters and collectively denoted as θ. The expected signal and background yields are dependent on these nuisance parameters: $s \to s(\theta)$ and $b \to b(\theta)$.

Observed limits

To compute the observed limits, a likelihood function $\mathcal{L}(data|\mu, \theta)$ can be built as

follows [139]

$$\mathcal{L}(data|\mu,\theta) = \text{Poisson}(data|\mu s(\theta) + b(\theta))\ p(\tilde{\theta}|\theta), \tag{5.5}$$

where $p(\tilde{\theta}|\theta)$ are the probability distribution functions for the nuisance parameters θ with $\tilde{\theta}$ being the default value of the nuisance parameters, *data* for this purpose refers to the information about the observed data yield or generated pseudo-data. In case of a binned likelihood, the term $\text{Poisson}(data|\mu s(\theta) + b(\theta))$ can be expressed as

$$\text{Poisson}(data|\mu s(\theta) + b(\theta)) = \prod_i \frac{\mu s_i + b_i}{n_i!} e^{-\mu s_i - b_i}, \tag{5.6}$$

which is a product of Poisson probabilities to observe n_i data events in the bin i. Given the likelihood function, the compatibility of *data* with the H_0 or H_1 hypothesis can be tested with the help of the test statistics $\tilde{q}_\mu$ which has the form of a profile likelihood ratio

$$\tilde{q}_\mu = -2\ln\frac{\mathcal{L}(data|\mu,\hat{\theta}_\mu)}{\mathcal{L}(data|\hat{\mu},\ \hat{\theta})}, \tag{5.7}$$

where the signal strength μ is a free parameter, $\hat{\theta}_\mu$ are the conditional maximum likelihood estimators of the parameters θ given the parameter μ and the measured data. The $\hat{\mu}$ and $\hat{\theta}$ are the parameter estimators at the global maximum of the likelihood.

The observed value $\tilde{q}_\mu^{obs}$ of the profile likelihood ratio expressed in Eq. 5.7 can be computed using the measured data and the maximum likelihood estimators of θ which best describe the observed data, it can be evaluated for both the H_0 and H_1 hypotheses. The CL_s method defines two p-values, the first one is p_μ testing the compatibility of the observation with H_1 and the second one, $1-p_b$, testing the compatibility of the observation with the background-only hypothesis H_0. The CL_s for a given signal strength μ is then defined as

$$\text{CL}_\text{s}(\mu) = \frac{p_\mu}{1-p_b}, \tag{5.8}$$

where p_μ can be written as

$$p_\mu = P(\tilde{q}_\mu \geq \tilde{q}_\mu^{obs}|s+b) \tag{5.9}$$

and $1-p_b$ as

$$1-p_b = P(\tilde{q}_\mu \geq \tilde{q}_\mu^{obs}|b). \tag{5.10}$$

For $\mu = 1$, the H_1 is excluded at $(1-\alpha)$ CL_s confidence level if $CL_s \leq \alpha$. Typically, the exclusion limits are derived for $\alpha = 0.05$. In the case that the μ parameter is not fixed to one, the exclusion limits are set on the cross section given a fixed branching fraction of a given signal model. In such procedure the signal strength μ is adjusted in order to correspond to the $CL_s = 95\%$. If for a given signal point the cross section is limited to a lower value than the theoretical cross section, the signal point is excluded. A contour line is drawn at the place where the limit on the cross section is equal to the theoretical cross section.

Expected limits

The expected limits can be determined via a similar method using generated background-only pseudo-data instead of observed data.

Thanks to the relation

$$p = \int_Z^\infty \frac{1}{\sqrt{2\pi}} e^{-x^2/2} dx, \tag{5.11}$$

the p-value computed from the test statistics can be converted to the significance Z with $Z\sigma$ denoting the significance in terms of the standard deviation σ of a Gaussian distribution. If considering the background-only hypothesis, the significance of 5 standard deviations corresponding to $p_b = 2.8 \times 10^{-7}$ suggests that the H_0 hypothesis is excluded at 5σ in favor of the H_1 hypothesis, therefore the discovery is claimed.

5.2.2 Triggers, data and simulated samples

In the full 2016 analysis several kinds of triggers are used: E_T^{miss}, single lepton, $e-\mu$ double lepton and single photon triggers. As the online thresholds for the single lepton triggers are higher than the cut applied offline for the lepton, the use of the E_T^{miss} triggers allows to select also events with a lower p_T lepton. To guarantee a high efficiency, an "OR" of these triggers is used in the analysis. The trigger requirements are given in Table 5.1. The trigger efficiency in the search regions of interest is greater than 99%. The data triggered by the double lepton trigger are used for checking the kinematics of the lost lepton background. Similarly the data triggered by the single photon trigger are used to cross-check the E_T^{miss} resolution in the 1ℓ background.

The SM background samples are generated by leading-order (LO) or next-to-leading-order (NLO) generators and processed by the full simulation of CMS. The LO samples generated by MADGRAPH_aMC@NLO 2.2.2 [74] generator configured to the LO with MLM matching [140] using the LO NNPDF3.0 [141] parton distribution functions are

for the $t\bar{t}$, W+jets, $t\bar{t}Z$ and γ+jets processes. The single top samples are generated by the NLO POWHEG 2.0 [142] generator. The MADGRAPH_aMC@NLO 2.2.2 in the NLO mode with FxFx [143] matching and the NLO NNPDF3.0 parton distribution functions is used to generate the majority of the rare processes, such as WZ and ZZ. The full hadronization, parton showering and modelling of the underlying events are then performed by PYTHIA 8.205 [71].

The description of the initial state radiation (ISR) jets in the $t\bar{t}$ and $t\bar{t}Z$ samples is improved by reweighting these samples based on the number of the ISR jets (N_{ISR}) in order that the jet multiplicity agrees between data and simulation. Measurements for N_{ISR} between one and six have been done and the data-to-simulation ratio has been found to be in the range between 0.92 and 0.51. The systematic uncertainty on this factor is taken to be half the deviation from the unity. The pileup distributions in data and generated samples largely differ and therefore the simulated samples should be reweighted for the different pileup profiles in data and simulation. The reweighting procedure is applied for the lost lepton and $W + jets \rightarrow 1\ell$ backgrounds as these processes have sufficient MC statistics in the signal regions. However for signal and the backgrounds with small yields in the signal regions it would only unreasonably enlarge the statistical uncertainty on the yield.

The signal samples are produced by the MADGRAPH_aMC@NLO 2.2.2 generator at the LO and injected into the fast simulation of the CMS detector. The same N_{ISR} reweighting procedure as discussed above is applied on the signal samples.

5.2.3 Object definition

In this section the object definition and the criteria on their selection for the full 2016 analysis are introduced.

Primary vertex The primary vertices in the event must pass good quality criteria. The primary vertex corresponding to the hard interaction is identified as the vertex which leads to the largest sum of p_T^2 of the physics objects belonging to this vertex.

Lepton The "selected" lepton for this analysis is a large p_T electron or muon isolated from any activity in the detector. The selected lepton must originate from the primary vertex, both electron and muon have p_T >20 GeV, but a different $|\eta|$ coverage: $|\eta| < 1.4442$ for the electron and $|\eta| < 2.4$ for the muon. Within this acceptance criteria the selection efficiency is more than 85% for electrons and 95% for muons. This analysis also defines a second category of leptons, called "veto" leptons, which

E_T^{miss} trigger Single lepton trigger	$E_T^{miss} > 120$ GeV and $H_T^{miss} = \left\vert\sum(\vec{p}_T^{\,\text{jets}}) + \vec{p}_T^{\,\text{lep}}\right\vert > 120$ GeV isolated electron (muon): $p_T^{\text{lep}} > 25$ (22) GeV, $\vert\eta\vert < 2.1$ (2.4)
Selected lepton Selected lepton isolation	electron (muon): $p_T^{\text{lep}} > 20$ GeV, $\vert\eta\vert < 1.442$ (2.4), medium ID $p_T^{\text{sum}} < 0.1 \times p_T^{\text{lep}}$, $\Delta R = \min[0.2, \max(0.05, 10\text{ GeV}/p_T^{\text{lep}})]$
Jets and b-tagged jets b tagging efficiency b tagging mistag rate	$p_T > 30$ GeV, $\vert\eta\vert < 2.4$ medium (tight) WP: 60-70 (35-50)% for 30<jet p_T <400 GeV medium (tight) WP : $\sim 1\%$ ($\sim 0.2\%$) for light-flavor partons
Veto lepton Veto lepton isolation	muon or electron with $p_T^{\text{lep}} > 5$ GeV, $\vert\eta\vert < 2.4$ $p_T^{\text{sum}} < 0.1 \times p_T^{\text{lep}}$, $\Delta R = \min[0.2, \max(0.05, 10\text{ GeV}/p_T^{\text{lep}})]$
Veto track Veto track isolation	charged particle-flow candidate, $p_T > 10$ GeV, $\vert\eta\vert < 2.4$ $p_T^{\text{sum}} < \min\left(0.1 \times p_T^{\text{lep}}, 6\text{ GeV}\right)$, $\Delta R = 0.3$
Veto hadronic tau Veto hadronic tau isolation	tau ID, $p_T > 20$ GeV, $\vert\eta\vert < 2.4$ $\Delta R = 0.4$

Table 5.1: The triggers and the object definition. p_T^{lep} is the p_T of the lepton and the p_T^{sum} is the scalar sum of the p_T of all PF candidates which are located in a cone around the lepton, but excluding the lepton itself. p_T^{sum} for the selected and veto lepton is computed from the charged and neutral PF particles, while for the veto track only charged particles are used. The label "light flavor" denotes that the jet originates from u, d or s quarks or gluons [129].

pass looser p_T threshold, isolation criteria, or identification than the selected one. A common isolation definition used for the majority of the SUSY analyses, differs from the standard CMS one. It is defined as a function of the sum of the p_T of PF candidates which are within a cone around the lepton. The isolation cone size parameter depends on the p_T of the lepton and the cone size parameter starts at 0.2 for p_T^{lep}<50 GeV and then changes to $10.0/p_T^{\text{lep}}$ for 50< p_T^{lep} <200 GeV. For p_T^{lep}>200 GeV the cone size parameter is of 0.05. This procedure ensures that in the case of boosted topologies when a lepton and a jet can be close to each other, the cone size decreases for the lepton not to be affected by the jet fragments in its proximity.

Jets and b-tagged jets The jets are reconstructed by the anti-kt [42] algorithm with a cone distance parameter of 0.4. The jet p_T is required to be higher than 30 GeV and the jet must be in the range $\vert\eta\vert < 2.4$. Either a medium or a tight working point (WP) of the b-tagging CSVv2 algorithm is used for the definition of the signal regions.

Veto on isolated tracks The majority of hadronically decaying tau leptons decay into

one charged track which is predominantly a charged hadron. Therefore the events with taus can be suppressed by vetoing events which have one isolated charged track from hadron. This veto also helps to suppress a second muon or electron in the event originating from the tau decay or the W decay.

Veto on hadronic tau This additional tau veto, using tau identification criteria, helps to veto the taus which do not pass the isolated track selection. It mainly helps to reduce the lost lepton background.

Missing transverse energy The missing transverse momentum referred to as "missing transverse energy" is used as defined in Section 1.3.6. Following the CMS recommendations, several additional E_T^{miss} filters, e.g. filters for bad or duplicate muons, are applied.

The summary of the object selection criteria is presented in Table 5.1.

5.2.4 Search variables

Discriminating variables are built from the objects defined in previous section and their properties, kinematics or multiplicities. The variables considered for the presented stop analyses to define the baseline search region (see Section 5.2.5) as well as the signal regions (Section 5.2.6) are introduced in the following subsections.

5.2.4.1 Number of leptons (N_ℓ)

The presented search focuses on final states with one charged lepton and therefore a requirement on the number of leptons to be equal to one must be imposed. The lepton is either an electron or a muon and the events with tau leptons are rejected. No additional lepton from the veto lepton category is allowed.

5.2.4.2 Number of jets (N_J)

As shown in blue in the example in Fig. 5.5, at least four jets are expected in the considered signal final states. But because of the low mass difference between the chargino and the neutralino in the T2tb model, the two jets from the hadronically decaying W boson have low p_T and thus they may not be selected, therefore only two jets are expected. In the case of a high Δm value, the decay products of the stops can be boosted and thus two or more jets can be merged into one, resulting to a reduced number of selected jets in final

state. The baseline selection requires to have at least two jets, but this variable is also later used for the definition of signal regions targeting different topologies.

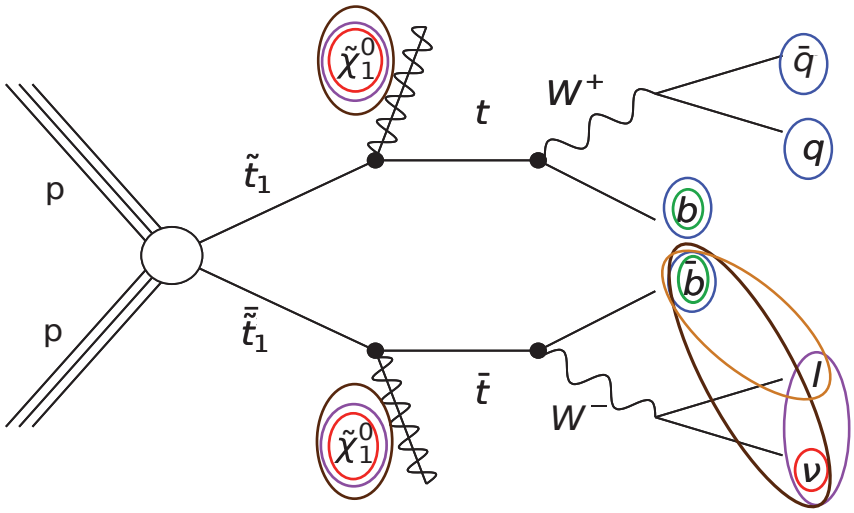

Figure 5.5: Diagram of the T2tt signal model supporting the choice of N_J (blue), E_T^{miss} (red), M_T (magenta), $\min\Delta\phi(j_{1,2}, E_T^{miss})$ (brown) and $M_{\ell b}$ (orange) as discriminating variables [130].

5.2.4.3 Number of b-jets (N_b)

In the diagram of Fig. 5.5 it can also be noticed that two jets in green are originating from b quarks. For this reason the number of selected b-tagged jets is one of the discriminating variables, which is in the baseline search region chosen to be larger or equal to one. In the signal regions where the $W + jets \to 1\ell$ background is dominant, the tight b-tagging working point is used to further suppress it, as the jets are expected to be mainly composed of light flavors.

5.2.4.4 Missing transverse energy (E_T^{miss})

The red circles in Fig. 5.5 show that there are two neutralinos and one neutrino originating from the leptonically decaying W boson in the final states of the signal processes. These particles escape from the detector and lead to missing momentum in the transverse plane. E_T^{miss} is very powerful in rejecting the SM backgrounds because they tend to have smaller values of E_T^{miss} as the sources of E_T^{miss} are more limited than in the case of the signal processes. However, because of the presence of two neutrinos and one lost lepton in the lost lepton background, the E_T^{miss} value of this background can be very large. This also applies for the processes of the $Z \to \nu\bar{\nu}$ background, where the source of E_T^{miss} are three neutrinos.

Therefore the baseline selection requires E_T^{miss} to be larger than 250 GeV. The E_T^{miss} distribution in the baseline search region for all relevant backgrounds and three selected signal scenarios is shown in the left plot of Fig. 5.6. The 1ℓ background is decomposed into two processes which are later referred to as "1ℓ from top" populated mainly by the $t\bar{t} \to 1\ell$ events and "1l not from top" populated by the $W + jets \to 1\ell$ process. The E_T^{miss} has also been, as expected, found to be a good variable for the definition of the signal regions.

5.2.4.5 Transverse mass of the lepton-E_T^{miss} system (M_T)

The M_T variable is defined as

$$M_T = \sqrt{2p_T^{\text{lep}} E_T^{miss}(1 - \cos(\phi))}, \tag{5.12}$$

where p_T^{lep} is the transverse momentum of the lepton and ϕ is the angle between the lepton and the direction of E_T^{miss} in the transverse plane. The combination of a selection on the M_T and E_T^{miss} ensures a drastic reduction of the SM background. The M_T variable is designed to suppress backgrounds where both the lepton and E_T^{miss} come from one W boson. In that case the E_T^{miss} corresponds to the neutrino of this W boson and the the M_T has an endpoint at the W boson mass (∼80 GeV). As shown in the diagram of Fig. 5.5, the leptonically decaying W boson is not the only source of the E_T^{miss} and therefore no endpoint is expected for the signal.

The baseline search region requires events with M_T larger than 150 GeV, suppressing mainly the 1ℓ background, as in that case the lepton and E_T^{miss} in both the $W + jets \to 1\ell$ and $t\bar{t} \to 1\ell$ processes originate from one W boson. It can be seen in the right plot of Fig. 5.6, that indeed the bulk of the one lepton events have a low M_T value, but a tail survives at high M_T. For the $t\bar{t} \to 1\ell$ process, the top quark constraints the kinematics of the W boson and therefore the tail in M_T is mainly caused by the E_T^{miss} resolution. The situation is different for the $W + jets \to 1\ell$ background, where the kinematics permits the off-shell production of W boson and consequently $m_{W^*} > 80$ GeV. For the lost lepton and $Z \to \nu\bar{\nu}$ backgrounds, there is no endpoint as the E_T^{miss} does not originate from one W boson.

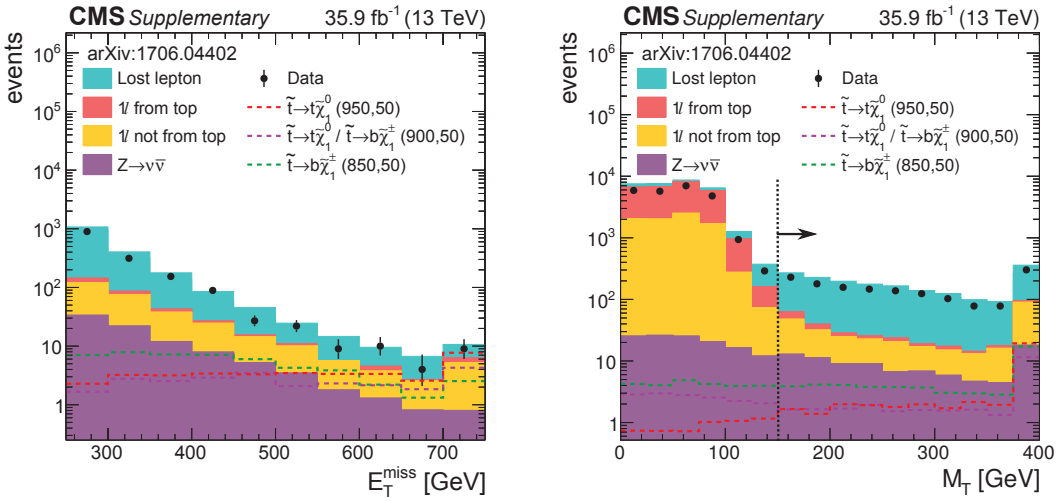

Figure 5.6: Data (black dots), background (full colored histograms) and signal (dashed lines) distributions of the E_T^{miss} (left) and M_T (right) variables after applying the baseline selection. The cut on M_T is not applied in the the right plot, but only indicated by the black arrow [144].

5.2.4.6 Minimal azimuthal angle between the direction of one of the two leading jets and the E_T^{miss} (min$\Delta\phi(j_{1,2}, E_T^{miss})$)

For the background events where a neutrino is the only source of E_T^{miss}, it is probable that this neutrino is close to the b quark originating from the same top decay. This appears for example for the $t\bar{t} \to 1\ell$ process. To exploit this particularity, one can define the variable $\text{min}\Delta\phi(j_{1,2}, E_T^{miss}) = \text{min}\{\Delta\phi(j_1, E_T^{miss}), \Delta\phi(j_2, E_T^{miss})\}$ where $\Delta\phi(j_i, E_T^{miss})$ represents the azimuthal angle between the direction of the jet i (j_1 being the leading jet, and j_2 the subleading one) and $\vec{E}_T^{miss}$. This variable is shown in the left plot of Fig. 5.7. In the case of the signal, as depicted in magenta in the diagram of Fig. 5.5, there are more sources of the E_T^{miss} and therefore there is no expected constraint on $\text{min}\Delta\phi(j_{1,2}, E_T^{miss})$. The chosen baseline requirement on the $\text{min}\Delta\phi(j_{1,2}, E_T^{miss})$ to be larger than 0.8 has been found to considerably reduce the suggested $t\bar{t} \to 1\ell$ process but also the $t\bar{t} \to 2\ell$ background while leading to a relatively small reduction of the signal.

5.2.4.7 Invariant mass of the system composed by the selected lepton and the closest b-tagged jet ($M_{\ell b}$)

When a lepton and a b-jet originate from a one top quark as displayed in Fig. 5.5, the $M_{\ell b}$ variable, computed as the invariant mass of the system composed by the selected lepton

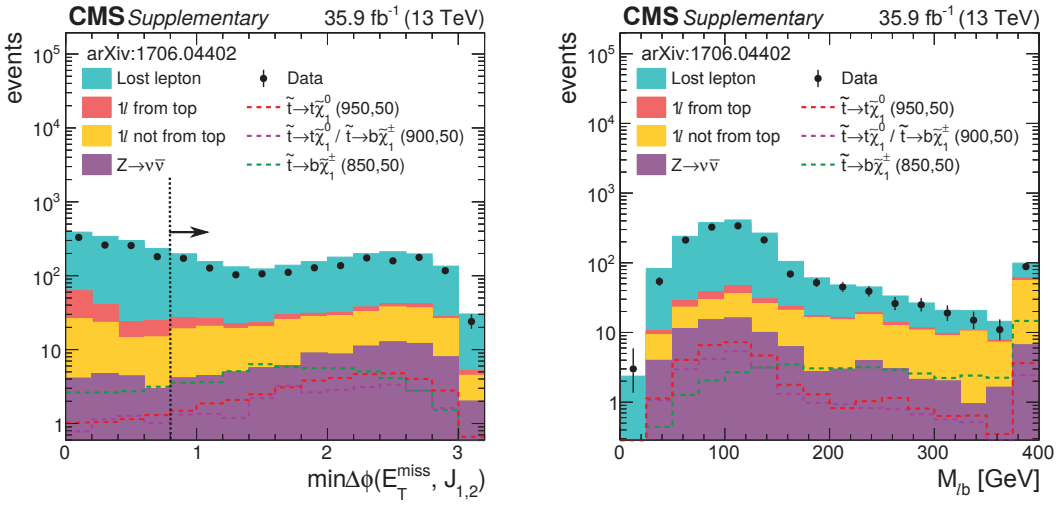

Figure 5.7: Data (black dots), background (full colored histograms) and signal (dashed lines) distributions of the $\min\Delta\phi(j_{1,2}, E_T^{miss})$ (left) and $M_{\ell b}$ (right) variables after applying the baseline selection. The cut on $\min\Delta\phi(j_{1,2}, E_T^{miss})$ is not applied in the the left plot, but only indicated by the black arrow [144].

and the closest b-tagged jet, presents a bound around

$$m_t\sqrt{1-\frac{m_W^2}{m_t^2}} \approx 153 \text{ GeV}, \tag{5.13}$$

where m_t is the mass of the top quark and m_W the W boson mass. This limit is true for backgrounds coming from $t\bar{t}$ decays, but also for the T2tt signal. On the other hand there is no limit for the $W + jets \to 1\ell$ background and the T2bW signal. Therefore this variable is not suitable for the baseline region definition, as putting a constraint on it could considerably reduce one of the targeted signals but it can be used later to define signal regions which discriminate among the signal scenarios as well as suppress part of the backgrounds. The distribution of the $M_{\ell b}$ variable for all relevant backgrounds and three different signals is shown in Fig. 5.7 after the baseline selection. It can be clearly noticed that the low $M_{\ell b}$ part of distribution is dominated by the lost lepton background and is more sensitive to the T2tt signal, while in the high $M_{\ell b}$ part the relative fraction of backgrounds coming from the $W + jets \to 1\ell$ process is increased and the T2bW signal shows a higher yield than the other signals.

5.2.4.8 Modified topness (t_{mod})

The topness variable [145] is a χ^2-like variable developed to suppress the background coming from the $t\bar{t} \to 2\ell$ process with one lost lepton. Its aim is to evaluate how well

an event agrees with the $t\bar{t} \to 2\ell$ hypothesis, given that one lepton is lost. It has been discovered that removing several terms from the topness variable, improves the signal discrimination in this analysis. The new variable called "modified topness" (t_{mod}) is obtained by minimization of variable S and is defined as

$$t_{mod} = \ln(\text{minS}), \text{ where } S(\vec{p}_W, p_{\nu,z}) = \frac{(m_W^2 - (p_\nu + p_\ell)^2)^2}{a_W^4} + \frac{(m_t^2 - (p_{b_1} + p_W)^2)^2}{a_t^4}, \quad (5.14)$$

with m_W and m_t being the masses of the W boson and the top quark, p_W, p_ν, p_ℓ, p_{b_1} being the momenta of the W boson supposed to be fully invisible due to the lost lepton, the neutrino, the selected lepton and the b-jet respectively. The parameters $a_W = 5$ GeV and $a_t = 15$ GeV are the resolution parameters. The first term in Eq. 5.14 aims to reconstruct the mass of the W boson whose lepton is selected. The purpose of the second term is to reconstruct the top mass of leg, for which the lepton is lost. There are different options how to chose the b-jet in the event. For this analysis the following procedure is chosen: The modified topness is computed for the three jets having the highest CSVv2 discriminator values, and then the jet which leads to the smallest modified topness is chosen.

Different backgrounds and signal models with different Δm populate the t_{mod} distribution shown in Fig. 5.8 differently, therefore this variable is valuable for the definition of signal regions. It can be noticed that the t_{mod} variable has a double peak shape. The left peak is populated by the events where the objects are correctly identified to originate from the given W boson and top quark, while in the one on the right at least one a object is wrongly taken for the computation of the modified topness.

5.2.4.9 An alternative variable discriminating against the lost lepton background (M_{T2}^W)

The purpose of the M_{T2}^W variable is similar to that of the modified topness, i.e. to reduce the lost lepton background. This variable similarly tries to reconstruct the event under the $t\bar{t} \to \ell\ell$ hypothesis with one lost lepton. Its definition is

$$M_{T2}^W = \min\{m_y, \text{ consistent with : } [p_1^2 = 0,\ (p_1 + p_\ell)^2 = p_2^2 = m_W^2,\ \vec{p}_{1,T} + \vec{p}_{2,T} = \vec{E}_T^{miss} \\ (p_1 + p_\ell + p_{b_1})^2 = (p_2 + p_{b_1})^2 = m_y^2]\}, \quad (5.15)$$

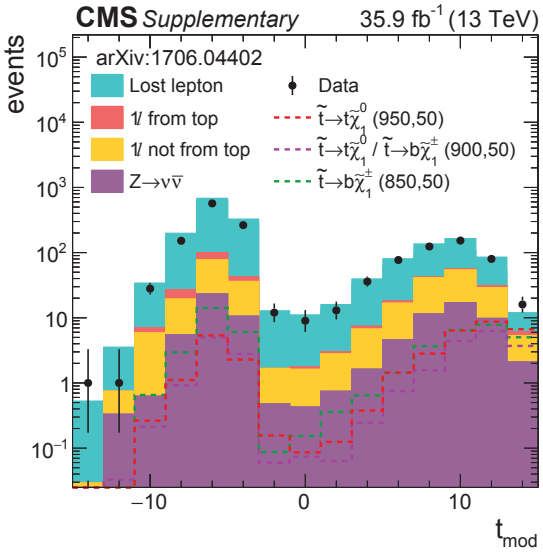

Figure 5.8: Data (black dots), background (full colored histograms) and signal (dashed lines) distributions of the t_{mod} variable after applying the baseline selection [144].

where m_y is the fitted mass of the mother particle and the different p_i represent the four-momenta of the neutrino (p_1) from the W boson whose lepton is selected, the invisible W boson (p_2), the two b-jets (p_{b_1} and p_{b_2}) and the selected lepton p_ℓ, respectively. The constraint on the mass m_W of W boson is used. The b-jets b_1 and b_2 selected from the three jets with the highest CSVv2 discriminator as the jets which lead to the lowest M_{T2}^W.

Following the definition of M_{T2}^W, an endpoint around the top mass is expected for the $t\bar{t}$ events with a lost lepton. It would be possible to use this variable for the baseline selection by requiring a high value of M_{T2}^W, but it has been found out that signals with low Δm also lead to small M_{T2}^W. In the 2015 and ICHEP2016 analyses [129, 130], the M_{T2}^W variable was used in the definition of signal regions. It shows a very similar behavior as the t_{mod} variable and with more statistics collected it has been found out that the t_{mod} is more discriminating in the full analysis phase-space than the M_{T2}^W variable. Therefore in the current analysis the M_{T2}^W variable is not used anymore.

5.2.4.10 Number of W-tagged jets (N_W)

For signals with high Δm, the top quarks originating from the stop decays are expected to be significantly boosted. The boost of the top quarks within the SM is less likely and therefore tagging of boosted objects could help the signal discrimination. As shown in Fig. 5.9 when the momentum of the hadronically decaying top quark is low, three resolved anti-kt jets with cone distance parameter of 0.4 are observed. With a growing boost of the top quark, the jets originating from the W boson or all three jets of the top quark can

be merged into one "fat" jet. The merged jets can be tagged by special W- or top-tagging techniques.

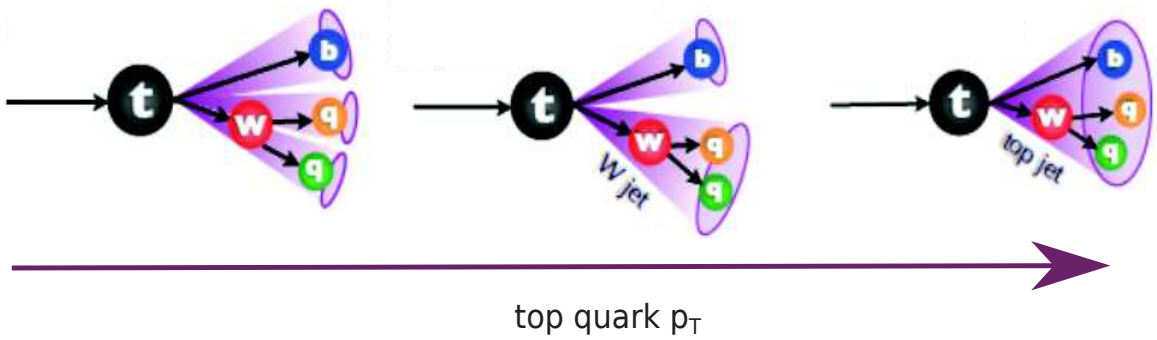

Figure 5.9: A schema of the jet configuration of a hadronically decaying top quark depending on its boost.

I have worked on the evaluation of the potential increase in sensitivity that W-tagging techniques could bring to the stop analysis. The study is performed in the context of the 2015 single lepton stop analysis [129] using data collected in 2015 at center-of-mass energy of 13 TeV and corresponding to an integrated luminosity of 2.3 fb^{-1}.

The standard jets used in the analysis are clustered by the ak4 algorithm. The boosted W jets are expected to be fat and therefore need to be re-clustered with a different cone distance parameter. In the study two possibilities are exploited, ak8 jets with a cone distance parameter of 0.8 and ak10 jets with a cone distance parameter of 1.0. The merged W jet should have a large transverse momentum and a mass around the mass of W boson. Therefore a requirement on the jet mass helps to identify a merged jet originating from a W boson. The raw mass of the jet is contaminated by initial state radiations, underlying events and pileup and therefore it must be cleaned from these contributions. Several "grooming techniques" of the jet mass are exploited by CMS collaboration, but in this study only the "pruned mass" is used, as it was the technique recommended by CMS for the W-tagging [146]. The pruning procedure [147] rejects large angle and soft constituents during the re-clustering iterations. Another variable used in W-tagging is called the N-subjettiness (τ_N) which aims to discriminate how much the jet is consistent with the N-jet hypothesis. For example the merged jet of a W boson should contain two jets and therefore be consistent with the 2-jet hypothesis, but not the with 3-jet one. The N-subjettiness ratio $\tau_{21} = \tau_2/\tau_1$ has a high discriminating power for merged W jets and therefore in this study a requirement on τ_{21} is used to tag merged W-jets. Typical distributions of the pruned mass and τ_{21} are shown in Fig. 5.10 taken from [148]. In the plots it can be noticed that W+jets events mostly contain unmerged W bosons and therefore they have a low pruned mass and lead to a broad τ_{21} distribution. The fraction of the pruned jets around 80 GeV, therefore merged W-jets, is enhanced in the case of $t\bar{t}$

events, leading to lower values of τ_{21}. Taking into account the discriminating variables, I design two selections of the W-tagged jets referred to as "ak8-W" and "ak10-W", presented in Table 5.2 and used in the following.

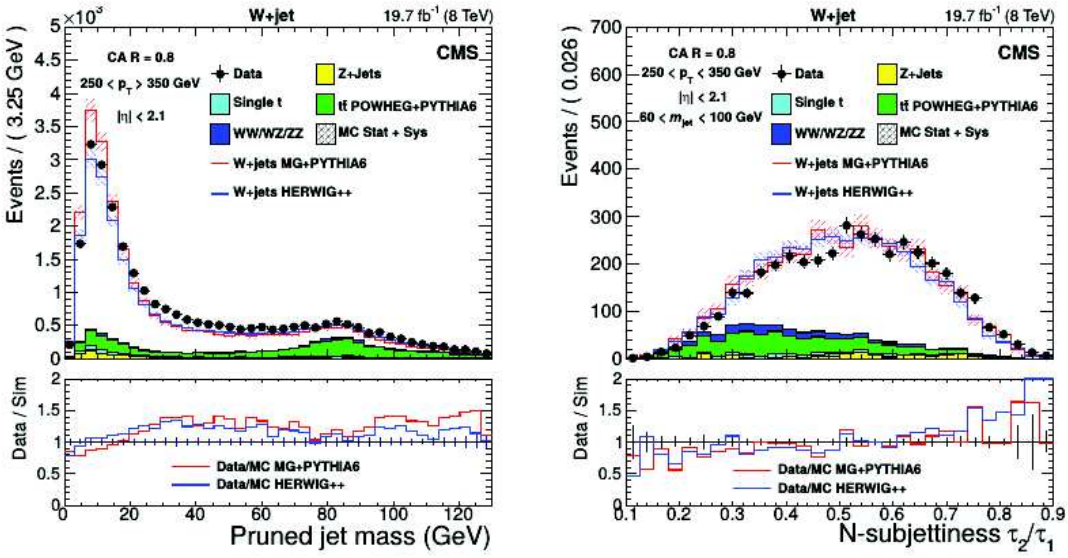

Figure 5.10: Data and simulation distribution of the jet pruned mass (left) and the N-subjettiness ratio τ_{21} (right) for W+jets events. The data-to-simulation ratios are shown at the bottom of the plots [148].

Name	Clustering algorithm	pruned mass $m_{W,p}$ [GeV]	τ_{21}	p_T [GeV]
ak8-W	ak8	60<$m_{W,p}$<100	<0.5	>200
ak10-W	ak10	60<$m_{W,p}$<100	<0.5	>200

Table 5.2: The definition of the "ak8-W" tagged and "ak10-W" tagged jet.

The 2015 analysis defines four categories of signal regions targeting signals with different kinematics. In this study, I focus only on the region groups addressing the high Δm phase space and referred to as "High Δm" and "Boosted High Δm" in Table 5.3. I redefine the signal regions based on the number of W-tagged jets (N_W) instead of E_T^{miss}, but kept the number of the signal regions the same. The new proposed signal regions are shown in Table 5.4.

To evaluate the benefits of the W-tagging, the expected significances in the default signal regions of Table 5.3 are compared to the expected significances of the proposed W-tagging signal regions in Table. 5.4. The significance, described in Section 5.2.1, is the expected significance when using generated pseudo-data with a signal strength of one, instead of the observed data. For this comparison all relevant backgrounds as well as three different T2tt signal points with different stop and neutralino masses ($m_{\tilde{t}_1}$, $m_{\tilde{\chi}_1^0}$) are used. These signal point masses in GeV are (900, 1), (800, 300) and (650, 450). In this

Name	N_J	M_{T2}^W [GeV]	E_T^{miss} [GeV]
High Δm	$\geq$4	>200	250<E_T^{miss}<350
	$\geq$4	>200	350<E_T^{miss}<450
	$\geq$4	>200	E_T^{miss}>450
Boosted High Δm	=3	>200	250<E_T^{miss}<350
	=3	>200	E_T^{miss}>350

Table 5.3: The signal regions of the 2015 analysis [129].

Name	N_J	M_{T2}^W [GeV]	E_T^{miss} [GeV]	N_W
High Δm W-tagging	$\geq$4	>200	250<E_T^{miss}<350	–
	$\geq$4	>200	E_T^{miss}>350	=0
	$\geq$4	>200	E_T^{miss}>350	=1
Boosted High Δm W-tagging	=3	>200	E_T^{miss}>250	=0
	=3	>200	E_T^{miss}>250	=1

Table 5.4: Proposed signal regions using the W-tagged jets multiplicity.

study the significances are computed for two different luminosity options (2.3 fb^{-1} and 10 fb^{-1}) and the two different selections of W-tagging definition in Table 5.2. The default signal regions and the newly proposed W-tagged signal regions are differently combined, the best performing combination of the signal regions is the combination of the "High Δm W-tagging" category with the "Boosted High Δm" category.

In Table 5.5, the significances of the best performing combination for both ak8-W and ak10-W are shown together with the significances of the default signal regions for three signal points and an integrated luminosity of 2.3 fb^{-1}. It can be noticed that using ak10-W jets leads to a larger significance than ak8-W jets. Although there is an increase in the significance up to around 20 % in some cases, the increase is not large enough to support the usage of complicated W-tagger, highly consuming in computing resources and providing a significant gain only for high Δm signals. It is important to note that, compared to what is at the end achieved with the full analysis, many simplifications are done in this study: an uncorrelated systematic uncertainty of 30% is used in each SR and per process, and the background yields are taken directly from simulated samples. Moreover it would be necessary to compute the W-tagging efficiency and eventually derive scale factors correcting differences between data and simulation. Therefore also a large effort would be needed to provide data-driven estimations of the backgrounds and the corresponding systematics.

When studying the significances for an integrated luminosity of 10 fb^{-1}, it has been found that the gain in significance raises up to around 30% when using the W-tagging

and therefore the W-tagging can be an interesting option for analyses based on data with larger integrated luminosity.

$\mathcal{L} = 2.3$ fb^{-1}	ak4 [128]	ak8-W	ak10-W
Signal points ($m_{\tilde{t}_1}$, $m_{\tilde{\chi}_1^0}$)	High Δm + Boosted High Δm	High Δm W-tagging + Boosted High Δm	High Δm W-tagging + Boosted High Δm
(900,1)	1.43	1.35	1.70
(800,300)	1.93	1.96	2.34
(650,450)	0.21	0.21	0.23

Table 5.5: Significances for three different T2tt signal points (first column) using the default SRs (second column) and then a mix of SRs defined by using "ak8-W" (third column) and "ak10-W" (fourth column) tagged jet multiplicity for an integrated luminosity of 2.3 fb^{-1}.

5.2.5 The baseline selection

Based on how the objects are selected or vetoed and which kinematic variables help to suppress the SM background while keeping high signal yields, the baseline search region of the full 2016 analysis is defined as follows:

- One good selected primary vertex
- Exactly one selected electron or muon
- No veto lepton, isolated track or hadronic tau
- At least two selected jets
- At least on b-jet passing the medium WP
- E_T^{miss} >250 GeV
- M_T>150 GeV
- min$\Delta\phi(j_{1,2}, E_T^{miss}) > 0.8$

5.2.6 Definition of the signal regions

In order to increase the sensitivity of the analysis to the signal, the baseline search region can be further divided into signal regions with the help of the discriminating variables defined in Section 5.2.4. For the nominal search there are 8 signal region groups denoted

from A to H, leading to 27 exclusive signal regions in total, which are based on selections on N_J, t_{mod}, $M_{\ell b}$ and E_T^{miss}. To further suppress $W + jets \rightarrow 1\ell$ background, the tight b-tagging WP is used in regions where $M_{\ell b}$ >175 GeV. An additional group I of four signal regions is created for the T2tt compressed spectrum where 100<Δm<225 GeV. The definition of the signal regions is shown in Table 5.6.

Group	N_J	t_{mod}	$M_{\ell b}$ [GeV]	E_T^{miss} [GeV]
A	2-3	>10	≤175	250-350, 350-450, 450-600, >600
B	2-3	>10	>175	250-450, 450-600, >600
C	≥4	≤0	≤175	250-350, 350-450, 450-550, 550-650, >650
D	≥4	≤0	>175	250-350, 350-450, 450-550, >550
E	≥4	0-10	≤175	250-350, 350-550, >550
F	≥4	0-10	>175	250-450, >450
G	≥4	>10	≤175	250-350, 350-450, 450-600, >600
H	≥4	>10	>175	250-450, >450
I	≥5	–	–	250-350, 350-450, 450-550, >550

Table 5.6: The 27 signal regions of the nominal analysis divided into groups A to H. In the high $M_{\ell b}$ signal region groups B, D, F and H the b-tagged jet must pass the tight working point instead of the medium one. The group I is composed of 4 exclusive signal regions for the T2tt compressed analysis, satisfying additional cuts described in the text.

In the compressed T2tt region the top quarks are produced off-shell or with a very low momentum, limiting the available momentum, and therefore their decay products have very low p_T consequently leading to low E_T^{miss}. Obviously, such kind of signal has different kinematics and the baseline selection and categorization into SRs must be adjusted to account for it. To pass the E_T^{miss} selection characteristic for SUSY signatures, the stop pair must be boosted against an initial state radiation (ISR), leading to the requirement of an additional jet in the event. The ISR jet should have the largest p_T, but such requirement does not help the overall signal discrimination as E_T^{miss} >250 GeV is already required. The jet with the highest p_T must fail the medium b-tagging working point in order to increase the probability that it comes from the ISR. The stop system is expected to be boosted in the opposite direction with respect to the ISR jet and thus the direction of objects originating from the stop pair decay, like the E_T^{miss} and the lepton, should have a similar direction. As the p_T of the objects in the compressed region is not large, putting a limit on lepton p_T has been found to be useful for the signal discrimination. Taking these considerations into account the following additional criteria are imposed for the compressed regions I:

- At least five jets
- One lepton with p_T^{lep}<150 GeV

– The leading jet is not b-tagged

– $\Delta\phi(E_T^{miss}, \ell)$<2.0

– min$\Delta\phi(j_{1,2}, E_T^{miss})$>0.5

In the previous versions of the analysis (2015 [129] and ICHEP2016 [130]), there was a lower number of signal regions, due to the smaller available data statistics. Also as discussed before in Section 5.2.4.9, the M_{T2}^W variable was used instead of t_{mod} in the definition of the majority of the signal regions. In the presented full 2016 analysis, a new discriminating variable $M_{\ell b}$ is introduced.

5.3 Background estimations

In this section, the estimations of all relevant background yields in the signal regions together with their systematic uncertainties are discussed. The lost lepton background, coming from the $t\bar{t} \to 2\ell$, single top (tW), $t\bar{t}V$ and diboson processes where one of the two leptons is missing, is the largest contribution in the signal regions with low $M_{\ell b}$ values and at least four jets. This background is estimated in control regions with two leptons (dilepton CR). The one lepton background, represented by the $W + jets \to 1\ell$, $t\bar{t} \to 1\ell$, and single top (s- and t-channel) processes, is largely suppressed by the E_T^{miss} and M_T cuts. After these cuts, the yield of the 1ℓ background coming from processes involving top quarks ($t\bar{t} \to 1\ell$ and single top in the s- and t-channel) is small in the signal regions and can be estimated from simulations. The $W + jets \to 1\ell$ process leads to a larger contribution especially in regions with high $M_{\ell b}$ and it is estimated in the control regions with zero b-tagged jets (0 b-tag CR). The $Z \to \nu\bar{\nu}$ background is the last relevant background group composed by the $t\bar{t}Z$ and WZ processes, in which the Z boson decays to neutrinos and one W boson decays leptonically. The yields of $Z \to \nu\bar{\nu}$ in the signal regions are estimated from simulation, and corrected by an overall normalization factor measured in a three lepton control region.

For the full 2016 analysis I was in charge to provide the estimation of the $Z \to \nu\bar{\nu}$ background. In this section the estimation of this background is therefore described first and then built on the knowledge of the $Z \to \nu\bar{\nu}$ background estimation method, the other background estimates are presented.

5.3.1 The $Z \to \nu\bar{\nu}$ background estimation

The $Z \to \nu\bar{\nu}$ background represents overall the smallest relevant group of backgrounds, but it is largely enhanced in signal regions with high E_T^{miss} and high t_{mod} values. The main contribution to the $Z \to \nu\bar{\nu}$ background comes from the $t\bar{t}Z$ process. However at low jet multiplicities, the WZ process becomes an important part of this background. The previous versions of this analysis estimated this background purely from simulation, because of the low statistics in the three lepton control region. Now with a larger dataset, the global normalization of these two processes is derived from a data-driven method, but the relative splitting of events between signal regions (shape) is taken from simulation. Nevertheless it is important to mention that in case the shapes of the discriminating variables differ between data and simulation, the background estimation can be influenced by migration of events between the signal regions. Therefore the target is to define as many control regions and the signal ones, once there is sufficient statistics, which is unfortunately not the case for $Z \to \nu\bar{\nu}$ background.

5.3.1.1 Principle of the data driven estimate

To explain the data-driven background estimation technique, let's consider only one signal region and one control region. The CR is a region enriched in events of the process under study and is typically defined similarly as the signal region, just changing a certain requirement. In the case of the $Z \to \nu\bar{\nu}$ background, the selection on the lepton multiplicity is modified: a three lepton control region is chosen to consider the Z boson decay into two leptons instead of two neutrinos. The definition of a control region is a trade-off between applying a selection as close as possible to the SR to avoid extrapolation and the need to collect enough statistics.

The relationship between the data (N^{Data}) and simulation (N^{MC}) yields in the SR and control CR can be written as follows

$$\frac{N^{Data,\ SR}}{N^{Data,\ CR}} = \frac{N^{MC,\ SR}}{N^{MC,\ CR}}. \tag{5.16}$$

Therefore the estimated background yield in the SR ($N^{Data_{Est},\ SR}$) can be obtained from the data yield in control region ($N^{Data,\ CR}$) and the simulation based transfer factor (TF^{MC}) transferring the yield from the control region to the signal region. To achieve this, Eq. 5.16 can be rewritten as

$$N^{Data_{Est},\ SR} = N^{Data,\ CR} \times \frac{N^{MC,\ SR}}{N^{MC,\ CR}} = N^{Data,\ CR} \times TF^{MC}. \tag{5.17}$$

Alternatively, Eq. 5.16 can be rearranged in terms of simulated yield in the signal region ($N^{MC,\ SR}$) and the normalization factor (NF^{CR}) determined in the CR

$$N^{Data_{Est},\ SR} = N^{MC,\ SR} \times \frac{N^{Data,\ CR}}{N^{MC,\ CR}} = N^{MC,\ SR} \times NF^{CR}. \tag{5.18}$$

However, in the analysis there is not only one single signal region and thus the background yield estimations in Eq. 5.17 or 5.18 need to be performed for each signal region separately. Ideally the same number of control regions as of signal regions should be used to keep the kinematics as close as possible between the SR and CR. Consequently there should be the same number of transfer factors or normalization factors as of signal regions, depending which equation is used (Eq. 5.17 or 5.18). The $Z \to \nu\bar{\nu}$ background estimation follows Eq. 5.18's strategy. But the three lepton control regions suffer from a lack of statistics and therefore only one control region can be used. In addition, ideally, one designed CR should address the background estimate of only one process. The situation is a bit more complicated for the $Z \to \nu\bar{\nu}$ background as both the $t\bar{t}Z$ and WZ processes populate the CR. Therefore in that case, two normalization factors, one for each process, are determined separately from a template fit of the N_b distribution in the three lepton control region as described in the following subsection. For the $Z \to \nu\bar{\nu}$ background the Eq. 5.18 can be rewritten as

$$N_{proc}^{Data_{Est},\ SR} = N_{proc}^{MC,\ SR} \times NF_{proc,\ 3\ell}^{CR}, \tag{5.19}$$

where $proc = t\bar{t}Z$ or WZ.

5.3.1.2 Scale factors from the three lepton control region

The normalization factors for the $t\bar{t}Z$ and WZ processes are taken from the paper [149] searching for BSM physics in final states with two leptons of same sign, E_T^{miss}, and jets. For this purpose a three lepton control region is defined by the requirements:

- Two leptons passing the nominal isolation and identification criteria as defined in [149], the leading lepton should have p_T >25 GeV and the trailing one a p_T >20 GeV
- A third lepton of p_T >10 GeV should pass the tight identification and must have an opposite sign and the same flavor as one of the leptons above; the formed lepton pair must have a mass within a ±15 GeV window around the Z boson mass
- $H_T = \sum_{jets} p_T$>80 GeV

– $N_J \geq 2$ with jet p_T >40 GeV

– No requirement on b-tagging

– $E_T^{miss} > 30$ GeV.

The $t\bar{t}Z$ and WZ processes are expected to have a different number of b-jets and therefore a fit of the b-jet multiplicity distribution allows to extract the normalization factors of $t\bar{t}Z$ and WZ. The CR bin with zero b-jet is composed at ∼70% by the WZ process, while the $t\bar{t}Z$ process represents around 70% of the rest of the b-jet distribution. In addition to these two processes, there is also a contribution to the control region from non-prompt leptons, the $t\bar{t}H$, $t\bar{t}W$, and WW processes as well as processes collectively denoted as "rare SM" and "$X+\gamma$". The rare SM contribution arises mainly from diboson (ZZ), triboson (WWW, WWZ, WZZ, ZZZ), Higgs (HZZ, VH where V=Z,W), same-sign WW from double-parton scattering (DPS WW), and rare top (tZq and $t\bar{t}t\bar{t}$) processes decaying to three leptons. The "$X+\gamma$" group is composed by processes where one of the selected leptons is an electron from an unidentified photon conversion, such processes being predominantly $W\gamma$, $Z\gamma$, $t\bar{t}\gamma$ and $t\gamma$.

The distribution of the number of b-jets in data is simultaneously fitted by the discussed simulated components, letting only the normalization of different contributions free to vary. This fit procedure results in a normalization factor for $t\bar{t}Z$ of 1.14 ± 0.30 and for WZ of 1.26 ± 0.09. The uncertainty on the normalization factors includes both the statistical uncertainty and an uncertainty on the shape of the b-jet distribution in the simulation. The post-fit distribution of number of b-jets in the three lepton control region is shown in Fig. 5.11.

5.3.1.3 Estimation of the $Z \to \nu\bar{\nu}$ background

The final estimations of the $t\bar{t}Z$ and WZ yields are computed according to Eq. 5.19 for which the simulated events are corrected by the object scale factors for the different lepton and b-tagging efficiencies in data and simulation, which is a standard procedure for all background estimates. On top of this, the events in the $t\bar{t}Z$ sample are reweighted in order to improve the modelling of jets coming from the ISR. Because the WZ process is generated at NLO, its yields in the signal regions can be negative. In this analysis, a SR with a negative yield is not allowed and its yield is reset to 0. The final $t\bar{t}Z$ and WZ yields are shown in Table 5.7. The uncertainties on the estimates include both the statistical and systematic uncertainties, which are described later in the following subsection.

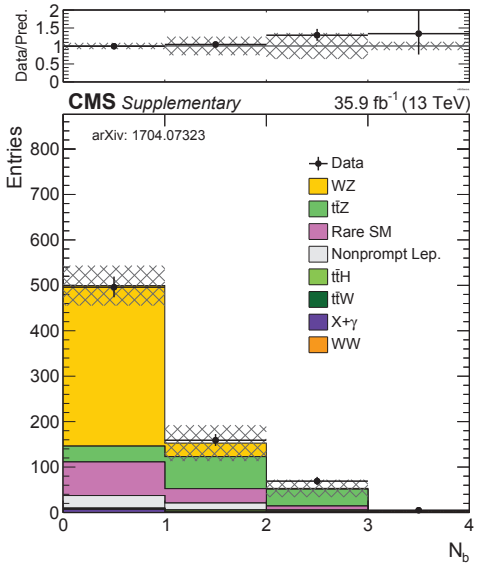

Figure 5.11: The post-fit distribution of the number of b-tagged jets in the three lepton control region [149]. The distribution in data is simultaneously fitted by the SM background components to obtain the normalization factors for the $t\bar{t}Z$ and WZ processes. The top panel shows the data-to-simulation ratio with an uncertainty composed by the statistical uncertainty and an uncertainty on the shape of the b-jet distribution in the simulation.

5.3.1.4 Systematic uncertainties on the $Z \to \nu\bar{\nu}$ background estimation

In general, there are three kinds uncertainties entering into the background estimate. The first one is the uncertainty on the theoretical quantities used for the production of the simulated samples. The second group arises, for example, from the differences in modelling of the physics objects in data and simulation. The third category comprises the uncertainty due to the limited statistics in simulated and control data sample. Many uncertainties are common to all background estimates and therefore here again, due to my personal involvement, the systematic uncertainties for the $Z \to \nu\bar{\nu}$ background is described in a detail. The differences for other backgrounds are discussed later.

Theoretical uncertainties

The "theoretical uncertainties" consists of uncertainties arising from the choice of the factorization and renormalization scale, particle distribution functions (PDFs) and the strong coupling constant (α_S). As for the $Z \to \nu\bar{\nu}$ processes the background yields in signal regions are taken from simulation and only normalized by an overall factor determined by the data-driven method, this background estimate is sensitive to the migrations of events between signal regions due to imprecise modelling of the theoretical parameters in the simulation. Because of the limited statistics in the signal regions, large fluctuations driven by the statistics are observed when varying the theoretical parameters. To avoid

	ttZ	**WZ**	**Total**
A 250$< E_T^{miss} <$**350**	3.33 ± 0.96	1.38 ± 0.58	4.71 ± 1.21
A 350$< E_T^{miss} <$**450**	1.85 ± 0.53	0.21 ± 0.53	2.05 ± 0.75
A 450$< E_T^{miss} <$**600**	1.15 ± 0.33	0.47 ± 0.39	1.62 ± 0.53
A $E_T^{miss} >$**600**	0.36 ± 0.11	0.36 ± 0.41	0.71 ± 0.40
B 250$< E_T^{miss} <$**450**	0.61 ± 0.18	0.93 ± 0.47	1.54 ± 0.52
B 450$< E_T^{miss} <$**600**	0.15 ± 0.05	0.20 ± 0.34	0.35 ± 0.33
B $E_T^{miss} >$**600**	0.09 ± 0.03	0.02 ± 0.26	0.11 ± 0.26
C 250$< E_T^{miss} <$**350**	14.28 ± 3.84	0.10 ± 0.62	14.38 ± 3.92
C 350$< E_T^{miss} <$**450**	3.83 ± 1.06	0.60 ± 0.48	4.43 ± 1.23
C 450$< E_T^{miss} <$**550**	1.06 ± 0.31	0.73 ± 0.39	1.79 ± 0.52
C 550$< E_T^{miss} <$**650**	0.40 ± 0.12	0.00 ± 0.00	0.40 ± 0.12
C $E_T^{miss} >$**650**	0.20 ± 0.06	0.00 ± 0.00	0.20 ± 0.06
D 250$< E_T^{miss} <$**350**	2.06 ± 0.56	0.95 ± 0.63	3.01 ± 0.91
D 350$< E_T^{miss} <$**450**	0.62 ± 0.18	0.55 ± 0.40	1.18 ± 0.41
D 450$< E_T^{miss} <$**550**	0.24 ± 0.07	0.21 ± 0.22	0.45 ± 0.24
D $E_T^{miss} >$**550**	0.09 ± 0.03	0.00 ± 0.00	0.09 ± 0.03
E 250$< E_T^{miss} <$**350**	7.88 ± 2.14	0.40 ± 0.44	8.27 ± 2.21
E 350$< E_T^{miss} <$**550**	3.34 ± 0.94	0.52 ± 0.39	3.87 ± 1.07
E $E_T^{miss} >$**550**	0.26 ± 0.08	0.03 ± 0.25	0.29 ± 0.26
F 250$< E_T^{miss} <$**450**	0.98 ± 0.27	0.13 ± 0.17	1.11 ± 0.33
F $E_T^{miss} >$**450**	0.21 ± 0.06	0.00 ± 0.00	0.21 ± 0.06
G 250$< E_T^{miss} <$**350**	2.89 ± 0.78	0.14 ± 0.15	3.03 ± 0.81
G 350$< E_T^{miss} <$**450**	2.51 ± 0.71	0.16 ± 0.18	2.67 ± 0.77
G 450$< E_T^{miss} <$**600**	1.80 ± 0.50	0.16 ± 0.16	1.96 ± 0.54
G $E_T^{miss} >$**600**	0.70 ± 0.20	0.00 ± 0.00	0.70 ± 0.23
H 250$< E_T^{miss} <$**450**	0.37 ± 0.11	0.00 ± 0.00	0.37 ± 0.11
H $E_T^{miss} >$**450**	0.33 ± 0.10	0.16 ± 0.17	0.49 ± 0.20
I 250$< E_T^{miss} <$**350**	3.66 ± 1.01	0.66 ± 0.43	4.33 ± 1.16
I 350$< E_T^{miss} <$**450**	1.57 ± 0.45	0.35 ± 0.34	1.93 ± 0.59
I 450$< E_T^{miss} <$**550**	0.58 ± 0.17	0.19 ± 0.20	0.77 ± 0.27
I $E_T^{miss} >$**550**	0.41 ± 0.13	0.17 ± 0.17	0.58 ± 0.22

Table 5.7: The estimated $t\bar{t}Z$ and WZ yields in the signal regions A to I with their uncertainties.

this, for the evaluation of the systematic uncertainties, the binning of the signal regions in $M_{\ell b}$ and t_{mod} is removed and only a binning in E_T^{miss} and N_J is kept. Effectively, we group signal regions across the groups A–B and C–H, the compressed region I is treated separately. To be sure that the uncertainty is not underestimated due to the grouping in $M_{\ell b}$ and t_{mod}, the distributions of these variables are studied for different values of the theoretical parameters. Only small variations (less than 2%) in the shape of $M_{\ell b}$ and t_{mod} are observed when varying the theoretical parameters, while the variations are large in the shapes of E_T^{miss} and N_J. First the relative uncertainties are evaluated in the grouped regions for $t\bar{t}Z$ and WZ separately, they are then used to compute the absolute uncertainties per process in the corresponding signal regions. The absolute uncertainties per process are propagated to evaluate the total absolute and relative uncertainty on the $Z \to \nu\bar{\nu}$ estimate in the signal regions. The theoretical uncertainties are discussed one by one in the following paragraphs.

Factorization and renormalization scales The cross section of a given process has a

remaining dependence on the choice of the factorization and renormalization scales. The theoretical $t\bar{t}Z$ cross section at 13 TeV is 839.3 fb [150], with a quoted scale uncertainty around 10%. As the normalization of the background estimate is derived from data, the scale uncertainty should only influence the shapes and consequently the migration of events between the signal regions. In this analysis both renormalization and factorization scales are varied simultaneously, while keeping the cross section constant. The uncertainty is then evaluated from the change of background estimate when varying the scales. The scale uncertainty on the $Z \to \nu\bar{\nu}$ estimation in each signal region is shown in Table 5.8, overall it is lower than 10%.

Parton distribution functions The NNPDF3.0 [141] set of parton distribution functions (PDF) is used for the production of simulated samples. To evaluate the uncertainty arising from the PDFs, 100 parameters of the PDFs are varied and each variation is used to calculate an event weight $y_{i,n}$, where i denotes the i-th event and n the n-th variation. Then the standard deviation of the PDF variations for an event i, computed as

$$\sigma_i = \sqrt{\frac{1}{99}\sum_{n=1}^{100}(y_{i,n} - \bar{y}_i)^2}, \text{ with } \bar{y}_i = \frac{1}{100}\sum_{n=1}^{100} y_{i,n}, \tag{5.20}$$

is used to evaluate the PDF uncertainties. Here again only the shape uncertainties are taken into account by keeping the normalization constant. The uncertainties due to PDFs go up to 10% as shown in Table 5.8 for the $Z \to \nu\bar{\nu}$ estimate in all signal regions.

Strong coupling constant α_S The uncertainties on the background estimate coming from α_S are as well evaluated with the help of event weights. The constant α_S is varied from its default value of 0.118 within its uncertainty to 0.117 and 0.119 [110]. The interest is in the shape uncertainties and therefore again the normalization is forced to be constant when varying α_S. The final uncertainties are of the order of 3% and are show in Table 5.8 for $Z \to \nu\bar{\nu}$ background estimate.

Figure 5.12 shows the E_T^{miss} distribution for the $t\bar{t}Z$ process in the grouped regions A–B (left) and C–H(right) with a band corresponding to combined uncertainties on the scales, PDFs and α_S. It can be noticed that the uncertainties are very small for low E_T^{miss}, but grow with E_T^{miss} up to around 10%.

Experimental uncertainties

The second group of systematic uncertainties is referred to as the "experimental uncertainties". Part of the uncertainties originate from a non-perfect modelling in the simulation

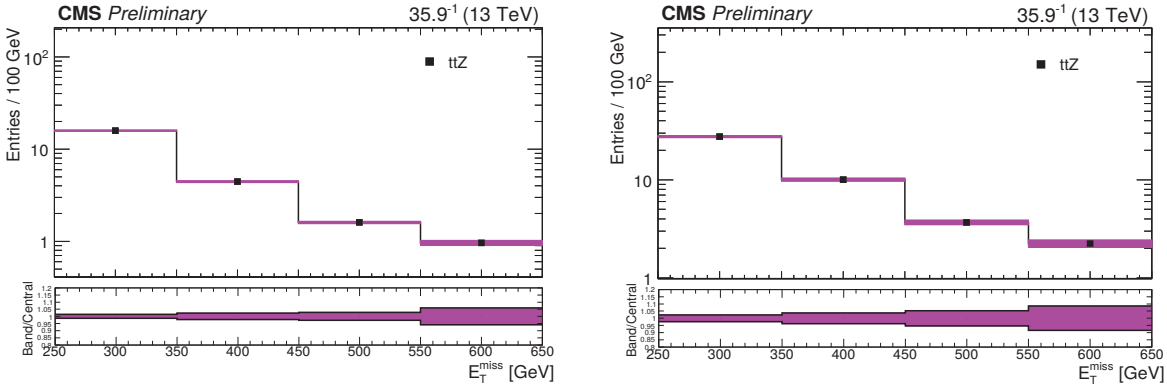

Figure 5.12: The predicted E_T^{miss} distribution of the $t\bar{t}Z$ process with a band coming from the combined uncertainties on scales, PDFs and α_S. The regions A–B (left) and C–H (right) are grouped in the $M_{\ell b}$ and t_{mod} variables. The ratio plots depict the maximal variations from the default.

of the efficiency to tag a jet (coming from a b quark or from a light parton) as a b-jet, or of the lepton ID/isolation efficiencies. These mis-modellings are corrected in simulation by the use of scale factors delivered by the CMS collaboration. The uncertainties on the background yield are evaluated from the variations of these scale factors within their uncertainties. The impact on the yields is presented in Table. 5.8 for the $Z \to \nu\bar{\nu}$ background estimate. The uncertainties on the b-tagging and lepton scale factors are typically of the order of a few percent, except for a few outliers caused by limited statistics in the simulated samples.

Another source of uncertainties arises from the Jet Energy Scale (JES). Jet Energy Corrections (JEC) must be applied on the reconstructed jets to obtain the correct energy of the jets. The uncertainties from the variations of the JES are of the order of a few percent, although in few signal regions with small statistics they can reach up to three or four tens of percent.

The uncertainty arising from differences in the pileup profile in data and simulation has been found to be extremely sensitive to the limited statistics and therefore, for the $Z \to \nu\bar{\nu}$ processes, one global uncertainty is evaluated by varying the PU in the baseline search region only. The systematic uncertainty on the PU is determined to be lower than one percent in the baseline region, but a conservative estimate of 3% is used to take into account variations due to categorization.

As, for the $t\bar{t}Z$ process, a ISR reweighting is applied, the uncertainty arising from this procedure has to be evaluated by varying the ISR weight. The uncertainty introduced by the ISR reweighting is evaluated to be lower than 10%.

The systematic uncertainty on the luminosity is provided by the CMS and is 2.5% [151].

The normalization uncertainty is computed by varying the normalization factors $NF^{CR}_{proc,\ 3\ell}$ within their uncertainty.

Uncertainty due to the limited statistics in samples

The dominant uncertainty comes from the limited statistics in the simulated samples. The statistical uncertainty varies from around 5% to 90%.

Break-down of the systematic uncertainties

The break-down of the systematic uncertainties on the $Z \to \nu\bar{\nu}$ background estimate is shown in Table 5.8 for all signal regions. The summarized typical order of magnitude of these uncertainties is presented in Table 5.9. As only the normalization factors are derived by a data-driven method and the shapes are taken from simulation, the uncertainties are very sensitive to the modelling of shape in the simulation. With one CR per each SR, a large part of the uncertainties would largely cancel in the $N^{MC,\ SR}/N^{MC,\ CR}$ ratio. For now, as the statistics in the three lepton control region is small, only one CR can be used, but with a higher integrated luminosity, a splitting of the three lepton control regions should be possible.

	MC stat.	SF_l	SF_b(light)	SF_b(heavy)	PU	PDFs	α_S	Scales	ISR	JES	Norm.	Total
A 250$< E_T^{miss} <$**350**	11.88	0.31	1.58	1.23	3.00	0.23	0.86	3.86	7.12	2.55	20.70	25.60
A 350$< E_T^{miss} <$**450**	25.04	0.35	3.63	0.77	3.00	3.33	0.61	1.31	9.09	0.37	24.38	36.61
A 450$< E_T^{miss} <$**600**	23.87	0.37	1.34	1.34	3.00	0.45	0.39	2.47	7.02	0.46	20.77	32.71
A $E_T^{miss} >$**600**	51.43	0.41	2.87	1.74	3.00	8.04	0.36	2.37	5.13	10.54	16.77	56.17
B 250$< E_T^{miss} <$**450**	29.98	0.50	1.67	1.23	3.00	1.17	0.76	2.86	3.97	1.01	14.74	34.01
B 450$< E_T^{miss} <$**600**	86.04	0.77	5.28	1.26	3.00	0.45	0.40	2.47	4.00	32.62	15.46	93.63
B $E_T^{miss} >$**600**	228.31	2.65	19.40	1.64	3.00	8.03	0.36	2.37	8.12	44.04	22.72	234.76
C 250$< E_T^{miss} <$**350**	4.56	0.45	0.06	0.68	3.00	0.81	0.60	1.77	0.40	4.78	26.18	27.26
C 350$< E_T^{miss} <$**450**	10.85	0.35	0.48	0.66	3.00	2.01	1.23	5.00	0.99	6.85	23.73	27.73
C 450$< E_T^{miss} <$**550**	20.70	0.31	4.53	0.26	3.00	1.89	1.34	4.86	2.03	4.52	18.54	29.25
C 550$< E_T^{miss} <$**650**	9.20	0.38	0.77	0.38	3.00	4.90	1.86	3.67	3.67	2.14	26.32	29.09
C $E_T^{miss} >$**650**	12.73	0.45	0.20	0.40	3.00	8.11	3.08	4.23	4.92	5.74	26.32	31.85
D 250$< E_T^{miss} <$**350**	19.82	0.31	0.72	0.41	3.00	0.81	0.60	1.76	0.82	9.76	20.24	30.20
D 350$< E_T^{miss} <$**450**	27.58	0.32	1.82	1.08	3.00	2.02	1.23	4.99	1.63	10.79	17.33	34.98
D 450$< E_T^{miss} <$**550**	47.40	0.33	4.96	0.22	3.00	1.88	1.33	4.85	2.24	17.87	17.31	54.17
D $E_T^{miss} >$**550**	18.94	0.44	0.06	0.83	3.00	7.53	2.44	2.55	7.31	7.15	26.32	35.14
E 250$< E_T^{miss} <$**350**	5.55	0.42	0.65	0.74	3.00	0.81	0.60	1.77	2.52	3.80	25.40	26.66
E 350$< E_T^{miss} <$**550**	10.40	0.40	0.01	0.83	3.00	1.97	1.26	4.96	0.66	7.23	23.72	27.63
E $E_T^{miss} >$**550**	87.72	0.77	7.05	0.02	3.00	7.55	2.47	2.51	2.26	1.66	24.61	91.86
F 250$< E_T^{miss} <$**450**	16.02	0.42	0.06	0.31	3.00	1.16	0.78	2.70	2.10	4.41	24.07	29.63
F $E_T^{miss} >$**450**	12.82	0.47	0.40	0.57	3.00	3.72	1.70	3.91	2.22	3.37	26.33	30.26
G 250$< E_T^{miss} <$**350**	5.75	0.39	0.01	1.71	3.00	0.81	0.60	1.77	2.09	3.44	25.42	26.68
G 350$< E_T^{miss} <$**450**	7.06	0.43	0.05	1.35	3.00	2.01	1.23	5.00	1.79	9.62	25.14	28.63
G 450$< E_T^{miss} <$**600**	9.01	0.37	0.19	1.27	3.00	2.63	1.54	4.72	0.51	5.15	24.77	27.64
G $E_T^{miss} >$**600**	7.00	0.47	0.19	1.01	3.00	8.01	2.34	1.74	0.68	15.62	26.32	32.70
H 250$< E_T^{miss} <$**450**	9.94	0.49	0.05	0.07	3.00	1.17	0.79	2.72	2.06	4.60	26.32	28.91
H $E_T^{miss} >$**450**	34.01	0.43	0.04	0.88	3.00	3.71	1.70	3.91	0.93	2.41	19.94	40.03
I 250$< E_T^{miss} <$**350**	9.76	0.38	0.78	0.47	3.00	0.21	0.32	3.91	4.30	5.32	23.38	26.72
I 350$< E_T^{miss} <$**450**	17.91	0.35	0.76	0.60	3.00	1.99	1.41	5.88	4.56	6.05	22.78	30.79
I 450$< E_T^{miss} <$**550**	25.04	0.51	4.83	0.35	3.00	1.89	1.62	4.90	5.38	4.89	21.64	34.80
I $E_T^{miss} >$**550**	29.62	0.40	0.22	0.68	3.00	1.82	1.55	7.48	4.76	6.34	20.76	37.98

Table 5.8: The break-down of the relative systematic uncertainties in % on the $Z \to \nu\bar{\nu}$ background estimation in each signal region (first column). The columns two to twelve report the uncertainties on MC statistics, the scale factor for lepton, for b-tagging applied on light jets, on heavy-flavor jets (i.e. originating from b or a c quark), pileup, PDFs, α_S, scales, ISR jets, JES and normalization, respectively.

5.3.2 The lost lepton background estimation

5.3.2.1 Data-driven estimation

The lost lepton background, is the dominant background due to the large tails in the E_T^{miss} and M_T distributions caused by the two neutrinos and the missing lepton. The majority of the lost lepton background arises from the $t\bar{t} \to 2\ell$ process. The background yields in the signal regions are estimated according to Eq. 5.17 from dilepton control regions. These control regions have a purity above 95% in the $t\bar{t}$, tW, $t\bar{t}V$ and diboson processes and therefore no correction for contamination from other processes is needed.

Events in the control regions pass the same selection as in the signal regions, except the veto on the second lepton which is reversed. Because of the small yields in the control regions with high E_T^{miss}, several control regions differing only by the E_T^{miss} range are merged together. Due to this combination of control regions, the background estimate

Source	**Typical range of values** [%]
MC statistics	5-88
Lepton SF	<1
b-tagging SF (light flavor)	1-7
b-tagging SF (heavy flavor)	<2
Pileup	3
PDFs	1-8
α_S	1-3
Scales	1-8
ISR	1-9
Jet energy scale	1-33
Normalization	15-26
Total	26-94

Table 5.9: The typical order of magnitude of a given uncertainty for the $Z \to \nu\bar{\nu}$ background.

in a given signal region has to be multiplied by a corresponding factor correcting for the E_T^{miss} extrapolation. The lost lepton background estimate in the signal region can then be written as

$$N_{lost\ \ell}^{Data_{Est},\ SR} = N_{2\ell}^{Data,\ CR,\ E_T^{miss}\ ext.} \times \frac{N_{lost\ \ell}^{MC,\ SR,\ E_T^{miss}\ ext.}}{N_{2\ell}^{MC,\ CR,\ E_T^{miss}\ ext.}} \times \frac{N_{lost\ \ell}^{MC,\ SR}}{N_{lost\ \ell}^{MC,\ SR,\ E_T^{miss}\ ext.}}, \quad (5.21)$$

where the $E_T^{miss\ ext.}$ denotes regions extrapolated in E_T^{miss}, i.e. the merged regions by removing the E_T^{miss} requirement. The first term on the right side is the observed yield in the control region, the second term corresponds to the transfer factor from the CR to the SR and the third factor is the simulation based E_T^{miss} extrapolation factor, which is equal to one if a given control region is not merged with another one.

The described extrapolation of control regions in the E_T^{miss} could lead to an imprecise estimate if the E_T^{miss} shapes in data and simulation differ. For this reason the shape of E_T^{miss} is checked in an region enriched top quark events. Contrary to the control regions using single lepton triggers, data used for the study of the E_T^{miss} shapes are triggered by a double lepton trigger with an electron-muon pair in the final state. Then the data-to-simulation ratio in E_T^{miss} bins is used as a correction of the simulated E_T^{miss} spectra.

The final estimates of the lost lepton background per signal region are shown in Table 5.10, together with their uncertainties including both the statistical and systematic uncertainties as described in following subsection.

5.3.2.2 Systematic uncertainties on the lost lepton background estimation

As for the $Z \to \nu\bar{\nu}$ background, the uncertainties on the lost lepton background estimate include the uncertainties due to limited statistics in simulation, lepton and b-tagging scale factors, PU, PDFs, α_S, scales, ISR reweighting and JES, although many of them largely cancel in the $N_{lost\ell}^{MC,\ SR}/N_{2\ell}^{MC,\ CR}$ ratio used for the estimation of the lost lepton background yields in the SRs.

In addition to these uncertainties, the following uncertainties are evaluated:

- The uncertainty arising from the trigger efficiency in the dilepton CR
- The uncertainty on the E_T^{miss} resolution which can cause a migration of events between signal regions: It cancels in the $N_{lost\ell}^{MC,\ SR}/N_{2\ell}^{MC,\ CR}$ ratio in case no E_T^{miss} extrapolation is needed. However in the case that the E_T^{miss} extrapolation is applied, the corresponding extrapolation factor is computed purely from the simulation and is directly sensitive to the E_T^{miss} resolution.
- The uncertainty arising from the different E_T^{miss} shapes in data and simulation: Because of the extrapolation in E_T^{miss}, the differences in E_T^{miss} shapes can also cause migration of events between the signal regions as described for the E_T^{miss} resolution
- The uncertainty on the efficiency of the hadronic tau and the isolated track vetoes: As the control region is defined by requiring a second lepton, the differences of efficiency for the hadronically decaying tau leptons between signal and control regions must be taken into account. Any variation on these efficiencies is propagated to the background yield to quantify its corresponding uncertainty.

As previously, the dominant uncertainty arises from the limited statistics in data and simulations which can go up to around 60%.

5.3.3 The one lepton background estimation

5.3.3.1 Data-driven estimation

The $W + jets \to 1\ell$ background represents the largest part of the 1ℓ background and is estimated from control regions with zero b-tagged jets. The control regions are defined in the same way as the signal regions, but no b-tagged jet is allowed in the event. When the medium b-tagging WP is used in the SR, this requirement is simply inverted in the CR. For the SRs requesting a tight b-tagging WP, a veto against tight b-tagged jet is applied

in the majority of cases. But in some control regions of high $M_{\ell b}$, a veto against medium b-tagged jets is used to reduce the systematics uncertainty and increase the purity. The $t\bar{t} \to 1\ell$ represents only a small contribution to the one lepton background and therefore is taken directly from the simulation.

In the zero b-tagged jet control regions, the $M_{\ell b}$ variable needs to be redefined as there is no b-tagged jet in the event. Instead of the closest b-tagged jet, the jet with highest CSVv2 discriminator is used to define $M_{\ell b}$ in this case. Contrary to the previous background estimations there is enough statistics to define a corresponding zero b-tag control region to each signal region. Unfortunately, the control regions are not pure in the $W + jets \to 1\ell$ process and the background estimate have to account for the contamination by other processes in the control regions. The $W + jets \to 1\ell$ background estimate in the signal regions can be then written as

$$N^{Data_{Est},\ SR}_{W+jets,\ \geq 1btag} = N^{Data,\ CR}_{W+jets,\ 0btag} \times \frac{N^{MC,\ SR}_{W+jets,\ \geq 1btag}}{N^{MC,\ CR}_{W+jets,\ 0btag}}, \tag{5.22}$$

where the first term on right side denotes the observed yield in the control region and the second term corresponds to the transfer factor from CR to SR for the W+jets process. Because of the contamination in the control regions by other processes, the $N^{Data,\ CR}_{W+jets,\ 0btag}$ obtained from the yield measured in the CR ($N^{Data,\ CR}_{all,\ 0btag}$) is corrected by a simulation based purity factor:

$$N^{Data,\ CR}_{W+jets,\ 0btag} = N^{Data,\ CR}_{all,\ 0btag} \times \frac{N^{MC,\ CR}_{W+jets,\ 0btag}}{N^{MC,\ CR}_{all,\ 0btag}}, \tag{5.23}$$

where $N^{MC,\ CR}_{all,\ 0btag} = N^{MC,\ CR}_{W+jets,\ 0btag}$+ the contaminating processes.

Because of the different $M_{\ell b}$ definition, a study based on simulation, comparing the shapes of this modified $M_{\ell b}$ between control and signal regions, has confirmed that these two shapes are in agreement.

As the contribution to the total background from the $t\bar{t} \to 1\ell$ process is lower than 10%, it is therefore reasonable to estimate the background yields directly from simulation. The $t\bar{t} \to 1\ell$ process appears in the signal regions mainly due to the E_T^{miss} resolution. As this background is purely estimated from simulation, a mis-modelling of the E_T^{miss} resolution could cause an imprecise estimate. The E_T^{miss} resolution is checked with the help of γ+jets data and simulated samples. The p_T spectrum of the photon in data and simulation is reweighted to match the p_T spectrum of the neutrino in the $t\bar{t} \to 1\ell$ process. Then a modified E_T^{miss} is computed as the sum of reweighted p_T^{γ} and the originally reconstructed E_T^{miss}. The data-to-simulation ratio for the modified E_T^{miss} distribution can

then reveal any E_T^{miss} resolution mis-modelling. It has been found out that the difference between data and simulation for the modified E_T^{miss} is large, up to 40%, but no scale factor is derived and this mis-modelling is only taken into account as a systematic uncertainty which is conservatively assessed to be 100%.

The final estimates of the one lepton background in the signal regions are shown in Table 5.10, together with their uncertainties including both the statistical and systematic uncertainties as described in the following subsection.

5.3.3.2 Systematic uncertainties on the one lepton background estimation

The uncertainties on the $W + jets \rightarrow 1\ell$ background estimate are very similar to the previous cases as they contain uncertainties due to the limited statistics in simulation, PU, JES, PDFs, scales, α_S, b-tagging and lepton scale factors, although here as well many of them largely cancel in $N^{MC,\ SR}_{W+jets,\ \geq 1btag}/N^{MC,\ CR}_{W+jets,\ 0btag}$ ratio used for the estimation of 1ℓ background yields in the SRs.

In addition to these already mentioned uncertainties, the following ones are evaluated:

- The uncertainty on the W+heavy flavors ($W+b,\ W+c,\ W+bb,\ ...$) cross section: For the background estimation, the simulation is used to determine a factor which transfers the data yield from the control to the signal region as can be seen in Eq. 5.22. Therefore the background estimate is sensitive on the modelling of the W+heavy flavors fraction in the simulation.
- The uncertainty on the contamination of control regions by other processes.

In this case, the dominant uncertainties arise not only from the limited statistics in data and simulation but also from the contamination in control regions by other processes than $W + jets \rightarrow 1\ell$. These uncertainties can reach up to 90%.

The uncertainty on the $t\bar{t} \rightarrow 1\ell$ estimate is evaluated to be 100% from the mentioned studies of the E_T^{miss} resolution. All the other sources of uncertainties are negligible.

5.4 Results and interpretation

5.4.1 Results

The results on the background estimates together with the observed data in the signal regions are shown in Table 5.10 for the full 2016 analysis. These results are graphically

presented in Fig. 5.14. In this figure the yields of three different signal models for a chosen signal point are also shown.

N_J	t_{mod}	$M_{\ell b}$ [GeV]	E_T^{miss} [GeV]	Lost lepton	1ℓ (top)	1ℓ (not top)	$Z \to \nu\bar{\nu}$	Total background	Data
≤ 3	> 10	≤ 175	$250-350$	53.9±6.2	< 0.1	7.2±2.5	4.7±1.2	65.8±6.8	72
≤ 3	> 10	≤ 175	$350-450$	14.2±2.4	0.2±0.2	4.1±1.4	2.1±0.8	20.5±2.9	24
≤ 3	> 10	≤ 175	$450-600$	2.9±0.9	0.1±0.1	1.7±0.7	1.6±0.5	6.4±1.3	6
≤ 3	> 10	≤ 175	> 600	0.6±0.5	0.3±0.3	0.8±0.3	0.7±0.4	2.4±0.8	2
≤ 3	> 10	> 175	$250-450$	1.7±0.8	< 0.1	5.6±2.2	1.5±0.5	8.9±2.4	6
≤ 3	> 10	> 175	$450-600$	0.02±0.01	< 0.1	1.6±0.6	0.4±0.3	1.9±0.7	3
≤ 3	> 10	> 175	> 600	0.01±0.01	< 0.1	0.9±0.4	0.1±0.3	1.0±0.5	2
≥ 4	≤ 0	≤ 175	$250-350$	346±30	13.2±13.2	9.7±8.6	14.4±3.9	383±34	343
≥ 4	≤ 0	≤ 175	$350-450$	66.3±7.9	2.3±2.3	2.5±1.7	4.4±1.2	75.5±8.5	68
≥ 4	≤ 0	≤ 175	$450-550$	12.1±2.8	0.6±0.6	0.5±0.5	1.8±0.5	15.0±2.9	13
≥ 4	≤ 0	≤ 175	$550-650$	3.4±1.5	0.1±0.1	0.3±0.2	0.4±0.1	4.1±1.5	6
≥ 4	≤ 0	≤ 175	> 650	5.9±2.8	< 0.1	0.4±0.4	0.2±0.1	6.6±2.9	2
≥ 4	≤ 0	> 175	$250-350$	26.0±4.3	3.1±3.1	7.5±3.0	3.0±0.9	39.7±6.2	38
≥ 4	≤ 0	> 175	$350-450$	10.4±2.6	0.6±0.6	1.6±0.7	1.2±0.4	13.7±2.8	8
≥ 4	≤ 0	> 175	$450-550$	1.7±0.9	0.4±0.4	0.6±0.3	0.5±0.2	3.1±1.1	2
≥ 4	≤ 0	> 175	> 550	1.1±0.8	< 0.1	1.0±0.6	0.09±0.03	2.2±1.0	1
≥ 4	$0-10$	≤ 175	$250-350$	43.0±5.9	1.7±1.7	5.7±3.0	8.3±2.2	58.7±7.2	65
≥ 4	$0-10$	≤ 175	$350-550$	9.1±2.0	0.5±0.5	1.2±0.5	3.9±1.1	14.7±2.4	23
≥ 4	$0-10$	≤ 175	> 550	0.6±0.3	0.3±0.3	0.3±0.2	0.3±0.3	1.5±0.6	1
≥ 4	$0-10$	> 175	$250-450$	4.4±1.4	0.3±0.3	3.1±1.3	1.1±0.3	8.9±1.9	9
≥ 4	$0-10$	> 175	> 450	0.10±0.17	< 0.1	0.2±0.3	0.2±0.1	0.6±0.2	0
≥ 4	> 10	≤ 175	$250-350$	9.5±2.3	0.8±0.8	1.1±0.9	3.0±0.8	14.3±2.7	12
≥ 4	> 10	≤ 175	$350-450$	5.9±1.8	0.7±0.7	0.7±0.5	2.7±0.8	10.0±2.1	9
≥ 4	> 10	≤ 175	$450-600$	3.8±1.3	0.1±0.1	0.4±0.3	2.0±0.5	6.3±1.5	3
≥ 4	> 10	≤ 175	> 600	0.8±0.6	0.7±0.7	0.3±0.4	0.7±0.3	2.4±1.0	0
≥ 4	> 10	> 175	$250-450$	0.5±0.3	< 0.1	1.0±0.6	0.4±0.1	1.9±0.7	0
≥ 4	> 10	> 175	> 450	0.2±0.2	0.1±0.1	0.5±0.3	0.5±0.2	1.3±0.4	2
Compressed region			$250-350$	67.5±8.9	5.3±5.3	5.0±1.8	4.3±1.2	82±11	72
Compressed region			$350-450$	15.1±3.5	1.0±1.0	0.8±0.3	1.9±0.6	18.9±3.7	30
Compressed region			$450-550$	2.4±1.3	0.1±0.1	0.4±0.2	0.8±0.3	3.7±1.4	2
Compressed region			> 550	3.9±2.0	0.1±0.1	0.2±0.2	0.6±0.2	4.8±2.0	2

Table 5.10: Observed data yields and background estimations in the 31 signal regions of the analysis, corresponding to an integrated luminosity of 35.9 fb^{-1}. The uncertainties of background include both the statistical and systematic parts [128].

5.4.2 Uncertainties on the signal yields

5.4.2.1 Uncertainties for the full 2016 analysis

The signal uncertainties are evaluated similarly as the background ones. As previously, the largest source of uncertainty is the limited statistics in the simulated samples which varies from 5 to 25%. The signal uncertainties with their typical values are summarized in Table 5.11.

Source	Typical range of values [%]
MC statistics	5–25
b-tagging SF	1–7
Pileup	1–4
Scales	2–4
ISR	2–15
Jet energy scale	1–20
Integrated luminosity	2.5
Trigger	2–4
Lepton SF	1–4
E_T^{miss} modelling	1–10
Total	7–38

Table 5.11: The typical order of magnitude of systematic uncertainties on the signal yields [128].

5.4.2.2 Discussion on a pileup uncertainty estimate for the 2015 analysis

For the 2015 version of the analysis [129] I performed studies of the dependency of the M_T and E_T^{miss} distributions in signal samples on the pileup. The results of this study are used to assess one of the systematic uncertainties on the signal yields.

The difference in the M_T and E_T^{miss} distributions as a function of pileup is evaluated starting for events passing the baseline selection except the requirement on the M_T and E_T^{miss} variables, respectively. The total number of events N is divided in bins according to the number of primary vertices (N_{vtx}) present in the event. In each bin i of the N_{vtx} distribution, the number of events passing the criterion M_T>150 GeV ($N_{i,M_T>150}$) is divided by the total number of events (N_i) in bin i and scaled by N. The same computation is performed for the number of events in bin i passing E_T^{miss} >250 GeV ($N_{i,E_T^{miss}>250}$). The evolution of the variables $N \cdot N_{i,M_T>150}/N_i$ and $N \cdot N_{i,E_T^{miss}>250}/N_i$ is shown in Fig. 5.13 as a function of N_{vtx} for the T2tt signal points with $m_{\tilde{t}_1}$=225 GeV and 25<$M_{\tilde{\chi}_1^0}$<150 GeV. In the plots it can be noticed that the distributions are not flat. Varying N_{vtx} by five units, which is the difference between the maxima of data and simulation pileup profiles, leads to an uncertainty up to around 7%. This value is used as an uncertainty for the low Δm signals. The variations are smaller for high Δm signals, leading to an uncertainty up to 2%.

In the full 2016 analysis, the pileup uncertainty is applied according to standard CMS SUSY group recommendations based on a study of N_{vtx} distribution [152].

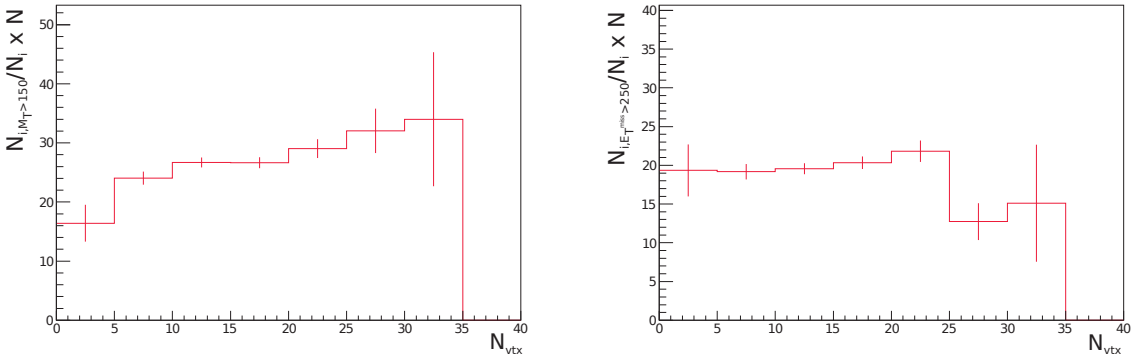

Figure 5.13: The evolution of the fraction of events with $M_T > 150$ GeV (left) and E_T^{miss} >250 GeV (right), multiplied by the total number of events, as a function of the reconstructed primary vertex multiplicity. The study has been performed in the context of the 2015 analysis.

5.4.3 Interpretation

In the signal regions of the full 2016 analysis, no significant excess is observed in data with respect to the SM expectation. Therefore the CL_s method described in Section 5.2.1 is used to interpret the results as exclusion limits on the considered SMS signal models. These limits on model production cross-sections are given as a function of the SUSY particles masses, in this case the stop and neutralino masses. They are obtained by combining all signal regions for a given signal point. A contour line is drawn when the upper limit on the NLO+NLL cross section is equal to the theoretical cross section computed in [153]. The signal points with an upper limit on the cross section which is lower than the theoretical cross section are considered as excluded. The signal yields entering the statistical procedure are corrected for a possible contamination in the control regions by SUSY signal, these corrections are around 5% to 10%.

The 95% confidence level (CL) upper limits on the T2tt ($pp \rightarrow \tilde{t}_1\bar{\tilde{t}}_1 \rightarrow t\bar{t}\tilde{\chi}_1^0\tilde{\chi}_1^0$) and T2tb ($pp \rightarrow \tilde{t}_1\bar{\tilde{t}}_1 \rightarrow t\bar{b}\tilde{\chi}_1^0\tilde{\chi}_1^-$) models are shown in Fig. 5.15 and 5.16 respectively. The results are displayed for both the 2015 analysis [129] corresponding to an integrated luminosity of 2.3 fb^{-1} (left) and the full 2016 analysis [128] corresponding to an integrated luminosity of 35.9 fb^{-1} (right). Both models assume unpolarized top quarks originating from stops.

The analysis of 2015 data combines searches for the stop quark pair production in all-hadronic final states and in the 1ℓ final state. Therefore in the left plots of Figs. 5.15 and 5.16, the expected limit from the 0ℓ (magenta dashed line) and 1ℓ (blue dashed line) are depicted. In the 2015 analysis, both observed (black line) and expected (red dashed line) limits are computed from the combination of the signal regions of both analyses,

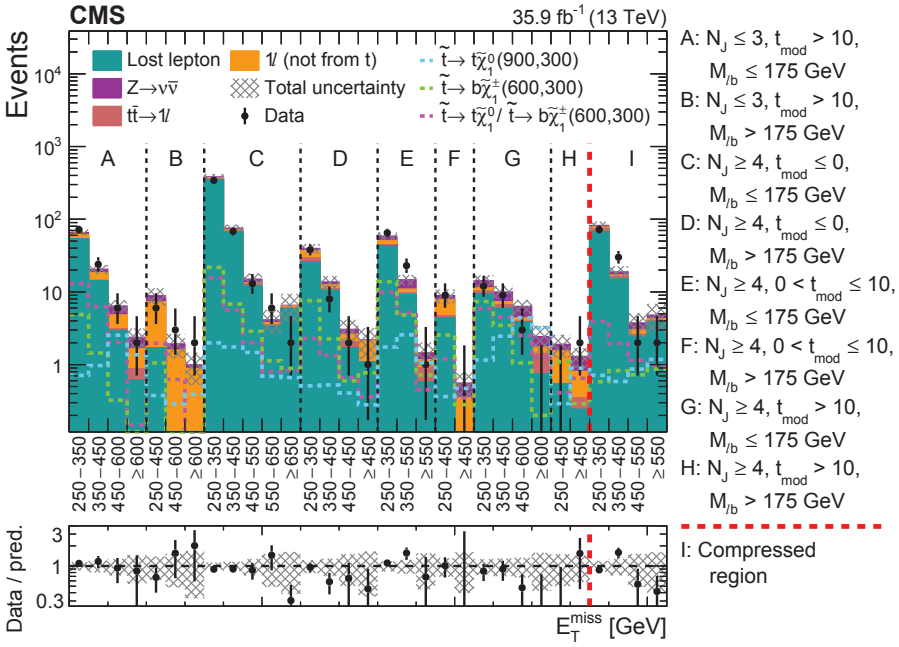

Figure 5.14: The presentation of the observed data (black dots), background estimates and expected signal for three different signal models in the 31 signal regions. The lost lepton background is shown in green, the 1ℓ background from $W + jets \to 1\ell$ (i.e. not from top) in yellow, the $Z \to \nu\bar{\nu}$ background in violet and the $t\bar{t} \to 1\ell$ contribution in red. The T2tt model ($\tilde{t}_1 \to t\tilde{\chi}_1^0$) with a stop mass of 900 GeV and an LSP mass of 300 GeV is shown in blue dashed line. The T2tb ($\tilde{t}_1 \to t\tilde{\chi}_1^0/\tilde{t}_1 \to b\tilde{\chi}_1^{\pm}$) and T2bW ($\tilde{t}_1 \to b\tilde{\chi}_1^{\pm}$) scenarios for a stop mass of 600 GeV and a neutralino mass of 300 GeV are shown in pink and green dashed lines, respectively. The red dashed line separates the signal regions of the nominal and optimized compressed analyses [128].

which are mutually exclusive. In the case of the T2tt model in Fig. 5.15, the 0ℓ analysis outperforms the 1ℓ analysis in the part of the mass plane where the stop is heavy and the LSP light, because of the larger signal acceptance. On the other hand the 1ℓ analysis is more sensitive in the region of a heavier LSP and an intermediate stop mass. The combined analysis of data corresponding to an integrated luminosity of 2.3 fb^{-1} excludes the stop masses between 280 and 830 GeV when the LSP is massless and LSP masses up to 260 GeV for a stop mass of 675 GeV.

The full 2016 analysis corresponding to an integrated luminosity of 35.9 fb^{-1} combines the four signal regions of the compressed analysis in the region $100 \leq \Delta m \leq 225$ GeV and the 27 signal regions of the nominal analysis everywhere else. The exclusion limits purely based on the 1ℓ search exclude stop masses up to 1120 GeV for a massless LSP and LSP masses up to 515 GeV for a stop mass of 950 GeV.

For comparison, ATLAS searches for the stop pair production in the single lepton final state [154] based on data corresponding to an integrated luminosity of 36.1 fb^{-1} exclude

the stop masses up to 940 GeV for a massless LSP in the T2tt model.

In both analyses, a region where the LSP is light and Δm is around the mass of the top quark appears as white in the T2tt plane and it is not interpreted because of a problematic modelling of quickly changing kinematics in this region. As mentioned, the signal samples are produced with FastSim and in this kinematic regime, large differences between FastSim and FullSim are observed. Therefore we have decided not to interpret in this region. Along the diagonal where the Δm is around the mass of the top quark, the neutralinos are produced almost at rest, leading to small E_T^{miss} and therefore the signal final state is very similar to these of the SM backgrounds. The 2015 analysis has almost no sensitivity there. The full 2016 analysis improved highly its sensitivity in this region by requiring a boost of the stop pair against an ISR jet which is enhancing the E_T^{miss} value of the event, but also due to an increase in the luminosity. A similar situation happens in the region where Δm is around the mass of W boson, but moreover this region suffers from a large contribution from the $W + jets \rightarrow 1\ell$ background. The sensitivity is also improved in the full 2016 analysis compared to the 2015 analysis due to an increase in the luminosity and thanks to the compressed selection.

Different signal regions bring different sensitivities in the Δm plane. For example, the signal regions with high E_T^{miss} are sensitive mainly to the signals with high Δm and push the limits for high stop and low LSP masses. The signal regions are also differently sensitive to different signal decay modes, the signal regions with a low modified topness are more sensitive to the T2tt signals, while the regions with a high modified topness target signals with intermediate charginos as in the T2bW scenario.

In the full 2016 analysis, the observed limit is stronger than the expected one. This is caused by upward fluctuations of the predicted SM backgrounds in the signal regions. In case of downward fluctuations, the expected exclusion limit would be stronger than the observed one.

The exclusion limits of the 2015 [129] and full 2106 analysis [128] are shown in Fig. 5.16 for the T2tb signal, for which the branching ratios of $\tilde{t}_1 \rightarrow t\tilde{\chi}_1^0$ and $\tilde{t}_1 \rightarrow b\tilde{\chi}_1^{\pm}$ are 50% each and $m_{\tilde{\chi}_1^{\pm}} = m_{\tilde{\chi}_1^0} + 5$ GeV. The combined analysis corresponding to an integrated luminosity of 2.3 fb^{-1} excludes stop masses up to 700 GeV for intermediate LSP masses, and LSP masses up to 210 GeV for a stop mass of around 500 GeV. This exclusion is mainly driven by the fully hadronic analysis due to its larger signal acceptance. The full 2016 analysis [128], corresponding to integrated luminosity of 35.9 fb^{-1}, excludes stop masses up to 980 GeV for a massless LSP and LSP masses up to 400 GeV for a stop mass of 825 GeV. There is a loss of sensitivity for regions of low Δm where the neutralinos are produced at rest and which might suffer by large SM backgrounds.

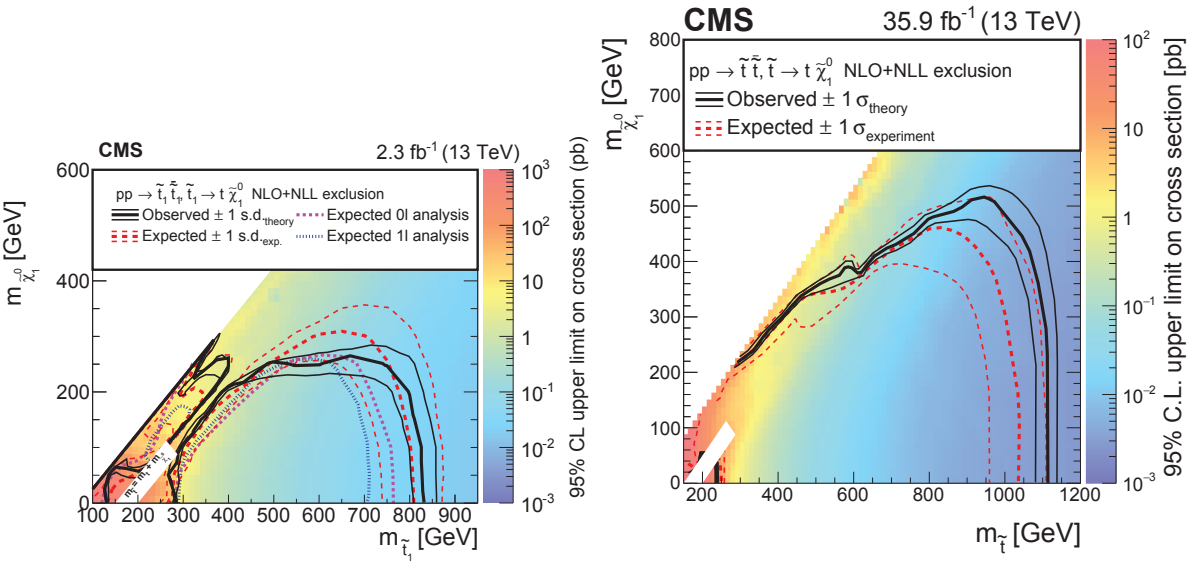

Figure 5.15: The exclusion limits at 95% CL on the T2tt model corresponding to an integrated luminosity of 2.3 fb^{-1} [129] (left) and 35.9 fb^{-1} [128] (right). The interpretation is provided in the context of SMS, in the plane of the stop mass vs the LSP mass. The color code shows the 95% CL upper limit on the cross section assuming a branching ratio of 100% in $\tilde{t}_1 \rightarrow t\tilde{\chi}_1^0$. The red and black contours represent the expected and observed exclusion limits, respectively. The blue and magenta lines in the left plot show the expected limits of 1ℓ and 0ℓ analyses, respectively. The area below the black thick curve indicates the excluded region of the signal points.

The last considered model is T2bW where $pp \rightarrow \tilde{t}_1\bar{\tilde{t}}_1 \rightarrow b\tilde{\chi}_1^+\bar{b}\tilde{\chi}_1^- \rightarrow bW^+\tilde{\chi}_1^0\bar{b}W^-\tilde{\chi}_1^0$ in 100% of the cases and for which the chargino mass is fixed by the condition $m_{\tilde{\chi}_1^\pm} = (m_{\tilde{t}}+m_{\tilde{\chi}_1^0})/2$. The 95% CL upper limit on this model obtained by the full analysis [128] is shown in Fig. 5.17. In this model stop masses are excluded up to 1000 GeV for a massless LSP and LSP masses up to 450 GeV for a stop mass of 800 GeV.

5.5 Conclusion

The excluded stop mass in the T2tt model has increased by around of 50 GeV in early Run 2 based on 2015 data compared to the strongest exclusion results of Run 1 presented in Fig. 4.7, despite the lower integrated luminosity. This increase in sensitivity is caused by the change of the center-of-mass energy from 8 TeV to 13 TeV as well as by an improvement in the optimization of the analyses. The analysis of data corresponding to an integrated luminosity of 35.9 fb^{-1} outperforms the combined analysis of data corresponding to an integrated luminosity of 2.3 fb^{-1} by almost 300 GeV in the stop mass exclusion of the T2tt and T2tb models for a massless LSP. The exclusion limit on the stop mass reaches the TeV range which is usually considered close to the naturalness boundary. But the

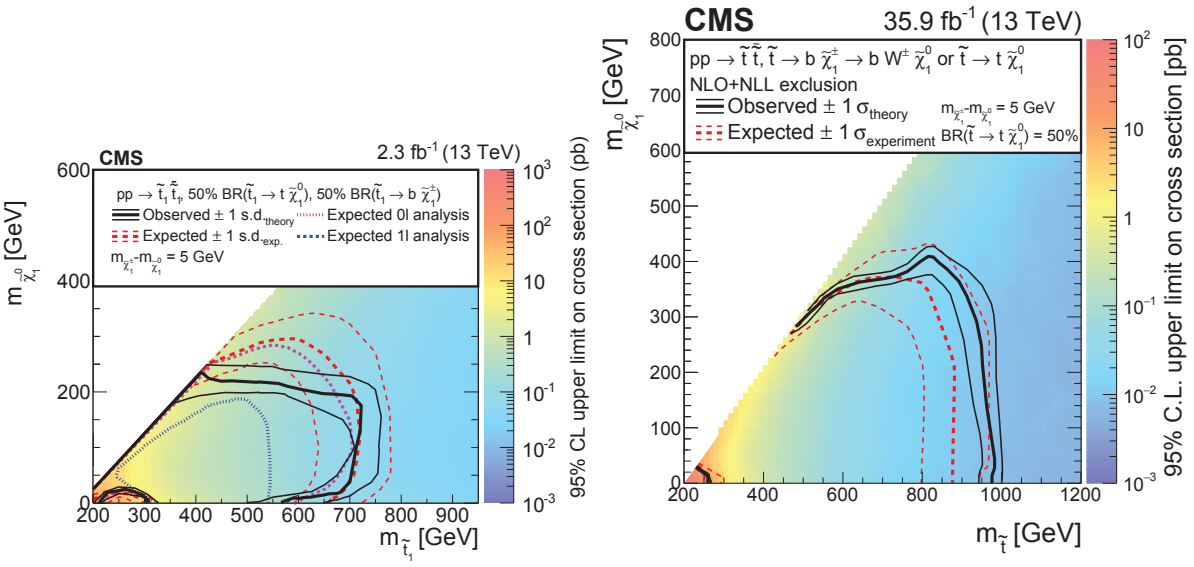

Figure 5.16: The exclusion limits at 95% CL on the T2tb model corresponding to an integrated luminosity of 2.3 fb^{-1} [129] (left) and 35.9 fb^{-1} [128] (right). The interpretation is provided in the context of SMS, in the plane of the stop mass vs the LSP mass. The color code shows the 95% CL upper limit on the cross section assuming a branching ratio of 50% in $\tilde{t}_1 \to t\tilde{\chi}_1^0$ and 50% in $\tilde{t}_1 \to b\tilde{\chi}_1^{\pm}$. The red and black contours represent the expected and observed exclusion limits, respectively. The blue and magenta lines in the left plot show the expected limits of 1ℓ and 0ℓ analyses, respectively. The area below the black thick curve indicates the excluded region of the signal points.

exclusion of the stop masses around 1 TeV happens only for the low LSP masses and there are still configurations in the Δm plane, which are uncovered and where the stops can have relatively low masses. Moreover, this limit is interpreted in terms of simplified model spectra and when considering more complex models the limits can become considerably weaker. For example Ref. [155] suggests that natural SUSY models might lead to final states with very soft visible particle spectra which would therefore be very difficult to be extracted from the SM backgrounds, making the search for them at the LHC very challenging.

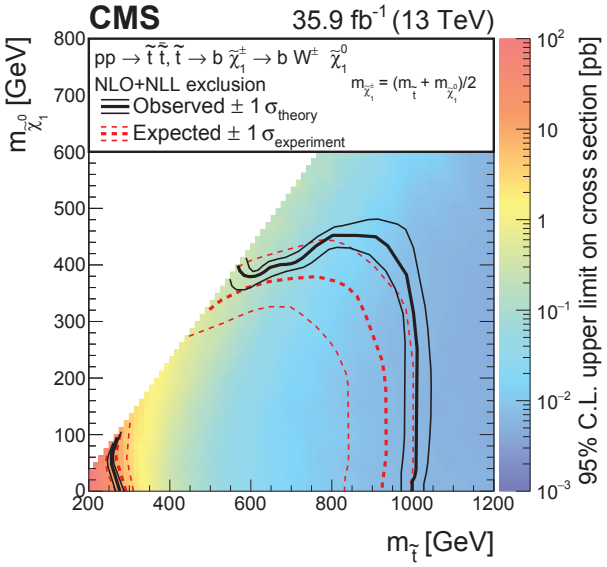

Figure 5.17: The exclusion limits at 95% CL on the T2bW model corresponding to an integrated luminosity of 35.9 fb^{-1} [128]. The interpretation is provided in the context of the SMS, in the plane of the stop mass vs LSP mass. The color code shows the 95% CL upper limit on the cross section. The red and black contours represent the expected and observed exclusion limits, respectively. The area below the black thick curve indicates the excluded region of the signal points.

5.6 Perspectives

As the exclusion limits on the stop mass are reaching the naturalness bound, a lot of efforts have recently been made to revisit this bound and find natural SUSY scenarios which are not excluded by the experiments. In this section I mainly present the ideas developed in Ref. [116], starting with a discussion on how the definition of the naturalness itself can impact the result. Then, I present some scenarios in the context of the MSSM and then I finish with briefly introducing the possibility of SUSY beyond the MSSM.

Ref. [116] first reflects on how to determine the naturalness. It discusses that if an observable O can be written as

$$O = a + b + f(b) + c, \tag{5.24}$$

it is claimed to be natural if all terms on the right hand side are of comparable values or smaller than O. If they are larger than the observable O, some degree of fine-tuning would then be needed to cancel the large terms between each other in order to end up with a small value of O. However in Eq. 5.24 the terms b and $f(b)$ are correlated and their sum should be used in place of the two terms alone. For example, if $f(b) = -b$,

the sum $b + f(b)$ is always equal to zero independently on the value of b without any fine-tuning. Therefore when evaluating the fine-tuning, only the independent terms or group of the terms should be compared between each other. The naturalness measure of the observable O can be defined as

$$\Delta = \frac{|\text{largest term on the right hand side}|}{|O|}. \tag{5.25}$$

We can now apply this naturalness criterion on the Higgs boson mass and find that the terms $m^2_{H,0}$ and Δm^2_H in Eq. 4.27 are independent. So to avoid the fine-tuning, each of them should be of the order of the measured mass of the Higgs boson. Within the MSSM, the SM Higgs boson mass, denoted as m_h, is given by the relation

$$m_h^2 \approx -2\mu^2(\Lambda) + m^2_{H_u}(\Lambda) + \delta m^2_{H_u}(\Lambda), \tag{5.26}$$

where all the terms are dependent on the energy cut-off Λ, μ is the higgsino mass parameter, m_{H_u} is the mass of H_u (gauge eigenstate of the Higgs bosons within the MSSM) and $\delta m^2_{H_u}$ is its radiative correction. In Eq. 5.26 the terms $m^2_{H_u}$ and $\delta m^2_{H_u}$ are correlated. Therefore when evaluating the naturalness, we must compare the independent terms $-2\mu^2$ and $(m^2_{H_u} + \delta m^2_{H_u})$. For further details see Ref. [116].

In Ref. [116] it is shown that requiring that the naturalness measure Δ_{EW} at the electroweak scale to be lower than 30, leads to a 3% fine-tuning or better. When we impose this criterion, the upper bound on the gluino mass is found to be 4 TeV and on the lighter stop to be 3 TeV. In that case, the lightest neutralinos and the lightest chargino are higgsino-like, these three sparticles are almost mass degenerate and their mass can go up to 300 GeV. The masses of the other charginos and neutralinos are expected to be at the TeV scale.

Requiring Δ_{EW}<30, we can also examine the mass spectrum of the lighter stop vs the LSP. For this purpose, the two-extra-parameter non-universal Higgs model (NUHM2) [156, 157] is used. The theoretical parameters in this model are varied but forced to obey the constraint $\Delta_{EW} < 30$ as well as the constraints from the measurements obtained by the LHC experiments: the lightest chargino is imposed to be heavier than 103.5 GeV, the masses of the gluinos and all other squarks, except $\tilde{t}_1$, are imposed to be larger than the masses excluded with the Run 1 LHC data, and the Higgs boson mass is set to be equal to 125 ± 2 GeV.

The possible configurations of the $\tilde{t}_1$ and LSP masses obtained by the described model are shown in Fig. 5.18. In this figure, the possible scenarios with $\Delta_{EW} < 15$ and $\Delta_{EW} < 30$ are shown with the red and blue crosses, respectively, together with the exclusion limits

based on the 12.9 fb^{-1} of data recorded in 2016 from the CMS collaboration [158] (red line) and a combination of analyses corresponding to 13.3 fb^{-1} [159, 160, 161] and 3.2 fb^{-1} [162] by the ATLAS collaboration (black line). The predicted exclusion limit and the discovery potential to be reached by the ATLAS collaboration in the fully hadronic search assuming an integrated luminosity of 3000 fb^{-1}, which is expected at the end of the HL-LHC program, is shown as the orange curve [163]. In this figure it can be first noticed that this model does not predict many scenarios in the compressed region. Then it can be seen that many signal scenarios are already excluded, but as well many scenarios will remain uncovered even analyzing the HL-LHC data. The predicted reach of the HL-LHC is up to around 1.4 TeV for the stop mass. More recent CMS projections, based on a luminosity extrapolation of the full hadronic search results using data up to the end of 2016, show that a stop mass up to 2 TeV can be excluded at HL-LHC with an integrated luminosity of 3000 fb^{-1} [164]. However, natural SUSY scenarios predict stop masses up to 3 TeV as seen in the Fig. 5.18

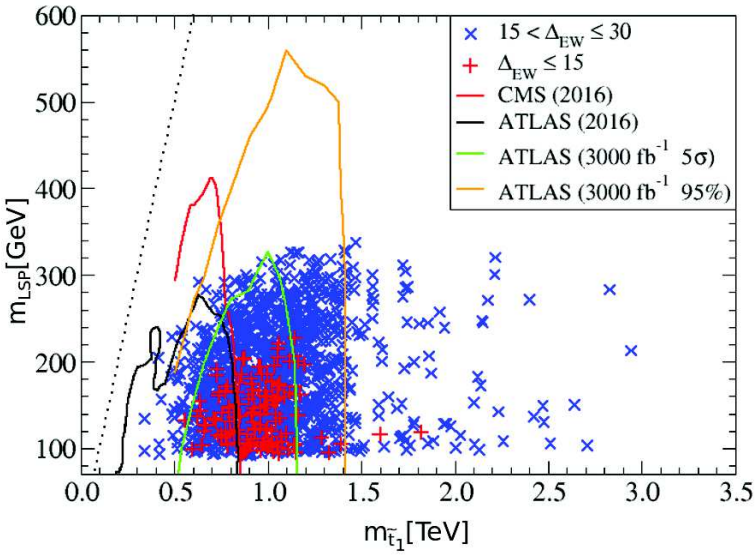

Figure 5.18: The plane of the $\tilde{t}_1$ vs LSP masses. The natural SUSY scenarios with $\Delta_{EW} < 15$ and $\Delta_{EW} < 30$ are shown in the red and blue crosses, respectively. Exclusion limits are depicted in red or black for the LHC results with an integrated luminosity of $\sim$ 13 fb^{-1} and the orange curve shows the extrapolation at the end of the HL-LHC. The green curve shows the discovery potential for the HL-LHC. The dotted line is drawn for the situation when the stop and the LSP have the same masses [116].

Ref. [116] also examines prospects for the stop discovery beyond HL-LHC and presents also the exclusion potential for HE-LHC and FCC as depicted in Fig. 5.19. The figure reveals that to probe a high stop mass of 3 TeV, a machine delivering collisions at a center-of-mass energy of 33 TeV would be needed.

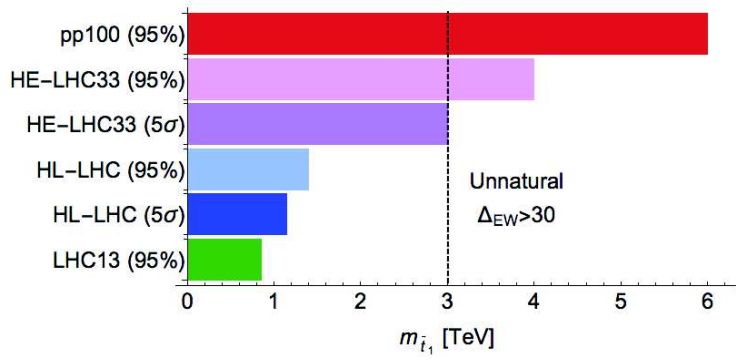

Figure 5.19: Potential of discovery (5σ) and exclusion (95%) of the stop $\tilde{t}_1$ mass for the past LHC searches with an integrated luminosity $\int \mathcal{L} \sim 13$ fb^{-1} and a center-of-mass energy $\sqrt{s}$ of 13 TeV, HL-LHC with $\sqrt{s} = 13$ TeV and $\int \mathcal{L} = 3000$ fb^{-1}, HE-LHC with $\sqrt{s} = 33$ TeV and $\int \mathcal{L} = 3000$ fb^{-1}, and a pp collider (FCC) with $\sqrt{s} = 100$ TeV and $\int \mathcal{L} = 3000$ fb^{-1} [116].

One may also examine what are the expectations on the SUSY mass spectrum from measurements other than the direct searches for the SUSY particles. One of the options is to study the branching ratio of the b quark to the s quark plus photon BR($b \to s\gamma$). This decay is possible in the SM via loops with W bosons and top quarks. Within the SUSY other loops are possible as well: these are mainly loops involving the stop and the chargino, and loops with the b quark and the charged Higgs boson. The branching ratio is measured to be BR($b \to s\gamma$) $= (3.01 \pm 0.22) \times 10^{-4}$ [165], the theoretical predictions within the SM give BR($b \to s\gamma$) $= (3.36 \pm 0.23) \times 10^{-4}$ [166]. The observed BR can be compared with the prediction of the BR for each scenario in the $\tilde{t}_1$ vs LSP plane. The compatibility of the measured and predicted branching ratios excludes stop masses lower than 500 GeV. In the majority of scenarios with a stop mass higher than 1.5 TeV, the predicted and measured BR are in agreement within 2σ. But lighter stops than 1.5 TeV in the majority of cases lead to the branching ratios not compatible with the observation [116].

One can also obtain constraints on the masses of the SUSY particles from the observed average cold dark matter density $\rho_{DM} \approx 1.2 \times 10^{-6}$ GeV/cm^3 [167, 110]. In the early universe, there should have been a thermal equilibrium between the SM and SUSY particles. As the universe cooled down, heavier sparticles could not be produced anymore, they only annihilated into the SM particles or decayed to the LSP which is in this paragraph considered to be a neutralino. Eventually, the LSPs also annihilated into the SM particles. With a continuous expansion of the universe, the annihilation rate became small and the LSPs experienced a "freeze-out". If the LSP is mostly higgsino- or wino-like, the LSP needs to be very heavy, of the order of 1 TeV or more, in order to reproduce the observed dark matter density. This model is not yet excluded by the LHC, but on the other hand, it is not natural. Another option is a bino-like LSP, but the mass of such LSP

is in the majority of parameter space already excluded by the LHC, given the constraint on the cold dark matter density. The non-excluded bino-like LSP leads to a too large cold dark matter density, but if making other assumptions, the dark matter density can agree with the observation. For example, we obtain an agreement if one of the sleptons is not too heavy. A large part of such light slepton scenarios is already excluded at the LHC (current measurements exclude slepton masses up to around 400 GeV). The cold dark matter density for the bino-like LSP scenario is also in agreement with observation in the compressed scenario, when the LSP mass is between m_t and m_t+100 GeV, where m_t is the mass of the top quark . The $\tilde{t}_1$ mass is required to be around 150 GeV larger than the LSP mass. In order to make this model natural, the obtained gluino and wino mass parameters ratio does not allow the unification at the GUT scale [131]. Although many possible scenarios are already ruled out by the requirements on the cold dark matter density, there are still parts of the parameter space which are uncovered. Moreover, the described considerations assume only simple thermal mechanism for the production of the LSP. If, for example, there are other production mechanisms or if the R-parity is broken, the conclusions do not have to hold.

There is also a possibility that the MSSM is not the realization of the SUSY chosen by nature and we should examine the non-minimal SUSY theories. For example in the MSSM, the R-parity is conserved, which protects the protons to decay. But there is no fundamental reason that R-parity should be conserved and it could be replaced by another symmetry which also protects protons to decay, like for example a symmetry which conserves the baryon number but not the lepton one. In the case R-parity is violated, the LSP can decay and therefore the signal production and final states differ from the ones assuming the R-parity conservation. Both pair and single SUSY particle productions are expected. Depending on the R-parity violation scenario, the LSP could decay to leptons or/and jets resulting in final states with a large number of charged leptons or/and jets. Another possibility is that the LSP has a long lifetime and produces a special signature in the detector (appearing tracks, ...). Several analyses targeting the R-parity violation scenarios are already in place and produced exclusion limits. But again, these models are simplified and the limits in more general models can be significantly weaker.

As discussed in the previous paragraphs, there are many realizations of SUSY which are already excluded. But on the other hand, it has been shown that there is still some room for natural SUSY. It has been discussed that the lighter stop could have mass up to 3 TeV and be beyond the reach of the LHC. It might be also needed to go beyond the MSSM and focus our searches on more general models.

Conclusion

This thesis presents three different studies based on the Run 2 data. The first two are measurements of the cluster properties in the CMS silicon strip tracker related respectively to the highly ionizing particles (HIP) and the charge sharing among neighboring strips (also known as cross talk). The last topic discussed in this document is the search for the supersymmetric partner of the top quark, called the stop.

In the first study of this thesis, I was interested in the highly ionizing particles in the silicon strip tracker. Already before the beginning of the Large Hadron Collider (LHC) operation, the highly ionizing particles were studied and identified to cause dead-time in the front-end electronics leading to a hit inefficiency in the silicon strip tracker. In the beam tests of the tracker modules, it was found that by decreasing the inverter resistor value of the front-end electronics, the dead-time can be shortened and therefore the design of the electronics was adjusted to mitigate this issue. Later no analysis with LHC collisions had been performed yet. So when an increase of the hit inefficiency in the strip tracker was observed in 2015-2016, a HIP was immediately identified as a possible explanation of it. I studied the HIP effect with collision events recorded in 2016 using a special data format in which no subtraction and suppression were applied at the back-end electronics level and therefore full information about all channels was available. They allowed me to confirm that the HIP induces a large charge on few channels and drives the remaining channels belonging to the same front-end electronics, the APV chip, towards lower charges up to the point when the signal is too small to be converted into light. Reaching this zero light level also induces a decreased spread of the charges on all channels within one APV, when excluding the channels reading a large charge. With these data I was able to measure the rate of the HIP events, i.e. the number of events with a HIP interaction to all events, to be around 4×10^{-3} for the first layer of Tracker Outer Barrel (TOB). I also evaluated the dead-time for this layer to be up to around 250 ns. It is of the same order as the dead-times evaluated in previous studies performed at the PSI beam test, namely a mean and maximal dead-times for the TOB modules of 100 ns and 275 ns, respectively.

However the HIP effect was not responsible for the observed inefficiencies and after the

largest source of inefficiency was found and fixed, a new set of data provided an opportunity to study the HIP effect in a greater detail disentangled of the previous issue. Because of the data-taking conditions, these new data permitted to perform a measurement of the HIP probability in a cleaner environment. The HIP probability was computed per pp interaction, i.e. rescaled by the peak pileup of the fill, in order to have the possibility to apply this probability to any LHC fill. The HIP probability in the silicon strip tracker was measured to be of the order of $10^{-4} - 10^{-3}$% depending on the tracker layer/wheel/ring. The HIP probabilities, already evaluated in the past from simulations and using beam test data, were derived per particle and therefore they cannot easily be compared with the current measurement. Moreover during the beam test, a different particle composition and energy spectra were present compared to the CMS environment.

The HIP probability itself cannot be decreased but we might investigate if the dead-time, and consequently the hit inefficiency, could be reduced. An option how to decrease the dead-time was identified and studied in the past [168]. This option is to maximize the pedestal subtracted data in order to decrease the chance that the channel charges are shifted beyond the measurable range. The pedestal is the mean strip activity when no particle is present and in the standard data-taking mode, not pedestals themselves are subtracted by the back-end electronics, but the pedestals minus a fixed offset, resulting in the positive mean channel charges after this subtraction. This offset can be further maximized, but it was found out that this option only increases the fake cluster multiplicity without improving the hit efficiency. Moreover this option reduces the dynamic range, resulting in larger charges to be truncated faster. However this test was performed before the fix of the largest source of inefficiency and it could be worth to repeat it now.

A measured HIP probability of $10^{-4} - 10^{-3}$% means that in case of a dead-time of 250 ns obtained from the first data and bunch spacing of 25 ns, an APV chip would never be fully efficient if the pileup were of the order of $10^4 - 10^5$. The current pileup during the summer 2018 is of the order of 40 interactions per bunch crossing and therefore far from the fully inefficient chip scenario. The inefficiency resulting from the HIP was recently calculated, using the dead-time of 250 ns and the measured HIP probability, to be of the order of 0.1-1%, for a pileup of 30 as in the representative run used for the 2018 hit efficiency measurement. This is of similar order as the measured 2018 hit inefficiency. Therefore the main source of the measured inefficiency now seems to come from the HIP effect. This inefficiency is not considered during the event simulation.

The second set of data also permitted to study the cluster charge, multiplicity and width in presence of a HIP event or right after. I found out that the fake cluster multiplicity is increased after the HIP event compared to a standard event not influenced by a HIP. However the HIP probability is low and therefore in average over the runs the

fake cluster multiplicity resulting from the HIP is of the same order of magnitude as the fake cluster multiplicity when no HIP had occurred. I observed that fake clusters induced by the HIP originate from the baseline distortions. For the first layer of TOB, I also estimated a lower limit on the probability that a track is reconstructed with at least one fake cluster originating from a HIP event. This probability was computed to be 0.002% and therefore is negligible. These fake clusters are not included in the simulation either, but as discussed, their impact is negligible and therefore it is reasonable to omit them from simulation.

Unfortunately, because of the data-taking conditions of the second data-taking period, it was impossible to measure the dead-time in them. The first data provided a better opportunity to measure the dead-time, but with the difficulty to precisely fix the time of the HIP occurrence. There are not any simple options of data-taking conditions suitable to measure the dead-time in future, in this paragraph I propose two more complex ideas of data-takings which could be considered. The first option would be to arrange data-taking in which events would be recorded every 25 ns during at least 15 bunch crossings not respecting any trigger rule, in order to have the possibility to track a given HIP in time. On top of it, it would be needed to reconsider the analysis strategy. For example, as we would not be interested in the HIP probability anymore, we could spot the HIP event by presence of a large peak, which appears only for few ns and therefore should better fix the time of the HIP event. But this approach could overload the system and therefore it would be needed to evaluate if such data-taking would be reasonable and how we could possibly avoid the overload. The second option would be to have a special fill and partially violate the trigger rules as well. In such fill we would need trains of two bunches and in each train we would need different time gap between the two bunches: in the first one 25 ns, the second one 50 ns, the third one 75 ns, etc. In these data we would have the time of HIP event fixed by the first bunch crossing in train and in the second one we could measure the hit efficiency. The dead-time would be the time gap between two bunch crossings in the same train in which the same hit efficiency is measured. In both these proposed data-takings, it would be needed to make sure, that the fake clusters from baseline distortions are not considered as real clusters by tracking and therefore that the fake clusters do not artificially increase the hit efficiency.

In the future upgrade of the silicon strip tracker for the High Luminosity LHC project (HL-LHC), we must pay attention to the HIP effect already at the design level. Ideally, it would be desired that the electronics is designed in a way that if a large charge is read by one channel, it does not affect the other channels belonging to the same chip as it is the case now. The HIP probability computed in this thesis is related to the module geometry and its distance from the interaction point and therefore cannot be easily extrapolated to

the future detector. Assuming that the tracker would remain the same and for a pileup of around 200 interactions per bunch crossing, the HIP rate per chip could be expected to be of the order of $10^{-2} - 10^{-1}$ %. In the reality, the detector will be upgraded and therefore the HIP probability and induced dead-time will change depending on the design of the tracker modules and the readout electronics.

The second study presented in this thesis focuses on the simulation of the CMS silicon strip tracker and the tracker conditions used in simulation in order to provide realistic results. These conditions change with the tracker operating conditions, e.g. the temperature, but also evolve with tracker ageing resulting from the radiation damage, for example the cross talk, i.e. the charge shared with the neighboring strips. As the majority of these conditions was never updated since the beginning of the Run 1, we decided therefore to revise the simulation and study the impact of the outdated conditions on the simulation of the clusters in the tracker. I found out that the change of conditions (except noise and gains) has a negligible impact on the cluster properties in many cases, but the change of the cross talk parameters largely impacts the cluster width and seed charge.

After having identified that the cross talk parameters cause large discrepancies in cluster shape distributions between data and simulation, a cosmic data-taking period was arranged in absence of magnetic field, dedicated to re-measure the cross talk parameters. As for the HIP studies, no subtraction and suppression of channel charges were applied on the back-end electronics level. In these data I spotted that the cross talk parameters evolve as a function of the time when the particle arrives to a given module. Therefore the cross talk needs to be measured at the correct timing, i.e. as when a particle originating from the pp interaction would reach a given module. Due to the trigger conditions, there was only sufficient statistics to measure the cross talk parameters in the barrel. I measured that the cross talk decreased for all barrel module geometries compared to the previous measurement. The sharing to the first neighboring strips in barrel decreased by around 18-27%, the change being larger for geometries closer to the interaction point i.e. with larger fluence and consequently larger radiation damage. The sharing to the second neighboring strips diminished by around 24%. To determine the cross talk parameters in disks and endcaps, I corrected the old cross talk parameters based on the change of the cross talk parameters in barrel and data to simulation comparisons of the mean cluster seed charge in collision events.

The cross talk parameters influence profoundly the cluster shape, but not the total cluster charge. The change of the cross talk might cause that the clusters which were slightly above the clustering threshold before do not have to pass it now and therefore are

not reconstructed anymore and vice versa. In addition, with the change of the cross talk parameters, the cluster position and its resolution change in simulation, resulting in small changes in tracking. Therefore the effect of a change of the cross talk may propagate up to some of the physics analyses, e.g. in searches for appearing/disappearing tracks. The object discriminators, mainly the b-tagging discriminators, which are strongly dependent on the tracking, are also influenced by it. The impact on the other physics objects and analyses, not largely dependent on tracking, is expected to be negligible.

It was shown that the cross talk parameters evolve as a function of the fluence and therefore they should be remeasured and updated regularly. Also more frequent measurements of the cross talk parameters could help us to understand why the cross talk is decreasing with respect to the previous measurement. The literature is stating that with an increasing fluence, the inter-strip capacitance should increase and the inter-strip resistance decrease. Both these changes should lead to the increase of cross talk, what was not observed. However the inter-strip resistance and capacitance are not the only factors influencing the signal formation, but there is more complex network of capacitances and resistances which has its impact on the cluster shape. Note that the cross talk was measured only in the deconvolution mode, so it should be updated for the peak mode as well. Nevertheless, the peak mode is not used in standard data-taking, but it could help us to investigate the decrease of the cross talk, by disentangling the effects of the deconvolution from other effects.

The cosmic data recorded in absence of magnetic field, which were used for the cross talk measurement, posed several constraints and difficulties. First, due to the trigger conditions there is insufficient statistics in the disks and endcaps. Even if the trigger would be re-designed, due to the η distribution of the cosmics, the data-taking would have to be long in order to collect sufficient statistics, which is difficult to arrange in the tight CMS schedule. The second large issue is related to the tracker timing when it samples the collected signal. The tracker has no special timing configuration for the cosmics and therefore the collision timing is always used. As the cross talk depends on timing, we need to use for the cross talk measurement only cosmics which arrive to the given module at the same time as a particle produced in the pp collision. Another ambiguity comes from the computation of the particle arrival time, which extrapolates all particles to the interaction point, even though they do not have to pass through there. Both the pseudorapidity coverage and the timing issues would be solved if it is possible to arrange a new data-taking of non suppressed collision data without magnetic field. But such data-taking is not compatible with the CMS program and priorities.

After the update of the cross talk parameters and conditions such as gains and noise updated by other members of the tracker local reconstruction group, the description by

the simulation of the in-time clusters in data was largely improved. It was identified that there are still several parameters which are outdated and could be updated in future, however these parameters do not largely change the cluster description. In this thesis on one hand I found out that the simulation is simplified and sometimes not realistic, but on the other hand developing more sophisticated models would not largely improve the description of the clusters in data by simulation. I also identified that already some existing parts of the simulation have only a negligible impact, i.e. the diffusion, and it could be good to evaluate what parts of the simulation are really needed in order to reduce the time needed for the event simulation.

Several improvements could be still included in the simulation of the out-of-time clusters. First, the pulse shape has changed due to the change of the APV parameter and therefore the pulse shape should be updated in order to reduce the simulated charge by a correct fraction. Secondly, it was shown that the cross talk depends on timing. The cross talk parameters were derived for in-time clusters and are not correct for out-of-time clusters. Ideally, the cross talk parameters should be parameterized as a function of the particle arrival time to the module. The out-of-time clusters need also to be well simulated as these clusters might be used by the tracking algorithm to reconstruct the tracks of the particles.

Few other interesting studies could be performed with the taken cosmic data and here I discuss few examples. In the past it was observed that there is a left-right asymmetry in the charge sharing. This effect could be as well studied with these data. Moreover, it is possible to study the cross talk and cluster properties as a function of the position where the track intercepts the strip plane, close and far from the strip. In the past it was also observed that there is an evolution of the cluster seed charge as a function of the strip number within one APV chip, this study could be repeated with these data. All these studies could help to better understand the formation of the signal, the features of the sensors such as non-uniformities in the electric field, and also the changes in the sensors properties resulting from their irradiation.

In the future tracker for the HL-LHC, the clustering will be largely different, only the binary information from the strip/macro-pixel will be sent, therefore the cluster seed charge and cluster charge will not be available and just the cluster width will be known. As the cluster width depends on cross talk, it will also be needed to measure the cross talk in the new tracker. Moreover it will be important to determine and monitor the cross talk in order to design and maintain the threshold for strip/macro-pixel charge to

be correctly set to one or zero.

The last part of the thesis is discussing a search for physics beyond the standard model. Despite its capability to well describe the majority of observed physics phenomena, the standard model (SM) of particle physics suffers from several shortcomings such as the hierarchy problem or the absence of a dark matter candidate. Due to these shortcomings, theories beyond the SM were proposed and one of them, the supersymmetry, became the most promising one because of its ability to address large part of the SM issues. In this thesis I presented a search for the supersymmetric partner of the top quark, the stop, with the CMS Run 2 data. This search targets the stop pair production, with three different possibilities for the decays of the stops: the two stops decay each to a top quark and a neutralino, or the two stops decay to a bottom quark and a chargino, or each stop decays differently as a mixture of the two previous cases. In all cases, the targeted signal final states contain one lepton, jets and missing transverse energy.

I was involved in three public releases of this search: one based on the data recorded in 2015 corresponding to an integrated luminosity $\int \mathcal{L}$ of 2.3 fb^{-1} [129], the second one based on the data recorded at the beginning of 2016 ($\int \mathcal{L} = 12.9$ fb^{-1}) [130] and the last one corresponding to $\int \mathcal{L} = 35.9$ fb^{-1} collected during the full 2016 pp data-taking period [128]. I was mainly involved in the last analysis, where I was responsible for the estimation of one of the SM backgrounds, in which a Z boson decays to two neutrinos. In this thesis I also exploited a technique for tagging of merged jets originating from a W boson and I showed that the gain of implementing such technique is growing with the integrated luminosity.

The searches for the stop pair production in different final states were already performed with the Run 1 data. The analyses exclude stop masses in terms of simplified model spectra with stops decaying to a top quark and a neutralino up to around 755 GeV for a neutralino mass below 200 GeV. With the increase of the center of mass energy and then also the integrated luminosity, it was soon possible to further probe the stop masses. No excess was found in the full 2016 data ($\int \mathcal{L} = 35.9$ fb^{-1}) with respect to the SM background predictions and therefore exclusion limits were derived. This analysis excluded stop masses up to 1120 GeV for a massless neutralino in terms of simplified model spectra where both stops decay to a top quark and a neutralino. In the case where both stops decay to a bottom quark and a chargino or in the case of mixed decay, the stop masses were excluded up to 1000 GeV and 980 GeV, respectively.

Despite the stop exclusion in the TeV range, there is still room for the natural supersymmetry and therefore the effort to search for stops is not diminishing. According to the

CMS predictions, with an integrated luminosity of 3000 fb^{-1} envisioned to be collected at the HL-LHC, it will be possible to probe the stop masses up to 2 TeV. An upgrade of the LHC to higher center of mass energies would permit us to go even further in the stop masses.

Before migrating to future projects, there are several directions how to improve the presented stop analysis for its future update based on data with a larger integrated luminosity. On the side of the SM backgrounds it is desired to use the data-driven methods for the background estimations in order to minimize a dependence on the simulation and consequently reduce the systematic uncertainties. The data-driven estimates are based on control regions, these control regions should be defined very similarly as the signal regions to avoid uncertainties due to extrapolations in variables. These extrapolations rely on the shapes of variables in simulation, and if not well modeled they largely increase the systematic uncertainties on the background estimates. On the side of the signal we discussed that the simplified event simulation is not reliable in the region of the 2D mass plane where $\Delta m(\text{stop}, \text{neutralino}) \sim m(\text{top})$ at low neutralino mass. This could be solved by using the full simulation of the detector in this particular kinematic region. Then also the analysis strategy can be reoptimized. It is possible to reoptimize the signal regions by finding optimal cuts but also trying to find better discriminating variables. Another option is to use more object taggers. Nowadays there is a variety of taggers targeting the W boson and top quark identification, not only targeted as a single merged jet, but also as completely resolved jets or partially merged jets. We could also consider not to perform a cut and count analysis but move to machine learning techniques providing discriminant between signal and background we can cut on.

Within the CMS collaboration a large variety of SUSY searches is performed. The stops are being sought in several different final states and the other predicted SUSY particles are targeted by dedicated searches as well. Many analyses search for SUSY within the context of the minimal supersymmetric standard model but there are also several searches which go beyond, e.g. searches allowing violation of the R-parity. In general the SUSY searches are interpreted in terms of simplified spectra. A lot of efforts are being done to reinterpret these searches in more realistic models. Another part of activities is the combination of searches to reach a better discovery/exclusion potential. The CMS experiment and in general the collider experiments do not provide the sole opportunity to search for supersymmetry. For example, supersymmetry can also be studied via direct dark matter detection experiments.

In summary, there are still many options for natural SUSY in term of parameter space and also many options how to search for it. Collider experiments are one of these options, and with increasing luminosity, energy and optimization of analyses they are providing

great opportunities to go beyond the current limits and further probe the uncovered phase-space.

Chapter A

Résumé en français de mes travaux de thèse: résultats principaux et discussion

Pendant ma thèse, je j'ai travaillé dans une équipe qui fait partie de la collaboration CMS. Le détecteur "Compact Muon Solenoid" (CMS) montré à la Fig. A.1 est un détecteur de physique des particules situé au CERN en Suisse, auprès du Large Hadron Collider (LHC), un accélérateur circulaire de particules de 27 km de long qui fournit des collisions de protons à une énergie dans le centre de masse de 13 TeV depuis 2015 (Run II).

Le programme de physique de CMS couvre principalement des mesures de précision du Modèle Standard (MS) avec un énorme effort dédié aux études du boson de Higgs, ainsi que la recherche de phénomènes au-delà du MS aussi appelée recherche de "nouvelle physique".

A.I Introduction

Cette thèse a commencé en octobre 2015, la même année que le début de la période de prise de données appelée Run 2 (2015-2018) au cours de laquelle l'énergie dans le centre de masse, la luminosité instantanée et la fréquence des collisions ont augmenté par rapport au Run 1 (2008-2013). Par conséquent, les possibilités d'analyses de processus physiques ont été largement étendues au prix d'une plus grande fluence du côté du détecteur, en particulier sur le trajectographe qui est le détecteur interne. Avec cette fluence croissante, le détecteur souffre d'une irradiation plus importante qui pourrait être à l'origine de problèmes de performance. De plus, le détecteur vieillit avec l'irradiation, entraînant une modification de certaines de ses caractéristiques. Par conséquent, il est très important de

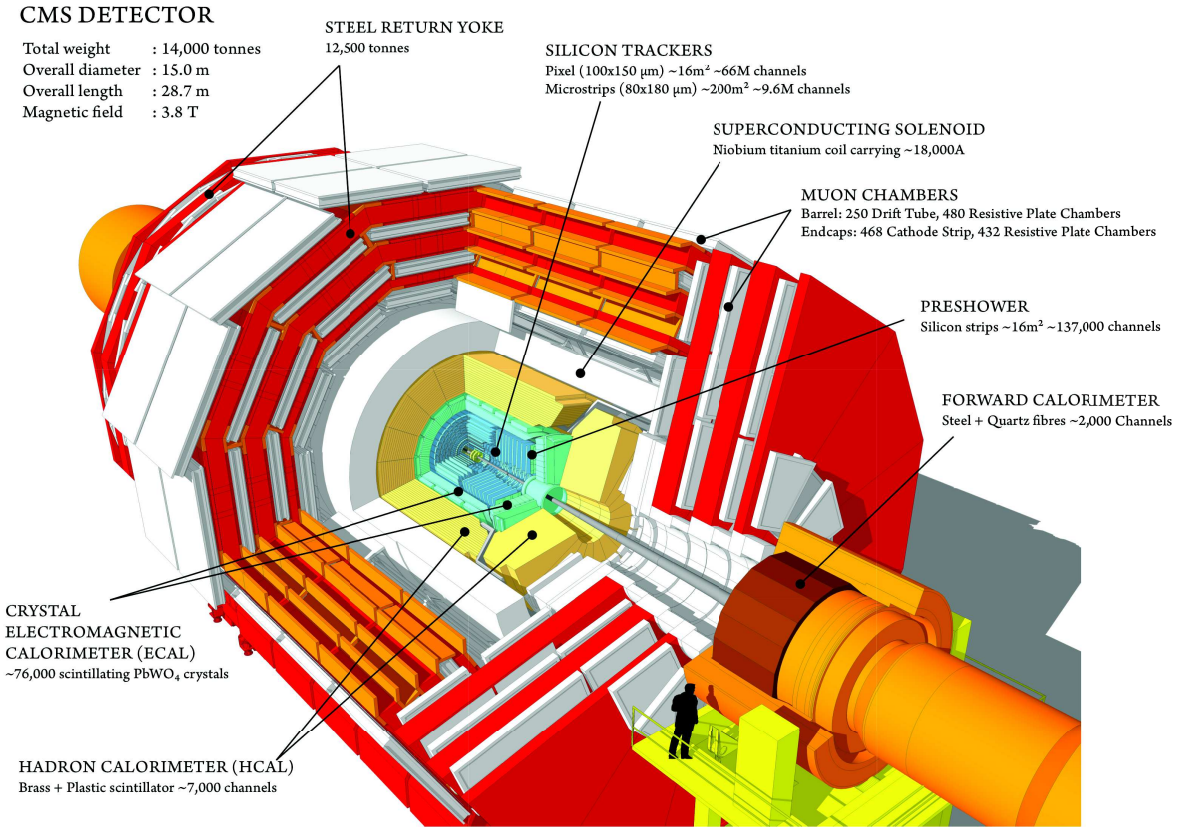

Figure A.1: Schéma du détecteur de CMS [13].

surveiller de près le détecteur, afin de conserver des performances stables et d'éviter tout impact négatif sur les analyses de physique. Dans les sections suivantes, je traiterai de deux groupes d'études sur lesquelles j'ai travaillé dans le cadre du trajectographe.

La physique des particules est décrite par le modèle standard dont la dernière pièce, le boson de Higgs, a été découverte en 2012 par les collaborations CMS et ATLAS. Bien que le modèle standard soit maintenant complet et décrive en général très bien les phénomènes physiques, il souffre de plusieurs défauts. Ce problème nous pousse à croire que le modèle standard est une théorie effective à basse énergie d'une théorie plus fondamentale à déterminer. Au fil des ans, de nombreuses théories ont été proposées et l'une d'entre elles, appelée supersymétrie, a suscité un intérêt particulier en raison de sa capacité à répondre à de nombreuses lacunes du modèle standard.

La supersymétrie introduit un nouveau partenaire pour chaque particule de modèle standard et, par conséquent, des recherches approfondies sur ces particules ont été et sont encore actuellement effectuées par la collaboration CMS, ainsi que par d'autres collaborations. La particule qui nous intéresse dans le cadre de cette thèse est le partenaire supersymétrique du quark top, le stop, qui devrait avoir une masse inférieure à environ 1 TeV en supersymétrie naturelle [111, 114, 115] et donc être accessible aux én-

ergies du LHC. Aucun signe de l'existence de stop n'a été observé au Run 1 [123], mais l'augmentation de la luminosité ainsi que l'énergie dans le centre de masse au Run 2 nous permettent de sonder des masses de stop au-delà de l'exclusion du Run 1.

A.II Dispositif expérimental

La description du détecteur Compact Muon Solenoid est donnée dans le premier chapitre, Chapitre 1, avec une brève introduction du Large Hadron Collider (LHC). Ce chapitre se concentre sur le trajectographe à pistes de silicium montré à la Fig. A.2, dont la compréhension approfondie est requise pour les chapitres suivants. Ce chapitre présente également la reconstruction des objets physiques correspondant aux particules traversant le détecteur.

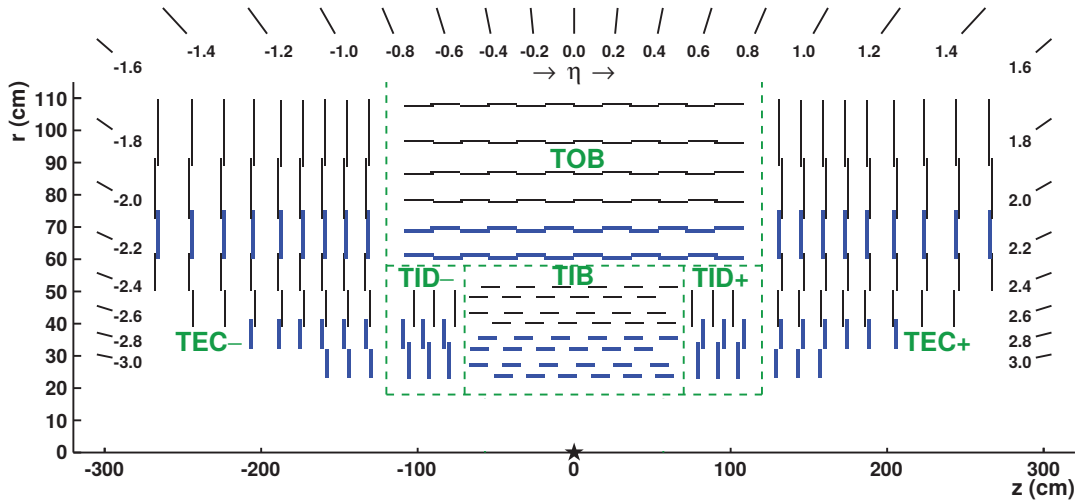

Figure A.2: Schéma de la vue longitudinale de la moitié supérieure du trajectographe à pistes de silicium CMS et de la disposition de ses partitions. L'étoile représente le point de interaction. Les modules en bleu sont en stéréo, alors que les modules mono sont en noir [20].

A.III Étude des particules hautement ionisantes dans le trajectographe de CMS

Dans le Chapitre 2, je me suis intéressée aux particules hautement ionisantes (HIP) dans le trajectographe à pistes de silicium. Déjà avant le démarrage du Large Hadron Collider, les particules hautement ionisantes ont été étudiées et identifiées comme pouvant causer un temps mort dans l'électronique frontale, entraînant une inefficacité dans le trajectographe

à pistes de silicium. Lors les tests en faisceau des modules du trajectographe, il avait été constaté qu'en diminuant la valeur de la résistance du convertisseur de l'électronique frontale, le temps mort pouvait être diminué [53] comme indiqué dans le Tableau A.1, et le design de l'électronique avait donc été ajustée pour atténuer ce problème. En 2015-2016, lorsqu'une augmentation de l'inefficacité de reconstruction des hits dans le trajectographe a été observée pouvant aller jusqu'à 7%, les HIP ont immédiatement été identifiés comme une explication possible.

J'ai étudié l'effet des HIP pour la première fois avec des données de collisions LHC. Les événements de collision enregistrés en 2016 dans un format de données spécial dans lequel aucune soustraction ni suppression n'ont été appliquées au niveau de l'électronique arrière, donnant accès aux informations complètes sur tous les canaux. Cette étude m'a permis de confirmer que le HIP induit une charge importante sur quelques canaux et a forcé les canaux restants connectés à la même puce électronique frontale, la puce APV, vers des charges plus faibles jusqu'au moment où le signal est trop petit pour être converti en lumière comme on peut l'observer sur la Fig. A.3. Lorsqu'on atteint ce niveau sans lumière émise, on observe également une réduction des différences entre les charges de tous les canaux d'un APV, en excluant les canaux lisant une charge associée du HIP. A partir de ces données, j'ai pu mesurer le taux d'événements HIP, c'est-à-dire le rapport entre le nombre d'événements ayant une interaction HIP et tous les événements. Ce taux est de 4 $\times 10^{-3}$ pour la première couche de Tracker Outer Barrel (TOB), trop bas pour être responsable des inefficacités observées en 2015 et 2016. J'ai également évalué le temps mort pour cette couche à environ 250 ns. Il est du même ordre que les temps morts évalués dans des études antérieures effectuées lors de tests en faisceau à PSI, à savoir un temps mort moyen de 100 ns et un temps mort maximal de 275 ns pour les modules TOB, respectivement.

Au cours de l'été 2016, la plus grande source d'inefficacité de reconstruction des hits dans le trajectographe a été identifiée et corrigée en modifiant la configuration de la puce APV. Selon les conditions de run, l'inefficacité de le reconstruction des hits après correction de la configuration APV est d'environ moins de 1%. Suite à cela un nouvel lot de données a été enregistré afin d'étudier l'effet HIP de manière plus détaillée. En raison des conditions de prise de données, ces nouvelles données ont permis de mesurer la probabilité d'avoir un HIP dans un environnement plus propre. La probabilité d'avoir un HIP (p_{HIP}) a été calculée par interaction proton-proton, c'est-à-dire que la fraction d'événements avec un HIP (f_{HIP}) été divisée par le taux maximal d'interactions simultanées (peak pileup: PU), $p_{HIP} = f_{HIP}/PU$, afin de pouvoir appliquer cette probabilité à toute configuration de structure des faisceaux du LHC. La probabilité d'avoir un HIP dans le trajectographe à pistes de silicium est représentée sur la Fig. A.4 et les mesures varient entre 10^{-4}

Type de capteur et R_{inv} [Ω]	Γ_{mean} [ns]	Γ_{max} [ns]
TIB 100 Ω	99.5 $\pm$ 12.0	200 $\pm$ 25
TIB 50 Ω	69.6 $\pm$ 9.4	250 $\pm$ 25
TOB 100 Ω	122.5 $\pm$ 12.6	275 $\pm$ 25
TOB 50 Ω	100.5 $\pm$ 3.6	275 $\pm$ 25
TIB $\Gamma_{mean}(50\ \Omega)/\Gamma_{mean}(100\ \Omega)$	0.70 $\pm$ 0.13	
TOB $\Gamma_{mean}(50\ \Omega)/\Gamma_{mean}(100\ \Omega)$	0.82 $\pm$ 0.09	

Table A.1: Le temps mort moyen (Γ_{mean}) et le temps mort maximal (Γ_{max}) de la puce APV induits par les événements HIP pour les lignes de base (i.e. la médiane calculées sur l'ensemble des 128 pistes lues par une puce APV) qui sont entièrement supprimées ($\sigma_{raw} <$ 1 ADC). Les temps morts ont été évalués pour deux géométries de module différentes (TIB et TOB) ainsi que pour deux valeurs de résistance de convertisseurs (100 et 50 Ω). Ces résultats ont été obtenus avec des données de tests en faisceau à PSI avant le début de l'exploitation du LHC [53].

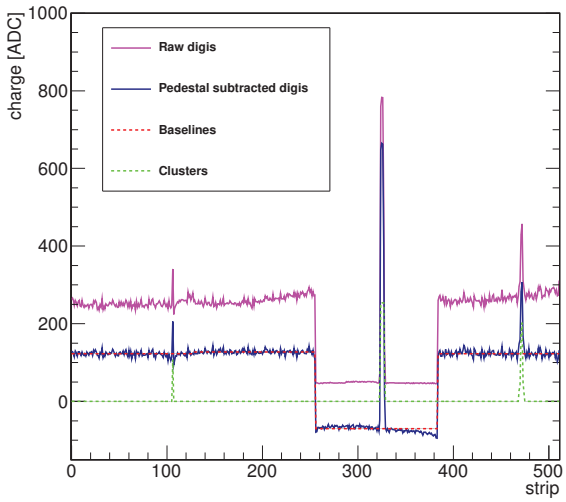

Figure A.3: Exemple de distributions du signal vu par les 512 pistes (strip) d'un module, sous format raw digis (en rose), après soustraction du piédestal (en bleu), après soustraction de la ligne de base (en rouge) et après soustraction des amas (en vert). Chaque ensemble de 128 pistes est lu par une puce APV. Le troisième APV dans le module montre un comportement induit par un événement HIP: une faible variation de charge pour les raw digis et un grand signal observé pour quelques canaux.

et 10^{-3}% selon sur la position dans les différentes partitions du trajectographe. Les probabilités d'avoir un HIP, déjà évaluées par le passé à partir de simulations et utilisant des données de tests en faisceau, ont été dérivées par particule et ne peuvent donc pas être facilement comparées à la mesure actuelle. De plus, lors des tests en faisceau, la composition des particules et leurs spectres en énergie étaient différents par rapport à l'environnement CMS.

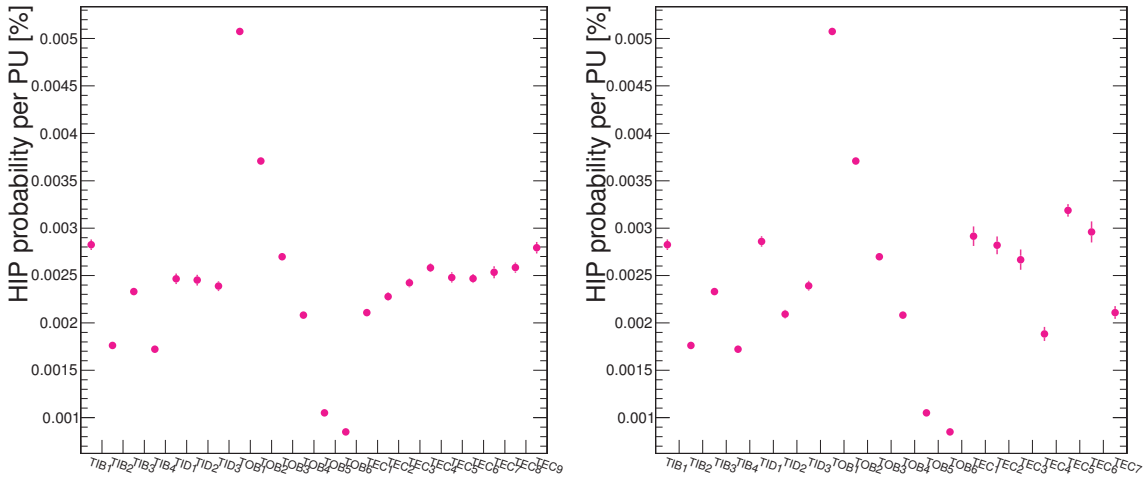

Figure A.4: Probabilité moyenne d'avoir un événement HIP par unité du pileup (PU) pour les couches du TIB et du TOB (aussi bien sur la figure de gauche que de droite) et pour les roues (à gauche) ou les anneaux (à droite) des partitions TID et TEC du trajectographe de silicium. Ces probabilités ont été calculées à partir du run 281604 enregistré en 2016 (2^e étude des HIP).

La probabilité d'avoir un HIP ne peut pas être diminuée, mais nous pourrions chercher si le temps mort et par conséquent l'inefficacité de reconstruction du hits des traces pourraient eux être réduits. Une option permettant de réduire le temps mort a été identifiée et étudiée dans le passé [168]. Cette option permet de maximiser les données après soustraction du piédestal[1] afin de réduire le risque que les charges des canaux soient décalées trop bas, au-delà de la plage mesurable. En réalité dans le mode de prise de données standard, c'est le piédestal moins un certain décalage fixe qui est soustrait par l'électronique back-end. Le choix de ce décalage pourrait être optimisé, mais il a été constaté que cette option ne fait qu'accroître la multiplicité des "faux" amas sans améliorer l'efficacité de reconstruction des hits. De plus, cette option réduit la plage dynamique, ce qui se traduit par des charges plus importantes à tronquer plus rapidement. Cependant, ce test a été effectué avec l'ancienne configuration de la puce APV et il pourrait être utile de le répéter maintenant.

Une probabilité d'avoir un HIP mesurée de $10^{-4} - 10^{-3}\%$ signifie que dans le cas d'un temps mort de 250 ns (obtenu grâce à la première étude de cette thèse), d'un espacement de 25 ns entre les paquets des particules du faisceau, la puce APV ne serait jamais pleinement efficace uniquement si le pileup était de l'ordre de $10^4 - 10^5$. Le pileup actuel au cours de l'été 2018 est de l'ordre de 40 interactions par croisement de faisceau et donc loin du scénario d'une puce totalement inefficace. L'inefficacité de reconstruction des hits

[1]Le piédestal est l'activité moyenne sur une piste quand aucune particule n'est présente.

résultant des HIP a récemment été calculée en utilisant un temps mort de 250 ns et la probabilité d'avoir un HIP mesurée, elle est de l'ordre de 0.1-1% pour un pileup de 30 comme pour le run représentatif utilisé pour la mesure de l'efficacité de reconstruction des hits en 2018. Cet ordre de grandeur est similaire à l'inefficacité mesurée en 2018. Par conséquent, la principale source de l'inefficacité mesurée semble désormais provenir de l'effet HIP. Cette inefficacité n'est pas prise en compte lors de la simulation des événements.

Le deuxième ensemble de données m'a également permis d'étudier la charge et la multiplicité des amas, présentées à la Fig. A.5, en présence d'un événement HIP ou juste après. J'ai découvert que la multiplicité de faux amas augmente après l'événement HIP par rapport à un événement standard non influencé par un HIP. Cependant, la probabilité d'avoir un HIP est faible et, par conséquent, en moyen sur le run, la multiplicité de faux amas résultant du HIP est du même ordre de grandeur que la multiplicité de faux amas en l'absence de HIP, le nombre étant deux ordres de grandeur inférieur au cas du out-of-time pileup. J'ai observé que les faux amas induits par le HIP proviennent de distorsions de la ligne de base. Pour la première couche du TOB, j'ai également estimé une limite inférieure sur la probabilité qu'une trace soit reconstruite avec au moins un faux amas provenant d'un événement HIP. Cette probabilité est de 0.002 % et donc négligeable. Ces faux amas ne sont pas non plus inclus dans la simulation. Mais comme on l'a vu, leur impact est négligeable, il est donc raisonnable de les omettre de la simulation.

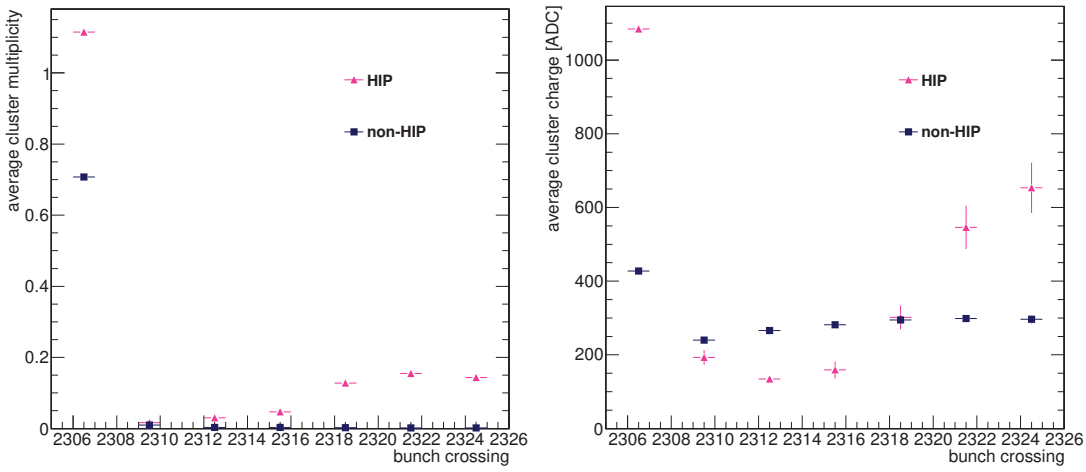

Figure A.5: Nombre d'amas moyenne (à gauche) et charge moyenne portée par les amas (à droite) en fonction du numéro d'identification du croisement de faisceau pour le run 281604. Le premier triangle rose représente l'événement HIP, les triangles suivants représentes les événements successifs (post HIP), tandis que les carrés bleus sont pour les événements non affectés par un HIP.

Malheureusement, en raison des conditions de prise de données utilisée pour la 2^{eme} étude, il était impossible de mesurer du temps mort. Les premières données ont fourni

une meilleure occasion de mesurer le temps mort, mais avec la difficulté de déterminer précisément le temps de l'occurrence du HIP. Il n'existe pas d'options simples de conditions de prise de données permettant de mesurer le temps mort à l'avenir. Dans ce paragraphe, je propose deux idées plus complexes de prises de données qui pourraient être envisagées. La première option consisterait à organiser la prise de données dans laquelle les événements seraient enregistrés tous les 25 ns pendant au moins 15 croisements de paquets, sans respecter aucune règle de déclenchement, afin de pouvoir suivre un HIP donné dans le temps. De plus, il serait nécessaire de reconsidérer la stratégie d'analyse. Par exemple, comme nous ne serions plus intéressés par la mesure de la probabilité d'avoir un HIP, nous pourrions repérer l'événement HIP en présence d'un grand pic, qui n'apparaît que pour quelques instants et devrait donc mieux déterminer le temps de l'événement HIP. Mais cette approche pourrait surcharger le système d'acquisition de CMS et il faudrait donc évaluer si une telle prise de données serait raisonnable et comment nous pourrions éventuellement éviter la surcharge. La deuxième option serait d'avoir un structure spéciale de remplissage du faisceaux du LHC et de violer partiellement les règles de déclenchement de CMS. Dans un tel scénario, nous aurions besoin de trains contenant uniquement deux paquets et pour chaque train, nous aurions besoin d'un intervalle de temps différent entre les deux paquets: pour le premier train les deux paquets seraient séparés par 25 ns, pour le second par 50 ns, pour le troisième par 75 ns, etc. Grâce à de telles données, nous aurions le temps de l'événement HIP fixé par le premier croisement du train et le second, nous permettrait de mesurer l'efficacité de reconstruction des hits. Le temps mort serait obtenu comme l'intervalle de temps entre deux croisements de paquets d'un même train pour lesquels la même efficacité de hit est mesurée. Pour ces deux propositions, il serait nécessaire de s'assurer que les faux amas issus des distorsions de la ligne de base ne sont pas considérées comme de bons amas lors de la reconstruction des traces et que, par conséquent, les faux amas n'augmentent pas artificiellement l'efficacité.

Pour future mise à niveau du trajectographe à pistes de silicium dans le cadre du projet High Luminosity LHC (HL-LHC), nous devons prêter attention à l'effet HIP dès la conception. Idéalement, il serait souhaitable que l'électronique soit conçue de telle manière que si une charge importante est lue par un canal, cela n'affecte pas les autres canaux appartenant à la même puce comme c'est le cas actuellement. La probabilité d'avoir un HIP calculée dans cette thèse est liée à la géométrie du module et à sa distance par rapport au point d'interaction et ne peut donc pas être facilement extrapolée à un futur détecteur. En supposant que le trajectographe resterait le même et pour un pileup d'environ 200 interactions par croisement de paquets, le taux de HIP par puce pourrait être de l'ordre de $10^{-2} - 10^{-1}\%$. En réalité, le détecteur sera mis à niveau et, par conséquent, la probabilité d'avoir un HIP et le temps mort induit changeront en fonction de la conception des modules du trajectographe et de l'électronique de lecture.

A.IV Amélioration de la simulation du trajectographe et mesure de la diaphonie

Le troisième chapitre, Chapitre 3, se concentre sur la simulation du trajectographe à pistes en silicium de CMS et sur les paramètres de trajectographe utilisés dans la simulation afin de fournir des résultats réalistes. Ces paramètres changent avec les conditions de fonctionnement du trajectographe, par ex. la température, mais évoluent également avec le vieillissement résultant des dommages causés par le rayonnement, par exemple la diaphonie ("cross talk"), c'est-à-dire la charge partagée avec les pistes voisines comme le montre la Fig. A.6. La majorité de ces conditions n'ayant jamais été mise à jour depuis le début du Run 1, nous avons donc décidé de réviser la simulation et d'étudier l'impact des paramètres obsolètes sur la simulation des amas dans le trajectographe. J'ai découvert que le changement de conditions (à l'exception du bruit et des gains) a un impact négligeable sur les propriétés des amas dans de nombreux cas, mais le changement des paramètres de la diaphonie affecte largement la largeur de l'amas et la charge de la piste collectant le signal maximal servant de graine à la formation de l'amas.

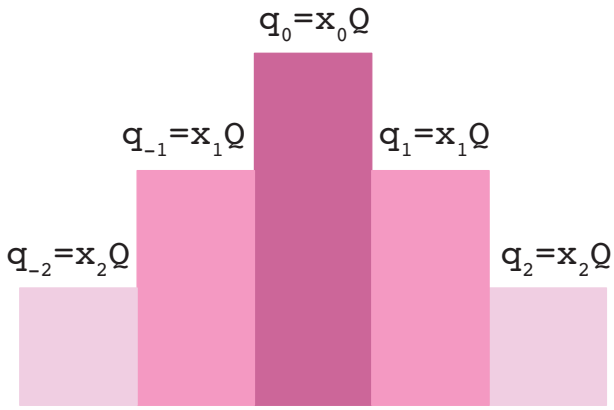

Figure A.6: Un schéma de partage de charge entre pistes voisines.

Après avoir identifié que les paramètres de la diaphonie provoquent des écarts importants dans les distributions de forme des amas entre les données et la simulation, comme le montre la Fig. A.7, nous avons utilisé des données correspondant au passage de muons cosmiques, dans le détecteur pour mesurer les paramètres de la diaphonie. Comme pour les études des HIP, aucune soustraction ni suppression de charge de canal n'ont été appliquées au niveau de l'électronique back-end. Dans ces données cosmiques, j'ai remarqué que les paramètres de la diaphonie évoluent en fonction du moment où la particule arrive dans un module donné. Par conséquent, la diaphonie doit être mesurée au bon moment, c'est-à-dire comme si une particule provenant de l'interaction proton-proton atteint un module donné. Ceci est particulièrement difficile pour des muons cosmiques arrivant de

façon aléatoire.

J'ai mesuré que la diaphonie diminuait pour toutes les géométries de module dans la partie centrale de CMS (ou tonneau) par rapport à la mesure précédente. Les paramètres nouvellement mesurés ainsi que les paramètres actuels utilisés dans la simulation sont indiqués dans le Tableau A.2. Le partage de charge avec les premières pistes voisines a diminué d'environ 18-27%, le changement étant plus important pour les géométries plus proches du point d'interaction, c'est-à-dire avec une plus grande fluence et, par conséquent, des dommages plus importants. Le partage de charge avec les deuxièmes pistes voisines a diminué d'environ 24%. En raison des conditions de déclenchement, il n'y avait pas suffisamment de statistiques pour mesurer les paramètres de la diaphonie dans les disques (TID) et les bouchons du trajectographe (TEC). Pour déterminer les paramètres de la diaphonie dans ces partitions, j'ai corrigé les anciens paramètres de la diaphonie en fonction du changement observé des paramètres dans le tonneau et tenant compte des comparaisons entre données et simulation de la charge moyenne des amas dans les événements de collision. Les résultats des mesures de la diaphonie sur les disques et les bouchons sont résumés dans le Tableau A.3. En mettant à jour les paramètres de la diaphonie dans la simulation, nous avons découvert que les nouvelles mesures améliorent largement la description de la forme des amas dans les données par simulation, comme illustré à la Fig. A.8.

Géométrie	Type	x_0	x_1	x_2
IB1	nouvelle mesure	0.836 ± 0.009	0.070 ± 0.004	0.012 ± 0.002
IB1	simulation	0.775	0.096	0.017
IB2	nouvelle mesure	0.862 ± 0.008	0.059 ± 0.003	0.010 ± 0.002
IB2	simulation	0.830	0.076	0.009
OB2	nouvelle mesure	0.792 ± 0.009	0.083 ± 0.003	0.020 ± 0.002
OB2	simulation	0.725	0.110	0.027
OB1	nouvelle mesure	0.746 ± 0.009	0.100 ± 0.003	0.027 ± 0.002
OB1	simulation	0.687	0.122	0.034

Table A.2: Valeurs de la diaphonie mesurées en 2018 comparées aux anciennes mesures de diaphonie utilisées actuellement pour la simulation des géométries du tonneau.

Les paramètres de la diaphonie influencent profondément la forme des amas, mais pas leur charge totale. Le changement de la diaphonie pourrait faire en sorte que les amas qui étaient précédemment légèrement au-dessus du seuil de clustering soient à présent en dessous et ne soient donc plus reconstruits, et vice versa. De plus, avec la modification des paramètres de la diaphonie, la position de l'amas et sa résolution changent lors de la simulation, entraînant de petits changements dans la reconstruction des traces. Par conséquent, l'effet d'une modification de la diaphonie peut se propager jusqu'à cer-

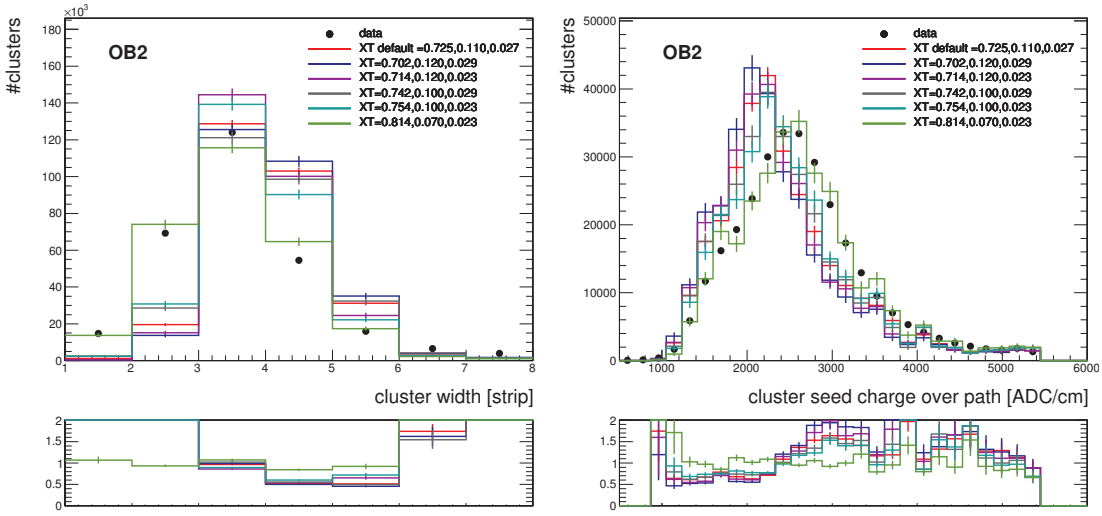

Figure A.7: Distributions de la largeur des amas (à gauche) et de la charge portée par la piste collectant le plus de signal dans l'amas (à droite) pour la géométrie OB2. Les données de collision sont représentées par les points noirs, différentes valeurs de la diaphonie XT sont utilisées dans la simulation (chaque set correspondant à une couleur différente). Le premier des trois nombres XT correspond à la fraction de charge induite sur la piste principale, les deuxième et troisième nombres représentent les fractions de charge induites sur les premiers et seconds voisins, respectivement. Les distributions simulées sont renormalisés au nombre d'amas dans les données. Les graphique inférieurs représentent le rapports des distributions des données par la simulation.

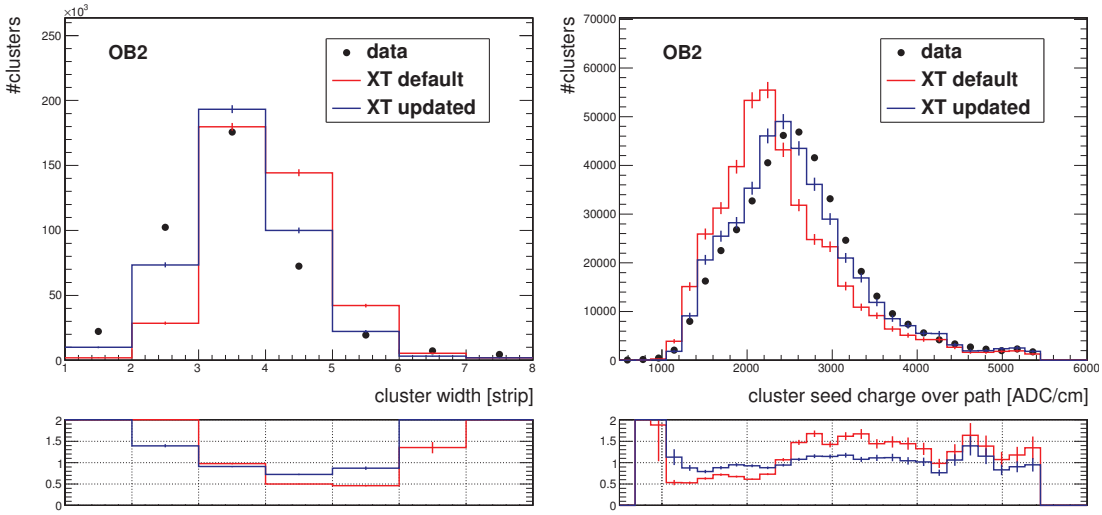

Figure A.8: Distribution de la largeur de l'amas (à gauche) et de la charge portée par la piste collectant le plus de signal dans l'amas (à droite) dans les données et la simulation pour la géométrie OB2, pour les paramètres de la diaphonie (XT) actuels (défaut, en rouge) et nouvellement mesurés (updated, en bleu). Les distributions simulées sont renormalisés au nombre d'amas dans les données. Les graphiques inférieurs représentent le rapport des données et simulation.

Géométrie	Type	x_0	x_1	x_2
W1a	nouvelle mesure	0.8571	0.0608	0.0106
W1a	simulation	0.786	0.093	0.014
W2a	nouvelle mesure	0.8861	0.049	0.008
W2a	simulation	0.7964	0.0914	0.0104
W3a	nouvelle mesure	0.8984	0.0494	0.0014
W3a	simulation	0.8164	0.09	0.0018
W1b	nouvelle mesure	0.8827	0.0518	0.0068
W1b	simulation	0.822	0.08	0.009
W2b	nouvelle mesure	0.8943	0.0483	0.0046
W2b	simulation	0.888	0.05	0.006
W3b	nouvelle mesure	0.8611	0.0573	0.0121
W3b	simulation	0.848	0.06	0.016
W4	nouvelle mesure	0.8881	0.0544	0.0015
W4	simulation	0.876	0.06	0.002
W5	nouvelle mesure	0.7997	0.077	0.0231
W5	simulation	0.7566	0.0913	0.0304
W6	nouvelle mesure	0.8067	0.0769	0.0198
W6	simulation	0.762	0.093	0.026
W7	nouvelle mesure	0.7883	0.0888	0.0171
W7	simulation	0.7828	0.0862	0.0224

Table A.3: Valeurs de la diaphonie actualisées pour les anneaux du TID (W1a, W2a, W3a) et du TEC (restant), comparées aux anciennes mesures utilisés dans la simulation.

taines des analyses de physique, par exemple dans les recherches de signatures de nouvelle physique qui cherchent des traces qui apparaissent tardivement ou disparaissent dans le trajectographe. L'identification des objets de physique, qui dépendent fortement du trajectographie, comme par exemple le b-tagging (identification des jets comme issus de quarks b) , peut également être influencée par un changement des paramètres de la diaphonie. L'impact sur les autres objets et analyses de physique, qui ne dépendent pas fortement du trajectographie, devrait être négligeable.

Il a été montré que les paramètres de la diaphonie évoluent en fonction de la fluence et doivent donc être réévalués et mis à jour régulièrement. De plus, des mesures plus fréquentes des paramètres de la diaphonie pourraient nous aider à comprendre pourquoi la diaphonie diminue par rapport à la mesure précédente. La littérature [88] indique qu'avec une fluence croissante, la capacité entre les pistes devrait augmenter et la résistance inter-pistes diminuer. Ces deux changements devraient entraîner une augmentation de la diaphonie, ce qui n'a pas été observé. Cependant, la résistance et la capacité entre les pistes ne sont pas les seuls facteurs qui influencent la formation du signal. Il existe un réseau plus complexe de capacités et de résistances qui ont un impact sur la forme

de l'amas. Notez que la diaphonie a été mesurée uniquement pour le mode principal d'échantillage du signal (mode déconvolution). Il faudrait donc également la mettre à jour pour le mode "peak". Bien que ce dernier mode ne soit pas utilisé dans la prise de données standard, il pourrait nous aider à étudier la diminution de la diaphonie en distinguant les effets de la déconvolution des autres effets.

Les données cosmiques enregistrées en l'absence de champ magnétique, qui ont été utilisées pour la mesure de la diaphonie, ont posé plusieurs contraintes et difficultés. Tout d'abord, en raison des conditions de déclenchement, les statistiques sur les disques et les bouchons sont insuffisantes. Même si le déclenchement était re-conçu, en raison de la direction d'arrivée des cosmiques, la prise de données devrait être longue afin de collecter suffisamment de statistiques dans ces zones-là, ce qui est difficile à organiser dans le calendrier serré du CMS. Le deuxième problème important est lié à la synchronisation du trajectographe lorsqu'il échantillonne le signal collecté. Le trajectographe n'a pas de configuration de synchronisation spéciale pour les cosmiques et, par conséquent, la synchronisation des collisions est toujours utilisée. Comme la diaphonie varie en fonction du temps dans l'échantillonnage du signal, nous ne devons utiliser pour la mesure de la diaphonie que les cosmiques dont le temps d'arrivée au module donné coïnciderait avec celui d'une particule produite lors d'une collision proton-proton. Une autre ambiguïté provient du calcul du temps d'arrivée des particules, qui extrapole toutes les particules au point d'interaction, même si elles ne sont pas passées par là. Tous ces problèmes pourraient être résolus s'il était possible d'organiser une nouvelle prise de données de collision en mode spécial d'acquisition (sans soustraction ni suppression de charge) et sans champ magnétique. Mais une telle prise de données n'est pas compatible avec le programme et les priorités de CMS.

Après la modification des paramètres de la diaphonie et des conditions tels que les gains et le bruit mis à jour par les autres membres du groupe de reconstruction locale du trajectographe, la description par la simulation des amas synchronisés avec les croisements de faisceaux ("en temps") dans les données a été grandement améliorée. Il a été identifié qu'il existe encore plusieurs paramètres qui sont obsolètes et pourraient être mis à jour à l'avenir, mais ces paramètres ne modifient pas largement la description des amas. Dans cette thèse d'une part, j'ai découvert que la simulation est simplifiée et parfois non réaliste, mais d'autre part, le développement de modèles plus sophistiqués n'améliorerait pas grandement la description des amas dans les données par simulation. J'ai également constaté que certaines parties de la simulation ont un impact négligeable, à savoir la diffusion, et il pourrait être utile d'évaluer quelles parties de la simulation sont réellement nécessaires pour réduire le temps nécessaire à la simulation d'événements.

Plusieurs améliorations pourraient encore être incluses dans la simulation des amas

non synchrones avec des collisions. Tout d'abord, la forme du signal a changé en raison de la modification de la configuration de la puce APV suite au problème d'inefficacités de reconstruction des hits discuté précédemment. Par conséquent, la forme du signal doit être mise à jour afin de réduire la charge simulée d'une fraction correcte. Deuxièmement, il a été montré que la diaphonie dépend du temps. Les paramètres de la diaphonie ont été dérivés pour les amas "en temps" et ne sont pas corrects pour les amas pas "en temps". Idéalement, les paramètres de la diaphonie devraient être estimés en fonction du temps d'arrivée des particules au module. Les amas pas "en temps" devraient également être mieux simulés, car ces amas pourraient être utilisés par l'algorithme de trajectographie pour reconstruire les traces des particules.

Pour aller plus loin avec les données cosmiques enregistrées, je propose ici quelques d'études intéressantes qui pourraient être réalisées. Dans le passé, on observait une asymétrie gauche-droite dans le partage des charges. Cet effet pourrait aussi être étudié avec les données que j'ai utilisées. De plus, il est possible d'étudier les propriétés de la diaphonie et d'amas en fonction de la position où la trace croise le plan des pistes, à proximité ou à distance de la piste. Dans le passé, il a également été observé qu'il existe une évolution de la charge portée par la piste de plus grande charge dans l'amas en fonction du numéro de la piste dans une puce APV, cette étude pourrait être répétée avec ces données. Toutes ces études pourraient aider à mieux comprendre la formation du signal, les caractéristiques des capteurs telles que les non-uniformités dans le champ électrique, ainsi que les modifications des propriétés des capteurs résultant de leur irradiation.

Dans le futur trajectographe pour le HL-LHC, le formation des amas sera complètement différente, seules les informations binaires de la piste/macro-pixel seront envoyées. Par conséquent, la charge de la piste de charge maximale et la charge totale de l'amas ne seront plus disponibles, seule la largeur de l'amas sera connue. Comme la largeur de amas dépend de la diaphonie, il sera également nécessaire de mesurer la diaphonie dans le nouveau trajectographe. De plus, il sera important de déterminer l'impact de la diaphonie sur le passage de seuil entre 0 et 1 pour la charge de la piste/macro-pixel, afin de fixer correctement le seuil et le surveiller au cours du temps.

A.V Recherche du partenaire supersymétrique du quark top

Le Chapitre 4 introduit le Modèle Standard (MS) et la Supersymétrie (SUSY). Malgré sa capacité à bien décrire la majorité des phénomènes physiques observés, le modèle standard de la physique des particules souffre de plusieurs inconvénients tels que le problème de

la hiérarchie ou l'absence d'un candidat pour la matière noire. En raison de ces lacunes, des théories au-delà du MS ont été proposées et l'une d'entre elles, la supersymétrie, est devenue la plus prometteuse en raison de sa capacité à traiter une grande partie des problèmes du MS.

Dans cette thèse, j'ai présenté au Chapitre 5 une recherche du partenaire supersymétrique du quark top, le stop, avec les données de CMS du Run 2. Cette recherche vise la production de paires de stops, avec trois possibilités différentes pour les désintégrations des stops: 1) les deux stops se désintègrent chacun un quark top et un neutralino (Fig. A.9 en haut à gauche), 2) la désintégration des deux stops en un quark et un chargino (Fig. A.9 en haut à droite), 3) chaque stop se désintègrent différemment comme un mélange des deux cas précédents (Fig. A.9 en bas). Dans tous les cas, les états finaux du signal ciblé contiennent un lepton, des jets et de l'énergie transverse manquante.

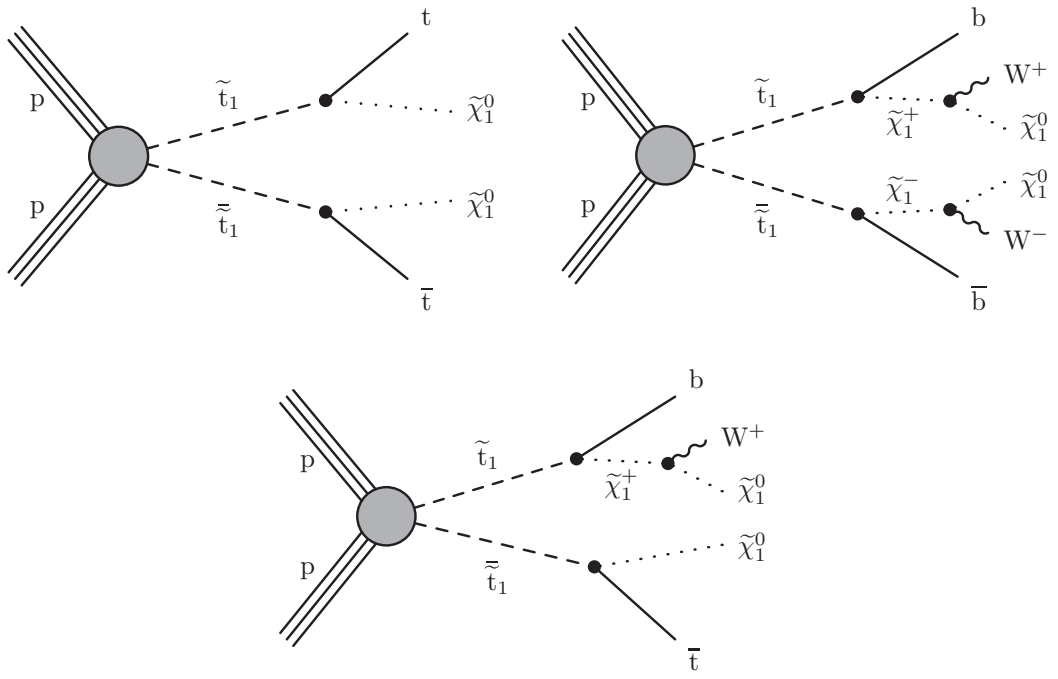

Figure A.9: Les diagrammes de modèles simplifiés pour la production direct de paires de stops. Dans le diagramme en haut à gauche, chaque stop se désintègre en $t\tilde{\chi}_1^0$ (T2tt), tandis qu'en haut à droite, il se désintègre en $b\tilde{\chi}_1^\pm$ (T2bW). Dans le diagramme en bas, la désintégration mixte de la paire de stops $\bar{t}\tilde{\chi}_1^0 b\tilde{\chi}_1^+$ est considérée [134].

J'ai été impliquée dans trois versions publiques de cette recherche: une basée sur les données enregistrées en 2015 correspondant à une luminosité intégrée $\int \mathcal{L}$ de 2.3 fb^{-1} [129], la seconde basée sur les données enregistrées début 2016 ($\int \mathcal{L} = 12.9$ fb^{-1}) [130] et la dernière correspondant à $\int \mathcal{L} = 35.9$ fb^{-1} collecté pendant toute la période de prise de données proton-proton de 2016 [128]. J'ai été principalement impliquée dans la dernière analyse, où j'étais responsable de l'estimation de l'un des bruits de fond de l'analyse con-

stitué des processus ttZ et WZ, dans lesquels un boson Z se désintègre en deux neutrinos. Je n'ai pas seulement estimé ce bruit de fond, mais j'ai également fourni les incertitudes systématiques sur ce bruit de fond. Les résultats peuvent être vus dans les Tableaux 5.7 et 5.9 du Chapitre 5. Dans cette thèse, j'ai également exploité une technique de marquage de jets boostés provenant d'un boson W et j'ai montré que le gain de mise en œuvre d'une telle technique augmente avec la luminosité intégrée.

Les recherches pour la production de paires de stops dans différents états finaux avec 0, 1 ou 2 leptons avaient déjà été effectuées avec les données Run 1 sous l'hypothèse de différents modes de désintégration. Ces analyses excluent dans le cadre de scénarios simplifiés avec des stops se désintégrant en un quark top et un neutralino des masses de stops jusqu'à environ 755 GeV pour une masse de neutralino inférieure à 200 GeV. Avec l'augmentation de l'énergie dans le centre de masse puis de la luminosité intégrée au Run 2, il est possible de sonder davantage les masses de stop. Comme on peut le voir sur la Figure A.10, aucun excès n'a été observé dans les données enregistrées en 2016 et correspondant à ($\int \mathcal{L} = 35.9$ fb $^{-1}$) quand on les compare aux prédictions de bruits du fond du MS et, par conséquent, des limites d'exclusion ont été posées. Cette analyse exclut les masses de stop jusqu'à 1120 GeV pour un neutralino sans masse en termes de modèles simplifiés où les deux stops se désintègrent en un quark top et un neutralino, comme le montre la Fig. A.11. Dans le cas où les deux stops se désintègrent en un quark bottom et un chargino ou dans le cas de désintégration mixte, les masses de stop ont été exclues jusqu'à 1000 GeV et 980 GeV, respectivement, comme présenté aux Fig. A.12 et A.13.

Malgré de l'exclusion du stop dans la gamme du TeV, il reste de la place pour la supersymétrie naturelle [116] et, par conséquent, l'effort de recherche des stops ne diminue pas. Selon les prévisions de la collaboration CMS, avec une luminosité intégrée de 3000 fb^{-1} devant être collectée au HL-LHC, il sera possible de sonder les masses de stop jusqu'à 2 TeV [164]. Une augmentation supplémentaire de l'énergie dans le centre de masse (projet HE-LHC) nous permettrait de sonder encore plus loin les masses de stop.

Avant de migrer vers des projets futurs, il existe plusieurs directions pour améliorer l'analyse de stop présentée dans cette thèse en vue d'une future mise à jour basée sur des données avec une luminosité intégrée plus grande. Pour l'estimation des bruits du fond, il est souhaitable d'utiliser des méthodes basées sur les données afin de minimiser la dépendance à la simulation et, par conséquent, de réduire les incertitudes systématiques. Les estimations des bruits du fond à partir des données sont basées sur des régions de contrôle, ces régions de contrôle doivent être définies de manière très similaire aux régions où nous cherchons le signal pour éviter les incertitudes dues aux extrapolations. Ces extrapolations reposent sur la forme des variables dans la simulation et, si elles ne sont

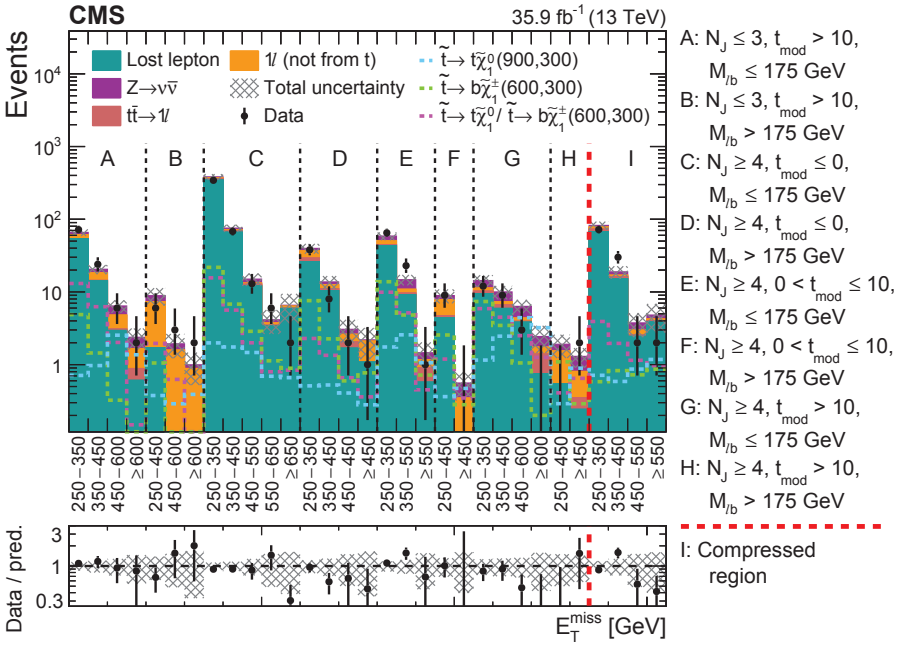

Figure A.10: Nombre d'événements observés dans les données (points noirs), des estimations de bruits du fond ainsi que 3 scénarios possibles de signaux dans les 31 régions de signal de l'analyse. Le bruit du fond correspondant à un lepton perdu est représenté en vert, le bruit du fond 1ℓ provenant du processus $W + jets \to 1\ell$ (c'est-à-dire pas du top) en jaune, le bruit du fond $Z \to \nu\bar{\nu}$ en violet et la contribution $t\bar{t} \to 1\ell$ en rouge. Le modèle T2tt ($\tilde{t}_1 \to t\tilde{\chi}_1^0$) avec une masse du stop de 900 GeV et une masse du neutralino de 300 GeV est représenté par une ligne pointillée bleue. Les scénarios T2tb ($\tilde{t}_1 \to t\tilde{\chi}_1^0/\tilde{t}_1 \to b\tilde{\chi}_1^{\pm}$) et T2bW ($\tilde{t}_1 \to b\tilde{\chi}_1^{\pm}$) pour une masse du stop de 600 GeV et une masse de neutralino de 300 GeV sont respectivement représentés par une ligne pointillé rose et une verte. La ligne pointillée rouge sépare les régions de signal de l'analyse nominale et de l'analyse dédiée à la région compressée avec $\Delta m(\text{stop}, \text{neutralino}) < 225$ GeV.

pas bien modélisées, elles augmentent largement les incertitudes systématiques sur les bruits du fond. Du côté du signal, la simulation simplifiée d'événements n'est pas fiable dans la région du plan de masses (m(stop), m(neutralino)) lorsque $\Delta m(\text{stop}, \text{neutralino}) \sim m(\text{top})$ à faible m(neutralino). Cela pourrait être résolu en utilisant la simulation complète du détecteur dans cette région cinématique particulière. Ensuite, la stratégie d'analyse peut également être réoptimisée. Il est possible de réoptimiser les régions de signal en trouvant des coupures optimales spécifique pour une luminosité donnée mais également en essayant de trouver de meilleures variables discriminantes. Une autre option consiste à utiliser des reconstructions différentes d'objets. Par exemple de nos jours, il existe une variété d'objets ciblant l'identification du boson W ou du quark top, non seulement comme un large jet unique regroupant tous les produits de la désintégration du W ou du top, mais également comme plusieurs jets complètement résolus ou des jets partiellement fusionnés. Nous pourrions également envisager de ne pas effectuer d'analyse de comptage, mais de passer à une analyse de forme d'une variable discriminante, en utilisant des techniques

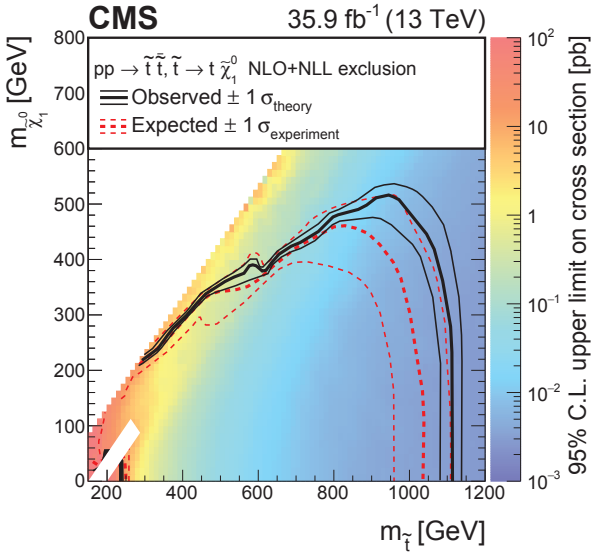

Figure A.11: Les limites d'exclusion à 95% CL sur le modèle T2tt correspondant à une luminosité intégrée de 35.9 fb^{-1}. L'interprétation est fournie dans le plan de la masse du stop par rapport à la masse du neutralino. Le code de couleur indique la limite supérieure de 95 % CL sur la section efficace en supposant un rapport de branchement de 100% pour $\tilde{t}_1 \to t\tilde{\chi}_1^0$. Les contours rouge et noir représentent respectivement les limites d'exclusion attendues et observées. La zone sous la courbe épaisse noire indique la région exclue des points de signal.

d'apprentissage multi-variées permettant d'établir une meilleure distinction entre le signal et le bruit du fond.

Au sein de la collaboration CMS, une grande variété de recherches SUSY est effectuée. Les stops sont recherchés dans plusieurs états finaux différents et les autres particules SUSY prédites sont également ciblées par des recherches dédiées. De nombreuses analyses recherchent SUSY dans le contexte du modèle supersymétrique minimal (MSSM), mais il existe également plusieurs recherches allant au-delà, par exemple des recherches permettant de violer la R-parité. En général, les recherches SUSY sont interprétées en termes de modèles simplifiés. De nombreux efforts sont déployés pour réinterpréter ces recherches dans des modèles plus réalistes. Une autre partie des activités est la combinaison de recherches pour atteindre un meilleur potentiel de découverte/exclusion. L'expérience CMS et en général les expériences de collisionneur ne constituent pas la seule opportunité de rechercher la supersymétrie. Par exemple, la supersymétrie peut également être étudiée par des expériences de détection directe de matière noire.

En résumé, il existe encore de nombreuses options pour une SUSY naturelle en termes d'espace de paramètres, ainsi que de nombreuses options pour la rechercher. Les expériences de collisionneur sont l'une de ces options et, avec l'augmentation de la luminosité, de l'énergie et de l'optimisation des analyses, elles offrent de grandes possibilités pour

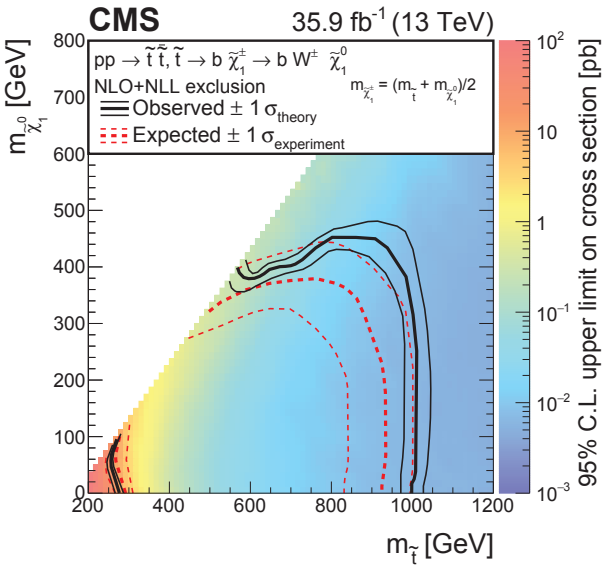

Figure A.12: Les limites d'exclusion à 95% CL sur le modèle T2bW correspondant à une luminosité intégrée de 35.9 fb^{-1}. L'interprétation est fournie dans le plan de la masse du stop vs la masse du neutralino. Le code couleur indique la limite supérieure de 95% CL sur la section efficace en supposant un rapport de branchement de 100% pour $\tilde{t}_1 \to b\tilde{\chi}_1^{\pm}$. Les contours rouge et noir représentent respectivement les limites d'exclusion attendues et observées. La zone sous la courbe épaisse noire indique la région exclue des points de signal.

dépasser les limites actuelles et explorer davantage l'espace de phase non couvert.

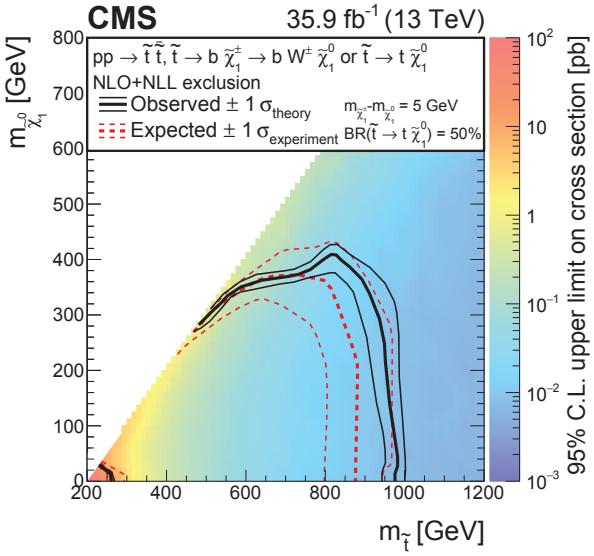

Figure A.13: Les limites d'exclusion à 95% CL sur le modèle T2tb correspondant à une luminosité intégrée de 35.9 fb $^{-1}$. L'interprétation est fournie dans le plan de la masse du stop par rapport à la masse du neutralino. Le code de couleur indique la limite supérieure de 95% CL sur la section efficace en supposant un rapport de branchement de 50% pour $\tilde{t}_1 \to t\tilde{\chi}_1^0$ et 50% pour $\tilde{t}_1 \to b\tilde{\chi}_1^{\pm}$. Les contours rouge et noir représentent respectivement les limites d'exclusion attendues et observées. La zone sous la courbe épaisse noire indique la région exclue des points de signal.

Bibliography

[1] L. Evans and P. Bryant. LHC Machine. *JINST*, 3:S08001, 2008.

[2] O. S. Bruning, P. Collier, P. Lebrun, S. Myers, R. Ostojic, J. Poole, and P. Proudlock. LHC Design Report Vol.1: The LHC Main Ring. *CERN-2004-003-V1, CERN-2004-003, CERN-2004-003-V-1*, 2004.

[3] E. A. Mobs. The CERN accelerator complex. Complexe des accélérateurs du CERN. *OPEN-PHO-ACCEL-2016-013*, Oct 2016. General Photo.

[4] G. Aad *et al.* [ATLAS Collaboration]. The ATLAS Experiment at the CERN Large Hadron Collider. *JINST*, 3:S08003, 2008.

[5] S. Chatrchyan *et al.* [CMS Collaboration]. The CMS Experiment at the CERN LHC. *JINST*, 3:S08004, 2008.

[6] K. Aamodt *et al.* [ALICE Collaboration]. The ALICE experiment at the CERN LHC. *JINST*, 3:S08002, 2008.

[7] A. A. Alves *et al.* [LHCb Collaboration], Jr. The LHCb Detector at the LHC. *JINST*, 3:S08005, 2008.

[8] G. Anelli *et al.* [TOTEM Collaboration]. The TOTEM experiment at the CERN Large Hadron Collider. *JINST*, 3:S08007, 2008.

[9] O. Adriani *et al.* [LHCf Collaboration]. The LHCf detector at the CERN Large Hadron Collider. *JINST*, 3:S08006, 2008.

[10] B. Acharya *et al.* [MoEDAL Collaboration]. The Physics Programme Of The MoEDAL Experiment At The LHC. *Int. J. Mod. Phys.*, A29:1430050, 2014.

[11] CMS Collaboration. CMS, the Compact Muon Solenoid : technical proposal. LHC Tech. Proposal. CERN, Geneva, 1994. CERN-LHCC-94-38, LHCC-P-1.

[12] CMS Collaboration. The CMS magnet project: Technical Design Report. Technical Design Report CMS. CERN, Geneva, 1997. CERN-LHCC-97-010, CMS-TDR-1.

[13] CMS Collaboration. CMS detector design. `http://cms.web.cern.ch/news/cms-detector-design`.

[14] F. Pantaleo. New Track Seeding Techniques for the CMS Experiment. PhD thesis, Hamburg U., 2017.

[15] V. Karimäki *et al.* [CMS Collaboration]. The CMS tracker system project. *CERN-LHCC-98-006, CMS-TDR-5*, 1997.

[16] LHC Experiments Committee. The CMS tracker. *CERN-LHCC-2000-016, CMS-TDR-5-add-1*, 2000.

[17] G. L. Bayatian *et al.* [CMS Collaboration]. CMS technical design report, volume II: Physics performance. *J. Phys.*, G34(6):995–1579, 2007.

[18] CMS Collaboration. Tracking@CMS. https://indico.cern.ch/event/615859/contributions/2485248/attachments/1517681/2369343/TrackingPOS17.pdf. Internal document.

[19] CMS Collaboration. Track Reconstruction Sequences. https://twiki.cern.ch/twiki/bin/view/CMSPublic/SWGuideTrackRecoSequences.

[20] S. Chatrchyan *et al.* [CMS Collaboration]. Description and performance of track and primary-vertex reconstruction with the CMS tracker. *JINST*, 9(10):P10009, 2014.

[21] R. Fruhwirth. Application of Kalman filtering to track and vertex fitting. *Nucl. Instrum. Meth.*, A262:444–450, 1987.

[22] D. A. Matzner Dominguez, D. Abbaneo, K. Arndt, N. Bacchetta, A. Ball, E. Bartz, W. Bertl, G. M. Bilei, G. Bolla, H. W. K. Cheung, et al. CMS Technical Design Report for the Pixel Detector Upgrade. *CERN-LHCC-2012-016, CMS-TDR-011, FERMILAB-DESIGN-2012-02*, 2012.

[23] M. Friedl. Strip Detector. http://www.hephy.at/user/friedl/diss/html/node28.html.

[24] S. Chatrchyan *et al.* [CMS Collaboration]. Description and performance of track and primary-vertex reconstruction with the CMS tracker. *JINST*, 9:P10009, 2014.

[25] CMS Collaboration. Strips Offline Plots 2016. https://twiki.cern.ch/twiki/bin/viewauth/CMS/StripsOfflinePlots2016. Internal document.

[26] CMS Collaboration. The CMS electromagnetic calorimeter project: Technical Design Report. Technical Design Report CMS. CERN, Geneva, 1997. CERN-LHCC-97-033, CMS-TDR-4.

[27] CMS Collaboration. The CMS hadron calorimeter project: Technical Design Report. Technical Design Report CMS. CERN, Geneva, 1997. CERN-LHCC-97-031, CMS-TDR-2.

[28] S. Chatrchyan *et al.* [CMS Collaboration]. Performance of the CMS Hadron Calorimeter with Cosmic Ray Muons and LHC Beam Data. *JINST*, 5:T03012, 2010.

[29] CMS Collaboration. The CMS muon project: Technical Design Report. Technical Design Report CMS. CERN, Geneva, 1997. CERN-LHCC-97-032, CMS-TDR-3.

[30] S. Chatrchyan *et al.* [CMS Collaboration]. The performance of the CMS muon detector in proton-proton collisions at sqrt(s) = 7 TeV at the LHC. *JINST*, 8:P11002, 2013.

[31] P. Traczyk. Collision and Cosmic Muon Timing Measurement. *CMS-IN-2010-013*, Apr 2010. Internal document.

[32] V. Khachatryan *et al.* [CMS Collaboration]. The CMS trigger system. *JINST*, 12:P01020, 2017.

[33] CMS Collaboration. CMS Luminosity. https://twiki.cern.ch/twiki/bin/view/CMSPublic/LumiPublicResults.

[34] G. L. Bayatian *et al.* [CMS Collaboration]. CMS Physics. *CERN-LHCC-2006-001, CMS-TDR-8-1*, 2006.

[35] A. M. Sirunyan *et al.* [CMS Collaboration]. Particle-flow reconstruction and global event description with the CMS detector. *JINST*, 12(10):P10003, 2017.

[36] S. Chatrchyan *et al.* [CMS Collaboration]. Performance of CMS muon reconstruction in pp collision events at $\sqrt{s} = 7$ TeV. *JINST*, 7:P10002, 2012.

[37] V. Khachatryan *et al.* [CMS Collaboration]. Performance of Electron Reconstruction and Selection with the CMS Detector in Proton-Proton Collisions at sqrt(s) = 8 TeV. *JINST*, 10(06):P06005, 2015.

[38] W. Adam, R. Fruhwirth, A. Strandlie, and T. Todorov. Reconstruction of electrons with the Gaussian sum filter in the CMS tracker at LHC. *eConf*, C0303241:TULT009, 2003. [J. Phys.G31,N9(2005)].

[39] CMS Collaboration. Performance of reconstruction and identification of tau leptons in their decays to hadrons and tau neutrino in LHC Run-2. *CMS-PAS-TAU-16-002*, 2016.

[40] V. Khachatryan *et al.* [CMS Collaboration]. Reconstruction and identification of τ lepton decays to hadrons and ν_τ at CMS. *JINST*, 11(01):P01019, 2016.

[41] V. Khachatryan *et al.* [CMS Collaboration]. Performance of photon reconstruction and identification with the CMS detector in proton-proton collisions at $\sqrt{s} = 8$ TeV. *JINST*, 10:P08010, 2015.

[42] M. Cacciari, G. P. Salam, and G. Soyez. The Anti-k(t) jet clustering algorithm. *JHEP*, 04:063, 2008.

[43] M. Cacciari, G. P. Salam, and G. Soyez. FastJet user manual. *Eur. Phys. J. C*, 72:1896, 2012.

[44] V. Khachatryan *et al.* [CMS Collaboration]. Jet energy scale and resolution in the CMS experiment in pp collisions at 8 TeV. *JINST*, 12:P02014, 2017.

[45] A. M. Sirunyan *et al.* [CMS Collaboration]. Identification of heavy-flavour jets with the CMS detector in pp collisions at 13 TeV. *JINST*, 13(05):P05011, 2018.

[46] CMS Collaboration. Performance of missing energy reconstruction in 13 TeV pp collision data using the CMS detector. *CMS-PAS-JME-16-004*, 2016.

[47] D. E. Groom and S. R. Klein. Passage of particles through matter: in Review of Particle Physics (RPP 2000). *Eur. Phys. J.*, C15:163–173, 2000.

[48] M. Huhtinen. Highly ionising events in silicon detectors. *CMS-NOTE-2002-011, CERN-CMS-NOTE-2002-011*, 2002.

[49] W. Adam *et al.* The effect of highly ionising particles on the CMS silicon strip tracker. *Nucl. Instrum. Meth.*, A543(2-3):463–482, 2005.

[50] M. J. French *et al.* Design and results from the APV25, a deep sub-micron CMOS front-end chip for the CMS tracker. *Nucl. Instrum. Meth.*, A466:359–365, 2001.

[51] L. L. Jones, M. J. French, Q. Morrissey, A. Neviani, M. Raymond, G. Hall, P. Moreira, and G. Cervelli. The APV25 deep submicron readout chip for CMS detectors. *Conf. Proc.*, C9909201:162–166, 1999.

[52] S. A. Baird *et al.* The front-end driver card for the CMS silicon strip tracker readout. In 8th Workshop on Electronics for LHC Experiments, Colmar, France, September 9-13, 2002, pages 296–300, 2002.

[53] R. J. Bainbridge. Influence of highly ionising event events on the CMS APV25 readout chip. PhD thesis, Imperial Coll., London, 2004.

[54] Istituto Nazionale di Fisica Nucleare. Detector prototypes. `http://hep.fi.infn.it/CMS/sensors/Siliconpage.html`.

[55] W. Shockley. Currents to conductors induced by a moving point charge. *Journal of Applied Physics*, 9(10):635–636, 1938.

[56] S. Ramo. Currents induced by electron motion. *Proc. Ire.*, 27:584–585, 1939.

[57] C. Bloch. Studies for the commissioning of the CERN CMS silicon strip tracker. PhD thesis, Vienna, Tech. U., 2008.

[58] E. Barberis *et al.* Capacitances in silicon microstrip detectors. *Nucl. Instrum. Meth.*, A342:90–95, 1994.

[59] G. Lutz. Correlated Noise in Silicon Strip Detector Readout. *Nucl. Instrum. Meth.*, A309:545–551, 1991.

[60] M. Friedl. The CMS silicon strip tracker and its electronic readout. PhD thesis, Vienna, Tech. U., 2001.

[61] I. R. Tomalin. Test-Beam Analysis of the Effect of Highly Ionising Particles on the Silicon Strip Tracker. *CERN-CMS-NOTE-2003-025, CMS-NOTE-2003-025*, 2003.

[62] R. Bainbridge, R. Chierici, G. Hall, L. Mirabito, and M. Raymond. The Effect of Highly Ionising Events on the APV25 Readout Chip. *CMS-NOTE-2002-038, CERN-CMS-NOTE-2002-038*, 2002.

[63] E. Butz. Virgin Raw Data Taking. `https://indico.cern.ch/event/512685/contributions/2167961/attachments/1273330/1887985/virgin_raw_test_2016_ebutz.pdf`. Internal document.

[64] S. Banerjee. Readiness of CMS Simulation Towards LHC Startup. *J. Phys. Conf. Ser.*, 119:032006, 2008.

[65] M. Hildreth, V. N. Ivanchenko, and D. J. Lange. Upgrades for the CMS simulation. *J. Phys. Conf. Ser.*, 898(4):042040, 2017.

[66] M. Hildreth, V. N. Ivanchenko, D. J. Lange, and M. J. Kortelainen. CMS Full Simulation for Run-2. *J. Phys. Conf. Ser.*, 664(7):072022, 2015.

[67] M. Hildreth. Simulation Basics. https://indico.cern.ch/event/596660/contributions/2412428/attachments/1411446/2159057/Simulation_Basics_2_17.pdf. Internal document.

[68] G. Boudoul, G. Franzoni, A. Norkus, A. Pol, P. Srimanobhas, and J. R. Vlimant. Monte Carlo Production Management at CMS. *J. Phys. Conf. Ser.*, 664(7):072018, 2015.

[69] CMS Collaboration. Generating events. https://twiki.cern.ch/twiki/bin/view/CMSPublic/WorkBookGeneration.

[70] CMS Collaboration. Generating events, introduction. https://twiki.cern.ch/twiki/bin/view/CMSPublic/WorkBookGenIntro.

[71] T. Sjöstrand, S. Ask, J. R. Christiansen, R. Corke, N. Desai, P. Ilten, S. Mrenna, S. Prestel, C. O. Rasmussen, and P. Z. Skands. An Introduction to PYTHIA 8.2. *Comput. Phys. Commun.*, 191:159–177, 2015.

[72] M. Bahr *et al.* Herwig++ Physics and Manual. *Eur. Phys. J.*, C58:639–707, 2008.

[73] C. Oleari. The POWHEG-BOX. *Nucl. Phys. Proc. Suppl.*, 205-206:36–41, 2010.

[74] J. Alwall, R. Frederix, S. Frixione, V. Hirschi, F. Maltoni, O. Mattelaer, H. S. Shao, T. Stelzer, P. Torrielli, and M. Zaro. The automated computation of tree-level and next-to-leading order differential cross sections, and their matching to parton shower simulations. *JHEP*, 07:079, 2014.

[75] S. Agostinelli *et al.* GEANT4: A Simulation toolkit. *Nucl. Instrum. Meth.*, A506:250–303, 2003.

[76] V. Lefébure, S. Banerjee, and I. González. CMS Simulation Software Using Geant4. *CMS-NOTE-1999-072, CERN-CMS-NOTE-1999-072*, 1999.

[77] S. Sekmen. Recent Developments in CMS Fast Simulation. *PoS*, ICHEP2016:181, 2016.

[78] CMS Collaboration. Comparison of the Fast Simulation of CMS with the first LHC data. *CMS-DP-2010-039, CERN-CMS-DP-2010-039*, 2010.

[79] A. Giammanco. The Fast Simulation of the CMS Experiment. *J. Phys. Conf. Ser.*, 513:022012, 2014.

[80] S. Abdullin, P. Azzi, F. Beaudette, P. Janot, and A. Perrotta. The fast simulation of the CMS detector at LHC. *J. Phys. Conf. Ser.*, 331:032049, 2011.

[81] CMS Collaboration. How to Configure and Run Detector Simulation and Digitization. https://twiki.cern.ch/twiki/bin/view/CMSPublic/WorkBookSimDigi.

[82] V. Lefebure. CMS Simulation Software Using Geant4: Hits and Sensitive Detectors. *CMS-IN-1999-054*, Dec 1999. Internal document.

[83] C. Delaere and L. Mirabito. Timing of the CMS tracker: Study of module properties. Technical Report CMS-NOTE-2007-027, CERN, Geneva, Oct 2007.

[84] E. Butz. Mitigation of the Strip Tracker Dynamic Inefficiency. https://indico.cern.ch/event/560226/contributions/2277448/attachments/1324704/1988050/wgm_vfp_change_ebutz.pdf. Internal document.

[85] A. Venturi. SiStrip Back Plane Correction Analysis. https://twiki.cern.ch/twiki/bin/viewauth/CMS/BackPlaneCorrections. Internal document.

[86] M. Tosi. CDC trigger. https://its.cern.ch/jira/browse/CMSLITDPG-74. Internal document.

[87] S. Chatrchyan *et al.* [CMS Collaboration]. Performance of the CMS Drift-Tube Local Trigger with Cosmic Rays. *JINST*, 5:T03003, 2010.

[88] F. Hartmann. Evolution of Silicon Sensor Technology in Particle Physics. *Springer Tracts Mod. Phys.*, 275:1–372, 2017.

[89] D. Griffiths. Introduction to Elementary Particles. Wiley-VCH, 2008.

[90] S. Chatrchyan *et al.* [CMS Collaboration]. Observation of a new boson at a mass of 125 GeV with the CMS experiment at the LHC. *Phys. Lett.*, B716:30–61, 2012.

[91] G. Aad *et al.* [ATLAS Collaboration]. Observation of a new particle in the search for the Standard Model Higgs boson with the ATLAS detector at the LHC. *Phys. Lett.*, B716:1–29, 2012.

[92] R. Alkofer and J. Greensite. Quark Confinement: The Hard Problem of Hadron Physics. *J. Phys.*, G34:S3, 2007.

[93] M. Grinfeld. Mathematical Tools for Physicists. Wiley-VCH, 2015.

[94] C.N. Yang and R. L. Mills. Conservation of Isotopic Spin and Isotopic Gauge Invariance. *Phys. Rev.*, 96:191–195, 1954.

[95] S. L. Glashow. Partial Symmetries of Weak Interactions. *Nucl. Phys.*, 22:579–588, 1961.

[96] A. Salam. Weak and Electromagnetic Interactions. *Conf. Proc.*, C680519:367–377, 1968.

[97] S. Weinberg. A Model of Leptons. *Phys. Rev. Lett.*, 19:1264–1266, 1967.

[98] D. J. Gross and F. Wilczek. Ultraviolet Behavior of Nonabelian Gauge Theories. *Phys. Rev. Lett.*, 30:1343–1346, 1973.

[99] K. G. Wilson. Confinement of Quarks. *Phys. Rev.*, D10:2445–2459, 1974.

[100] F. Englert and R. Brout. Broken Symmetry and the Mass of Gauge Vector Mesons. *Phys. Rev. Lett.*, 13:321–323, 1964.

[101] G. S. Guralnik, C. R. Hagen, and T. W. B. Kibble. Global Conservation Laws and Massless Particles. *Phys. Rev. Lett.*, 13:585–587, 1964.

[102] G. Bertone, D. Hooper, and J. Silk. Particle dark matter: Evidence, candidates and constraints. *Phys. Rept.*, 405:279–390, 2005.

[103] C. L. Bennett *et al.* [WMAP Collaboration]. Nine-Year Wilkinson Microwave Anisotropy Probe (WMAP) Observations: Final Maps and Results. *Astrophys. J. Suppl.*, 208:20, 2013.

[104] F. Zwicky. On the Masses of Nebulae and of Clusters of Nebulae. *Astrophys. J.*, 86:217–246, 1937.

[105] V. C. Rubin, N. Thonnard, and W. K. Ford, Jr. Rotational properties of 21 SC galaxies with a large range of luminosities and radii, from NGC 4605 /R = 4kpc/ to UGC 2885 /R = 122 kpc/. *Astrophys. J.*, 238:471, 1980.

[106] M. Sami. A Primer on problems and prospects of dark energy. *Curr. Sci.*, 97:887, 2009.

[107] M. Kobayashi and T. Maskawa. CP Violation in the Renormalizable Theory of Weak Interaction. *Prog. Theor. Phys.*, 49:652–657, 1973.

[108] Y. Fukuda *et al.* [Super-Kamiokande Collaboration]. Evidence for oscillation of atmospheric neutrinos. *Phys. Rev. Lett.*, 81:1562–1567, 1998.

[109] Q. R. Ahmad *et al.* [SNO Collaboration]. Measurement of the rate of $\nu_e + d \rightarrow p + p + e^-$ interactions produced by ^8B solar neutrinos at the Sudbury Neutrino Observatory. *Phys. Rev. Lett.*, 87:071301, 2001.

[110] C. Patrignani *et al.* [Particle Data Group Collaboration]. Review of Particle Physics. *Chin. Phys.*, C40(10):100001, 2016.

[111] S. P. Martin. A Supersymmetry primer. *Adv. Ser. Direct. High Energy Phys.18,1(1998)*, pages 1–98, 1997.

[112] R. Haag, J. T. Lopuszanski, and M. Sohnius. All Possible Generators of Supersymmetries of the s Matrix. *Nucl. Phys.*, B88:257, 1975.

[113] S. R. Coleman and J. Mandula. All Possible Symmetries of the S Matrix. *Phys. Rev.*, 159:1251–1256, 1967.

[114] R. Barbieri and G. F. Giudice. Upper Bounds on Supersymmetric Particle Masses. *Nucl. Phys.*, B306:63–76, 1988.

[115] M. Papucci, J. T. Ruderman, and A. Weiler. Natural SUSY Endures. *JHEP*, 09:035, 2012.

[116] H. Baer, V. Barger, N. Nagata, and M. Savoy. Phenomenological profile of top squarks from natural supersymmetry at the LHC. *Phys. Rev.*, D95(5):055012, 2017.

[117] C. F. Berger, J. S. Gainer, J. L. Hewett, and T. G. Rizzo. Supersymmetry Without Prejudice. *JHEP*, 02:023, 2009.

[118] S. Paßehr and G. Weiglein. Two-loop top and bottom Yukawa corrections to the Higgs-boson masses in the complex MSSM. *Eur. Phys. J.*, C78(3):222, 2018.

[119] H. Nishino *et al.* [Super-Kamiokande Collaboration]. Search for Proton Decay via p —> e+ pi0 and p —> mu+ pi0 in a Large Water Cherenkov Detector. *Phys. Rev. Lett.*, 102:141801, 2009.

[120] D. Alves *et al.* Simplified Models for LHC New Physics Searches. *J. Phys.*, G39:105005, 2012.

[121] J. Alwall, P. Schuster, and N. Toro. Simplified Models for a First Characterization of New Physics at the LHC. *Phys. Rev.*, D79:075020, 2009.

[122] S. Chatrchyan *et al.* [CMS Collaboration]. Interpretation of Searches for Supersymmetry with simplified Models. *Phys. Rev.*, D88(5):052017, 2013.

[123] CMS Collaboration. Summary of comparison plots in simplified models spectra for the 8TeV dataset. https://twiki.cern.ch/twiki/bin/view/CMSPublic/SUSYSMSSummaryPlots8TeV.

[124] V. Khachatryan *et al.* [CMS Collaboration]. Search for direct pair production of supersymmetric top quarks decaying to all-hadronic final states in pp collisions at $\sqrt{s} = 8$ TeV. *Eur. Phys. J.*, C76(8):460, 2016.

[125] LHC SUSY Cross Section Working Group. SUSY Cross Sections. https://twiki.cern.ch/twiki/bin/view/LHCPhysics/SUSYCrossSections.

[126] ATLAS Collaboration. Summary plots from the ATLAS Supersymmetry physics group. https://atlas.web.cern.ch/Atlas/GROUPS/PHYSICS/CombinedSummaryPlots/SUSY/.

[127] A. Hoecker. Physics at the LHC Run-2 and Beyond. Physics at the LHC Run-2 and Beyond. *arXiv:1611.07864*, pages 153–212. 61 p, Nov 2016. Lecture notes from the 2016 European School of High-Energy Physics, 15-28 June 2016, Skeikampen, Norway (61 pages, 56 figures).

[128] A. M. Sirunyan *et al.* [CMS Collaboration]. Search for top squark pair production in pp collisions at sqrt(s)=13 TeV using single lepton events. *arXiv:1706.04402*, 2017.

[129] A. M. Sirunyan *et al.* [CMS Collaboration]. Searches for pair production of third-generation squarks in $\sqrt{s} = 13$ TeV pp collisions. *arXiv:1612.03877, Eur. Phys. J.*, C77(5):327, 2017.

[130] CMS Collaboration. Search for direct top squark pair production in the single lepton final state at $\sqrt{s} = 13$ TeV. *CMS-PAS-SUS-16-028*, 2016.

[131] S. P. Martin. Exploring compressed supersymmetry with same-sign top quarks at the Large Hadron Collider. *Phys. Rev.*, D78:055019, 2008.

[132] A. M. Sirunyan *et al.* [CMS Collaboration]. Search for supersymmetry in proton-proton collisions at 13 TeV using identified top quarks. *Phys. Rev.*, D97(1):012007, 2018.

[133] A. M. Sirunyan *et al.* [CMS Collaboration]. Search for new phenomena with the M_{T2} variable in the all-hadronic final state produced in proton–proton collisions at $\sqrt{s} = 13$ TeV. *Eur. Phys. J.*, C77(10):710, 2017.

[134] CMS Collaboration. SUSY Diagrams. https://github.com/CMS-SUS-XPAG/SUSYDiagrams/blob/master/diagrams.

[135] J. F. Gunion and H. E. Haber. Two-body Decays of Neutralinos and Charginos. *Phys. Rev.*, D37:2515, 1988.

[136] J. M. Duarte. Naturalness confronts nature: searches for supersymmetry with the CMS detector in pp collisions at $\sqrt{s} = 8$ and 13 TeV. PhD thesis, Caltech, 2017.

[137] G. Aad *et al.* [ATLAS Collaboration]. Search for top squark pair production in final states with one isolated lepton, jets, and missing transverse momentum in $\sqrt{s}$ =8 TeV *pp* collisions with the ATLAS detector. *JHEP*, 11:118, 2014.

[138] A. L. Read. Presentation of search results: The CL(s) technique. *J. Phys.*, G28:2693–2704, 2002.

[139] ATLAS Collaboration, CMS Collaboration, and LHC Higgs Combination Group. Procedure for the LHC Higgs boson search combination in Summer 2011. Technical report, CERN, Geneva, Aug 2011. CMS-NOTE-2011-005. ATL-PHYS-PUB-2011-11.

[140] J. Alwall *et al.* Comparative study of various algorithms for the merging of parton showers and matrix elements in hadronic collisions. *Eur. Phys. J.*, C53:473–500, 2008.

[141] R. D. Ball *et al.* [NNPDF Collaboration]. Parton distributions for the LHC Run II. *JHEP*, 04:040, 2015.

[142] S. Alioli, P. Nason, C. Oleari, and E. Re. A general framework for implementing NLO calculations in shower Monte Carlo programs: the POWHEG BOX. *JHEP*, 06:043, 2010.

[143] R. Frederix and S. Frixione. Merging meets matching in MC@NLO. *JHEP*, 12:061, 2012.

[144] CMS Collaboration. Search for top squark pair production in the single lepton final state in pp collisions at sqrt(s) = 13 TeV (SUS-16-051). https://twiki.cern.ch/twiki/bin/view/CMSPublic/PhysicsResultsSUS16051-PAPER. Supplementary material.

[145] M. L. Graesser and J. Shelton. Hunting Mixed Top Squark Decays. *Phys. Rev. Lett.*, 111(12):121802, 2013.

[146] CMS Collaboration. W/Z-tagging of Jets. https://twiki.cern.ch/twiki/bin/view/CMS/JetWtagging#W_Z_tagging_of_Jets. Internal document.

[147] S. D. Ellis, C. K. Vermilion, and J. R. Walsh. Techniques for improved heavy particle searches with jet substructure. *Phys. Rev.*, D80:051501, 2009.

[148] V. Khachatryan *et al.* [CMS Collaboration]. Identification techniques for highly boosted W bosons that decay into hadrons. *JHEP*, 12:017, 2014.

[149] A. M. Sirunyan *et al.* [CMS Collaboration]. Search for physics beyond the standard model in events with two leptons of same sign, missing transverse momentum, and jets in proton–proton collisions at $\sqrt{s} = 13\,\text{TeV}$. *Eur. Phys. J.*, C77(9):578, 2017.

[150] D. de Florian *et al.* Handbook of LHC Higgs Cross Sections: 4. Deciphering the Nature of the Higgs Sector. *FERMILAB-FN-1025-T, CERN-2017-002-M*, 2016.

[151] CMS Collaboration. CMS Luminosity Measurements for the 2016 Data Taking Period. Technical Report CMS-PAS-LUM-17-001, CERN, Geneva, 2017.

[152] CMS Collaboration. SUSY recommendations for full 2016 results targeting Moriond 2017. https://twiki.cern.ch/twiki/bin/view/CMS/SUSRecommendationsMoriond17. Internal document.

[153] C. Borschensky, M. Krämer, A. Kulesza, M. Mangano, S. Padhi, T. Plehn, and X. Portell. Squark and gluino production cross sections in pp collisions at $\sqrt{s} = 13$, 14, 33 and 100 TeV. *Eur. Phys. J.*, C74(12):3174, 2014.

[154] M. Aaboud *et al.* [ATLAS Collaboration]. Search for top-squark pair production in final states with one lepton, jets, and missing transverse momentum using 36 fb^{-1} of $\sqrt{s} = 13$ TeV pp collision data with the ATLAS detector. *JHEP*, 06:108, 2018.

[155] H. Baer, V. Barger, P. Huang, and X. Tata. Natural Supersymmetry: LHC, dark matter and ILC searches. *JHEP*, 05:109, 2012.

[156] D. Matalliotakis and Hans Peter Nilles. Implications of nonuniversality of soft terms in supersymmetric grand unified theories. *Nucl. Phys.*, B435:115–128, 1995.

[157] H. Baer, A. Mustafayev, S. Profumo, A. Belyaev, and X. Tata. Direct, indirect and collider detection of neutralino dark matter in SUSY models with non-universal Higgs masses. *JHEP*, 07:065, 2005.

[158] CMS Collaboration. Search for direct top squark pair production in the fully hadronic final state in proton-proton collisions at sqrt(s) = 13 TeV corresponding to an integrated luminosity of 12.9/fb. *CMS-PAS-SUS-16-029*, 2016.

[159] The ATLAS collaboration. Search for the Supersymmetric Partner of the Top Quark in the Jets+Emiss Final State at sqrt(s) = 13 TeV. *ATLAS-CONF-2016-077*, 2016.

[160] The ATLAS collaboration. Search for top squarks in final states with one isolated lepton, jets, and missing transverse momentum in $\sqrt{s} = 13$ TeV pp collisions with the ATLAS detector. *ATLAS-CONF-2016-050*, 2016.

[161] The ATLAS collaboration. Search for direct top squark pair production and dark matter production in final states with two leptons in $\sqrt{s} = 13$ TeV pp collisions using 13.3 fb^{-1} of ATLAS data. *ATLAS-CONF-2016-076*, 2016.

[162] M. Aaboud *et al.* [ATLAS Collaboration]. Search for new phenomena in final states with an energetic jet and large missing transverse momentum in pp collisions at $\sqrt{s} = 13$ TeV using the ATLAS detector. *Phys. Rev.*, D94(3):032005, 2016.

[163] ATLAS Collaboration. Prospects for benchmark Supersymmetry searches at the high luminosity LHC with the ATLAS Detector. Technical Report ATL-PHYS-PUB-2013-011, CERN, Geneva, Sep 2013.

[164] L. Shchutska. Review: The way forward for SUSY at LHC and beyond. https://indico.in2p3.fr/event/13763/contributions/15246/attachments/12662/15547/5_LesyaShchutska.pdf.

[165] A. Abdesselam *et al.* [Belle Collaboration]. Measurement of the inclusive $B \to X_{s+d}\gamma$ branching fraction, photon energy spectrum and HQE parameters. In Proceedings, 38th International Conference on High Energy Physics (ICHEP 2016): Chicago, IL, USA, August 3-10, 2016, 2016.

[166] M. Misiak *et al.* Updated NNLO QCD predictions for the weak radiative B-meson decays. *Phys. Rev. Lett.*, 114(22):221801, 2015.

[167] P. A. R. Ade *et al.* [Planck Collaboration]. Planck 2015 results. XIII. Cosmological parameters. *Astron. Astrophys.*, 594:A13, 2016.

[168] CMS Collaboration. Loss of Hit Efficiency due to HIP. https://twiki.cern.ch/twiki/bin/viewauth/CMS/SiStripHitEffLoss. Internal document.

Université de Strasbourg

Markéta Jansová

Search for the supersymmetric partner of the top quark and measurements of cluster properties in the silicon strip tracker of the CMS experiment at Run 2

Résumé : Cette thèse présente trois études différentes basées sur les données de CMS du Run 2. Les deux premières sont des mesures des propriétés des amas dans le trajectographe à pistes de silicium de CMS, liées respectivement aux particules hautement ionisantes (HIP) et au partage de charge entre les pistes voisines (également appelé diaphonie). Le dernier sujet abordé dans ce document est la recherche du partenaire supersymétrique du quark top, appelé stop.

Une augmentation de l'inefficacité de reconstruction des hits dans le trajectographe à pistes de silicium de CMS a été observée au cours des années 2015 et 2016. Les particules hautement ionisantes ont été identifiées comme une cause possible de ces inefficacités. Cette thèse apporte des résultats qualitatifs et quantitatifs sur l'effet HIP et sa probabilité. Le HIP n'était pas la source la plus importante d'inefficacité et, une fois la source identifiée et corrigée, les nouvelles données révèlent qu'après cette correction, le HIP représente à présent la principale source d'inefficacité.

La seconde étude présentée porte sur les conditions utilisées dans la simulation du trajectographe par CMS afin de fournir des résultats réalistes. Ces conditions changent avec les conditions de fonctionnement du trajectographe et évoluent avec le vieillissement du trajectographe résultant des dommages causés par le rayonnement. Nous avons constaté que les paramètres de diaphonie obsolètes avaient une grande incidence sur la forme de l'amas. Dans cette thèse, les paramètres ont été réévalués et il a été confirmé que les nouveaux paramètres améliorent grandement l'accord des amas entre données et simulation.

La dernière partie décrit en profondeur la recherche de stop en utilisant les données collectées en 2016 (correspondant à $\int \mathcal{L} = 35.9$ fb^{-1}) avec un lepton dans l'état final. Aucun excès n'a été observé par rapport aux prédictions attendues par le modèle standard et les résultats ont été interprétés en terme de limites d'exclusion sur des modèles simplifiés.

Mot-clés : physique des particules, LHC, CMS, supersymétrie, trajectographe à pistes de silicium, simulation, particules hautement ionisantes, diaphonie

Abstract : This thesis presents three different studies based on the CMS Run 2 data. The first two are measurements of the cluster properties in the CMS silicon strip tracker related respectively to the highly ionizing particles (HIP) and the charge sharing among neighboring strips (also known as cross talk). The last topic discussed in this document is the search for the supersymmetric partner of the top quark, called the stop.

An increase in the hit inefficiency of the CMS silicon strip tracker was observed during the years 2015 and 2016. The highly ionizing particles were identified as a possible cause of these inefficiencies. This thesis brings qualitative and quantitative results on the HIP effect and its probability. The HIP was found not to be the largest source of inefficiency at that time and once the source was identified and fixed, the new data revealed that after this fix the HIP now represents the major source of the hit inefficiency.

The second study presented in this thesis focuses on the conditions plugged in CMS tracker simulation in order to provide realistic results. These conditions change with the tracker operating conditions and also evolve with tracker ageing resulting from the radiation damage. We identified that the outdated cross talk parameters largely impact the cluster width and seed charge. In this thesis the parameters were remeasured and it was confirmed that the new parameters largely improve the agreement of clusters between data and simulation.

The last part describes deeply the stop analysis using data recorded in 2016 (corresponding to $\int \mathcal{L} = 35.9$ fb^{-1}) with single lepton in the final state. No excess was observed in the full 2016 data ($\int \mathcal{L} = 35.9$ fb^{-1}) with respect to the standard model background predictions and therefore exclusion limits in terms of simplified model spectra were derived.

Keywords: particle physics, LHC, CMS, supersymmetry, CMS silicon strip tracker, simulation, highly ionizing particles, cross talk